Photoprotective effects of flavones on low-dose UVA-induced damage in normal and aged skin fibroblasts

Inaugural-Dissertation

zur Erlangung des Doktorgrades

der Mathematisch-Naturwissenschaftlichen Fakultät

der Heinrich-Heine-Universität Düsseldorf

vorgelegt von

Sarah Zerres

aus Düsseldorf

Düsseldorf, April 2021

aus dem Institut für Biochemie und Molekularbiologie I

der Heinrich-Heine-Universität Düsseldorf

Gedruckt mit der Genehmigung der

Mathematisch-Naturwissenschaftlichen Fakultät der

Heinrich-Heine-Universität Düsseldorf

Berichterstatter:

1. Prof. Dr. Wilhelm Stahl

2. Prof. Dr. Vlada Urlacher

Tag der mündlichen Prüfung:

23.09.2021

Eidesstattliche Erklärung

Ich versichere an Eides Statt, dass die Dissertation von mir selbständig und ohne unzulässige fremde Hilfe unter Beachtung der „Grundsätze zur Sicherung guter wissenschaftlicher Praxis an der Heinrich-Heine-Universität Düsseldorf“ erstellt worden ist.

Diese Dissertation wurde bisher keiner anderen Fakultät vorgelegt und es wurden keine vorherigen Promotionsversuche unternommen.

_____

Datum und Unterschrift

Content

Table 1.1 Abbreviations

2-ME	2-mercaptoethanol
Ado	adenosine
ADP	adenosine diphosphate
ADPR	adenosine diphosphate ribose
AMP	adenosine monophosphate
ATP	adenosine triphosphate
BrdU	5-bromo-2'-deoxyuridine
CPD	cylcobutane pyrimidine dimer
CT	control treated cells
ddH_20	purified water
DIAS	drug-induced accelerated senescence
DMSO	dimethyl sulfoxide
DNA	desoxyribonucleic acid
Doxo	doxorubicin
ECAR	extracellular acidification rate
ECM	extracellular matrix
ELISA	enzyme-linked immunosorbent assay
FCS	fetal calf serum
g	gravitational force
h	hours
HO-1	hemeoxygenase 1
MDA	malondialdehyde
MMC	mitomycin c treated cells
NAD^+	nicotinamide adenine dinucleotide
NER	nucleotide excision repair
NHDF	normal human dermal fibroblasts
OCR	oxygen consumption rate
OIS	oncogene-induced senescence
PC	phosphatidylcholine
ROS	reactive oxygen species
RT	room temperature
SASP	senescence-associated secretory phenotype
SA-β-Gal	senescence associated β -galactosidase
SEM	standard error of the mean
sham	unirradiated control
SPF	sun protection factor
UPLC	ultra performance liquid chromatography
UVA	ultraviolet A
v/v	volume by volume
w/w	weight by weight
γ-H2AX	phosphorylated form of histone H2AX

1 Introduction

1.1 The skin

Human skin is the organisms largest and most important barrier to external threats and often the site of first contact. External threats can result from exposure to UV radiation, toxic compounds, e.g. in cigarette smoke and pathogen encounter, to name a few. During evolution, each skin layer has optimized its function, ranging from thermoregulation and insulation to protection and stability. The three layers of human skin consist of an upper layer called epidermis, the dermis and the subcutis. The epidermis and the dermis are separated by a basal layer (stratum basale). This monolayer of basal cells has the task to regenerate keratinocytes and also hosts melanocytes[1]. The epidermis consists of mainly one cell type called keratinocyte. The keratinocyte progressively loses function and viability during its migration that started at the basal membrane (its origin) and ends as the outermost layer of skin. During this process, which takes 40 to 56 days (not including cell renewal at the basal membrane), keratinocytes lose their nucleus and with it more and more functions[2]. When reaching the outermost position, they are dehydrated and flat and called corneocytes. These fully differentiated keratinocytes are loosely stacked and provide a first barrier towards external factors, e.g. pathogens[3]. The second cell type located in the epidermis is called melanocyte. This cell, destined to produce and distribute the pigment melanin to neighbouring keratinocytes, is positioned at the basal layer. There, one melanocyte is responsible for pigmentation of several keratinocytes and therefor plays an integral part in photoprotection[4]. The epidermis is supported from the dermis underneath. The dermal layer of human skin provides stability, resistance to mechanical stress and harbours capillaries that also supply the epidermis[1]. The dermis makes up the most area of the skin layers and hosts the most prominent cell type, the fibroblast, which will be described in the following section. The third layer of skin is called subcutis and is composed mainly of adipose tissue. The subcutis provides an energy storage platform, insulation and shock absorption[1].

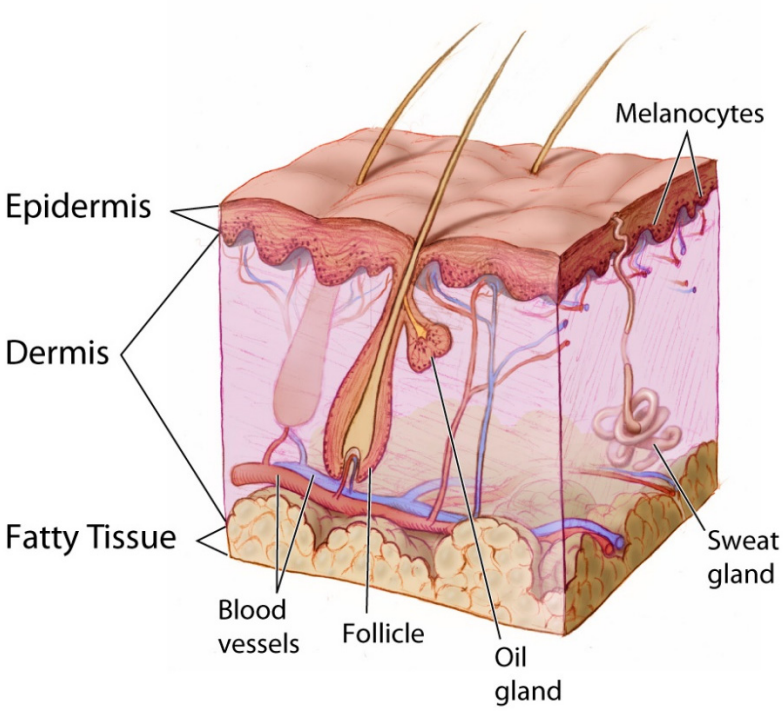

Figure 1.1 Layers of human skin. Taken from reference 5[5].

1.1.1 The fibroblasts of the skin

Fibroblasts make up the majority of cells of the dermis and are also abundant in many other tissues of the human body. This specified cell type has a spindle-like morphology and is responsible for connectivity and elasticity of the skin by excretion of structurally and functionally important proteins for the extracellular matrix (ECM). The ECM is a scaffold in tissues and provides resistance to mechanical forces, but it also modulates some cellular functions, e.g. via physiological ROS signalling[6]. The most abundant protein in a human body, collagen, is produced by fibroblasts and excreted to form the major component of the ECM. Other ECM proteins are elastin, fibronectin, laminin and glycosaminoglycans. The distinct composition of the ECM at varying locations in the human body modifies its function. In the last years, the importance of the ECM and therefore the fibroblasts for disease progression has been studied. The ECM is implicated in the pathogenesis of fibrosis, osteoarthritis and cancer and potentially many other diseases[7].

1.1.2 Fibroblasts and their role in intercellular signalling

Skin fibroblasts are implicated in signalling with several other cell types from the epidermis and dermis, e.g. with keratinocytes for the cause of wound healing[8]. As the major cell type residing in the dermis, which is populated by a variety of immune cells, fibroblasts are able to contact immune cells via paracrine signalling. The immune cells of the dermis, e.g. dendritic cells and macrophages, play a key role in wound healing and inflammation, mediated via purinergic signalling[9]. Through purinergic signalling, fibroblasts regulate these processes[10]. Extracellular purinergic signalling involves release of adenosine triphosphate (ATP) and nicotinamide adenine dinucleotide (NAD^+), which are degraded by several ectonucleotidases located on the cell surface of fibroblasts and immune cells[11,12]. As shown in Figure 1.2, ATP is converted to adenosine diphosphate (ADP) by the ectonucleoside triphosphate diphosphohydrolase-1 (CD39) and then further degraded to adenosine monophosphate (AMP). It can also be directly converted to AMP by the low-affinity ectonucleotide pyrophosphatase/phosphodiesterase-1 (CD203a). AMP is metabolized to adenosine (Ado) via activity of the ecto-5'-nucleotidase (CD73).

Another possibility for AMP and subsequent Ado generation is via cleavage of NAD^+ by means of the NAD^+-glycohydrolase (CD38) and following activity of CD203a or by CD203a alone. Ado can be further degraded by the adenosine deaminase (ADA) to inosine and via metabolization of inosine to hypoxanthine by the activity of purine nucleoside phosphorylase (PNP).

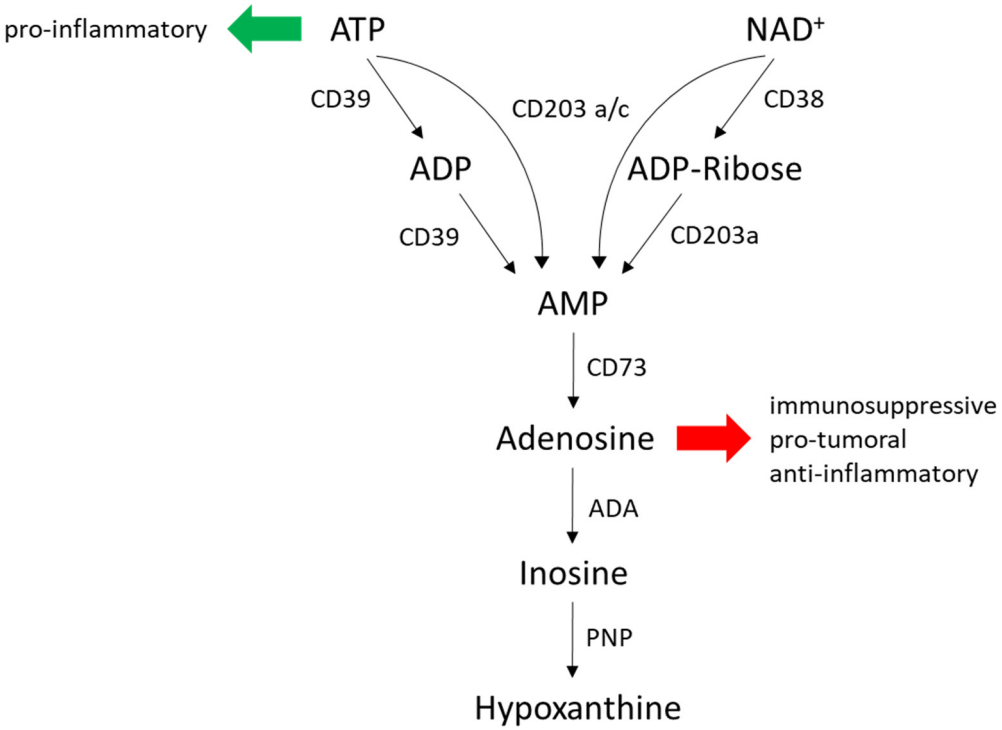

Figure 1.2 Extracellular degradation of ATP and NAD⁺ to adenosine and its derivatives in purinergic signalling. Based on and modified from reference 13[13]. ATP, adenosine triphosphate; ADP, adenosine diphosphate; AMP, adenosine monophosphate; NAD⁺, nicotinamide adenine dinucleotide; ADA, adenosine deaminase; PNP, purine nucleoside phosphorylase

ATP is released by cells suffering a damaging insult, thus creating a signal for immune cells to eliminate the damaged cell (pro-inflammatory)[12]. Some cancer cell lines and patient biopsies have been shown to overexpress CD73, as reviewed by Gao et al.[14]. The overexpression of CD73 can divert the pro-inflammatory ATP signal into the contrary, by degrading it to ADP, AMP and subsequently adenosine. A persistently increased adenosine concentration is known to have immunosuppressive functions[15]. In a physiological setting, adenosine signalling is important for a balanced immune reaction, preventing prolonged or overshooting immune reactions, thereby promoting homeostasis[12]. Recently, a differentiated type of fibroblasts, cancer associated fibroblasts (CAFs), has been characterized, which overexpresses CD73[16]. Those CAFs are part of the tumor microenvironment and have been linked to poor clinical outcome when expressed in high levels[16]. Exploitation of the CD73 function is seemingly not only used by cancer cells themselves to provide an immunosuppressive and tumor-permissive environment, but might also be provided by CAFs. Adenosine receptors on immune cells are

responsible for the induction of immunosuppressive signalling. Several immune cells have been shown to carry receptors responsive to purinergic signalling, e.g. neutrophils, macrophages and dendritic cells[9]. Adenosine has been shown to reduce natural killer cell activity and impair macrophage chemotaxis and function[17,18]. Therefore, fibroblasts contribute to diverting immune cells by adenosine signalling in some cases. Furthermore, tumor cells rely on the modification of the extracellular matrix by fibroblasts in order to migrate and to induce angiogenesis, a dependency that is called tumor-stroma interaction[19].

As outlined above, fibroblasts are not passive cells but participate in communication with other cell types and therefore play a pivotal role in physiology and pathologies of the skin.

1.2 Ultraviolet radiation

Ultraviolet (UV) radiation is a component of the electromagnetic spectrum of light emitted from the sun. It covers wavelengths from 100 to 400 nm and is divided into three wavelength regions: UVA, UVB and UVC. UVC radiation does not reach the earth's surface, but would theoretically be the most dangerous type of UV radiation to life on earth as it is the most energetic wavelength region, causing direct DNA damage (λ_{max} = 250 - 280 nm). UVB radiation is absorbed by DNA as well, but the wavelengths from 280 to 315 nm have a lower frequency and therefore have lower energy. UVB radiation is not filtered as strongly by the atmosphere as UVC and therefor reaches the skin of humans. The most abundant type of UV radiation reaching the surface of the earth is UVA radiation, covering wavelengths from 315 to 400 nm. The frequency of UVB radiation allows penetration only into the epidermis, while UVA radiation with lower frequency penetrates the dermis. For a long period of time, it has been postulated that the main damaging effect of UVA radiation can be ascribed to the production of reactive oxygen species (ROS) and consequently oxidative damage to macromolecules. However, recently, it has been shown that UVA radiation induces even higher amounts of cyclobutane pyrimidine dimers (CPDs), a photolesion of the DNA, than oxygenated bases[20]. Additionally, these CPDs are repaired slower than UVB-induced CPDs in whole human skin and in skin cells, all pointing towards an underestimated damaging efficacy of UVA radiation[20–22].

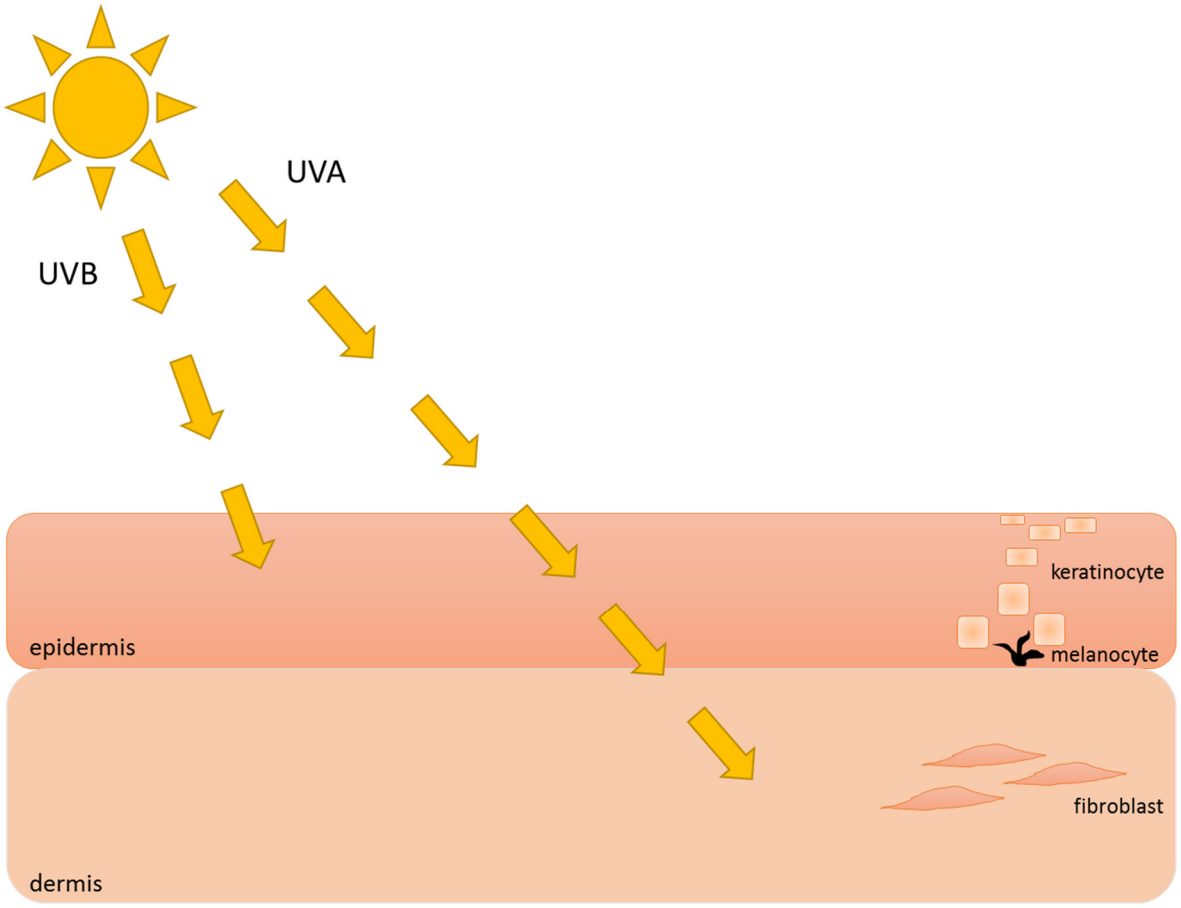

Figure 1.3 Penetration depth of UVA and UVB radiation into human skin.

1.2.1 Exposition to UV radiation: benefits and risks

It is estimated by Godar et al., that an indoor working European receives an annual UV dose of 10000 to 20000 J/m². Of note, this dose is increased by 30 % or more when a vacation is included in the calculation[23]. The acute amount of UV radiation an individual is challenged with depends on the time of day and year, the longitude and altitude of the location, the particulate matter in the air, ozone, ground reflection and cloud cover. During summer, the position of the sun towards earth (solar zenith angle) is most favourable for high exposure due to the angle in which it is located to the earth, followed by spring, fall and then winter[23]. Especially at times when the sun is at zenith (noon), the highest amount of UVB radiation reaches the earth's surface due to less atmosphere to cross, while earlier and later timepoints allow mostly longwave UVA radiation to pass[24]. UVA radiation is less impacted by time of the day compared to UVB radiation, indicating that mornings and evenings do not severely decrease exposure to those wavelengths[25]. Exposure to UV radiation is increased by altitude and proximity to the equator. Air pollution, ozone and clouds scatter or interact with photons

from the sun and therefore decrease UV radiation that reaches an individual. Reflection from ground structures like sand and water influences UV exposure, as well, but reflection from snow poses the greatest risk[23]. The individual risk is influenced by a person's features, e.g. skin colour, tanning behaviour and genetic predispositions, as well. Genetic disorders, that render an individual prone to UV-induced cellular damage, are not common, but very severe. Xeroderma pigmentosum (XP) is induced by a defect in proteins responsible for nucleotide excision repair (NER)[26]. A defect in NER by mutations in one of the involved proteins leads to accumulation of UV-induced lesions. Individuals with XP suffer from development of several skin conditions and cancers early in their life and have a shortened life expectancy[27].

As another risk factor, natural and artificial tanning should be mentioned. The increased use of tanning beds with increasingly high and unnatural proportions of UVA radiation, often exceeding recommended thresholds, pose a short- and long-term risk to human health[28]. The use of tanning beds has been linked to an increased risk of melanoma formation[29]. The doses achieved by artificial tanning are often far exceeding the irradiance achieved by exposure to midday sun in summer in Greece[28].

The risks, although known, are often undermined by the positive marketing for vitamin D production in the skin upon exposure to sunlight. Sufficient vitamin D levels are important for calcium and phosphorus homeostasis and are produced upon exposure to UVB radiation[30]. Despite the need for a controlled and wisely dosed exposure to UVR, especially UVB radiation for vitamin D production, most alterations caused by UV radiation negatively affect the organism.

1.2.2 Photochemistry

To understand the interaction of photons emitted from the sun and cellular structures in the skin, the basics of photochemistry have to be explained. Photons can be absorbed by chromophores in the skin, of which heme, flavins, tryptophan, melanin and others have been proposed[31]. The responsible structural features are often those parts of a molecule comprising of conjugated, delocalized π-electrons. Upon absorption of a photon, the chromophore is excited and is promoted from the ground state to a higher excited energy level. For most molecules, the excited energy state upon photon absorption is the excited singlet state[32]. From the excited singlet state, the molecule has several possible pathways to return to the ground state: by emitting a photon via fluorescence or by vibrational relaxation and thermal

energy dissipation[32]. However, it can also directly react with other molecules, e.g. substrates in the skin. Another possibility is the conversion to an excited triplet energy state via intersystem crossing. Intersystem crossing is a process in which a molecule can transit from a singlet state to a triplet state in a non-radiative way. The excited triplet state can then lower its energy state to the ground state by phosphorescence or vibrational decay[32]. The excited triplet state molecule can undergo reactions with other molecules, as well (see 1.2.5, photosensitization processes)[32]. Since the singlet state of a molecule is less stable than the excited triplet state, the majority of subsequent reactions occurs between excited triplet state molecules and other molecules[32,33].

1.2.3 UVA and the skin

There are many reasons for why UVA radiation should not be considered an inferior insult to human health compared to UVB radiation. It was shown, that UVA radiation induces melanin production[34], a protective process initiated by melanocytes in the epidermis. In keratinocytes, UVA radiation induced DNA strand breaks which might favor tumorigenesis[35]. The detailed effects of UVA radiation on macromolecules (DNA, proteins, lipids) will be described below, together with how UVA radiation affects the immune system and the process of inflammation.

1.2.4 DNA damage

Damage to DNA can be induced via direct absorbance of photons or via secondary reactions. These secondary induced DNA lesions have been found to be induced due to ROS generation via UVA and subsequent damage mediated by singlet oxygen ($^1O_2$) and hydroxyl radicals ($OH^{\cdot}$) to bases[36]. Direct absorbance of energy from photons of UVB and UVC wavelengths is known to cleave double bonds in pyrimidines. Neighbouring pyrimidines might rearrange to form a bulky lesion called cyclobutane pyrimidine dimer (CPD) via a 2 + 2 cycloaddition. Upon excitation of the C5=C6 double bond in each pyrimidine base, two single C-C bonds form to yield a cyclic connection. But CPDs are also induced by UVA radiation, although the absorbance of DNA in the UVA range is less. It has been shown in keratinocytes and melanocytes, that UVA- and UVB-induced CPD levels were comparable[37]. Ikehata et al. have also shown, that CPDs are the main cause for UVA-induced mutagenicity in mouse skin by analysis of mutation pattern[38]. CPD formation may arise via photosensitization mechanisms. Excitation of endogenous chromophores leads to their excitation to an excited singlet state with a short half-life. Upon intersystem crossing, a more stable triplet state may form. If the

energy of this triplet state is sufficiently high (above the triplet energy of a thymine base), a triplet-triplet energy transfer may induce CPD formation[39]. As thymine has a lower triplet state energy than other bases, they might be the most prominent acceptor for triplet triplet energy transfers[38]. Indeed, T-T dimers are the most common lesions in UVA irradiated cells, followed by C-T and T-C dimers and only scarcely C-C dimers[40].

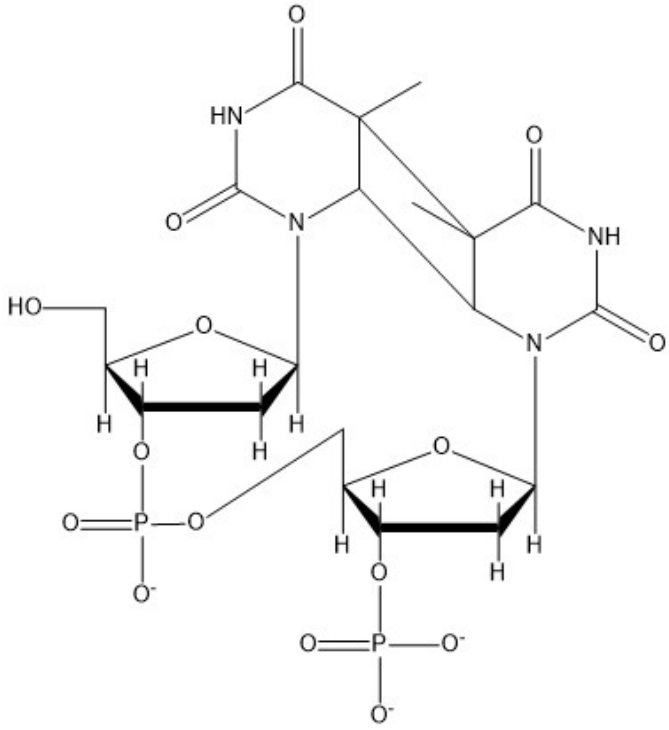

Figure 1.4 Cyclobutane pyrimidine dimer (CPD) between two adjacent thymines.

Other forms of UVA-induced DNA damage are the pyrimidine (6-4) pyrimidone photoproduct (6-4 PP) and its photoisomerization product, the Dewar valence isomer. The 6-4 PP shows a single bond connection between two neighbouring pyrimidine bases. If this photolesion is excited by UV radiation, a Dewar valence isomer can form. However, both lesions appear less frequently in UVA-irradiated cells than CPDs[41].

1.2.5 Oxidative damage

UVA radiation was long believed to induce DNA damage only via secondary reactions, by increasing intracellular levels of ROS. This process involves endogenous photosensitizers like porphyrins and flavins[42,43], that absorb the energy of UVA photons and transfer the energy to cellular molecules (substrates). The substrate molecules therefore do not need to absorb in the UV region. Oxidative photosensitization reactions are distinguished by their primary interacting molecules and can be divided into type I and type II reactions. In both reactions, a

sensitizer is excited by photons (sens*) and then dissipates that energy to a substrate. If a sensitizer is excited, a singlet energy state is adapted. This singlet state is labile and so a long-lived triplet state is preferentially adapted by intersystem crossing. The sensitizer in triplet state (^{3}sens*) can react with molecules in the vicinity and lead to either formation of ROS or substrate radicals via electron and energy transfer reactions.

Type I reactions involve direct interaction of the photosensitizer with the substrate. The triplet excited sensitizer accepts an electron from or donates an electron to a substrate in the vicinity, e.g. DNA, via an electron transfer reaction. In the case of guanine, a guanine cation radical is formed along with a sensitizer anion radical. Via reaction with oxygen, the guanine cation is oxidized to form 8-oxo-7,8-dihydroguanine (8-oxoG)[44]. In fact, the main UVA-induced oxidative damage to DNA is the oxidation product of a guanine base (8-oxoG)[20]. This might coincide with the low oxidation potential of guanine in comparison to the other bases[45]. Although oxidative damage was long believed to be the main threat of UVA radiation to cellular DNA, it was shown that CPDs are the main lesion induced by UVA, not 8-oxoGua[21,22]. Between both lesions, a ratio of 5 was described for many skin cell types except melanocytes[41].

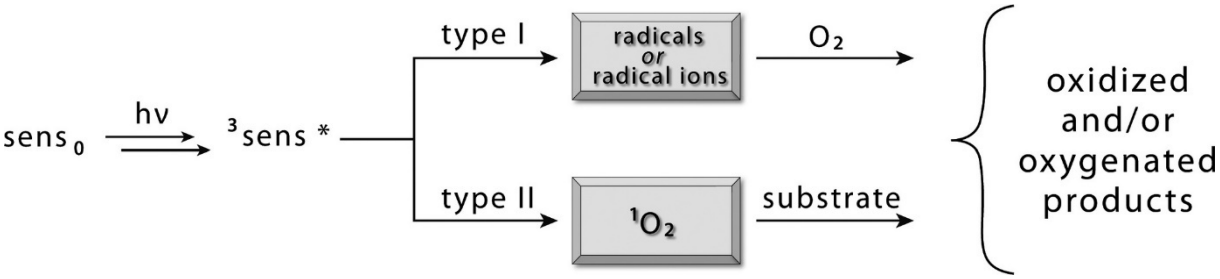

Figure 1.5 Photosensitization reactions type I and type II. Republished with permission of John Wiley & Sons - Books, from Type I and Type II Photosensitized Oxidation Reactions: Guidelines and Mechanistic Pathways, American Society for Photobiology, 93, 2017; permission conveyed through Copyright Clearance Center, Inc.[44].

In type II reactions, the photosensitizer first reacts with molecular oxygen. Via energy transfer from the excited sensitizer, oxygen changes from ground state (triplet) to the singlet state and singlet oxygen ($^1O_2$) is formed[44]. This oxygen state is more reactive than the ground state and can itself react with a substrate, e.g. DNA[44]. Singlet oxygen is also a precursor for the formation of other damaging oxygen species, e.g. hydrogen peroxide (H_2O_2) and hydroxyl radical ($OH^{\cdot}$).

The hydroxyl radical only has a short lifetime compared to other ROS but is very reactive[44]. These additionally formed ROS can in turn also react with DNA[45].

There are several lines of evidence suggesting that photosensitization is a UVA-dependent mechanism. A photosensitizer-like drug, azathioprine, has been shown to increase the susceptibility of drug-receiving patients to UVA radiation, but not to UVB radiation, indicating the specificity of photosensitization to the UVA wavelength region[46]. Furthermore, the photosensitization process is used in the psoralen and UVA phototherapy (PUVA), using exogenous photosensitizers like psoralens and non-toxic doses of UVA light to treat epidermal conditions like psoriasis[45].

Oxidation of lipids is another process induced by UVA radiation[47]. Reactive oxygen species formed by UVA radiation initiate a chain reaction in lipids, e.g. from cellular membranes. This alteration can lead to a decreased membrane integrity. In detail, ROS produced by UVA radiation abstract a hydrogen from lipids such as polyunsaturated fatty acids (PUFA) to form a lipid radical ($L^{\cdot}$). Oxygen can then add to the oxidized lipid to form a lipid peroxy radical ($LOO^{\cdot}$). Upon further hydrogen abstraction of another PUFA by the $LOO^{\cdot}$, a second lipid radical ($L^{\cdot}$) and a lipid hydroperoxide (LOOH) are formed. This chain reaction can be terminated by addition of antioxidants. One major decomposition product of a UVA-initiated chain reaction is malondialdehyde (MDA). It is a degradation product of PUFAs and can be used in the determination of oxidative stress as a marker for lipid peroxidation[48].

Further, protein oxidation is occurring in response to UVA radiation. Protein oxidation includes proteins of the DNA repair systems, e.g. NER, among many others[49]. In general, all amino acid side chains are prone to oxidation, especially S-groups in methionine and cysteine. Of note, the effects of oxidation and DNA damage cannot be viewed as distinct processes, but are likely to affect one another as seen by oxidatively impaired repair of CPDs. Cells of xeroderma pigmentosum variant patients (XP-V) are proficient in NER but deficient in the translesion synthesis pathway responsible for replication of damaged DNA, skipping over CPDs[50]. In XP-V cells, UVA radiation increased oxidative damage and inhibited DNA replication and lesion removal, possibly by oxidatively modified repair enzymes. Treatment with the antioxidant N-acetylcysteine (NAC) improved the removal of CPD lesions, suggesting a potent role of oxidative stress in UVA-induced cytotoxicity and the link between oxidative stress and DNA damage[50].

1.2.6 Inflammation

The primary, general inflammatory response of the skin to UV radiation is the initiation of vasodilation[51]. Consequently, increased blood flow leads to induction of erythema, a reddening of the skin. Erythema is often used in studies comparing UV responses in patients. A minimal erythemal dose (MED) describes the dose of irradiation after which a slight distinction between normal and reddened skin can be made. It applies to UVA and UVB and describes a subjective assessment by eye. Up to a certain threshold, UV dose and MED are proportional[52]. Further alterations in inflamed skin due to UV radiation include vascularization, melanogenesis and increase in skin thickness[51]. The leading causes for vasodilation and erythema is the release of prostaglandins and nitric oxide (NO) with additional roles of other cytokines[51]. UVA radiation induced erythema, in contrast to UVB radiation, was not found to be dependent on prostaglandin signalling[51]. However, it is known that UVA radiation increases NO levels in skin through upregulation of nitric oxide synthase and the release of NO from endogenous donor molecules[53]. The time course of UVA-induced erythema is different to UVB-induced erythema[54]. UVA radiation also directly increases the levels of inflammation markers, e.g. interleukins (IL-1α, IL-1β, IL-6, IL-8) and intercellular adhesion molecule (ICAM1)[25]. As with other UV-induced effects, primarily those of UVB radiation on human skin have been investigated in regard to inflammation. Irradiation of the skin with UVB can cause the appearance of sunburn cells. Those cells have suffered an irreparable DNA damage and thus initiate apoptosis[55]. Furthermore, UVB radiation causes release of cytokines and prostaglandins with pro-inflammatory functions, which will not be discussed in detail here[56].

1.2.7 Immunosuppression

Although UVA radiation and its effect on the immune response has long been unstudied, due to the focus on UVB investigations, it is now established that UVA radiation induces immunosuppression, which is a prerequisite for cancer formation. As an example, UV-induced tumors, that have been transplanted into immunocompetent mice, regressed, while tumors transplanted into UV-irradiated mice proliferated[57]. Immunosuppression is likely mediated by the direct effect of UVA radiation on immune cells and via secondary effect from ROS generation[56]. UVA irradiated mice show a decrease in the number of epidermal Langerhans cells, an immune cell type involved in antigen presentation[57]. Antiviral and antibacterial genes were downregulated upon UVA irradiation and the interferon alpha/beta (IFNα/β) signalling

cascade, which also has implications for tumor suppression, was inhibited in reconstituted skin[25]. Recurring herpes simplex virus infections after UV exposure are likely to be caused by the previous finding. Furthermore, human memory and recall immunity, e.g. to nickel, were decreased upon UVA irradiation[58]. The PUVA therapy, a photosensitization process with UVA light, has been shown to increase the susceptibility to a specific type of skin cancer, the squamous cell carcinoma (SCC)[59]. Additional evidence for UVA-induced immunosuppression comes from a study showing that the ability of sunscreens to prevent immunosuppression was found to correlate with the sunscreens UVA-photoprotection efficacy[60]. Noteworthy, UVA-induced immunosuppression has been observed with UV doses that are experienced in everyday life[58].

UVA penetrates deeper into the skin than UVB and therefore has access to different immune cells situated in the dermis, e.g. T lymphocytes, mast cells and dendritic cells[61]. Hence, UVA radiation might actively address a larger pool of immune cells than UVB radiation. Fibroblasts, as it is the main cell type in the dermis, might have an important role in the immunomodulatory response to UVA radiation. Indeed, CAFs, one specialized type of fibroblast, have been shown to mediate the immunosuppression cancer cells are dependent on[19].

1.2.8 Photoaging

UVA radiation is the major contributor to photoaging or premature aging of the skin[62]. Photoaging is one factor of extrinsic aging that adds to the process of intrinsic aging discussed in the aging section. This accelerated aging affects complexion and decreases the functionality of the skin. The contribution of photoaging to the intrinsic aging process depends on the cumulative exposure, duration and intensity of UVA exposure, which can be modulated by photoprotective measures[63].

The phenotype of photoaged skin is dominated by deep wrinkles, uneven pigmentation, rough texture and lack of hydration and can be distinguished from the phenotype of intrinsically aged skin[64]. The disbalance between matrix metalloproteinases (MMPs) and tissue inhibitor of matrix metalloproteinases (TIMPs) is responsible for many of the signs of photoaging. MMPs are responsible for remodelling of the ECM during wound healing, development, angiogenesis, tumor invasion and other processes. MMPs degrade structural proteins of the ECM and can be divided into substrate-specified classes, e.g. collagenases, gelatinases,

stromelysins[7]. The precursor zymogens of these proteinases are activated extracellularly[7]. UVA radiation has been shown to increase the synthesis and secretion of several MMPs in fibroblasts and thereby increases signs of photoaging by degradation of connective tissue in the skin[65]. This process is presumably induced by singlet oxygen[66]. As a result, UVA radiation promotes skin deterioration.

1.2.9 DNA repair mechanisms

Generally, UV-induced lesions in nuclear DNA are mainly repaired via two complex mechanisms, the nucleotide excision repair (NER) and the base excision repair (BER). The BER is a process locating, incising and repairing a single modified or damaged base and is described to predominantly act on endogenous oxidative damage[67]. The NER is mainly responsible for repair of CPDs and related photoproducts and cleaves several nucleotides at the lesion site[67]. The importance of NER is well explained by diseases like XP (as described above), where a lack of repair proteins leads to accumulation of mutagenic lesions and early onset of UV-induced cancer development.

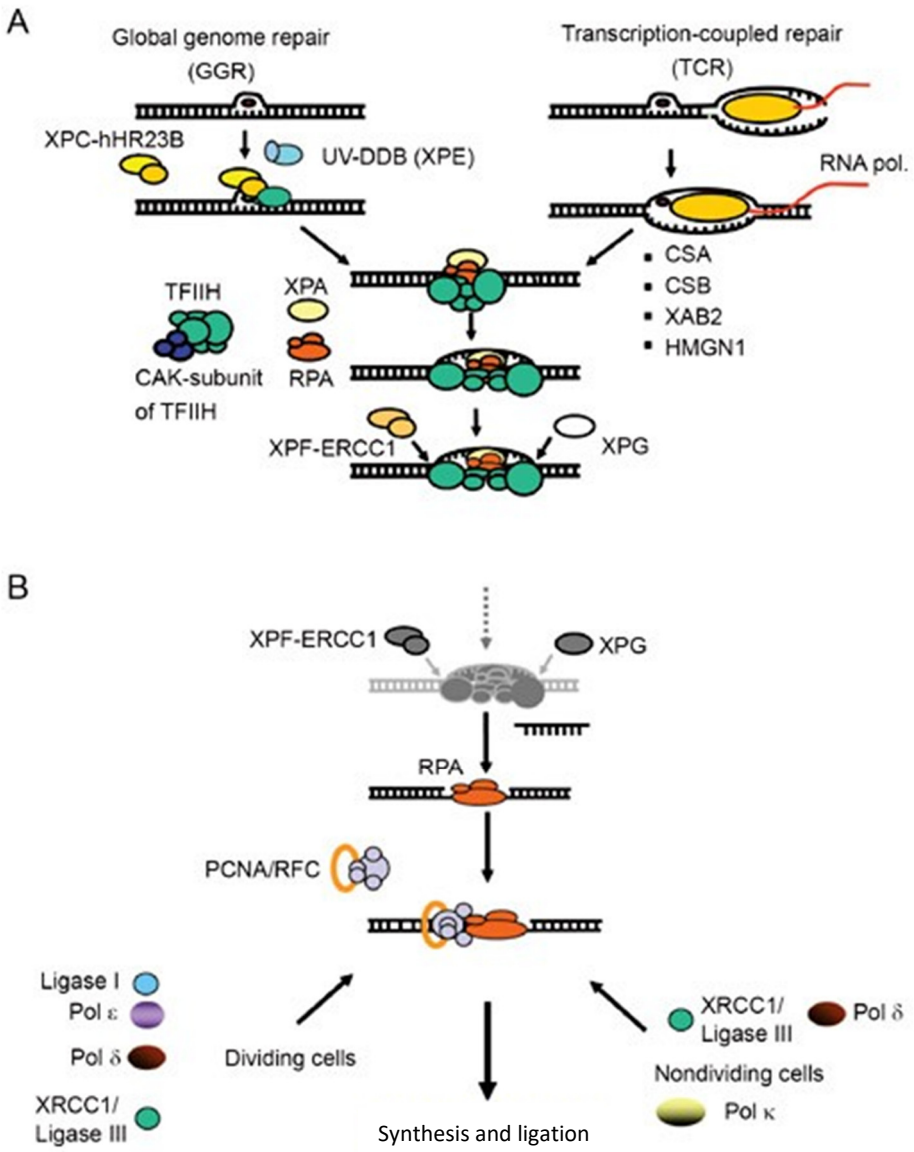

Figure 1.6 Schematic depiction of the nucleotide excision repair pathways. Damage recognition in TC-NER and GG-NER (A) and ligation steps (B) are shown and explained in the text below. Reprinted by permission from Springer Nature Customer Service Centre GmbH: Springer Nature, Cell Research, Transcription-coupled nucleotide excision repair in mammalian cells: molecular mechanisms and biological effects, Fousteri, M., Mullenders, L. (2008)[68].

NER can be divided in the transcription-coupled NER (TC-NER) and the global genome NER (GG-NER). The latter repairs photoproducts irrespective of transcription, while TC-NER repairs mainly on the actively transcribed DNA strand. TC-NER is initiated upon stalling of the RNA polymerase II (Pol II), a process occurring after distortion of the DNA by CPDs. It is hypothesized, that the prolonged interaction of Cockayne syndrome group B (CSB) with Pol II is the trigger for TC-NER, and not the detection of the lesion itself[68]. Stalling of Pol II is initiated

upon encounter with distorting or bulky lesions only, excluding oxidized purines and other lesions from TC-NER activation[69]. The mechanism of NER involves a complex network of proteins that have well-regulated spatiotemporal functions. The mechanisms of GG-NER and TC-NER differ, but are believed to converge at the end. In GG-NER, a complex including Xeroderma Pigmentosum complementation group C (XPC) binds to single stranded DNA, while for CPD detection, a specialized ultraviolet-damaged DNA damage binding protein (UV-DDB) complex including DNA damage binding protein 1 and 2 (DDB1, DDB2) is required[70]. This complex then recruits the XPC complex. The transcription initiation factor II H (TFIIH) complex together with replication protein A (RPA) and XPA is able to bind to XPC and form an open repair complex[67]. Helicase action of XPD and XPB in the TFIIH complex unwinds DNA and excision can occur[68]. For this, an incision is made by use of other XP (as described below) proteins on either side of the lesion several bases away. The gap is then filled by polymerases and ligated by ligases. In TC-NER, the DNA damage is recognized by CSA and CSB. The stalled polymerase II is shifted away from the lesion site by the CSA-CSB complex to reveal the damage to TFIIH. XPA binds to TFIIH, if the complex is located at a lesion, which presents a lesion verification step, followed by recruitment of endonucleases[68]. On the opposing DNA strand, RPA complexes stabilize the intermediate state of unwound DNA. A lesion-containing oligonucleotide (around 30 nucleotides) is released by 3´endonuclease XPG and 5´endonuclease XPF-ERCC1 and the gap is filled by DNA synthesis, followed by DNA ligation[69].

A NER-independent repair mechanism for UV-induced DNA lesions is proposed by Mazouzi et al., although this has yet to be shown for UVA radiation[71].

1.2.10 UVA radiation and skin cancer

Skin cancer is the most common malignancy with increasing incidences worldwide. Since it was estimated, that more than 90 % of various skin cancers can be linked to UV-exposure, UV radiation is one of the major carcinogens[72]. Skin cancers can be divided into non-melanoma skin cancers (NMSC) and melanoma. The latter is the deadliest form of skin cancer, but with lower incidence than non-melanoma skin cancers. Worldwide, the incidence for melanoma of the skin has been increasing for decades with especially high incidences in the elderly population[73]. NMSCs are further divided into more specified cancer types, the most abundant being the basal cell carcinoma and the squamous cell carcinoma. The latter accounts for around 75 % of all deaths in the category of NMSCs[74]. For all of these cancers, UV radiation is

the leading cause[75,76]. The occurrence of the NER-deficient disease XP, in which patients were extremely sun-sensitive and prone to skin cancer development, led the way to the understanding that UV radiation and skin cancer are tightly linked[49]. There are several lines of evidence suggesting a pivotal role for UVA radiation in the development of certain skin cancers, as e.g. the discovery of UVA fingerprint mutations in the germinative layer of squamous cell carcinoma[77].

1.3 Photoprotection

Skin cells have had millions of years of coevolutionary adaption to exogenous and endogenous threats like reactive oxygen species, so their defence mechanisms are able to counteract moderate amounts of stress via a complex network of enzymes, respective cofactors and antioxidants. As reactive oxygen species are a product of physiological cell activity, a differentiation between eustress and distress can be made. Eustress can be perceived as physiological levels of ROS that are responsible for signalling[78]. Distress challenges the cellular defence network to an extent where damage to macromolecules outbalances the capacity of cellular antioxidant systems. UV radiation is one of the extrinsic factors challenging the redox homeostasis in cells. A major effect of UVA radiation is the generation of reactive oxygen species in cells. Therefore, in some way, protection from UV-induced ROS is a measure of photoprotection.

The antioxidant systems generally available to eukaryotic cells are of enzymatic and non-enzymatic nature. Glutathione (γ-glutamyl-cysteinyl-glycine, GSH) is a constitutively present antioxidant with the ability to scavenge radicals. In turn, a GSH radical and subsequently glutathione disulfide (GSSG) is formed which is recycled by the glutathione reductase (NADPH dependent)[79]. The formation of GSSG is also coupled to the detoxification of H_2O_2 and other peroxides by the glutathione peroxidases (GSH-Px)[79]. Another enzyme detoxifying H_2O_2 is catalase. The reaction products are water and oxygen. A precursor of H_2O_2, superoxide anion ($O_2^{\cdot-}$), is detoxified by the enzyme superoxide dismutase (SOD). Further antioxidants protecting the skin from ROS are the lipophilic vitamin E (tocopherol), the hydrophilic vitamin C (ascorbate) and carotenoids (e.g. β-carotene) amongst a large variety of other components of the antioxidant network[79,80].

Another important pathway in the cellular defence comprises NF-E2-related factor-2 (Nrf2). Upon oxidative stress or other modifications of the inhibiting Kelch-like ECH-associated

protein (Keap1), Nrf2 ubiquitination is prevented and translocation into the nucleus can occur. There, Nrf2, together with one of the small MAF proteins, binds to the antioxidant response element/electrophilic response element (ARE/EpRE)[81]. This binding activates the transcription of around 200 cytoprotective genes, including antioxidative and detoxifying genes, as well as genes regulating immunity, inflammation and cell growth[82]. The stress-inducible isoform hemeoxygenase-1 (HO-1) is amongst the antioxidant proteins under influence of Nrf2 signalling[83]. Repression of the Nrf2-mediated antioxidative pathway is implicated in a disease of premature aging, the Hutchinson-Gilford progeria syndrome (HGPS)[84]. Furthermore, Nrf2 has been shown to be upregulated by low-dose UVA radiation in dermal fibroblasts[85].

Melanin, the pigment responsible for the perception of a tanned skin, is another participant in skin photoprotection. It provides a sun protection factor (SPF) of around 2-3 by absorbing photons mainly from the UVB region[86]. However, melanin has shown deleterious effects in combination with UVA light. The distinction between eumelanin and pheomelanin provided the first data for a damage enhancing role of the latter. Pheomelanin synthesis requires the presence of antioxidants and depletes the antioxidant defence for subsequent UV light insults[87]. Later, the dependency of UVA-induced melanoma formation on the presence of melanin was discovered[88].

1.3.1 Exogenous vs. endogenous photoprotection

Endogenous photoprotection, via naturally occurring compounds in the skin or via oral supplementation, relies on the physicochemical function of molecules within a cell and requires systemic distribution. Therefore, one of the essential functions of endogenous photoprotectants is their bioavailability and uptake in the target cell. Uptake is often limited by conversion of the parent compound via detoxifying and conjugating processes (phase I/II). Once this obstacle is overcome by a suitable structure, the molecule can exert its function. One function of endogenous photoprotecting compounds might be the scavenging of reactive oxygen and nitrogen species via antioxidant properties. By doing so, direct damage resulting from UV-derived ROS or subsequent reactions can be inhibited. Another function of endogenous photoprotecting compounds is their ability to induce pathways responsible for upregulation of defence genes, e.g. through activation of the ARE[89]. Compounds that are used endogenously for photoprotection range from carotenoids to flavonoids and will be discussed in section 1.3.2.

Exogenous or topical photoprotection relies mainly on physical scattering and reflection or on absorption of UV light and is less dependent on a specific target cell type or tissue distribution, as its mere task is to shield the skin from damaging UVR without cellular interaction. Shielding can be achieved by absorption of photons due to a suitable structure that contains a conjugated π electron system as in the case of aromatic compounds, e.g. flavonoids, or in certain carotenoids, e.g. phytofluene and phytoene[90]. The more conjugated double bonds present in the system, the higher the wavelengths that are absorbed. Most carotenoids absorb in the visible wavelengths because of their long conjugated double bond chain, while phytoene and phytofluene with their three or five double bonds absorb in the UVB and UVA region, respectively[90]. Flavones, containing aromatic rings, show absorbance in the UVB and UVA region, as well.

Topical photoprotection can be provided by sunscreens. There are several sunscreen formulations with different modes of action available. Although the function is always provided by chemicals, they are divided into organic-chemical and physical-mineral sunscreens[91]. Organic-chemical sunscreens absorb photons and are thereby excited to a higher energy state. They can divert that energy as heat dissipation and subsequently achieve their ground state energy level. Chemical UV filters, like oxybenzone, have been regularly found systemically after application, although they are not desired to penetrate the skin in order to be recognized as safe[92]. Some of the ingredients in chemical sunscreen formulations have been found to act as hormonal disruptors *per se* or after UV-induced structural changes[93]. Physical-mineral sunscreens act immediately as they form a layer above the skin that absorbs or reflects photons. The most prominent mineral sunscreen agents are titanium dioxide (TiO_2) and zinc oxide (ZnO)[94]. Formulations with mineral compounds often leave a white cast on the skin, as they provide protection by the mostly opaque layer they form. Most recently, nanosized TiO_2 and ZnO have been developed and used in sunscreen formulations, although their use is still critically discussed[92]. Due to the decreased particle size, they can penetrate into the skin more easily, e.g. through wounds and hair shafts, which is undesired and decreases their protective function. To achieve the declared SPF as indicated on a sunscreen product, even and thorough application is essential. In laboratory conditions and for measurement of the SPF, 2 mg/cm² of the sunscreen are tested, which is the recommended dose to be applied to the skin[95].

Most commonly, several UV filters and agents are introduced into a sunscreen formulation to either increase the effective range of absorbance or to provide a support for the active UV filter. By adding antioxidants to the formulation, damage through unabsorbed UV rays can be minimized and photoinduced alterations of the UV filter itself are decreased. The addition of beneficial, not necessarily UV-absorbing compounds is called booster effect and improves the products stability and efficacy[92].

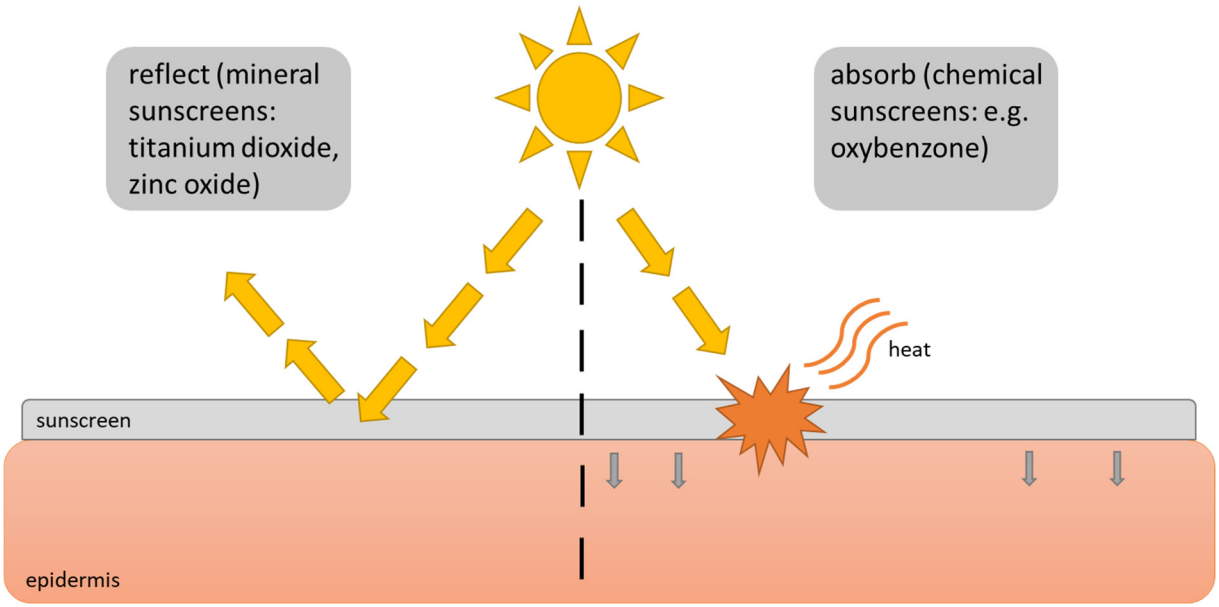

Figure 1.7 Simplified depiction of topical photoprotection.

1.3.2 Natural substances in photoprotection

Natural compounds are valuable tools for prevention of a variety of the aforementioned UVA-induced effects on skin cells. Due to the high diversity of phytochemicals, a combination of several can, in theory, prevent manifold effects. However, with the diversity of natural compounds even among just one class of phytochemicals, e.g. flavonoids, their bioavailability, stability and distribution is highly various and complicates their use[96]. Of the many available natural compounds, mainly produced by plants, most are part of the human diet to a certain extent. Carotenoids are probably the best investigated phytochemicals in regard to photoprotection. Carotenoids have been shown to assist in photoprotection of human skin, e.g. by scavenging ROS[97]. Intervention studies with supplementation of ß-carotene or lycopene have led to increased MEDs and protection from erythema after several weeks of supplementation[98]. Carotenoids have further been investigated for their regulatory effect on inflammation in animals and humans, showing prevention of NFκB signalling[99]. However,

there are optimal concentrations for use of each compound and supplementation should not be carried out without knowledge of the levels at which the compound exhibits prooxidant effects[100].

Compounds from marine organisms and algae have been under investigation lately, as their location and exposure to UV light under extreme conditions provides the need for optimal photoprotection for the species. Some of these compounds show promising results in cell culture. For example, mycosporine-like amino acids have shown antioxidative properties and activated Nrf2-dependent defence additionally to their absorbing function[101].

It should be considered, that photoprotective effects of natural substances that completely replace topical sun protection are yet to be discovered. Most natural compound provide some extent of photoprotection, but the capacities are more or less limited due to issues of bioavailability or non-equal distribution in the skin[102]. Therefore, it is essential to combine endogenous and exogenous protection from the sun for optimal results.

1.4 Flavonoids

Flavonoids, a major group of plant secondary metabolites, are widely produced from all around the plant kingdom for protection from UV rays and infestation by insects and fungi but also for petal pigmentation[103]. Their structure is based on a flavan backbone as shown in Figure 1.8. Flavonoids are further classified by substitutions on the C ring[104].

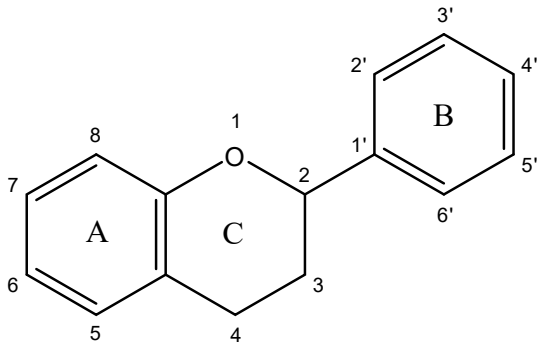

Figure 1.8 Flavan backbone of flavonoids. A and B depict the phenyl rings, connected by a 3-carbon bridge forming a heterocyclic ring C.

Flavones are a large subgroup of flavonoids. Their structure consists of a flavan backbone that is extended by a double bond between C2 and C3 and oxidation at C4 (see Figure 1.9)[103]. Flavones are responsible for white and blue flower colors in combination with

anthocyanins[105]. In plants, flavones are present mainly as glycosides, usually conjugated at the 7-O position, but other conjugates are detected, as well[103]. The great variety of flavonoids and flavones is caused by altered substituents on the basic structure backbone and addition of double bonds. Increased number and connectivity of double bonds leads to an increase in electron delocalization and therefor photon absorption at different wavelengths. Flavones have shown some beneficial functions, e.g. antioxidative capacity in cell culture, animal studies and human trials, although studies on other flavonoids are more abundant[106]. Flavone-rich foods have been tested in intervention studies, providing increased activities of endogenous enzymes with antioxidant function, lowered total cholesterol levels and anti-inflammatory effects[103]. The general flavone structure shows absorbance in the region 310 - 350 nm and a second absorbance maximum from 250 - 290 nm[107]. Due to their absorbance spectra, flavones might exert protective effects against UV radiation via absorption of UVB and UVA light.

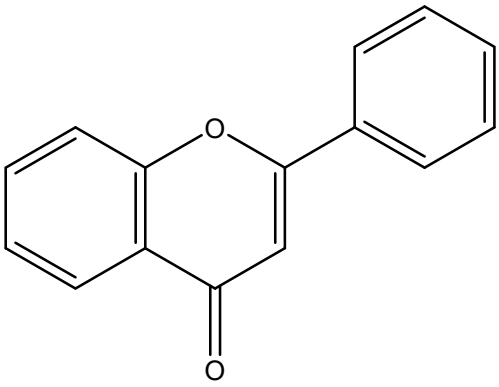

Figure 1.9 Structure of a flavone.

The compounds used in this thesis comprise luteolin, tricetin, nobiletin and tangeretin.

1.4.1 Luteolin

2-(3,4-dihydroxyphenyl)- 5,7-dihydroxy-4-chromenone (luteolin) is a polyhydroxylated flavone from a variety of non-edible and edible plants (vegetables, herbs, fruits). It mainly occurs in leafy green plants and is therefore taken up by the human diet in a relatively large amount. Examples for plants with high luteolin content are celery, parsley and peppermint[96]. In plants, luteolin is present as an aglycone and in combination with sugar moieties[108]. Its average daily intake by humans differs between countries and was estimated to be between 0.1 mg and 4 mg[96].

Although there have been some studies on the beneficial effect of luteolin in plant extracts on human health, in many of these studies it cannot clearly be distinguished between effects of the overall active substances in the tested foods and an effect from luteolin alone[108]. Luteolin is known as a potent antioxidant due to its structure. Additionally, luteolin has shown protective effects in keratinocytes against UVB radiation via attenuating ROS, DNA damage and inflammatory signalling[109,110]. UVA-induced upregulation of MMP1 and increase in IL-6 secretion was shown to be decreased by luteolin in fibroblasts via p38 MAPK signalling[111]. Several other studies show anti-inflammatory, antioxidant and chemopreventive functions of luteolin[108]. Taken together, luteolin is a promising candidate for further studies on photoprotection.

1.4.2 Tricetin

5,7-dihydroxy-2-(3,4,5-trihydroxyphenyl)chromen-4-one (tricetin) is the second polyhydroxyflavone examined in this thesis. It is found specifically in pollen from the Myrtacea family and consequently occurs in honey from Eucalyptus[112,113]. Tricetin was found to comprise around 30 % of the total flavonoid content in the honey from most Eucalyptus species[114]. Although luteolin was found in Eucalyptus honey, as well, both flavones do not occur often together in other food sources. Tricetin is therefore less extensively available in the human diet.

Due to its structure, tricetin has often been studied for its antioxidant activity. Singh et al. found tricetin to be a major antioxidant as compared to the control compound α-tocopherol *in vitro* and *in vivo*. The antioxidant effect was assigned to the three hydroxy groups on the B-ring[115]. Tricetin has further been found to have anti-inflammatory function in a mouse model by Geraets et al.[116]. In studies with cancer cell lines, tricetin was shown to suppress osteosarcoma and oral cancer migration and metastasis[117,118]. As with luteolin, tricetin was found to exert some of its functions via MAPK signalling[117].

1.4.3 Nobiletin

2-(3,4-dimethoxyphenyl)-5,6,7,8-tetramethoxychromen-4-one (nobiletin) is a polymethoxylated compound from citrus fruits. Different species of citrus contain nobiletin in the order of 4 - 1600 mg/kg fresh weight, with tangerines containing the highest concentrations[119]. It is predominantly found in the peel of citrus fruits compared to the juice and is therefore less well available in the human diet compared to polyhydroxylated flavones,

e.g. luteolin[120]. However, due to the O-methylation, nobiletin and other polymethoxylated flavones show superior oral bioavailability compared to polyhydroxylated flavones[120]. Enzymatic conjugation with glucuronic acid and methyl or sulfo groups are described for hydroxylated flavones, with subsequent excretion[121]. As a result, hydroxylated flavones appear only to minimal amounts in organs and plasma. Methoxylated flavones are less prone to conjugation and elimination and are found in organs and plasma in higher concentrations[122].

Many studies on beneficial functions of polymethoxylated flavones like nobiletin exist. Nobiletin was shown to induce G1 cell cycle arrest and inhibit growth of several cancer cell lines ranging from breast and colon to prostate and prevent adenocarcinoma formation in a rat model[120]. In SCC and glioblastoma cell culture, nobiletin has shown anti-proliferative effects[123]. In a study on mice, nobiletin displayed inhibitory effects on inflammation signalling and subsequently attenuated tumor delevopment[124].

1.4.4 Tangeretin

5,6,7,8-tetramethoxy-2-(4-methoxyphenyl)-4H-1-benzopyran-4-one (tangeretin), as nobiletin, is sourced predominantly from citrus fruits, e.g. from tangerine peels. In the albedo of different citrus species, tangeretin is present in levels up to 28 mg/g dried sample[125].

Tangeretin showed anti-proliferative effects on malignant cells in the same study with nobiletin[123]. In rats, tangeretin decreased signs of rheumatoid arthritis via attenuation of oxidative stress and inflammatory signalling[126]. In HepG2 cells, tangeretin exhibited cytoprotective effects via upregulation of the MAPK-Nrf2-ARE pathway[127]. Further, tangeretin exhibited cell cycle arresting function in colorectal, breast and colon cancer cells, as well as inhibition of NFκB signalling in lung epithelial carcinoma cells[120]. In relation to UV radiation, tangeretin showed an inhibiting effect on cyclooxygenase-2 expression in UVB-irradiated mouse epidermis[128]. In this study, tangeretin blocked MAPK signalling and ROS formation.

1.5 Aging

With improving technologies and therapies, mankind has been able to extend the medium lifespan and the quality of life at older age. Nevertheless, especially with increasing age, malfunctions and deterioration of organs accumulate, as well as development of cancers. In graphs recording demographic distribution of cancers in the global population, an increase in nearly all cancers is seen with age[129]. To discuss aging, the term aging has to be defined first. Aging can be investigated in whole organisms (organismal aging) or in subsets like a cell population (cellular aging). Further distinctions can be made according to the source contributing to aging, e.g. extrinsic and intrinsic aging. However, aging is a process involving both extrinsic and intrinsic factors. Aging commonly describes the deterioration of an organism over time with increasing loss of functions on the sub-organismal level and is often accompanied by an increased rate of formation of degenerative but also hyperplastic diseases that subsequently lead to death[130]. The mechanism behind aging is not yet understood in detail. The process of senescence is better known. Senescence describes the permanent loss of proliferative capacity in cells, which suppresses hyperproliferation, e.g. tumorigenesis[130]. In case of irreparable DNA damage and other factors that exhaust the repair machinery, senescence is initiated as a protective mechanism. It is initiated and sustained via two pathways, the p53/p21 and the p16/pRB pathways[130]. The tumor suppressor p53 is a cyclin-dependent inhibitor of the cell cycle and its overexpression or chronic activation leads to the induction of senescence, whereas its transient activation is important for DNA damage repair[130]. The p16 expression increases with age and is activated by DNA-independent stressors and ensures cell cycle arrest in the G1 phase[131].

Senescent cells show a distinct secretome of cytokines, growth factors and immunomodulatory chemokines, which has been termed the senescence-associated secretory phenotype (SASP). Senescence markers commonly used in the literature are the loss of proliferation upon stimulation, an increase in size, a flattened morphology and the overexpression of β-galactosidase (therefore termed senescence-associated β-galactosidase)[130]. These markers can only be used for validation of senescence when combined, since not all senescent cells from different tissues display the same senescence markers and some of these markers have been shown in non-senescent cells.

Senescence does not ultimately lead to cell death. At least in cell culture, senescence cells can exist almost indefinitely[131]. Aging and senescence are distinctive but linked processes. Senescence is supposed to contribute to aging, as an increase in senescent cell numbers can be found in aged skin[132]. This accumulation of senescent cells might compromise functionality of a tissue at some point or deplete the regenerative population of cells and contribute to aging[131]. Several features of senescent cells (e.g. the SASP) also contribute to the increased formation of diseases seen during aging. However, the exact connection between both processes is still a matter of investigation.

1.5.1 Theories of aging

Several theories of aging exist, that describe the possible causes of the process of organismal deterioration. The most popular theory of aging was postulated by Hayflick and Moorhead in 1961[133]. They found a finite capacity of fibroblasts in culture to proliferate upon serial cultivation. Hayflick and Moorhead established the idea of telomere shortening as the cause for the observed replicative senescence. The participation of telomere length in aging was supported by Harley in 1990[134].

The involvement of ROS in the aging process was postulated by Harman[135]. The theory of free radicals describes the accumulation of ROS-induced damage that leads to an accumulation of defective organelles and cells with age. This was later expanded to yield the mitochondrial theory of aging[136]. The mitochondrial theory of aging describes an accumulation of mitochondrial damage with age, fuelled by ROS, subsequent damage to mitochondrial DNA (mtDNA) and consequently accumulation of mitochondrial dysfunction that accelerates organismal aging.

Since then, more aging theories and possible contributors emerged. A decisive role for tumor suppressor p53 was established as the gatekeeper to apoptosis or senescence of cells[137]. Hyperproliferative cells were either guided towards programmed cell death (apoptosis) or towards senescence. The accumulation of senescent cells is likely to contribute to malfunctional tissues and therefore might contribute to aging.

Nowadays, the concept of antagonistic pleiotropy for senescence is also widely discussed[138]. From an evolutionary point of view, senescence might provide benefits in early life due to inhibition of hyperproliferation. In later life, senescence might contribute to the onset of malignancies. Exhaustion of stem cells that have undergone senescence prevents optimal

tissue renewal. Furthermore, senescent cells provide a senescence-associated secretory phenotype (SASP) that has been linked to inflammation, immune- and growth modulation[139]. The concept of antagonistic pleiotropy was also applied to melanin, the pigment produced by melanocytes in the epidermis upon irradiation. Its prime task is shielding of the skin from harmful UV rays. However, melanin also exerts detrimental effects leading to DNA damage formation and subsequently cancer[88]. Cancer formation increases by age and melanin might therefore be an example of the antagonistic pleiotropy concept. The occurrence of several examples of antagonistic pleiotropy are a good basis for adding this concept to the theories of aging.

Aging has long been related to inflammation. Several theories about inflammation and aging exist, linking an imbalance between ROS and counteracting processes by age to increased susceptibility to inflammation[140]. Probably the most recent theory linking aging and inflammation is called senoinflammation and involves chronic inflammation in its concept. The driver for chronic inflammation is described to be senescent cells, contributing to the aging process mainly via the SASP[141].

None of the theories might be the exclusive explanation for aging and some are presented with limitations, e.g. the lack of correlation between telomere length and longevity in some species or the immortality of cancer cells despite their increased ROS levels[142]. It is likely that a combination of several aging theories might contribute to the definition and understanding of aging.

1.5.2 The aging skin

This section focusses on the alteration in the dermis of intrinsically aged skin. Due to the continuous exposure of the skin to external stressors, the differentiation between intrinsic and extrinsic aging is difficult. To circumvent this issue, most studies are performed on unexposed skin areas, e.g. the upper inner arm or buttock. Aged dermis shows manifold ultrastructural and histological alterations compared to young dermis. Aged skin appears thin and pale skin with decreased normal hair growth on the scalp but increased hair growth at other sites, e.g. ear and nose[143]. The main constituent of the dermis, collagen, is reduced in density and its fibrils are prone to fragmentation[144]. The disruption of the connective collagen network might promote injury after mechanical stress. Vascularization of the dermis is decreased, probably resulting in the paleness and decreased surface temperature, as well as

a deteriorating supply of the epidermis, which is not vascularized. The number of mast cells in the dermis decreases, which might be the cause for the avascular phenotype, as they play a role in capillary vessel formation[143]. The decrease in vascularity and the thinning of subcutaneous fat area might be the cause for hypothermia in the elderly due to decreased insulation. Increased MMP levels have been found in aged skin, resulting in degradation of ECM components, e.g. collagen. Furthermore, blood vessel wall thickness decreases and together with the deterioration of elastin and collagen network might prime skin of the elderly for bruising[143].

Aging of fibroblasts leads to an impairment in ECM-fibroblast connection and in alteration of excreted molecules; matrix-degrading proteins exceed matrix-forming proteins[144]. This vicious cycle of secreted matrix metalloproteinases and impaired connectivity to the ECM leads to an overall loss of dermis structure and functionality.

1.5.3 Aged skin and UVA radiation

Hardly any studies are available investigating the differences of UVA-induced damage and responses in young and aged skin. From the few studies that were published, most cover the wavelengths in the UVB region.

Gilchrest et al. have observed a decreased responsiveness of aged patients to UV exposure, measured by onset of erythema and by edema formation[145]. They suppose a decreased inflammatory response as the cause for decreased UV-sensitivity. However, their study design does not allow to distinguish between a reduced or a delayed response. Furthermore, they used radiation including UVB and UVA wavelengths.

In studies on skin fibroblasts from differently aged donors, low dose UVA radiation did only induce few alterations in gene expression levels that were different between the age groups[146]. MMP-3, a proteinase for matrix proteins, was induced in young but less in older fibroblasts. SHC-transforming protein 1 (SHC1), which participates in apoptosis and oxidative stress signalling, was not affected in young but upregulated in older cells. Other genes involved in DNA repair, inflammation and antioxidant defence were not significantly altered between groups after treatment with UV[146]. It should be noted, that the study groups only consisted of 5 donors each group.

Some studies investigated permeation of sunscreens into young and aged skin in mice with no difference[147]. However, the model for senescent skin was obtained from 24-week old mice and might therefor only marginally depict the situation in aged human skin[148].

It seems there is yet essential information to gain in regard to aging skin and UV radiation, especially in response to irradiation with the UVA wavelengths.

1.6 Aim of the thesis

Present developments of human behaviour towards UVR exposure and the parallel increase in human life span with increasing rates of skin cancer amongst the elderly highlight the importance of adapted photoprotection. Formerly unrecognized or only marginally described threats to human skin imposed by the UVA region of sunlight will be highlighted in this thesis. Specifically, this thesis aims to investigate the impact of low-dose UVA radiation on fibroblasts, a major constituent of human skin. Low doses of UVA radiation are achievable by relatively shorts periods outdoors, with nearly no effect of cloud cover or time of day. These specificities of the UVA wavelength region, along with deeper penetration into the skin, distinguish the longer wavelengths of UVA from shorter UVB wavelengths. The effects of UVB radiation on skin are well-known, while studies on UVA radiation are less abundant and often include high doses that seem difficult to achieve under real conditions. UVA radiation was only recently recognized as a threat to human health besides premature aging of the skin (photoaging), leading to an abundance of UVB protective sunscreens on the market with little to no efficacy in the UVA region. This thesis aims at elucidating candidate secondary plant metabolites as possible photoprotecting compounds in sunscreens (exogenous) or as supplements (endogenous). The group of flavonoids is well-studied and contains promising compounds due to their structure-related absorbance spectra. Here, four flavones, a subgroup of flavonoids, will be investigated regarding their stability, photostability, toxicity, cellular uptake, reactivity with thiols, capability to inhibit lipid peroxidation and ROS production. Furthermore, they will be tested for their ability to exogenously or endogenously prevent decreases in cell viability after irradiation. Finally, the flavones will be tested in a topical application in a cream base, mimicking their performance in a sunscreen.

The model systems used will range from cell-free buffer solution, liposome preparations to cell culture studies with normal human dermal fibroblasts. To extend the knowledge gained on the effects of low-dose UVA radiation and the photoprotection by flavones, a model for

artificial and accelerated senescence will be employed. In this drug-induced accelerated aging model, the responses to low-dose UVA radiation will be studied, compared to young, normal fibroblasts. As a working hypothesis, differences between young and aged cells in general and in response to UVA radiation are presumed. As a consequence, sun protection strategies will need adaptation to meet the altered cellular responses to UV exposure between young and aged cells. Hence, uncovering those differences might aid in developing suitable, adapted photoprotection strategies.

As a final aim of this thesis, flavones suitable as photoprotecting agents will be suggested with implications for sun protection in the young and elderly.

2 Material and Methods

2.1 Equipment and consumables

Table 2.1 Equipment and consumables

Name	Company	Origin
µCuvette® G1.0 for BioSpectrometer	Eppendorf	Hamburg
analytical scale "TE 124S"	Sartorius	Göttingen
BioSpectrometer®	Eppendorf	Hamburg
blotting apparatus "Trans-Blot SD"	Bio-Rad	Hercules (CA, USA)
cell culture dish (3, 6, 9 cm) Cellstar®	Greiner bio-one	Frickenhausen
cell culture flask (175 cm^2) Cellstar®	Greiner bio-one	Frickenhausen
cell culture plate (6, 24, 48, 96 well) Cellstar®	Greiner bio-one	Frickenhausen
cell scraper	Greiner bio-one	Frickenhausen
centrifuge "5417R"	Eppendorf	Hamburg
chemiluminescence detection system „Fusion SL"	Vilber Lourmat	Eberhardzell
cotton swab	Meditrade	Kiefersfelden
cylinder, graduated (50 ml, 100 ml, 500 ml, 1 L)	VWR International	Darmstadt
electrophoresis system	Thermo Scientific	Langenselbold
FACS tubes	Becton & Dickinson	Heidelberg
Falcon® Cell Culture Insert Companion Plates	Corning	Corning (NY, USA)
Falcon® tube (15 ml, 50 ml)	Greiner bio-one	Frickenhausen
flow cytometer "BD FACSCanto™ II"	Becton & Dickinson	Heidelberg
Hamilton syringe	Hamilton Bonaduz AG	Bonaduz (CH)
heating block "Peqlab"	VWR International GmbH	Darmstadt

heating block "Techne Dri-Block DB3"	Thermo-Dux	Wertheim
homogenizer „Branson Sonifier 250"	G. Heinemann Ultraschall- und Labortechnik	Schwäbisch Gmünd
HPLC autosampler L-7200	Merck-Hitachi	Darmstadt
HPLC autosampler LaChrom Elite L-2200	Merck-Hitachi	Darmstadt
HPLC column "Supelco Suplex™ pKb-100" (250 x 4.6 mm)	Merck-Hitachi	Darmstadt
HPLC column "Supelcosil™ Suplex™ pKb-100" (25 cm x 4.6 mm, 5 µm)	Merck-Hitachi	Darmstadt
HPLC column oven L-7360	Merck-Hitachi	Darmstadt
HPLC degasser L-7614	Merck-Hitachi	Darmstadt
HPLC detector LaChrome L-7420	Merck-Hitachi	Darmstadt
HPLC fluorescence detector L-7480	Merck-Hitachi	Darmstadt
HPLC interface D-7000	Merck-Hitachi	Darmstadt
HPLC pump L-7100	Merck-Hitachi	Darmstadt
HPLC pump LaChrome L-7100	Merck-Hitachi	Darmstadt
incubator "HERACell VIOS 250 i"	Binder	Tuttlingen
light microscope "eclipse Ts2-FL"	Nikon	Amsterdam (NL)
magnetic stirrer	IKA®-Werke	Staufen
membrane filter GV 0.2 µm	Merck-Millipore	Darmstadt
Neubauer cell counting chamber	Laboroptik	Lancing (UK)
pH-meter "pH211"	Hanna Instruments	Vöhringen
pipet boy	Integra Biosciences	Biebertal
pipets (0.5-10 µl, 10-100 µl, 100-1000 µl)	Eppendorf	Hamburg
plate reader "FLUOstar OPTIMA"	BMG Labtech	Ortenberg
plate reader "Tecan infinite® M200 pro"	Tecan Group AG	Männedorf (CH)
polyvinylidene difluoride (PVDF) membrane "Amersham™ Hybond™"	GE Healthcare Lifescience	München

power supply "EV245/EV231"	Consort bvba	Turnhout (BE)
quartz cuvette (10 mm)	Hellma	Müllheim
quartz cuvette (cylindric)	Hellma	Müllheim
reaction tubes	Eppendorf	Hamburg
rotary evaporator	Büchi	Flawil (CH)
scale	Sartorius	Göttingen
SDS-PAGE apparatus „XCell Sure Lock™" Invitrogen™, Novex®	Thermo Scientific	Carlsbad (CA, USA)
SDS-PAGE cassettes (1.5 mm) Invitrogen™, Novex®	Thermo Scientific	Carlsbad (CA, USA)
SDS-PAGE pocket spacer (1.5 mm) Invitrogen™, Novex®	Thermo Scientific	Carlsbad (CA, USA)
Seahorse "XFe96 Analyzer"	Agilent Technologies	Santa Clara (CA, USA)
Seahorse XF Cell Mito Stress Test Kit	Agilent Technologies	Santa Clara (CA, USA)
Seahorse XFe96 Flux Pak (sensor cartridges, microplates, calibrant)	Agilent Technologies	Santa Clara (CA, USA)
semi-micro cuvette, PS	Sarstedt	Nümbrecht
shaker	neoLab®	Heidelberg
sterile bench "Safe 2020"	Thermo Scientific	Langenselbold
stripettes (5 ml, 10 ml, 25 ml) Cellstar®	Greiner bio-one	Frickenhausen
transwells for 24-well plate, 8 µm pore size	Corning	Corning (NY, USA)
ultrasonic bath "Sonorex Super 10P"	Bandelin	Berlin
UPLC "Aquity H-Class Bio"	Waters	Milford (MA, USA)
UPLC column "Van Guard Cortecs C18+ 90Å, 1.6 µm, 2.1 mm x 5 mm"	Waters	Milford (MA, USA)
UPLC vial, screw top, 300 µl	Waters	Milford (MA, USA)
UV irradiation system "Bio-Sun"	Vilber Lourmat	Eberhardzell
UV-Vis spectrophotometer "DU730"	Beckman Coulter	Krefeld

vortex machine	Scientific Industries	Bohemia (NY, USA)
vortex machine "VF2"	IKA Janke & Kunkel	Staufen
water bath "aquiline AL 25"	Lauda	Lauda-Königshofen
water purification system "Milli-Q academic"	Merck-Millipore	Darmstadt
Whatman® paper (GB003)	GE Healthcare Lifescience	München

2.2 Chemicals and media

Table 2.2 Chemicals and media

Name	Company	Origin
1,1,3,3-tetramethoxypropane (TMP)	Sigma-Aldrich	Steinheim
2-mercaptoethanol (2-ME)	Sigma-Aldrich	Steinheim
acetic acid (99.8 - 100.5 %), AnalaR® NORMAPUR® ACS	VWR International	Darmstadt
acetonitrile, LiChrosolv®, isocratic grade	Merck	Darmstadt
adenosine	Bio-Techne	Minneapolis (MN, USA)
adenosine diphosphate (ADP)	Bio-Techne	Minneapolis (MN, USA)
adenosine monophosphate (AMP)	Bio-Techne	Minneapolis (MN, USA)
adenosine triphosphate (ATP)	Bio-Techne	Minneapolis (MN, USA)
ammonium persulfate (APS)	Merck KGaA	Darmstadt
butylated hydroxytoluene (BHT)	Sigma-Aldrich	Steinheim
Coomassie brilliant blue R 250	Sigma-Aldrich	Steinheim
Cremaba HT cream base	Spinnrad	Bad Segeberg
DC™ Protein Assay reagent A	Bio-Rad Laboratories GmbH	Feldkirchen
DC™ Protein Assay reagent B	Bio-Rad Laboratories GmbH	Feldkirchen

DC™ Protein Assay reagent S	Bio-Rad Laboratories GmbH	Feldkirchen
dichloromethane	Merck	Darmstadt
dimethyl sulfoxide (DMSO) (≥ 99.5 %)	Sigma-Aldrich	Steinheim
disodium phosphate	Merck	Darmstadt
Dulbeccos's Modified Eagle's Medium - high glucose (DMEM)	Sigma-Aldrich	Steinheim
Dulbeccos's Modified Eagle's Medium - low glucose (DMEM)	Sigma-Aldrich	Steinheim
Dulbeccos's Phosphate Buffered Saline (PBS)	Sigma-Aldrich	Steinheim
egg yolk powder	Sigma-Aldrich	Steinheim
ethanol (70 %)	Merck	Darmstadt
fetal calf serum (FCS)	PAN-Biotech	Aidenbach
GlutaMAX ™	gibco	Darmstadt
H_2DCF-DA (2',7' –dichlorofluorescin diacetate)	Sigma-Aldrich	Steinheim
Hanks' Balanced Salt Solution (HBSS)	gibco	Darmstadt
Hoechst 33342 solution (20 mM)	Thermo Scientific™	Carlsbad (CA, USA)
hydrochloric acid (25 %)	Merck	Darmstadt
hydrochloric acid (HCl) (25 %, 0.2 M)	VWR International	Darmstadt
hydrogen peroxide (H_2O_2)	Sigma-Aldrich	Steinheim
luteolin (≥ 98 %)	Sigma-Aldrich	Steinheim
L-α-phosphatidylcholine	Sigma-Aldrich	Steinheim
Matrigel basement membrane matrix	Corning	Corning (NY, USA)
methanol, LiChrosolv®	Merck	Darmstadt
Midori Green DNA Stain	Nippon Genetics	Tokyo (JP)
milk powder	Carl Roth	Karlsruhe
monosodium phosphate	Merck	Darmstadt

MTT (3-(4,5-dimethylthiazol-2-yl)-2,5-diphenyltetrazolium bromide)	Sigma-Aldrich	Steinheim
nicotinamide adenine dinucleotide (NAD^+)	Bio-Techne	Minneapolis (MN, USA)
nobiletin (≥ 97 %)	Sigma-Aldrich	Steinheim
ortho-phosphoric acid (≥ 85 %), EMSURE® ACS, ISO	VWR International	Darmstadt
penicillin (10000 U)/streptomycine (10 mg/ml)	Sigma-Aldrich	Steinheim
phosphatase inhibitor cocktail 2	Sigma-Aldrich	Steinheim
phosphoric acid (85 %)	Merck	Darmstadt
prestained Page Ruler	Thermo Scientific™	Carlsbad (CA, USA)
ProLong Gold DAPI	Thermo Scientific™	Carlsbad (CA, USA)
protease inhibitor cocktail	Sigma-Aldrich	Steinheim
Rotiphorese® Gel 40	Carl Roth	Karlsruhe
Seahorse XF DMEM medium, pH 7.4	Agilent Technologies	Santa Clara (CA, USA)
sodium chloride (NaCl) (≥ 99.5 %)	Carl Roth	Karlsruhe
sodium dihydrogen phosphate (NaH_2PO_4)	Merck KGaA	Darmstadt
sodium dodecyl sulfate (SDS)	Sigma-Aldrich	Steinheim
T4 endonuclease V (10000 U/ml)	New England Biolabs	Ipswich (MA, USA)
tangeretin (≥ 99.5 %)	Sigma-Aldrich	Steinheim
TEMED (N,N,N',N'-Tetramethylethane-1,2-diamine) (99 %)	Carl Roth	Karlsruhe
thiobarbituric acid (TBA)	Merck	Darmstadt
tricetin (≥ 99 %)	Extrasynthese	Lyon (FR)
Tris (2-Amino-2-(hydroxymethyl)propane-1,3-diol)	Carl Roth	Karlsruhe
Triton X-100	Sigma-Aldrich	Steinheim
trypsin - EDTA solution (1x)	Sigma-Aldrich	Steinheim

Tween® 20	Merck KGaA	Darmstadt
Western Blot stripping buffer "restore"	Thermo Scientific™	Carlsbad (CA, USA)

2.3 Buffer and solutions

Table 2.3 Buffer and solutions

Buffer and solutions	Stock concentration	Ingredients
anode 1	1x	0.3 M Tris (36.34 g) 10 % methanol (100 ml) in 1 L ddH_2O pH 10.4
anode 2	1x	25 mM Tris (3.03 g) 10 % methanol (100 ml) in 1 L ddH_2O pH 10.4
cathode	1x	25 mM Tris (3.03 g) 40 mM glycine (3 g) 10 % methanol (100 ml) in 1 L ddH_2O pH 9.4
Comet assay electrophoresis buffer	1x	75 ml (10 N) NaOH 12.5 ml (200 mM) EDTA in 2.5 L ddH_2O pH 13
Comet assay enzyme reaction buffer	10x	400 mM HEPES 1 M KCl 5 mM EDTA 2 mg/ml BSA in 1 L ddH_2O

		pH 8
Comet assay lysis buffer	1x	10 mM Trizma 300 mM NaOH 100 mM EDTA 2.5 M NaCl in 900 ml ddH_2O pH 10
Comet assay lysis buffer (at the day of the assay)	1x	1.5 ml Triton X-100 135 ml Comet assay lysis buffer
Comet assay neutralization buffer	1x	0.4 M Trizma in 1 L ddH_2O pH 7.5
Coomassie destaining solution	1x	450 ml methanol 100 ml acetic acid In 1 L ddH_2O
Coomassie staining solution	1x	2.5 g Coomassie 450 ml methanol 100 ml acetic acid In 1 L ddH_2O
Low melting point agarose (LMP)	1x	0.6 g LMP in 50 ml PBS
lysis buffer	1x	protease-inhibitor 1:10 phosphatase-inhibitor 1:100 in 1 % SDS
Magnetic Activated Cell Sorting (MACS) buffer	1x	2 mM EDTA 0.5 % BSA 500 ml PBS

Midori Green staining solution	1x	1.5 µl Midori Green in 100 ml ddH_2O
MTT stock solution		5 mg MTT in 1 ml PBS
SDS running buffer	10x	10 g SDS 30.3 g Tris 144.1 g glycine in 1 L ddH_2O
SDS running buffer	1x	1 g SDS 3.03 g Tris 14.41 g glycine in 1 L ddH_2O
SDS sample buffer (Laemmli)	4x	40 % glycerol 20 % 2-mercaptoethanol 12 % SDS 0.4 % bromophenol blue
separating gel (12 %)	1x	3 ml Rotiphorese gel 40 2.5 ml 1.5 M Tris pH 8.8 100 µl SDS (10 %) 100 µl APS (10 %) 10 µl TEMED in 4.3 ml ddH_2O
separating gel buffer	1.5 M	1.5 M Tris (90.86 g/500 ml) in 500 ml ddH_2O pH 8.8
sodium phosphate buffer	0.1 mM	6.89 mg NaH_2PO_4 in 500 ml ddH_2O pH 7.4

stacking gel (5 %)	1x	720 µl Rotiphorese gel 40 650 µl 1 M Tris pH 6.8 50 µl SDS (10 %) 50 µl APS (10 %) 5 µl TEMED in 3.5 ml ddH_2O
stacking gel buffer	1 M	1 M Tris (60.57 g/500 ml) in 500 ml ddH_2O pH 6.8
TBS (Tris-buffered saline)	10x	0.5 M Tris (60.57 g/L) 1.5 M NaCl (87.44 g/L) in 1 L ddH_2O pH 7.5
TBST (Tris-buffered saline with Tween® 20)	1x	100 ml 10x TBS 0.1 % (v/v) Tween® 20 in 1 L ddH_2O

2.4 Antibodies

Table 2.4 Primary antibodies

Name	Company	Origin
anti-CD38-APC	Miltenyi Biotec	Bergisch Gladbach
anti-CD39-APC-Vio	Miltenyi Biotec	Bergisch Gladbach
anti-CD73 PE/Cy7	Becton Dickinson	Heidelberg
mouse anti-ß-tubulin	Proteintech	Rosemont (IL, USA)
rabbit anti-hemeoxygenase-1	Abcam Biochemicals	Cambridge (UK)
rabbit anti-γ-H2AX (phospho-Ser139)	Sigma-Aldrich	Steinheim

Table 2.5 Secondary antibodies

Name	Company	Origin
HRP-conjugated goat anti-rabbit IgG	Dianova	Hamburg
HRP-conjugated rabbit anti-mouse IgG	Agilent Technologies	Santa Clara (CA, USA)

2.5 Software

Table 2.6 Software

Name	Company	Origin
BioRender	BioRender	Toronto (CA)
ChemDraw Professional	Perkin Elmer	Hamburg
CometScore	Tritek	Sumerduck (VA, USA)
FACSDiva™	Becton & Dickinson	Heidelberg
FlowJo	Becton & Dickinson	Heidelberg
FusionCapt Advance	Vilber Lourmat	Eberhardzell
Microsoft Office 2019	Microsoft	Hamburg
OPTIMA 2.0	BMG Labtech	Ortenberg
PRISM 8	Graphpad Software	San Diego (CA, USA)
Review Empower 3	Waters	Milford (MA, USA)
Tecan i-control	Tecan Group AG	Männedorf (CH)
Wave	Agilent Technologies	Santa Clara (CA, USA)

2.6 Kits

Table 2.7 Kits

Name	Company	Origin
BrdU cell proliferation assay	Cell Signaling Technology	Danvers (MA, USA)
DNA extraction kit "QIAamp"	Qiagen	Hilden
high sensitivity CPD ELISA kit Ver. 2	Cosmo Bio	Tokyo (Japan)

Seahorse Mito Stress Test	Agilent Technologies	Santa Clara (CA, USA)
senescence detection kit (SA-ß-Gal)	Biovision	Milpitas (CA, USA)

2.7 Cell lines

Table 2.8 Cell lines

Name	Company	Origin
cutaneous squamous cell carcinoma (SCL-1)	Prof. Fusenig, DKFZ	Heidelberg
normal human dermal fibroblasts (NHDF), C-12300	PromoCell GmbH	Heidelberg

2.8 Cell Culture

Normal human dermal fibroblasts (NHDF) were purchased from Promocell. Originally, they are derived from human juvenile foreskin. Cutaneous squamous cell carcinoma cells (SCL-1), originating from the face of a 74-year old woman, were a gift from Prof. Fusenig[149]. NHDF and SCL-1 were cultured under conditions given below. Full medium consisted of DMEM (low glucose) supplemented with 10 % FCS, penicillin (100 U/ml), streptomycin (100 µg/ml) and GlutaMAX™ (2 mM). Starvation medium was prepared according to the full medium recipe without FCS. Cells were kept in a humidified 37 °C incubator with 5 % CO_2 (v/v) at all times unless stated otherwise. For all experiments, cells were used in a subconfluent state.

2.8.1 Freezing of cells

In order to preserve cell lines, they were occasionally frozen as a backup stock. Therefore, approximately 1 x 10^6 cells were trypsinized with trypsin-EDTA (3 ml for a 175 cm² flask) for 10 minutes. Thereafter, the reaction was stopped by the addition of 10 ml full medium. The cells were then counted and transferred to centrifugation tubes. After centrifugation for three minutes at 800 x g at room temperature, supernatant was removed and the pellet resuspended in a solution containing full medium, supplemented with 20 % FCS and 10 % DMSO. Subsequently, the cells were transferred into cryo vials and immediately transferred to - 80 °C.

2.8.2 Thawing of cells

Aliquots that were stored at - 80 °C were thawed for two minutes in a 37 °C warm water bath and immediately mixed with 2 ml of full medium. Then, cells were transferred to a prepared cell culture flask (175 cm^2) containing 25 ml of full medium. After approximately four hours, attachment of the cells to the new flask was verified by microscopy and the medium was replaced by full medium to remove DMSO.

2.8.3 Cell-culture maintenance

Depending on the density in which the fibroblasts were seeded, they needed to be passaged once or twice a week. In order to passage them, cells in flasks were washed with PBS and trypsinized with 3 ml 0.05 % Trypsin EDTA solution for 10 minutes in a 37 °C incubator with 5 % CO_2 (v/v). Detachment of cells from the flasks was verified with a microscope and 10 ml full medium was added to stop the trypsinization. Counting of the cells was performed by pipetting 10 µl of the cell suspension onto a Neubauer counting cell. All cells present in the four quadrants visible under the microscope were counted. The cell number was divided by 4 and multiplied by 10000 to yield the final cell number per ml of cell suspension. The required number of cells for experiments was then diluted in full medium and seeded onto new flasks.

2.8.4 Mycoplasma detection

Regular tests for mycoplasma contamination are mandatory for cell cultures. For this, cells were seeded onto a cover glass in dishes and cultivated for one or two days. Cells were then washed with PBS and fixed with methanol. A drop of ProLong Gold DAPI stain was placed on an object slide and the cover glass (with the cell-containing side down) was placed on top. Cells were then checked for DAPI (blue) staining outside of the nucleus using fluorescence microscopy. DAPI staining outside of the cell is an indicator for mycoplasma contamination.

2.8.5 Stock solutions of substances

The purchased substances were dissolved in DMSO and stored as a stock solution at - 20 °C or at 4 °C according to the manufacturers data sheet. For incubation of cells with the flavones, the incubation time and concentration varied depending on the experiment (see specific method for detailed information).

2.9 UV irradiation

A Biosun radiation system was used to irradiate cells in cell culture dishes or plates. The irradiation system was equipped with four UVA lamps (20 W, 365 nm). Irradiation was

performed in HBSS without cell culture dish or plate lid. The system yielded an output of 4 - 4.5 mW/cm², resulting in an irradiation time of 35 minutes for a total amount of 10 J/cm² UVA or around two hours for a dose of 45 J/cm² UVA. Unirradiated controls (sham) were placed in the radiation system simultaneously to the irradiated cells, but were completely covered in aluminum foil. This way, the same conditions and timepoints were achieved and a parallel handling of both irradiated and unirradiated cells was possible. Spectral output (intensity of light at each wavelength) was measured with a fibre-coupled spectrometer "Qmini" from RGB photonics.

2.10 Spectrophotometry

Spectra of substances were recorded in a spectrophotometer using 1 cm quartz cuvettes. A blank was subtracted from all spectra using a cuvette containing only the solvent.

2.10.1 Stability

Stability of the flavones (50 µM) was measured in phosphate buffer (0.1 mM, pH 7.4) at timepoint 0 and 15 minutes after preparation at room temperature. For this, changes in the absorbance spectrum over time were considered as instability. A second approach for stability testing by HPLC is described below (see 2.12).

2.10.2 Photostability

Photostability of flavones was measured by detection of changes in their absorbance spectrum after irradiation. The flavones were diluted in 0.1 mM phosphate buffer to a concentration of 100 µM. Before or directly after irradiation with increasing doses of UVA (10, 20 and 40 J/cm²), spectra were measured. For detection of the photostability in liposomes (see 2.11), 100 µM of the respective flavone was incorporated into liposomes. 2 ml of the samples were either left unirradiated (sham) or were irradiated in 3 cm cell culture dishes without lid with UVA doses of 10, 20 and 40 J/cm². Then, the solution was centrifuged, the supernatant discarded and the remaining "pellet" dried at room temperature and resuspended in dichloromethane for measurement in a spectrophotometer. A second approach investigated the spectra of the supernatants of the liposomes after the centrifugation step.

2.10.3 Thiol reactivity

Thiol groups in proteins provided by the amino acid cysteine are essential for a proteins three-dimensional conformation and therefore essential for its function.

Assessment of the thiol reactivity of flavones was performed using spectrophotometric analysis. Certain functional groups of the flavone may react with thiol-bearing substances, e.g. 2-mercaptoethanol (2-ME). As result of the interaction, absorption spectra can be shifted, especially when the conjugated double bond system is interrupted. Alexandra Zepina contributed to the thiol reactivity experiment.

A 25 mM concentration of 2-mercaptoethanol was prepared in 0.1 mM phosphate buffer. Flavones were added to 1 ml of the previous solution to achieve an end concentration of flavones of 50 µM. Directly after addition of the flavone or the positive (50 µM cardamonin) and negative (DMSO according to the respective flavone, min. 0.1 %, max. 1.43 %) control compound, the solution was transferred to a 1 cm quartz cuvette and a spectrum was obtained (200 - 500 nm) every minute over a time period of 15 minutes. As a blank, only phosphate buffer was used.

2.11 Liposome preparation

Liposomes were used in this thesis in order to provide a second model system for flavone testing in context with their possible use as photoprotectants in a cream formulation.

Multilamellar liposomes were prepared by dissolving 200 mg phosphatidylcholine or egg yolk in 40 ml dichloromethane (5 mg/ml). The solution was then vacuum-dried using a rotary evaporator (approximately 2 mbar) at 25 - 30 °C with supplied cooling. A thin, homogenous layer of lipids remains at the walls of a round-bottom flask. Then, 40 ml phosphate buffer (100 mM, pH 7.4) was added under rotation (5 minutes). Finally, the solution was sonicated at maximum output in an ultrasonic bath for 5 minutes. For the preparation of flavone-containing liposomes, the compounds were added to the phosphate buffer before sonication.

2.12 Cellular uptake and stability of substances via HPLC

In the investigation of substances and their effects on cells, it is essential to determine their cellular uptake. Furthermore, the stability of the substances in media and solutions is of interest for correct data interpretation. Here, stability and cellular uptake of flavones was measured by means of HPLC analysis.

2.12.1 Cell culture

Cell culture dishes (3 cm) were prepared with about 50000 cells per dish. After one day, the subconfluent fibroblasts were washed with 2 ml PBS. Then, 2 ml of different concentrations

of the substances (luteolin: 10 and 50 µM; tricetin: 1 and 50 µM; nobiletin: 5 and 50 µM; tangeretin: 10 and 60 µM) in starvation medium were added to the cells for 0, 2 or 24 hours. After the incubation time, the medium was collected and stored in liquid nitrogen directly. The cells were washed twice with PBS. Finally, 500 µl PBS were added and the cells were removed by scraping. The cell suspension in PBS was then transferred to an Eppendorf tube.

2.12.2 Sample preparation

The tubes containing the cell suspension in PBS was centrifuged at 1700 x g for 6 minutes at 4 °C. The supernatant was discarded while the cell pellet was suspended and vortexed in 100 µl ice-cold methanol. After a second centrifugation at 14000 x g for 10 minutes at 4 °C, the pellet was stored at - 20 °C for protein quantification and the supernatant was immediately stored in liquid nitrogen for further HPLC analysis.

2.12.3 HPLC analysis

In order to measure the uptake of flavones into cells, an HPLC method was established. Using a SUPELCOSIL Suplex pKb-100 column (25 cm x 4.6 mm, 5 µm), the analysis of tangeretin was performed with a mobile phase of methanol:acetonitrile:water:isopropanol (324:264:400:12, v/v/v/v) and detection at 324 nm. For nobiletin, the mobile phase was unaltered, but detection was performed at 332 nm. For luteolin, the mobile phase consisted of methanol:water (0.2 % phosphoric acid (85 %)) (800:200, v/v) and the detection was performed at 355 nm. Tricetin measurements were performed with a mobile phase of methanol:water:acetic acid (81:14.3:4.7, v/v/v) and a detection at 354 nm. The injection volume was 50 µl. The flow rate was set as 1 ml/min.

For the calculation of cellular uptake, protein quantification in the sample pellet was performed (see cell lysis and protein quantification below). The concentration of the flavone was calculated and is given in µg/mg protein.

For measurements of substance stability, flavone solutions with a concentration of 10 µM in methanol or starvation medium were prepared and kept at room temperature. Every hour (from 0 to 5 hours) and after 24 hours, 100 µl from the 10 µM stock solutions were transferred to an HPLC vial and 50 µl were injected. The concentration was calculated using a standard curve of the respective compound.

2.13 Measurement of malondialdehyde / lipid peroxidation

The measurement of malondialdehyde (MDA) was used to estimate lipid peroxidation in samples, as MDA is a byproduct of the oxidative chain reaction leading to oxidized lipids[150]. Of note, MDA is not an exclusive indicator of lipid peroxidation. Several other reactive aldehydes, like 4-hydroxynonenal, are products of lipid peroxidation, as well. Nevertheless, MDA measurements are a common practice for the assessment of lipid peroxidation in the literature.

2.13.1 Cell culture

To obtain a subconfluent cell layer, 250000 cells were seeded onto 6 cm cell culture dishes in 3 ml full medium for one day. Cells were then washed with 2 ml PBS and incubated with 50 µM of the respective flavone in starvation medium for two hours at 37 °C. Controls were only incubated with starvation medium. Then, cells were washed again and irradiated with 10 J/cm² UVA in 1 ml HBSS. Afterwards, HBSS was removed and stored for measurements at - 80 °C.

2.13.2 Sample preparation and derivatization

Cell suspensions or liposomes were centrifuged and pellets were suspended in 150 µl H_2O. Medium from 2.13.1. was used as such. 50 µl of the suspension or medium were added to 200 µl thiobarbituric acid (TBA, 0.4 % in HCl (0.2 M)). 25 µl butylated hydroxytoluene (BHT, 0.05 % in ethanol) was added to prevent further oxidation. A blank was prepared exchanging the sample volume for 50 µl H_2O. The solution was heated to 95 °C for 30 minutes and subsequently cooled at 4 °C. The solution was then diluted 1:1 with the mobile phase and centrifuged at 21000 rpm for 5 minutes.

2.13.3 Photometric measurement of malondialdehyde

Egg yolk liposome samples were preferentially measured using spectrophotometry. Samples were treated with TBA and BHT according to step 2.13.2. 1 ml of the sample was transferred to a cuvette without further dilution. Absorbance at 532 nm was measured in a spectrophotometer.

2.13.4 HPLC analysis

An HPLC method for the specific detection of MDA in supernatants from phosphatidylcholine liposomes and cell cultures was established. Samples were run on a Supelco Suplex pKb-100 column (250 x 4.6 mm) as stationary phase. The mobile phase consisted of sodium phosphate

buffer (monosodium phosphate, 50 mM):acetonitrile (60:40, v/v) with a pH of 6.5. A standard curve was prepared using tetramethoxypropane (TMP) in concentrations from 0.2 to 20 µM. Supernatants from the sample preparation step (see 2.13.2) were transferred into HPLC vials and placed in the autosampler. The injection volume was 50 µl and the flow rate was 1 ml/min. Excitation and emission of the fluorescence detector were set at 513 and 550 nm, respectively.

2.14 H_2DCF-DA assay / measurement of intracellular reactive oxygen species (ROS)

The intracellular level of ROS was measured using 2',7'-dichlorodihydrofluorescein diacetate (H_2DCF-DA), a cell-permeable probe, which is cleaved in the cytosol to form 2',7'-dichlorofluorescin (DCFH) due to the action of intracellular esterases. ROS from intracellular sources oxidize DCFH to form fluorescent 2',7'- dichlorofluorescein (DCF) which can be measured spectrophotometrically. Although not all ROS species can be detected and it is not specific for a certain type of ROS, this assay gives a good estimate of the general oxidative load in a cell[151,152]. ROS that are able to oxidize non-fluorescent DCFH to fluorescent DCF are, e.g. peroxynitrite ($ONOO^-$), hydrogen peroxide (H_2O_2) only in combination with ferrous iron (Fe^{2+}), and the hydroxyl radical ($OH^{\cdot}$).

For basal ROS measurements, 10000 cells were seeded into a 24-well plate and allowed to attach to the plate for 24 hours. Cells were washed with HBSS and 1 ml of 10 µM H_2DCF-DA solution was added and incubated for 30 minutes at 37 °C. After a double wash step with HBSS to remove excess probe, another 500 µl of PBS were added and measurement of fluorescence was performed in a pre-heated (37 °C) plate reader with excitation set at 485 nm and emission set at 520 nm. Fluorescence was recorded every 5 minutes for 90 minutes.

For determination of the effect of flavones on intracellular ROS levels, 8000 cells were plated into a 24-well plate and were cultivated for three days at 37 °C and 5 % CO_2 (v/v) in full medium. Washing of the cells with 1 ml HBSS preceded a treatment with 1 ml of 10 µM H_2DCF-DA for 30 minutes in a 37 °C incubator. Afterwards, cells were washed twice with HBSS and either treated with 2 mM H_2O_2, 50 µM of the respective flavone or a corresponding DMSO control. Immediately after treatment, fluorescence was measured every 5 minutes over the course of 50 minutes as described above.

A second approach included a preincubation with the substances before measurement of ROS. After three days in culture as described above, cells were washed and preincubated for two hours at 37 °C with the respective substances (50 µM) or DMSO. Following a wash step with

HBSS, 1 ml of a 10 µM H_2DCF-DA solution was added for 30 minutes at 37 °C. After two final wash steps with HBSS, a final addition of 500 µl HBSS or treatment with 2 mM H_2O_2 as the positive control was performed. Fluorescence was immediately measured as described above.

A third approach was employed to investigate possible effects on ROS levels of the selected flavones after or during irradiation with 10 J/cm² UVA. Cells in 24-well plates after three days in culture as stated in experiments above were washed with 1 ml PBS and incubated at 37 °C with 1 ml of the corresponding flavone dilution in starvation medium (50 µM) or DMSO for two hours. Then, cells were washed with PBS and received either 500 µl HBSS or 500 µl HBSS supplemented with 50 µM flavone or DMSO. Cells were irradiated with 10 J/cm² UVA. After irradiation, cells were washed with HBSS and incubated with DCF as stated above.

2.15 Cell viability assay

The MTT assay relies on colorimetric measurement of the generation of formazan salts from 3-(4,5-dimethylthiazol-2-yl)-2,5-diphenyltetrazolium bromide (MTT), which depends on the activity of mitochondrial enzymes and relates to cell viability[153]. The MTT assay therefor provides an indirect measure of cell viability and can be used to determine the indirect cytotoxic effect of treatments and compounds on the investigated cell type.

2.15.1 Toxicity of substances

The MTT assay was used to evaluate possible toxic effects of the flavones in NHDF. Alexandra Zepina contributed to the toxicity testing of the flavones.

At the beginning of the experiment, 8000 cells per well were plated onto 24-well plates and incubated at 37 °C for 72 hours. Afterwards, cells were washed with PBS and incubated with either 2 mM H_2O_2 for four hours as a positive control, DMSO or with flavones for two or 24 hours. For luteolin, concentrations of 10, 30, 50, 70, 90 and 110 µM were used. For tricetin, tangeretin and nobiletin, concentrations of 5, 10, 30, 50, 70 and 90 µM were used. After two or 24 hours of incubation, cells were washed with PBS and incubated with 500 µl MTT (1:10 in starvation medium) for two hours at 37 °C. Finally, cells were washed again and 500 µl DMSO were added to extract the formazan salts. Absorption was measured at a wavelength of 540 nm using a plate reader.

2.15.2 UV-sensitivity

Sensitivity of normal human dermal fibroblasts, DMSO-treated and MMC-treated cells (NHDF, CT and MMC) towards UVA radiation was measured with the MTT assay using different doses of UVA as well as different periods of post incubation time. The doses for irradiation were 10, 30, 38 and 45 J/cm² UVA. A faster or more severe decrease in viability in one of the cell types in response to a certain UVA dose was interpreted as increased UV sensitivity and vice versa. For this experiment, around 20000 cells per 3 cm cell culture dish were plated in full medium and allowed to proliferate for three days. Then, cells were washed with PBS and irradiated in 2 ml HBSS with the respective UVA doses in duplicates. Afterwards, cells were washed with PBS again and either directly used for viability measurement or post-incubated for 24 hours in starvation medium at 37 °C. After the post incubation time, cells were incubated with MTT as described before and absorbance was measured.

2.15.3 Phototoxicity and photoprotection of substances

The MTT assay was also applied to test for possible phototoxic or photoprotective effects of the flavones. To investigate the phototoxicity of a substance, MTT assays were used to test whether the substance diminished NHDF cell viability in combination with UVA radiation. A decrease in viability beyond the decrease caused by a toxic dose of UVA can be interpreted as phototoxicity, especially if the substance itself without UV does not cause a decrease in cell viability. In the same way, the photoprotective properties of the substances can be investigated. An increase of cell viability above the value from irradiated cells indicates a protective effect. In this approach, two different sets of experiments were performed in parallel. In the first set, cells were preincubated with the compound for 2 hours and the compound was removed before irradiation. In the second set, cells were preincubated with the substances and the compounds were present in the medium during irradiation. With the first setting, mainly the contribution of intracellularly present compound was evaluated (endogenous protection), whereas in the second mainly extracellular effects (exogenous protection) were determined.

Cells were plated on 3 cm cell culture dishes in a density of 20000 cells per dish. After three days, cells were washed with PBS and preincubated with substances in starvation medium for two hours. Flavones were used in a concentration of 50 µM. H_2O_2 was used as a positive control at 2 mM. All cells were preincubated with the flavones, except one set of sham

controls, 45 J/cm² UVA controls, as well as the positive control to determine these effects individually. For samples with the flavone present during irradiation, 50 µM of the respective substance was added to HBSS prior to irradiation. Irradiation was performed with all dishes except for the H_2O_2 control. Cells without flavones were incubated only with starvation medium. After washing with PBS, cells were irradiated with 45 J/cm² UVA in 2 ml HBSS. Unirradiated controls (sham) were covered in foil to avoid penetration of light but were located in the same irradiation chamber as the irradiated samples. After irradiation, cells were washed again and 1 ml MTT was added as described before. Finally, DMSO extractions were pipetted into a 48 well plate for measurement of absorbance in the plate reader.

2.15.4 Photoprotection in a cream formulation

On the basis of the recommendations and guidelines from COLIPA, the European commission and the Food and Drug Administration regarding *in vitro* sunscreen testing and by adaption of methods from Brugè et al., a method for the evaluation of photoprotection of substances was established[95,154–156]. To investigate the efficacy of flavones to absorb or reflect photons in a basic cream product, a protocol was established by use of the MTT cell viability assay in NHDF.

To evaluate the photoprotective effect of flavones in a cream formulation with regard to a possible future use in sunscreen products, a commercially available cream base was obtained and modified with flavones. The basal ingredients were as follows: Aqua, Caprylic/Capric Triglyceride, Alcohol, hydrogenated phosphatidylcholine, Butyruspermum Parkii Butter, Squalane, Ceramide 3. The cream was stored at 4 °C and warmed to room temperature prior to experiments. Luteolin and tricetin were chosen for cream experiments and warmed to room temperature, as well. For supplementation with flavones, 0.1 % (w/w) of luteolin or tricetin was incorporated into the cream by mixing the appropriate volume or a DMSO control volume into the cream. The recommended amount of cream was weighted according to the COLIPA regulations (2 mg/cm²). 28 mg were needed to cover the area of two cover glasses that covered the area of a 3 cm cell culture dish. The cream alone or the cream supplemented with the flavones was spread across the cover glasses with a gloved finger, leaving a relatively homogenous and translucent layer of cream on the glass.

Cells in 3 cm culture dishes were prepared as described before. Creams were prepared immediately before use. When placed in the irradiation chamber, the lid was removed and replaced by the cover glasses. A control with cream without supplementation of flavones and

a cover glass control without cream was applied, as well, to test for absorbance of glass and cream. One control dish was left without cover glass. Dishes were then irradiated with 45 J/cm² UVA. After irradiation, cover glasses were removed and cells were treated according to the cell viability assay procedure.

2.16 Protein analyses

2.16.1 Cell culture

In a 6 cm cell culture dish, 150000 cells per dish were cultivated in 3 ml full medium for two days. Then, cells were washed with 3 ml PBS and irradiated in 2 ml HBSS with 10 J/cm² UVA. Afterwards, they were either directly lysed (see below) or post-incubated for several hours in starvation medium. After one to 24 hours, cells were lysed.

2.16.2 Cell lysis

Medium from cells was removed. The cells were washed with PBS and incubated with 50 µl per dish of 1 % SDS lysis solution for 30 seconds on ice. Afterwards, cells were detached from the dish with a cell scraper and transferred to an Eppendorf tube for storage at - 20 °C.

2.16.3 Protein quantification (modified Lowry assay)

Quantification of protein levels in different samples is important in order to compare expression of the protein of interest in relation to a housekeeping protein. A modified Lowry assay was used (DC protein assay kit). The principle is based on a biuret reaction, where copper ions interact with peptide bonds, followed by a reduction step of copper. Reduced copper interacts with a folin-phenol reagent, leading to the formation of a blue molecule, allowing the determination of protein levels by colorimetric measurement[157]. Frozen samples from the cell lysis step were sonicated on ice. Then, 5 µl of sonicated sample were incubated with provided reagents (200 µl reagent B, 25 µl reagent A') for 15 minutes in the dark and the absorption at 750 nm was measured in a plate reader. As correction for the background, absorption from the DC protein reagents alone was subtracted from sample values and the amount of sample needed yielding 20 µg protein was calculated using a standard curve.

2.16.4 SDS-PAGE

The sodium dodecyl sulphate-polyacrylamide gel electrophoresis (SDS-PAGE) is a common method to separate proteins by their molecular weight. It was developed by Laemmli in 1970 and was used in countless studies since[158]. Defined sample volumes containing 20 µg protein

were mixed with 5 µl loading buffer and heated to 95 °C in order to denature proteins. Samples were then subjected to a 12 % SDS polyacrylamide gel. As a marker, 5 µl prestained Page Ruler was used. The tank was filled with running buffer and a current was applied with 25 mA and maximal voltage (300 V) per gel for 20 minutes in order to collect the protein bands. Then, the current was increased to 45 mA per gel for approximately 30 minutes to achieve protein separation.

2.16.5 Western blotting

Western Blotting is the most commonly used technique for visualization of proteins from gels after electrophoresis. Semi dry Here, the protein pattern is transferred to a membrane using an electrical current. Proteins patterns can then be detected using specific antibodies (see Table 2.4) or general protein dyes. The SDS gel (see 2.16.4) was transferred to a blotting machine and arranged between blotting papers soaked in anode or cathode buffer. A PVDF membrane was activated in methanol for 5 minutes. Beneath the gel, the PVDF membrane was placed, to which the protein bands were transferred using a current of 60 mA and maximal voltage (300 V) for two hours.

2.16.6 Immunodetection

After blotting, the membrane was blocked in TBS-T containing 5 % milk powder for one hour to prevent unspecific binding of the antibodies. Subsequently, the membrane was incubated with the primary antibody (1:1000 in TBS-T containing 5 % milk powder) at 4 °C under rotation overnight. Then, membranes were washed in TBS-T three times and incubated with the respective secondary antibodies (1:15000 in TBS-T containing 5 % milk powder) for one hour at room temperature. After final three wash steps, the membrane was covered with enhanced chemiluminescence (ECL) reagent consisting of a peroxide solution and a signal enhancer. In a Fusion detection system coupled with a CCD camera, protein bands were illuminated for different periods of time and digitally captured. Protein bands were semi-quantified using the reference ß-tubulin protein band utilizing the Fusion software.

2.17 Comet assay

The Comet assay was the first single cell electrophoresis established by Ostling and Johanson in 1984 in order to measure UV-induced double-strand DNA damage in a microelectrophoretic system[159]. An improved version with alkaline instead of neutral conditions was developed by Singh et al. in 1988, which was used in this thesis[160].

2.17.1 Cell culture

For a three-day incubation at 37 °C, 20000 cells were seeded onto 3 cm cell culture dishes. Cells were washed twice with PBS and were then irradiated with 10 J/cm² UVA in 2 ml HBSS. Cells were then washed again with PBS, trypsinized and resuspended in 800 µl full medium.

2.17.2 Alkaline comet assay

One day before use, agarose-coated object slides and lysis buffer were prepared. For the object slides, 1 g agarose was dissolved in 100 ml PBS and heated in a microwave. Temperature was then kept at 60 °C while clean object slides were dipped in the agarose solution, wiped at the back and left to dry overnight. For preparation of the lysis buffer, 1.5 ml Triton X-100 were added to 135 ml lysis buffer as described in the material section (see 2.3).

After cell treatment on the day of the experiment, trypsinized cells were centrifuged at 200 x g for 4 minutes at 4 °C. After disposal of the supernatant, cell pellets were mixed with 200 µl of low melting point agarose, distributed onto coated object slides and covered with a coverglass. Agarose was hardened for 5 minutes on ice racks and left in 4 °C cold lysis buffer overnight. Next, slides for alkaline treatment were washed in water. For lesion-specific enzyme treatment, see 2.17.3. Object slides were wiped dry at the back and placed in the electrophoresis device. Cold alkaline unwinding solution was added until samples were fully submerged and cells were incubated for 30 minutes at room temperature. Then, all samples were subjected to electrophoresis (25 V, 300 mA, 25 minutes). The current over the entire device (1.18 V/cm) is close to the recommended 1 V/cm in guidelines. Afterwards, slides were washed in water, incubated in ethanol (80 %) for 5 minutes and left to dry in the dark overnight. The next day, samples were incubated with 100 µl midori green staining solution (1.5 µl midori green dye in 100 ml water) for two hours and visualized using an inverted microscope with epi-fluorescence. At least 50 comets per sample were counted and analyzed for their amount of DNA in tail (in percent). The analysis program calculates the amount of damaged DNA by defining a comet as all adjoining pixels in a comet shape and measuring the pixel intensity at each location within that shape. Several read out parameters can be obtained from the program, e.g. comet length, tail length and comet area. Here, the percentage (%) of DNA in the comet tail was used, which is calculated by dividing the tail intensity by the comet intensity, multiplied by 100.

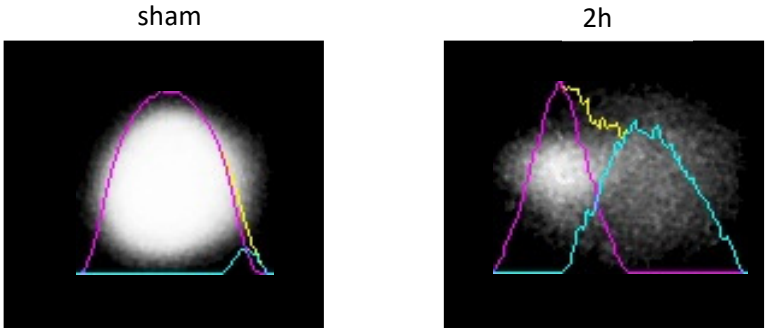

Figure 2.1 Depiction of example parameters (head area, pink; tail area, blue; total area, yellow) used for comet calculation by the CometScore software. The image on the left depicts a comet after sham treatment, the image on the right depicts a comet two hours after irradiation with 10 J/cm² UVA.

2.17.3 Lesion-specific comet assay

A further improvement of the comet assay by Gedik et al., who incorporated exogenous addition of a DNA repair enzyme, allows for the detailed observation of specific DNA lesions[161,162]. For visualization of cyclobutane pyrimidine dimer formation in DNA, the enzyme T4 endonuclease V (T4endoV) was used. It has a dual function. The enzyme cleaves damaged DNA at sites of T-T, C-T and C-C dimers via its N-glycosylase activity, leaving an apurinic site, which is subsequently cleaved by its AP lyase activity[163].

After incubation in lysis buffer overnight (see 2.17.2), cells were shortly submersed in cold enzyme reaction buffer. The backsides of the object slides were wiped dry and 50 µl of enzyme solution per sample were added to the respective samples. Enzyme solution contained enzyme buffer (T4 PDG reaction buffer, provided, 1x), BSA (100 µg/ml, 1:100) and the respective enzyme (1:1000) per 50 µl solution. Samples were covered again and incubated at 37 °C for 30 minutes in a box layered with wet tissue paper. Afterwards, object slides were washed in water and treated according to the protocol for the alkaline Comet assay.

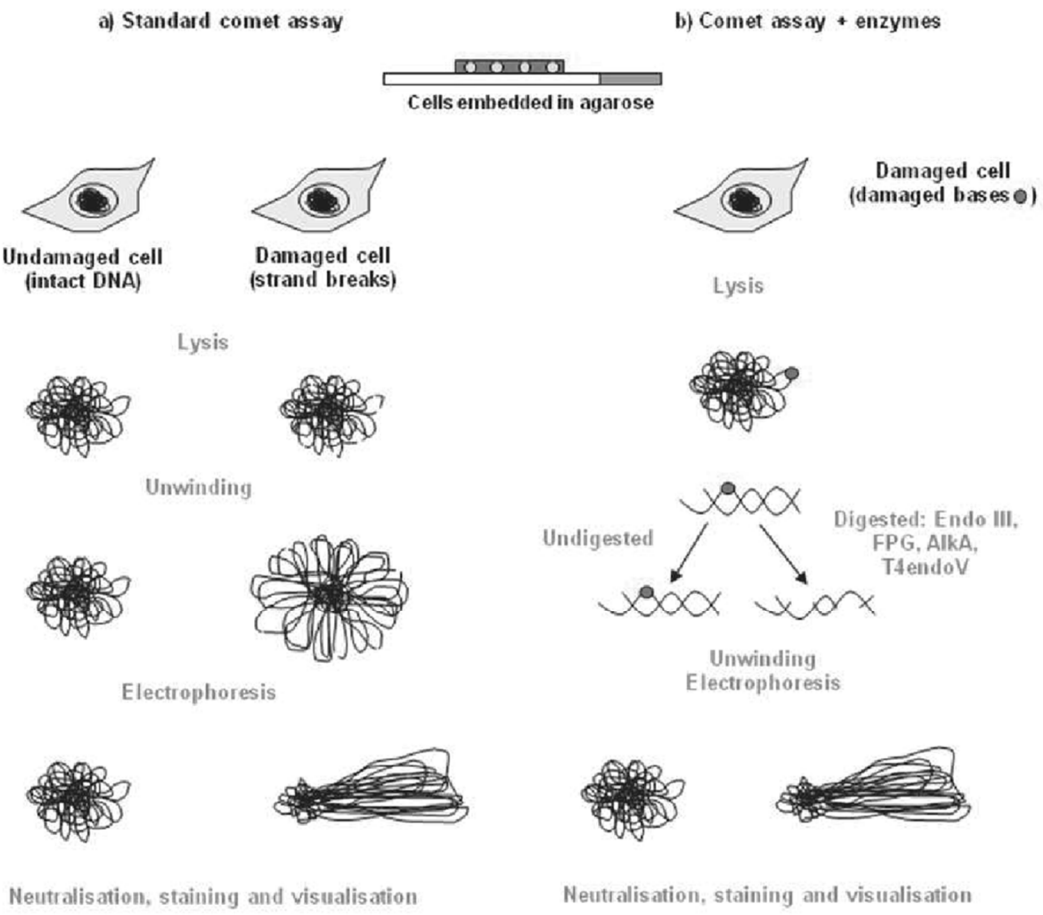

Figure 2.2 Depiction of the standard and the repair enzyme comet assay procedure. Taken from Azqueta et al., licensed under CC BY 3.0[164]*.*

2.18 Immunodetection of CPDs via ELISA

The enzyme-linked immunosorbent assay (ELISA) "High Sensitivity CPD/Cyclobutane Pyrimidine Dimer ELISA Kit Version 2" was used to determine the formation and repair of UV-induced pyrimidine dimers in DNA extracted from cell samples. The protocol uses an antibody specific for detection of CPDs (clone TDM-2). The second antibody is biotinylated to which site the streptavidin-peroxidase binds. The product of the reaction between peroxidase, H_2O_2 and o-phenylenediamine (OPD) is a colorimetrically detectable dye that is measured at 492 nm spectrophotometrically.

2.18.1 Cell culture

Cells were seeded onto 3 cm culture dishes in full medium with a density of 20000 cells per dish. After three days in culture, irradiation was performed. Therefore, cells were washed with 2 ml PBS and irradiated with 10 J/cm² UVA in 1 ml HBSS. After irradiation, cells were washed again and post-incubated in starvation medium for 0 to 6 hours at 37 °C. Then, cells were

washed and 500 µl PBS was added. Cells were detached from the dish by scraping. Cells from two dishes were collected and pooled in a 2 ml Eppendorf tube.

For experiments including repair inhibition with X80, irradiation was followed by a subsequent incubation with 100 µM X80 in starvation medium at 37 °C. Every hour, the same concentration was added to the medium without medium exchange. For aphidicolin treatment, cells were preincubated with 2.9 µM aphidicolin in starvation medium for 24 hours, followed by irradiation as mentioned above.

Experiments with flavones and subsequent CPD measurement included a two-hour preincubation at 37 °C with 50 µM of luteolin or tricetin in starvation medium. Then, cells were irradiated with 10 J/cm² in HBSS, followed by a post-incubation at 37 °C in starvation medium from 0 to 4 hours.

2.18.2 Sample preparation

Collected cell suspensions from 2.18.1 were centrifuged at 10000 x g for 15 seconds at 4 °C. Supernatants were discarded and pellets were stored at - 80 °C.

2.18.3 DNA extraction

For detection of CPDs in samples, DNA extraction from the cell pellet was achieved using a Qiagen DNA extraction kit. Cell pellets were resuspended in 200 µl PBS with 20 µl proteinase K (600 mAU/ml solution). After addition of the lysis buffer, samples were pulse-vortexed for 15 minutes. Following an incubation at 56 °C for 10 minutes, ethanol was added, samples pulse vortexed and solutions transferred to QIAamp Mini spin columns. Centrifugation at 6000 x g for one minute yielded a filtrate, that was discarded. Then, a wash buffer was applied, and columns were centrifuged again at 6000 x g. Filtrates were discarded once again and a second wash buffer was applied, followed by a centrifugation at 20000 x g for three minutes. For the elution step, a new tube was used and centrifugation at 6000 x g for one minute with DNAse-free water yielded extracted DNA. DNA concentrations were measured spectrometrically at a wavelength of 260 nm using a 1 mm cuvette and 1 µl of the sample.

2.18.4 Enzyme-linked immunosorbent assay (ELISA)

Instructions from the manufacturer of the CPD ELISA Kit were followed. In brief, extracted DNA samples were diluted to 0.4 µg/ml in assay diluent and heat-denatured (100 °C for 10 minutes), and then cooled for 15 minutes on ice. Then, 50 µl of the solution was applied in

duplicates to a protamine sulfate precoated 96-well plate. Wells were partly dried overnight in a 37 °C incubator, followed by additional and complete drying underneath a safety bench for three hours at 37 °C. Dried wells were washed and incubated with a blocking reagent for 30 minutes, followed by an additional wash step and incubation with the primary antibody for CPD detection for 30 minutes. Wells were washed and incubated with the secondary biotinylated antibody, followed by washing and incubation with the streptavidin-coupled peroxidase for 30 minutes. After the last wash, o-phenylenediamine dihydrochloride (OPD)-containing substrate solution was freshly prepared and pipetted onto the wells for 30 minutes. Finally, stop solution was added and absorption was measured at 492 nm using a plate reader. All steps were performed at 37 °C.

2.19 Real-time bioenergetics measurement (Seahorse analysis)

The Seahorse flux analyzer allows for real-time measurements of cellular oxygen consumption rates (OCR) and other parameters regarding bioenergetics using mitochondrial-targeted toxins in a fixed sequence of injection. In principle, the injection of specific toxins reveals the amount of cellular respiration that is used for ATP production, basal respiration, non-mitochondrial respiration, maximal respiration and the spare respiratory capacity. In addition, the Seahorse analyzer measures the extracellular acidification (ECAR) in the medium, indicative for non-mitochondrial ATP production from glycolysis. Once the respective cell line has been characterized for their general responsiveness to the mitochondrial toxins oligomycin and FCCP (carbonyl cyanide-4 (trifluoromethoxy) phenylhydrazone), a defined test can be performed, e.g. the mitochondrial stress test.

2.19.1 Cell line characterization

Each cell line was pre-assayed in the flux analyzer in order to determine the suitable amount of injected toxin as well as a suitable cell number per well. For this, varying cell numbers and concentrations of FCCP were tested and optimal conditions were used for further experiments. FCCP concentrations from 0.125 to 0.5 µM (low range) were tested, as well as concentrations from 0.5 to 2 µM (high range). Cell numbers from 4000 to 18000 cells per well were tested for all three cell types (NHDF, CT, MMC).

2.19.2 Mitochondrial stress test

The mitochondrial stress test reveals proportions of oxygen consumption that are attributable to a certain part of respiration, e.g. for ATP production. Therefore, effects of substances and

treatments on specific parts of cellular respiration can be studied. Here, the basal responsiveness to mitochondrial toxins between different cell types was evaluated, as well as the effect of UVA radiation on respiration.

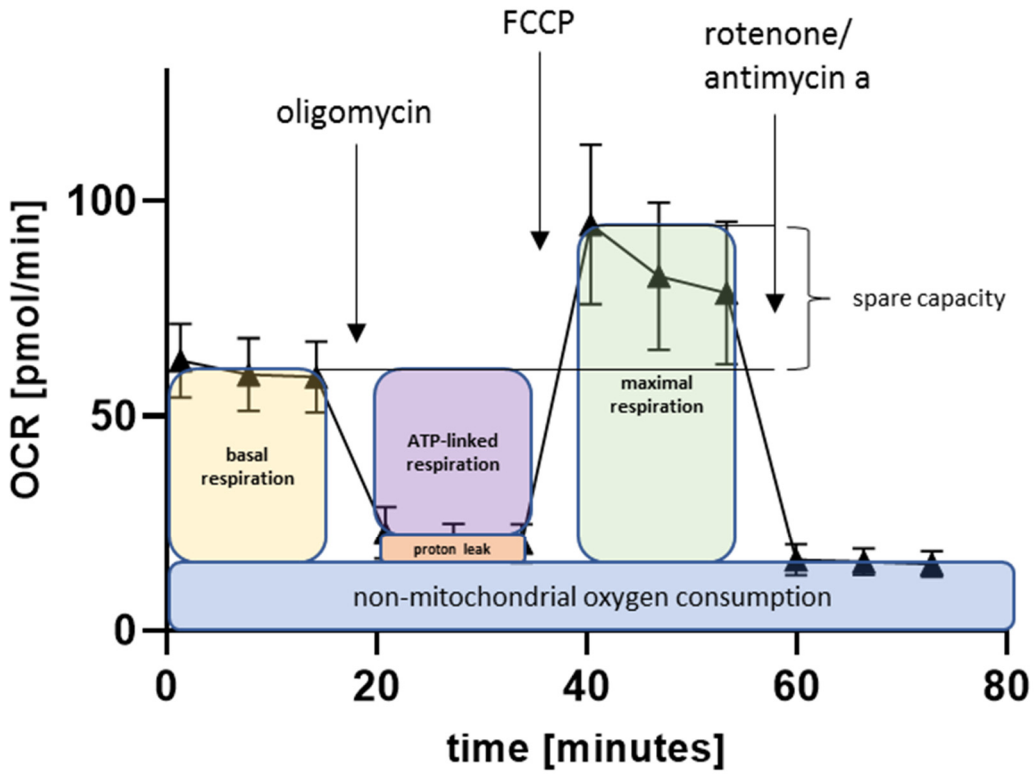

Figure 2.3 Mito stress test profile for the Seahorse XF flux analyzer showing an example OCR after sequential injection of mitochondrial inhibitors and calculated parameters.

The Seahorse flux analyzer was preheated to 37 °C one day before the experiment. For experiments without irradiation, cells were seeded onto Seahorse 96-well plate wells (17000 cells/well NHDF, 15000 cells/well CT, 12000 cells/well MMC) in 80 µl starvation medium, left to settle for one hour at room temperature and incubated overnight at 37 °C and 5 % CO_2. Simultaneously, a Seahorse sensor was calibrated overnight at 37 °C in a non-CO_2 incubator with 200 µl calibrant per well. At the day of the experiment, cells were washed and incubated with Seahorse medium for one hour in a non-CO_2 incubator. Seahorse DMEM medium was supplemented with glucose (1 g/l), 1 % pyruvate and 1 % glutamax and adjusted to pH 7.4. Meanwhile, the ports of the sensor plate were loaded with oligomycin, FCCP and rotenone/antimycin a, providing a concentration of 1, 2 and 1 µM per well upon injection, respectively. The plate with the loaded sensor cartridge was then inserted into the flux analyzer and calibrated for 20 minutes. After that, the cell culture microplate was inserted and

the experiment started. Basal respiration was measured, followed by injection of oligomycin, FCCP and rotenone/antimycin a in a fixed sequence as shown in Figure 2.3. Before and after each injection, three measurements were taken for OCR and ECAR. At least 8 replicates per experiment per treatment were measured in three independent experiments. At the end of the experiment, cells were stained with Hoechst solution for 5 minutes to determine DNA content for normalization and estimation of cell numbers. Excitation and emission in a plate reader were set at 361 nm and 486 nm, respectively.

For experiments with irradiation, a new procedure was established. For MMC cells, 320000 cells per dish, for NHDF and CT cells, 280000 cells per dish were seeded onto 10 cm cell culture dishes. After three days in full medium, cells were washed with 8 ml PBS and irradiated in 4 ml HBSS. Then, cells were washed in PBS, trypsinized (additionally, careful use of a cell scraper was needed for detachment of intact cells) and counted. These cells were seeded into the Seahorse plate wells in 80 µl starvation medium (NHDF 17000 cells/well, CT 15000 cells/well, MMC 12000 cells/well). Cells were left to settle for one hour at room temperature and were then incubated for 24 hours at 37 °C and 5 % CO_2 in order to attach to the Seahorse plate. Then, the normal Seahorse protocol was followed as described above.

Parameters given in the results are calculated automatically by the Seahorse software “wave”. The non-mitochondrial oxygen consumption shows the minimum rate measured after injection with rotenone/antimycin a. For the basal respiration, baseline respiration before oligomycin injection is subtracted by the non-mitochondrial proportion of respiration. Maximal respiration is the maximal value after FCCP injection minus the non-mitochondrial respiration. Proton leak is calculated by subtracting the non-mitochondrial respiration from the lowest rate measurement after injection with oligomycin. The ATP production is given when the last value before oligomycin injection is subtracted by the minimum rate value after oligomycin. Finally, the spare respiratory capacity is calculated by subtracting the maximal value of the maximal respiration and the last value of the basal respiration measurement.

2.20 Flow cytometry (FACS analysis)

Fluorescence-activated cell scanning (FACS) was used to differentiate cell types for the occurrence of surface proteins and size. The principle of flow cytometry is based on the channeling of single cells through laser beam. A detector measures forward and sideward scattered light (FSC and SSC), as well as fluorescence signals from optional fluorescent dyes.

FSC and SSC measures indicate cell size and granularity, while fluorescence signals can indicate the expression level of specific targets of antibodies, in this case of cell surface proteins CD38, CD39 and CD73. The measurement for expression levels of CD38, CD39 and CD73 was performed on a BD FACSCanto flow cytometer using specific fluorophore-labelled antibodies.

2.20.1 Cell culture

For NHDF and CT cells, 217000 cells per 10 cm cell culture dishes were used, while for MMC cells 105000 cells per dish were seeded in 8 ml full medium and cultivated for three days at 37 °C. Cells were then washed with 4 ml PBS and irradiated with 10 J/cm² UVA in 4 ml HBSS. After a second wash, cells were trypsinized for 10 minutes with 500 µl Trypsin-EDTA. Cells were lightly scraped from the dish using a cell scraper. Trypsinization was stopped by adding 3.5 ml FCS-supplemented medium and cells from one dish were divided into four flow cytometry tubes on ice. To obtain cell pellets, suspensions were centrifuged for 5 minutes at 400 x g at 4 °C.

2.20.2 Sample preparation

The supernatant was discarded and the respective antibody was added (see material). The suspension was softly vortexed and incubated for 15 minutes in the dark on ice. For CD73 staining, the antibody was diluted 1:200 in MACS buffer. CD38 and CD39 antibodies were diluted 1:50 in MACS buffer. After the staining, 1 ml MACS buffer was added, followed by centrifugation for 5 minutes at 300 x g at 4 °C. Then, the supernatant was removed and 200 µl MACS buffer with DAPI (1 mg/ml, 1:200 in MACS buffer) was added immediately before subjecting the samples to flow cytometry.

2.20.3 FACS analysis

Cell size was measured by use of the Forward Scatter (FSC) parameter. Cells were gated for their size and granularity using FSC and Sideward Scatter (SSC). Small particles of debris were excluded and the remaining population was then gated for DAPI-staining negative cells to exclude dead or dying cells from the analysis. Following this exclusion, cells were gated for the respective surface proteins, CD38, CD39 and CD73, using the BD FACS Diva software.

2.21 UPLC measurement of ATP/NAD^+ derived metabolites

Adenosine triphosphate (ATP) and nicotinamide adenine dinucleotide (NAD^+) are key molecules in bioenergetics. Here, ATP, NAD^+ and their derivatives are used to investigate the implication of cell surface proteins CD38, CD39 and CD73 in the ATP/NAD^+/adenosine axis.

After extracellular addition, ATP can be metabolized to its derivatives adenosine diphosphate (ADP), adenosine monophosphate (AMP) and adenosine (Ado) by CD39 and CD73. NAD^+ is first metabolized to ADP-ribose via CD38 and subsequently to Ado via the shared part of the pathway catalyzed by CD73. The formation and degradation of all involved metabolites was investigated in young and artificially aged cells with or without prior irradiation with a low dose of UVA.

2.21.1 Cell culture

For all three cell types (NHDF, CT and MMC) 10000 cells were seeded onto 6-well plates in starvation medium one day before irradiation to prevent proliferation and to achieve an even cell number. Cells were washed with PBS and irradiated with 10 J/cm² UVA in 1 ml HBSS for approximately 35 minutes. After irradiation, cells were washed with HBSS. To obtain samples for UPLC analyses, the cells were incubated with 1 ml of the respective substrate. Substrate concentrations were as follows: AMP (20 µM in HBSS), NAD^+, ATP and adenosine (2 µM in HBSS). After 10 minutes, 250 µl of the medium of each well were collected in UPLC vials and stored on ice. After 20 minutes, 250 µl were collected again and stored on ice. All samples were then transferred to liquid nitrogen for storage until measurement in the UPLC system. Aliquots of the substrates were measured to obtain the baseline value (see Figure 3.42, value at 0 minutes).

2.21.2 Metabolite detection

For detection of ATP- and NAD^+-derived metabolites, an UPLC system from Waters supplied with a Van Guard Cortecs C18+ (90Å, 1.6 µm, 2.1 mm x 5 mm) column was used. A linear gradient of mobile phase A and B was prepared. Mobile phase A consisted of 200 mM KH_2PO_4 and 200 mM KCl at pH 6. Mobile phase B was prepared with 200 mM KH_2PO_4, 200 mM KCl and 7.5 % acetonitrile at pH 6. The amount of mobile phase B in the gradient was changed as follows: timepoint 0 minutes = 0 %, timepoint 7 minutes = 9 %, timepoint 26.51 minutes = 100 %, timepoint 30.51 minutes = 100 %, timepoint 30.52 minutes = 0 %. The re-equilibration time after each run was 8 minutes. The column temperature was 17 °C. The autosampler setting was set at 4 °C and a flow rate of 0.25 ml/min was employed. A standard for each metabolite was used for identification of peaks and for quantification. The detection wavelength was 254 nm.

2.22 Drug-induced accelerated senescence

Several methods for the induction of transient senescence in cell cultures are available. H_2O_2 or doxorubicin are examples for substances inducing reversible senescence[165,166]. Here, a more recent and stable induction of cellular senescence was used. The accelerated aging of fibroblasts was induced by a process called drug-induced accelerated senescence (DIAS) using the ROS producing compound mitomycin c (MMC), as described[167].

2.22.1 Cell culture

NHDF, as the precursor for the artificially aged cells, were seeded onto 10 cm cell culture dishes in full medium with a density of 60000 cells per dish and allowed to grow for three days. Half of the prepared dishes was labelled for MMC treatment, while the other half was used for CT cells (DMSO treatment). Cells were incubated with 200 nM MMC per dish in 8 ml starvation medium for 24 hours. As a control, cells were treated with DMSO accordingly. After 24 hours, cells were washed with 8 ml PBS and incubated with full medium for 24 hours. The next day, cells were washed and incubated with 200 nM MMC or DMSO for the second time for 24 hours. Then, cells were washed and incubated with full medium for 24 hours. The next day, cells were trypsinized with 1.5 ml trypsin for 10 minutes and the detachment stopped by adding 8.5 ml full medium. Cells were counted and seeded according to the experiment. For use in the flux analyzer, 180000 cells per 10 cm dish of CT or NHDF were used, while 200000 cells per dish were used for MMC cells. For use in protein expression experiments, 160000 cells of all three cell types were seeded. For 24-well plates, 8000 cells of all cell types were seeded. For further experiments, artificially aged cells were used three to five days after end of the treatment, as signs of cellular senescence, e.g. increase in size, became visible during treatment and were most evident 5 days after the end of the treatment.

2.23 Cell proliferation measurement / BrdU incorporation assay

Cell proliferation can be measured following the incorporation of the pyrimidine analog 5-bromo-2'-deoxyuridine (BrdU) into DNA. Here, a kit was used following the manufacturers protocol.

10000 cells of each cell type (NHDF, CT and MMC) were seeded onto 96-well plates. After 24 hours, cells were washed with PBS and incubated with either 10 % FCS as a positive control, 10 µM doxorubicin as a negative control or starvation medium for 24 hours. Then, BrdU was added according to the manufacturers protocol. After 24 hours, BrdU containing medium was

removed and a provided fixing and denaturing solution was added for 30 minutes. Then, cells were incubated with the detection antibody for one hour. After a triple wash step, secondary antibody was added and incubated for 30 minutes, followed by a final triple wash step. 3,3', 5,5"-tetramethylbenzidine (TMB) was added as a substrate for horse radish peroxidase (HRP) conjugated to the secondary antibody for 30 minutes. Right before measurement of absorption at 450 nm, stop solution was added. All steps were performed at room temperature.

2.24 Senescence-associated ß-galactosidase staining (SA ß-Gal)

Positive staining for senescence-associated ß-galactosidase is exclusive for senescent cell and can therefore be used as a biomarker of cellular aging[132]. Therefore, this method was used to detect aged fibroblasts *in vitro*.

15000 cells (NHDF, CT and MMC) per well of a 24-well plate were seeded in 1 ml of full medium. At the day of the assay, 20 mg/ml 5-bromo-4-chloro-3-indolyl-β-D-galactopyranoside (X-Gal) in DMSO was freshly prepared in a polypropylene vial. X-Gal is a chromogenic substrate for ß-galactosidase. After washing of the cells with 500 µl PBS, 250 µL formaldehyde-containing fixative solution (provided) was added for 15 minutes. Following a double wash step with 500 µl PBS, 250 µl of freshly prepared staining solution containing a staining supplement (provided) and 20 mg/ml X-Gal was added over night in a non-CO_2 incubator at 37 °C. After 24 hours, cells were analyzed using an inverted cell culture microscope and 10 x magnification. For each well, 5 pictures were taken and analyzed for general cell number and number of SA ß-Gal positive cells.

2.25 Invasion assay

The ability to invade tissues is one hallmark of cancer[168]. The invasion assay is often used to investigate compounds for their anti-invasive properties by inhibiting invasion of cancer cells through an artificial basal membrane into a site of chemoattractive environment. The assay principle is based on the Boyden chamber assay[169]. The assay consists of two compartments, the lower of which contains a chemoattractant, while the upper compartment holds the cell culture monolayer on an artificial basement membrane with a pore size of 8 µm covered with a Matrigel coating. Here, the invasion of cancer cells into an environment formed by secreted substance from either CT or MMC cells was investigated. The number of invaded cells can be

used to determine the tumor permissiveness of the microenvironment formed by the MMC or CT secretome.

2.25.1 Cell culture

Cancer cells (SCL-1) from cell culture flasks were trypsinized and counted. 40000 cells per well were seeded into transwells of a 24-well transwell plate in 400 µl starvation medium (DMEM high glucose). For this, 400 µl of the cell suspension was slowly added to the rehydrated transwells (see below). The bottom of the well was filled with 400 µl of starvation medium (DMEM high glucose), the transwells were lowered into that medium and the whole plate was incubated for 24 hours at 37 °C. Three replicates per treatment were used.

2.25.2 Conditioning of medium

The invasion assay is often used to measure invasion of cancer cells through a semipermeable membrane towards a chemoattractant. In this thesis, not a single chemoattractant was used but the medium from CT and MMC cells, harboring the whole secretome.

MMC or CT cells were seeded on 10 cm dishes in full medium at a density of 300000 cells per dish for MMC cells and 225000 cells per dish for CT cells. After 48 hours, cells were washed with PBS and 8 ml starvation medium was added. After another 48 hours, this conditioned medium was transferred into 2 ml Eppendorf tubes and stored at - 20 °C for use in the invasion assay.

2.25.3 Preparation of the transwells

Cell culture 24-well plates with transwells (pore size 8 µm) were covered with 50 µl cold Matrigel (1:30 in PBS). The layer was covered with 200 µl sterile water and the plate left to dry under a sterile bench for 72 hours. After that time, the wells were rehydrated with 100 µl sterile water.

2.25.4 Invasion assay procedure

Conditioned medium was thawed at 37 °C. Medium from the bottom of the wells was aspirated and replaced with 400 µl of conditioned medium. Conditioned medium was centrifuged prior to use in the invasion assay at 15000 x g for one minute to remove cell culture debris and other particles. The top well (transwell) contained the cells, Matrigel and starvation medium (DMEM high glucose). The plate was then incubated at 37 °C for 48 hours to allow for invasion of cancer cells.

2.25.5 Preparation for microscopy

Medium from transwells was aspirated and transwells were dipped in a container of PBS as a wash step. First with a bigger cotton swab and second with a smaller cotton swab, the Matrigel was carefully removed from the membrane. Wells were washed twice in PBS. Transwells were incubated in 400 µl ice cold methanol for 20 minutes. Wells were then washed with PBS three times and left to dry for 30 minutes. When dry, wells were shortly dipped into a well filled with Coomassie staining solution and directly washed in a well with water. If staining was too intense, wells were dipped into destaining solution, washed with water and then used for microscopy. Transwells were then placed with the membrane down on an object slide and investigated under a microscope with the lowest possible magnification, so that one well was entirely covered by taking five pictures. Blue Coomassie staining allowed for a counting of cells that were invaded through the Matrigel and the membrane into the bottom well filled with conditioned medium.

2.26 Statistical analysis

All experiments were performed in at least three independent experiments (n = 3) with two or more technical replicates, unless otherwise stated. Error bars represent standard error of the mean (SEM).

Statistics were calculated using the Prism 8 software. For evaluation of differences, students *t*-test or the one-way Anova with Dunnett's or Tukey's multiple comparison post-hoc test were used. The p-value was set at 0.05.

3 Results

UV-radiation poses a risk for the skin causing diseases and aging. While the initiation of skin cancer has been mainly attributed to UVB irradiation, UVA exposure was associated with skin aging. However, recent research provided evidence that UVA imposes a further damage likely implicated in skin cancer initiation and progression. Research on molecular UVA effects was mainly performed at high dose levels with final loss of cell functions and death. However, little is known on the biological impact of low dose UVA exposure comprising a dose range achieved upon a typical lifestyle. In the present study, low-dose UVA-dependent alterations in human dermal fibroblasts were investigated including DNA, lipid and protein associated damage as well as energy metabolism. Additionally, flavones as possible photoprotective agents in the prevention of UVA-induced damage in a model system of human dermal fibroblasts are evaluated. Lastly, the differences of young and artificially aged fibroblasts in response to physiological UVA doses with possible implications for photoprotection strategies in the elderly are studied.

3.1 Establishment of irradiation doses

Normal human dermal fibroblasts (NHDF) were established as a model system. Cells were irradiated with doses of UVA up to 45 J/cm² and cell viability was determined with the MTT assay directly after irradiation (0h) or 24h after UVA exposure (Figure 3.1). The emission spectrum of the irradiation source is depicted in Figure Figure 3.1 A, proving that the lamp covers the entire UVA range from 320 to 400 nm with a peak at 365 nm. Exposure of NHDF to UVA light in the dose range of 0 - 20 J/cm² had no statistically significant toxic effect as determined 0 and 24h post irradiation (Figure 3.1 B). Small, statistically non-significant increases in cell viability were determined 24h after irradiation with 5 - 20 J/cm² UVA, indicating possible growth stimulatory effects of moderate UVA doses. Based on earlier experiments, a dose of 45 J/cm² was selected to prove cytotoxicity of UVA. As expected, less than 25 % of the cells survived at this dose level at 0 and 24 hours. Based on the present experiments, mainly a non-toxic dose of 10 J/cm² UVA was applied to study effects of low dose UVA exposure.

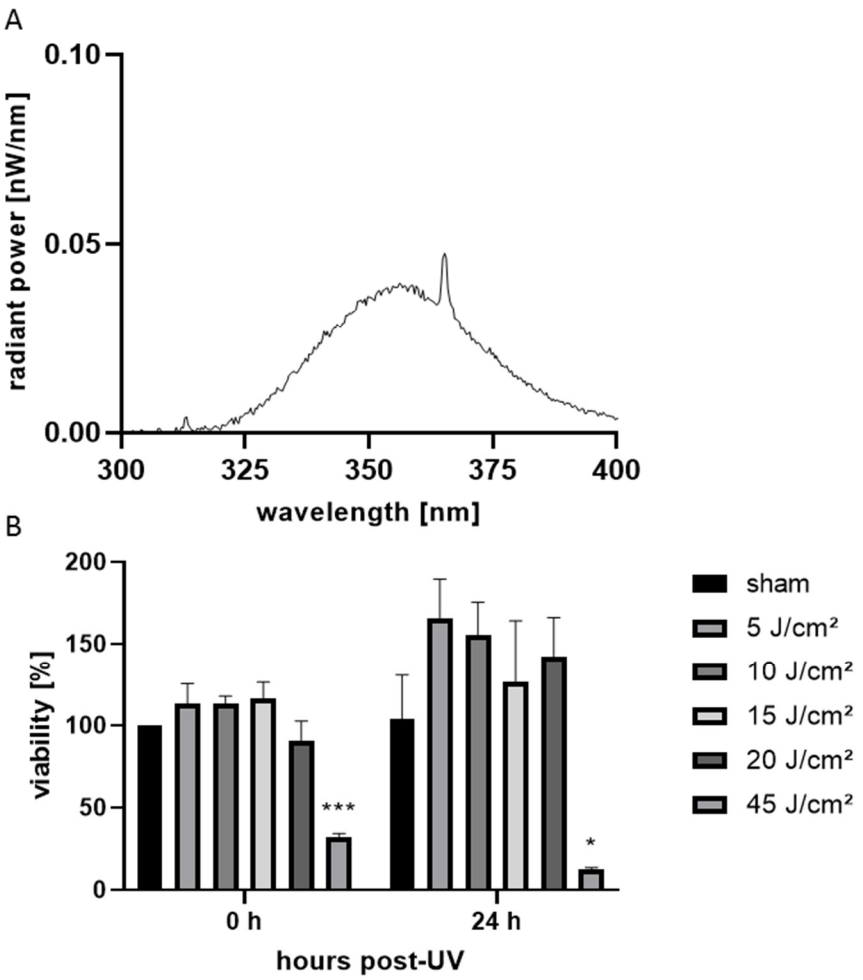

*Figure 3.1 Viability of NHDF after irradiation with UVA light. The emission spectrum of the UVA lamp in the irradiation system is depicted in the range between 300 and 400 nm (A). The viability of fibroblasts irradiated with UVA doses from 5 to 45 J/cm² is shown for 0 and 24 hours post incubation (B). The unirradiated control at the 0-hour timepoint after irradiation is set as 100 %. Viability was determined using the MTT assay. Data represent means ± SEM. Unpaired student's t-test was used for the determination of statistical significance to the respective control. *p < 0.05, **p < 0.01, ***p < 0.001*

3.2 Selection and stability testing of the flavones

After selection and evaluation of the biological test system, including cells and UV doses, flavonoids likely suitable as photoprotectants were chosen. Based on their structure, luteolin, tricetin, nobiletin and tangeretin were selected as candidate molecules (Figure 3.2).

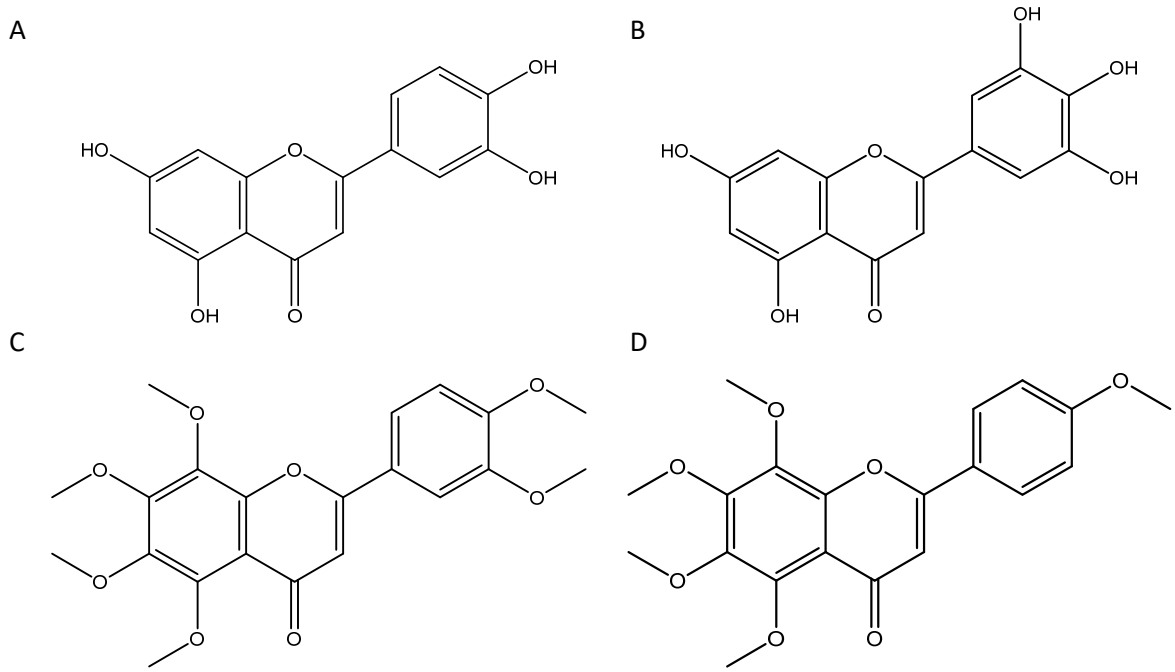

Figure 3.2 Chemical structures of the flavones luteolin (A), tricetin (B), nobiletin (C) and tangeretin (D).

All four compounds belong to the flavonoid subgroup of flavones with the typical backbone of 2-phenylchromen-4-one. Luteolin (A) and tricetin (B) carry hydroxyl groups at similar positions of the A-ring. The B ring of luteolin is substituted with two OH-groups while tricetin carries three hydroxyl groups. In contrast, nobiletin (C) and tangeretin (D) are substituted with methoxy groups at positions 5, 6, 7 and 8 of the A-ring and two respectively one methoxy group at the B-ring.

Flavones with free hydroxyl groups are effective antioxidants, an effect mainly mediated by phenol-chinone redox systems. Blocking free -OH groups prohibits such antioxidant mechanisms of action.

Due to their structure flavones absorb UV light. In order to determine the UV range covered by the selected compounds, their absorption spectra in phosphate buffer (pH 7.4) between 230 and 500 nm were recorded (Figure 3.3).

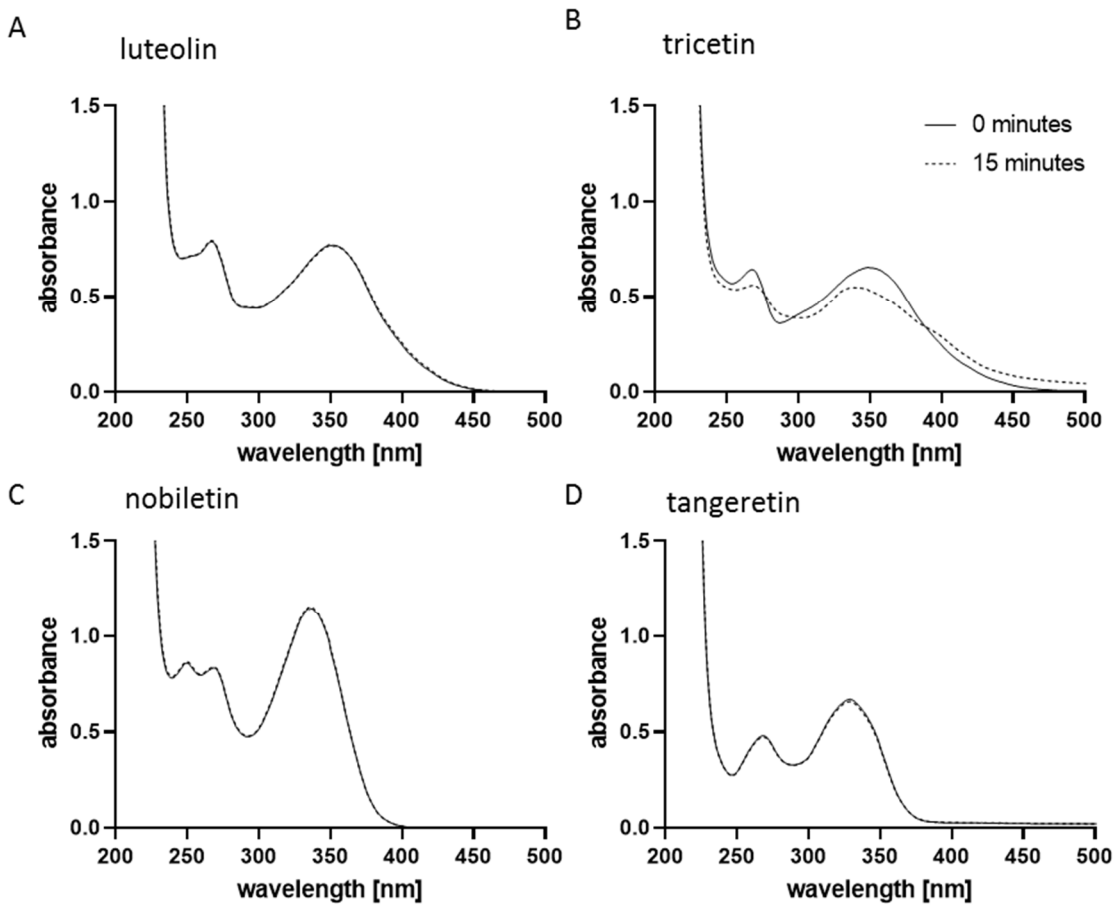

Figure 3.3 Absorption spectra and stability of the substances in phosphate buffer. Absorbance spectra of 50 µM luteolin (A), tricetin (B), nobiletin (C) and tangeretin (D) are shown in the wavelength region from 200 to 500 nm. Measurements were performed in 0.1 mM phosphate buffer (pH 7.4, RT) at 0 and 15 minutes.

Figure 3.3 displays that all compounds show major absorption in the UVA range (320 - 400 nm) with maxima of about 350 nm for luteolin (A) and tricetin (B) and 340 nm for nobiletin (C) and tangeretin (D). Recorded spectra after 15 min of incubation at room temperature showed no difference for luteolin (A) nobiletin (C) and tangeretin (D) indicating stability in aqueous solution at the given setting. A minor decrease in total absorption was found for tricetin (B).

In order to obtain information on cellular uptake, HPLC methods to determine flavones were established.

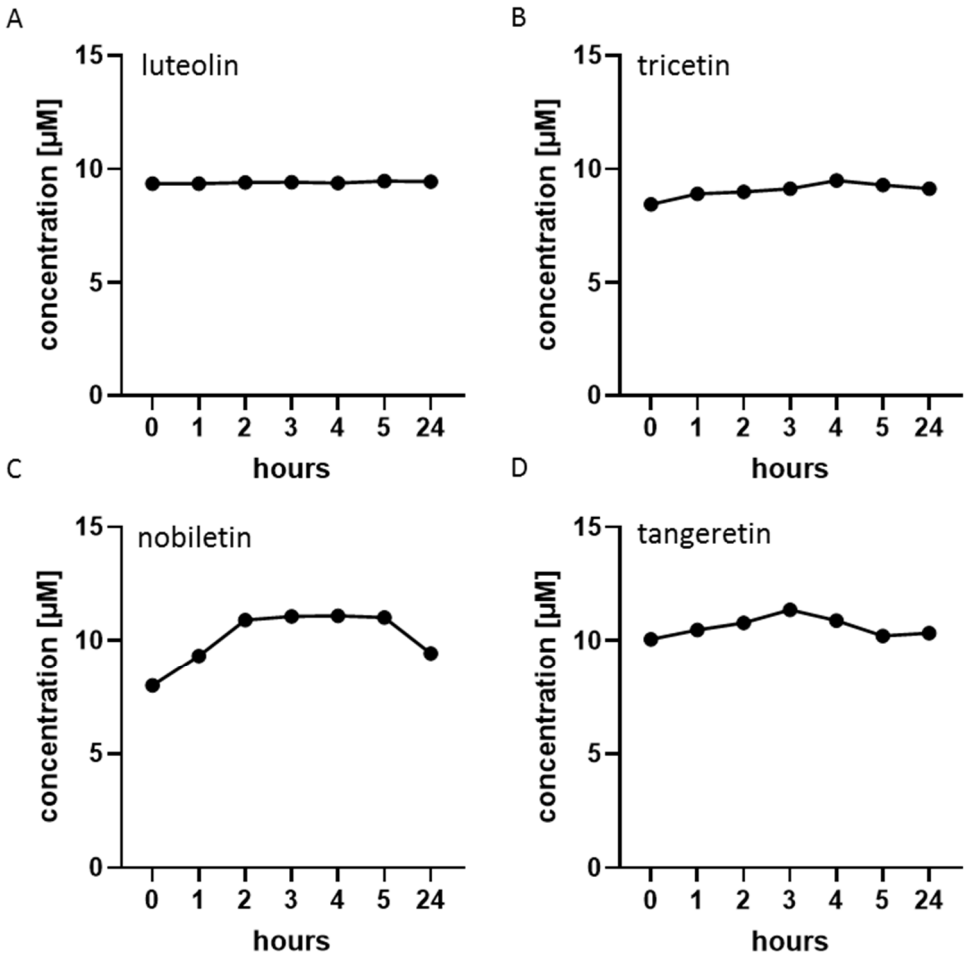

Figure 3.4 Changes in the concentration of the four flavones in methanol over time. Luteolin (A), tricetin (B), nobiletin (C) and tangeretin (D) concentrations were determined by means of HPLC. A 10 µM solution of each substance was prepared and the concentration was followed over time at RT.

All methods were sufficiently selective and sensitive to measure flavone concentrations. The compounds proved to be sufficiently stable in methanolic stock solutions at room temperature (Figure 3.4). Starting levels of 10 µM were almost recovered by HPLC measurements and maintained for 24h for luteolin (A), tricetin (B) and tangeretin (D). At 0h the level of nobiletin was below the expected value but further increased to 10 µM which might be due to a solution phenomenon or analytical problem.

By means of HPLC, the stability and recovery of flavones was also studied in starvation medium used for cell culture (Figure 3.5). The expected starting level of 10 µM was only recovered for luteolin (A) and nobiletin (C). The latter proved to be stable in medium for 24 hours, whereas

the luteolin concentration in medium dropped between 5 and 24 hours of incubation. In the case of tangeretin (D) less than 50 % of the expected starting level was recovered but the compound was found to be stable up to 24 hours. This may be due to an analytical shortfall related to absorption effects of the compound to medium constituents or plastic ware. Recovery of tricetin (B) is also poor, furthermore, the level of the compound in medium dramatically decreases within the first hour of incubation.

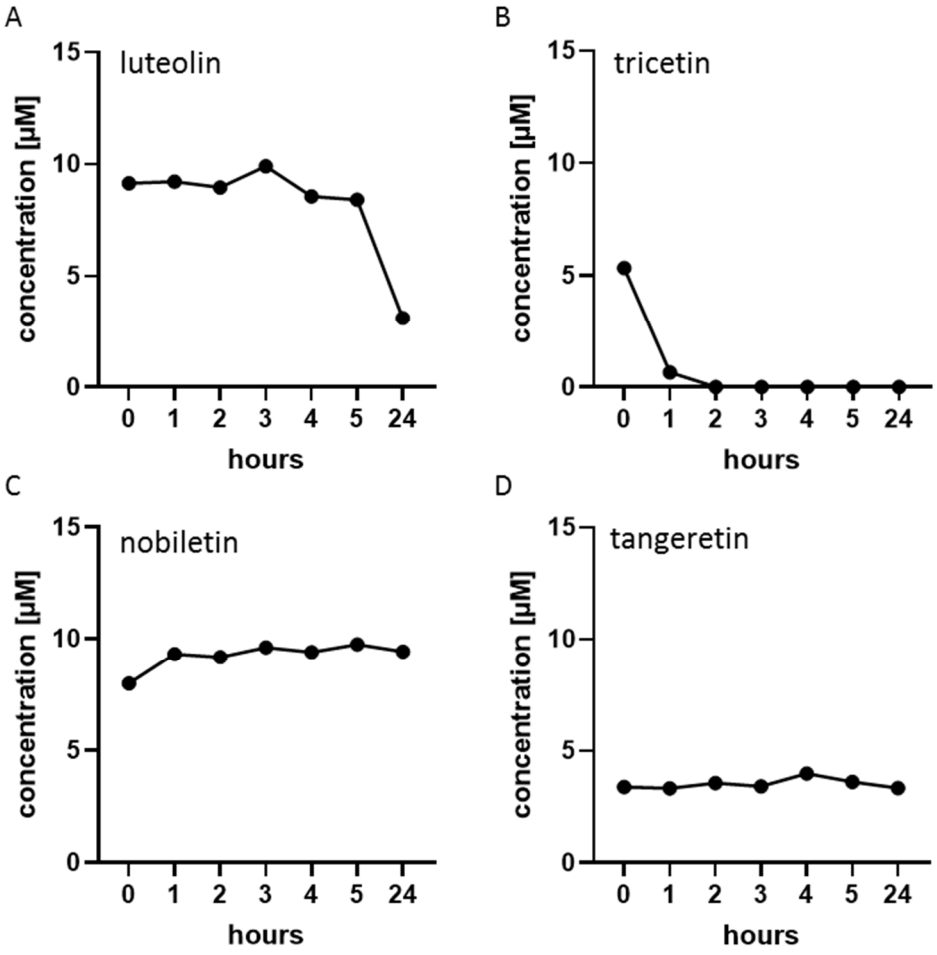

Figure 3.5 Changes in the concentration of the four flavones in starvation medium over time. Luteolin (A), tricetin (B), nobiletin (C) and tangeretin (D) concentrations were determined by means of HPLC. A 10 µM solution of each substance was prepared and the concentration was followed over time at RT.

It can be concluded from Figure 3.5, that luteolin is stable in starvation medium for at least 5 hours, while nobiletin is stable for at least 24 hours. Tricetin shows poor stability in medium

with a quick degradation directly after preparation. Tangeretin is stable over time, but the concentration determined by HPLC does not reflect the applied concentration.

3.3 Cellular uptake of the flavones

For the determination of cellular uptake, NHDF were incubated with the selected flavones at two different concentrations. After different periods of incubation (0, 2, 24h) cells and medium were separated by centrifugation and the flavone levels were determined in a methanolic extract of the cell pellet by means of HPLC. Concentrations are given in µg flavone/mg protein (Figure 3.6).

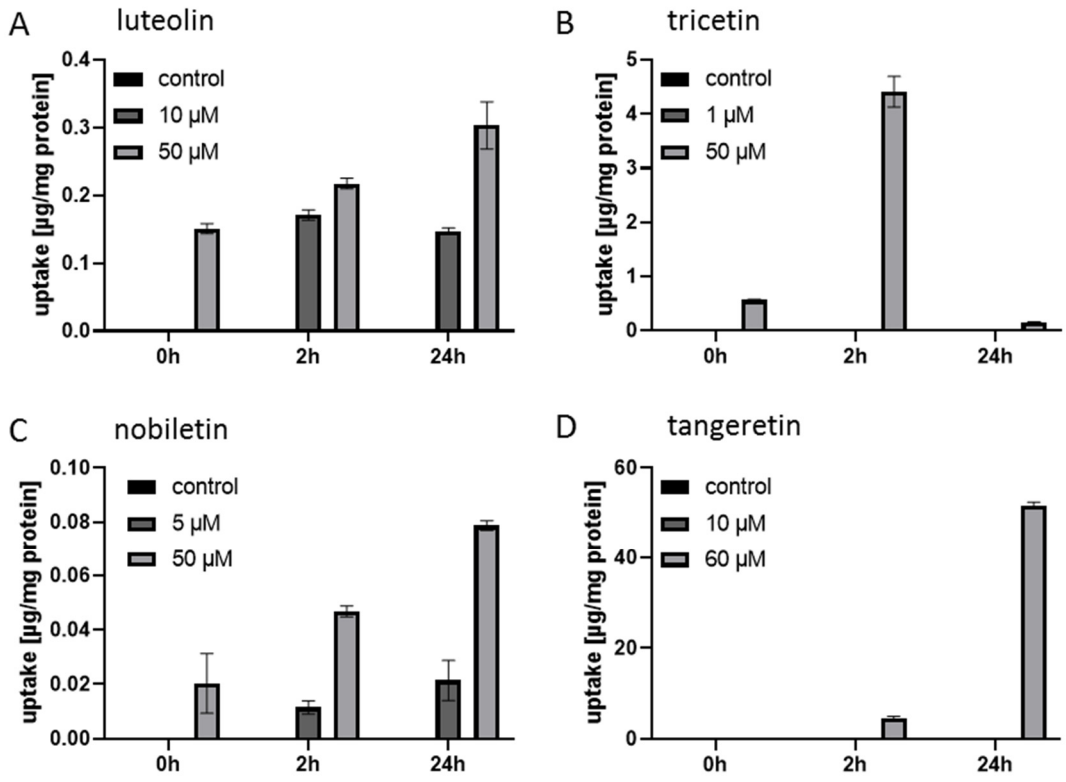

Figure 3.6 Cellular uptake of luteolin, tricetin, nobiletin and tangeretin by NHDF. Cells were incubated with different concentrations of the substances (luteolin: 10 and 50 µM (A); tricetin: 1 and 50 µM (B); nobiletin: 5 and 50 µM (C); tangeretin: 10 and 60 µM (D)) for 0, 2 or 24 hours in starvation medium. Flavone levels were measured by HPLC; concentrations are given in µg per mg protein. Data represent means ± SEM.

Cellular uptake of the compounds was considerably different regarding levels and time course (Figure 3.6). After incubation with a low dose of 1 µM tricetin (B) and 10 µM tangeretin (D), no parent compound was detectable in NHDF at any incubation time. However, considerable

levels of tricetin and tangeretin were detectable after incubation with 50 and 60 µM at 2h and 24h of incubation, respectively. Absolute levels of luteolin (A) and nobiletin (C) in cells were much lower but already detectable at incubation with the compounds at 10 and 5 µM. In summary, data on the uptake of luteolin, tricetin, nobiletin and tangeretin by NHDF are inconsistent and difficult to interpret. Selective transfer mechanisms and/or analytical problems associated with the affinity of compounds to cellular components may have influenced the results.

3.4 Toxicity of the flavones on NHDF

Flavones are naturally occurring compounds ingested with the diet and most are considered safe. However, for their use in cell culture, possible toxic effects of the compounds were studied in a dose range selected for further experiments at 2 and 24 hours post incubation. To determine the effect of the chosen flavones on cell viability, NHDF were exposed to increasing amounts of the compounds and their toxicity was studied using the MTT assay (Figure 3.7). The concentrations used were adapted according to information from the literature and therefore differ slightly between compounds, but all cover the range between 0 and 90 µM.

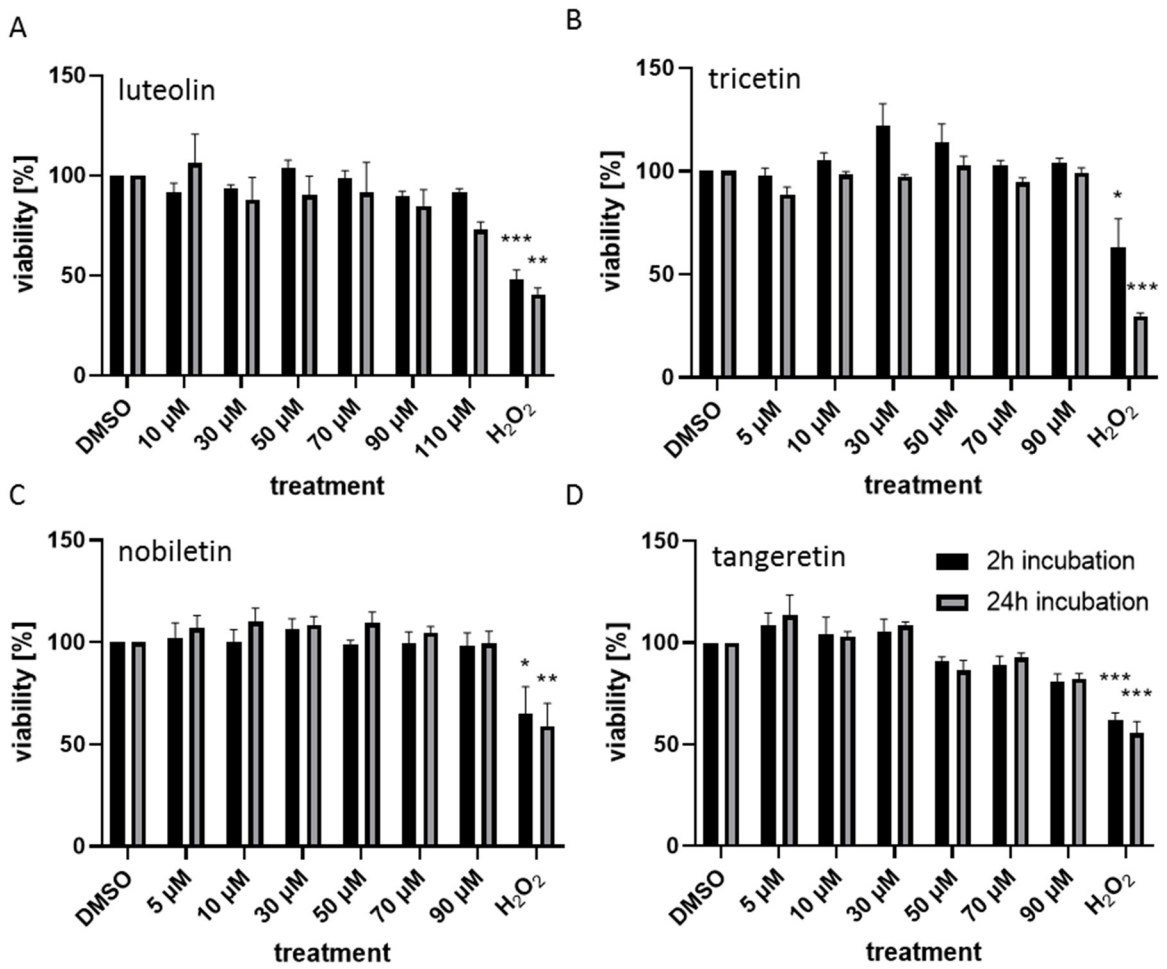

*Figure 3.7 Viability of NHDF after incubation with varying concentrations of the tested substances. Luteolin-induced effects on toxicity are shown for a concentration range from 10 to 110 µM (A). Tricetin (B), nobiletin (C) and tangeretin (D) were tested in a concentration range from 5 to 90 µM. For all substances, two and 24 hours preincubation were tested. MTT assay was applied for viability testing. H_2O_2 (2 mM) was used as a positive control. The solvent control (DMSO) was set at 100 %. Data represent means ± SEM. One-way anova with Dunnett's post-hoc test was performed to the respective DMSO control. *p < 0.05, **p < 0.01, ***p < 0.001*

In the present assay setting (Figure 3.7), no statistically significant decrease of cell viability was observed when cells were incubated with luteolin (A), tricetin (B), nobiletin (C) and tangeretin (D) in the range of 0 - 90 µM for two and 24 hours. Upon exposure of NHDF to H_2O_2 (positive control), cell viability was significantly diminished by about 40 to 60 % at 2 and 24h of incubation. Moderate, but not statistically significant elevation of viability observed at some

dose levels, e.g. tricetin 30 and 50 µM at 2h (B) may be related to stimulatory effects on cell growth of the flavones at lower doses.

Based on the data evaluated, a flavone concentration of 50 µM was selected as a suitable non-toxic dose in the cell system. A two-hour preincubation time elaborated by uptake studies was chosen for further experiments.

3.5 Photostability of the flavones

Another aspect involved in the evaluation of photoprotective compounds relates to their stability upon UV-irradiation. UV-dependent decomposition likely impairs protection by changing UV absorbing properties[170]. But also undesired side effects mediated by decomposition products such as increased sensitivity, irritation or allergic responses may occur[171].

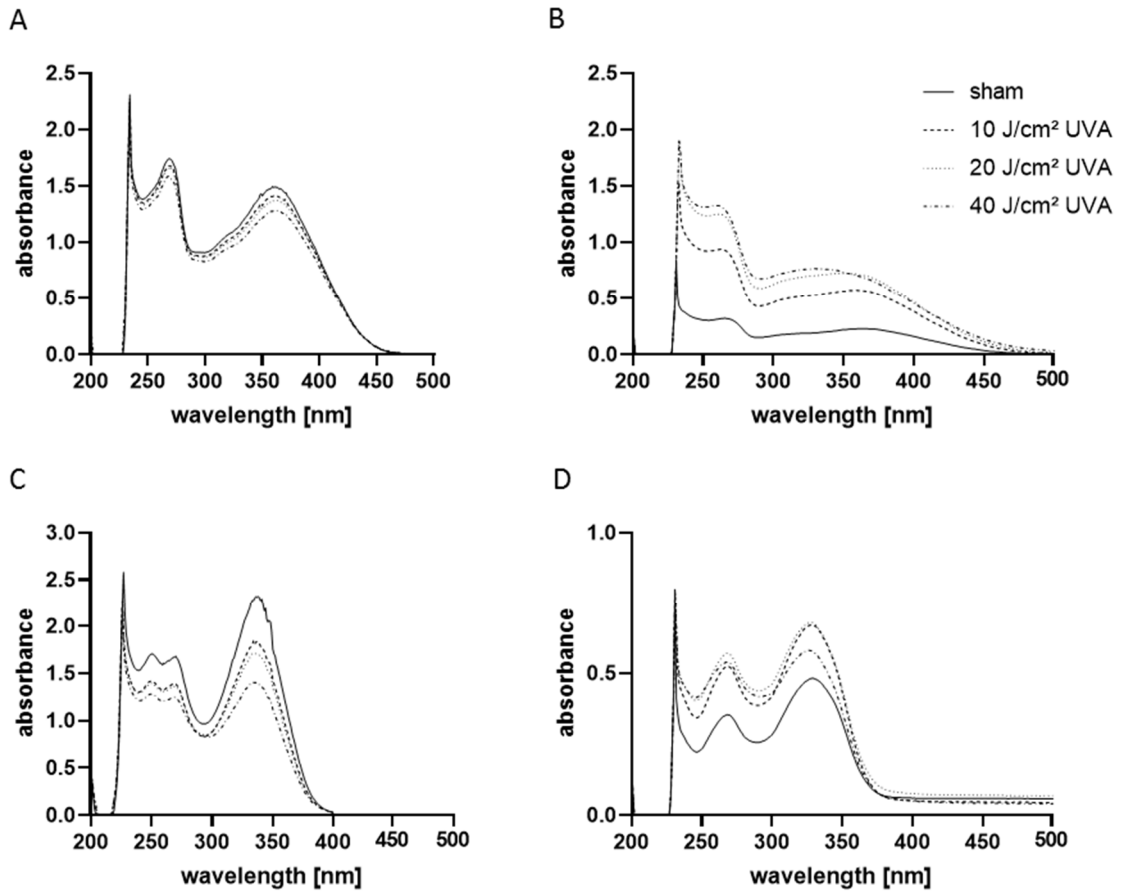

Figure 3.8 Photostability of the substances. Absorbance spectra of 100 µM luteolin (A), tricetin (B), nobiletin (C) and tangeretin (D) dissolved in phosphate buffer (0.1 mM) were measured after irradiation with 10, 20 or 40 J/cm² UVA or without irradiation (sham).

The absorbance spectra of luteolin (A), tricetin (B), nobiletin (C) and tangeretin (D) dissolved in 0.1 mM phosphate buffer were determined before irradiation and directly after irradiation with UVA at doses of 10, 20, and 40 J/cm² (Figure 3.8). A moderate, dose-dependent loss of the compound was observed for luteolin (A). A significant decrease in absorption indicating a loss of the parent compound was determined upon irradiation of nobiletin (C) in aqueous solution. A general increase in absorption was observed when tricetin (B) and tangeretin were exposed to UVA at different dose levels which might be due to problems related to proper dissolution of the compounds.

In order to overcome solution problems and test the stability of the flavones in another system, their photostability in liposomes was determined. Liposomes are lamellar constructs with hydrophilic and lipophilic compartments. They are frequently used to provide suspensions with compounds incorporated in the liposomal structure, e.g. cream-based formulations of bioactive compounds. Samples were obtained by adding the substances to liposomes, that were prepared using phosphatidylcholine (see 2.11 Liposome preparation). Flavone-containing liposomes (100 µM) were irradiated with UVA or sham treated. Afterwards, a liposomal pellet was obtained by centrifugation. The pellet was resuspended in dichloromethane for measurement in a spectrophotometer.

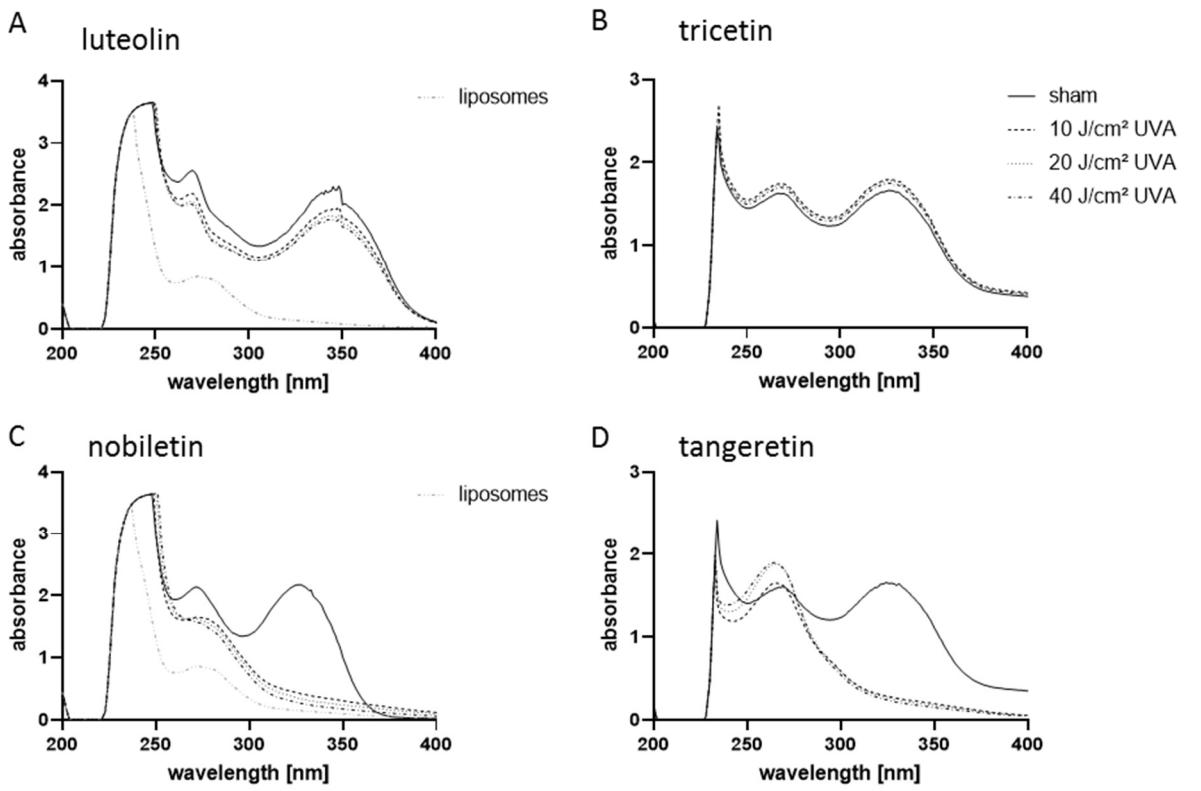

Figure 3.9 Photostability of the substances in liposomes. Absorbance of flavones in liposomes, containing 100 µM luteolin (A), tricetin (B), nobiletin (C) or tangeretin (D), was measured over a wavelength range from 200 to 400 nm. Before, samples were either left unirradiated (sham) or were irradiated with 10, 20 or 40 J/cm² UVA. A negative control containing only liposomes is shown in A and C.

In Figure 3.9, the absorbance spectra of the four flavones in liposomes are shown unirradiated and after irradiation with increasing doses of UVA. Luteolin absorbance is unaltered after irradiation (A) and the absorbance spectrum shows the same maxima as in phosphate buffer (compare Figure 3.8). For tricetin, the absorbance in liposomes is slightly shifted towards lower wavelengths, showing a shift from the previous maximum at 360 nm in buffer to 330 nm in liposomes (B). The absorbance is unaltered by UVA radiation up to 40 J/cm². Nobiletin absorbance is altered by all applied UVA doses (C). The previous maximum at 340 nm is lost, while only the second maximum at 265 nm remains visible but decreased. The absorbance of tangeretin shows similar alterations, as the maximum at 330 nm decreases, but the maximum at 270 nm increases (D). An absorbance spectrum of control liposomes containing no substance is shown in A and C.

To further investigate the changes in absorbance in nobiletin and tangeretin containing liposomes, the supernatant of the liposomes after centrifugation was examined. Luteolin and nobiletin were chosen as representative substances for hydroxylated and methoxylated flavones, to examine differences in their photostability.

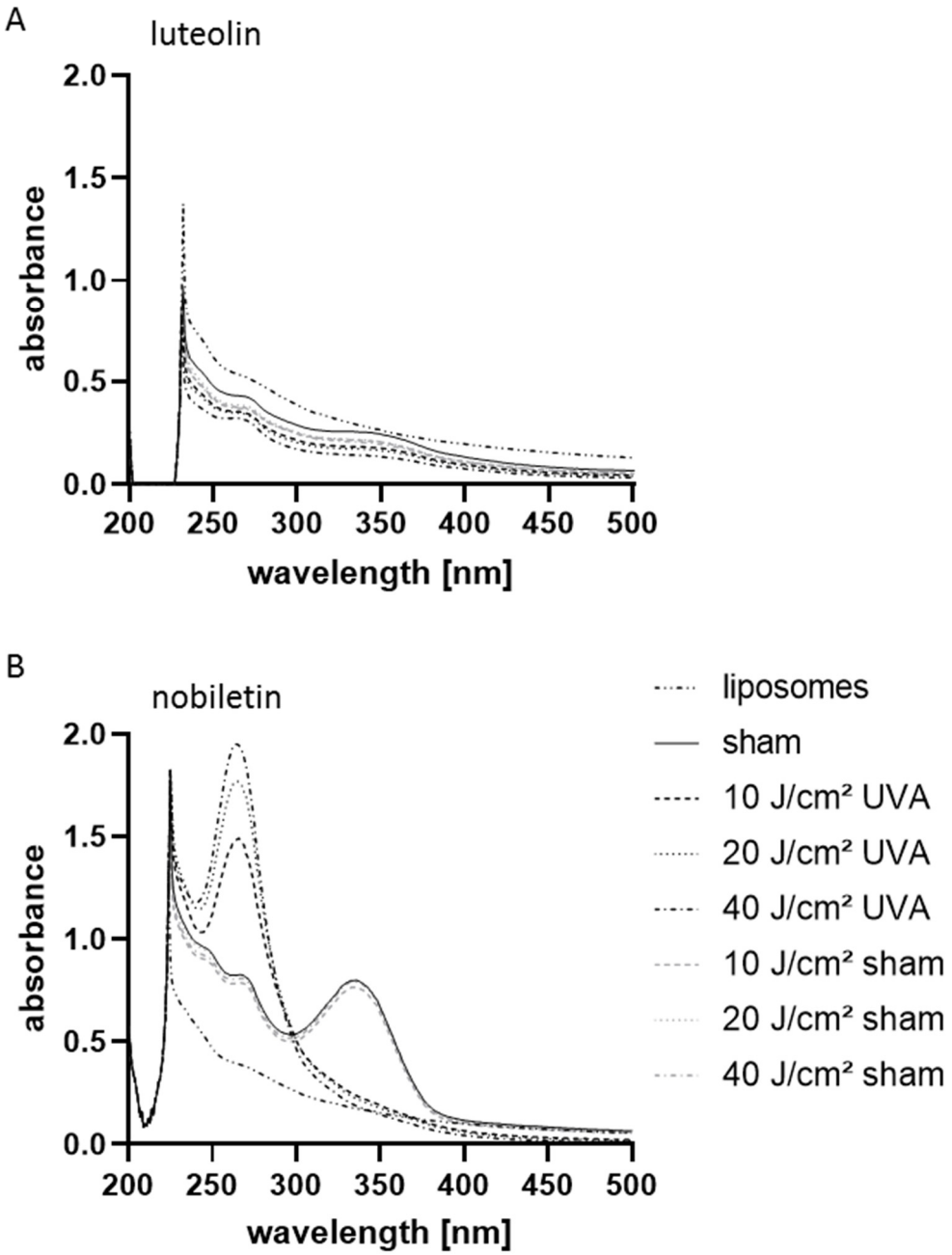

Figure 3.10 Investigation of the liposomal supernatants. Absorbance spectra of 100 µM nobiletin (A) or luteolin (B) in supernatants of liposomes were measured in the wavelength region from 200 to 500 nm. Prior to measurement, samples were irradiated with increasing doses of UVA (10, 20 and 40 J/cm²) or left unirradiated (sham) for the same time period under similar settings. Absorbance spectra of liposomes without substances are given in A and B.

In Figure 3.10, the absorption spectra of the supernatant of liposomes loaded with luteolin or nobiletin are shown. The absorption spectra of the supernatant of liposomes containing luteolin indicate that only minor amounts of the compound are released from liposomes (A).

Apparently, no degradation product is formed and released into the aqueous compartment during incubation (sham) or irradiation with increasing doses of UVA. In contrast, some parent compound is found in the supernatant of liposomes loaded with nobiletin (B). The level it not affected by incubation time (sham). However, upon irradiation with UVA, nobiletin decomposes and a decomposition product is found in the supernatant with an absorption peak at about 270 nm. The amount of product apparently increases with increasing UVA doses.

3.6 Measurements of lipid peroxidation

For further investigation of the effects of the two structurally different flavones on radiation-relevant parameters, an HPLC method for the detection of lipid peroxidation was developed. Malondialdehyde (MDA) is a product of lipid peroxidation and its formation can be used to assess the level of oxidation of lipids. It is known that UVA radiation induces the oxidation of lipids, therefore, the prevention of lipid oxidation was chosen as a readout for the antioxidant properties of the flavones. In order to examine suitable settings for the determination of MDA levels in a cell-free system, two sources of phosphatidylcholine were evaluated. On the one hand, egg yolk was used, which is rich in phosphatidylcholine but also contains a large amount of other lipids along with vitamins and carotenoids. On the other hand, purified phosphatidylcholine (PC) was used. Both egg yolk and PC (5 mg/ml) were prepared in phosphate buffer. UVB radiation was used as a reference, as it is known to produce a detectable amount of MDA starting from doses below 1 J/cm² UVB[172].

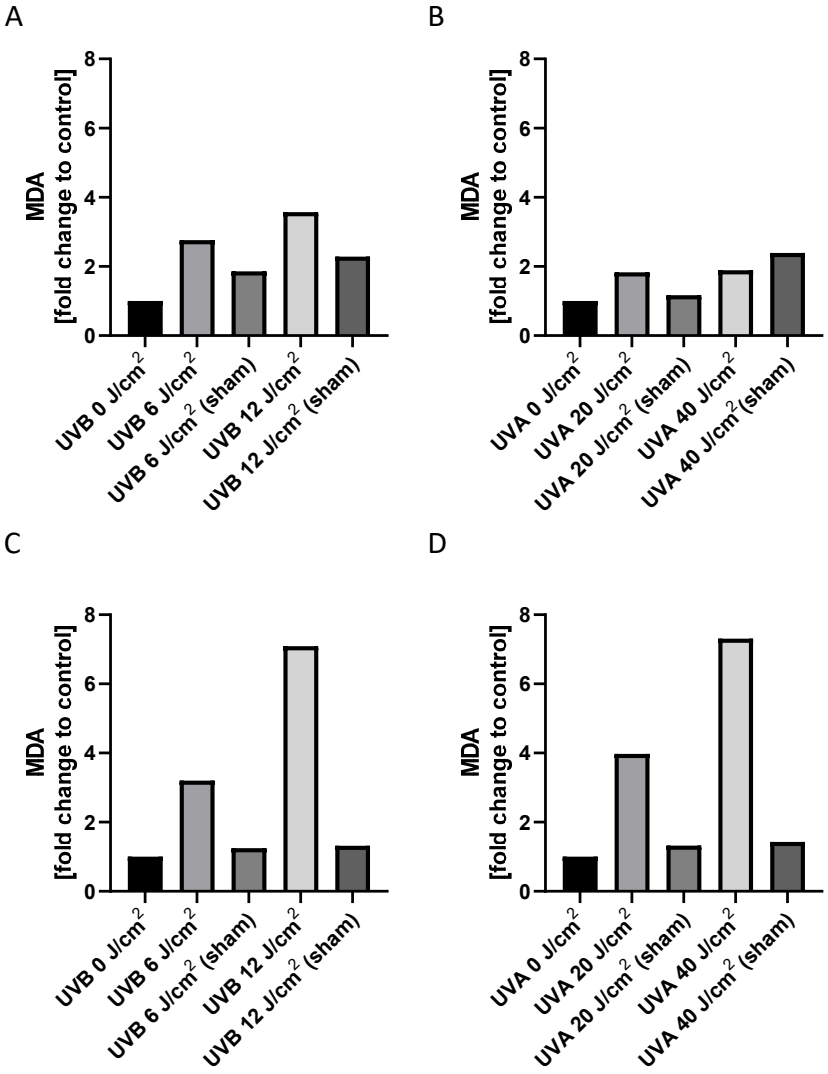

Figure 3.11 Irradiation of liposomes from egg yolk and PC with UVA or UVB. Formation of MDA was determined photometrically by absorbance at 532 nm. Egg yolk liposomes were irradiated with 6 or 12 J/cm² UVB (A), with 20 or 40 J/cm² UVA (B) or left unirradiated for the appropriate time period (sham). PC liposomes were irradiated with 6 or 12 J/cm² UVB (C), 20 or 40 J/cm² UVA (D) or left unirradiated for the respective time period (sham). N = 1.

Irradiation of egg yolk liposomes with UVB light leads to a dose-dependent increase in MDA levels measured using photometric determination of absorbance at 532 nm (Figure 3.11 A). However, the effect of UVA irradiation on MDA formation in egg yolk liposomes is less pronounced (B). Time after preparation, caused by different irradiation durations, influences MDA levels in egg yolk, as well, seen by the increase in MDA levels in sham samples (A and B). In contrast, irradiation of PC liposomes with both UVA and UVB was associated with dose-dependent elevations of MDA (C and D). In general, the levels of MDA were low in egg yolk

compared to those seen in PC, rendering PC the superior compound for liposome generation. Based on these data, liposomes generated from PC were chosen as a model system to study the effects of flavones on lipid oxidation.

To assess the capacity of the two representative flavones, luteolin and nobiletin, to prevent MDA formation, PC liposomes containing 100 µM of one of the flavones were irradiated with low and high doses of UVA and the amount of MDA was measured using HPLC.

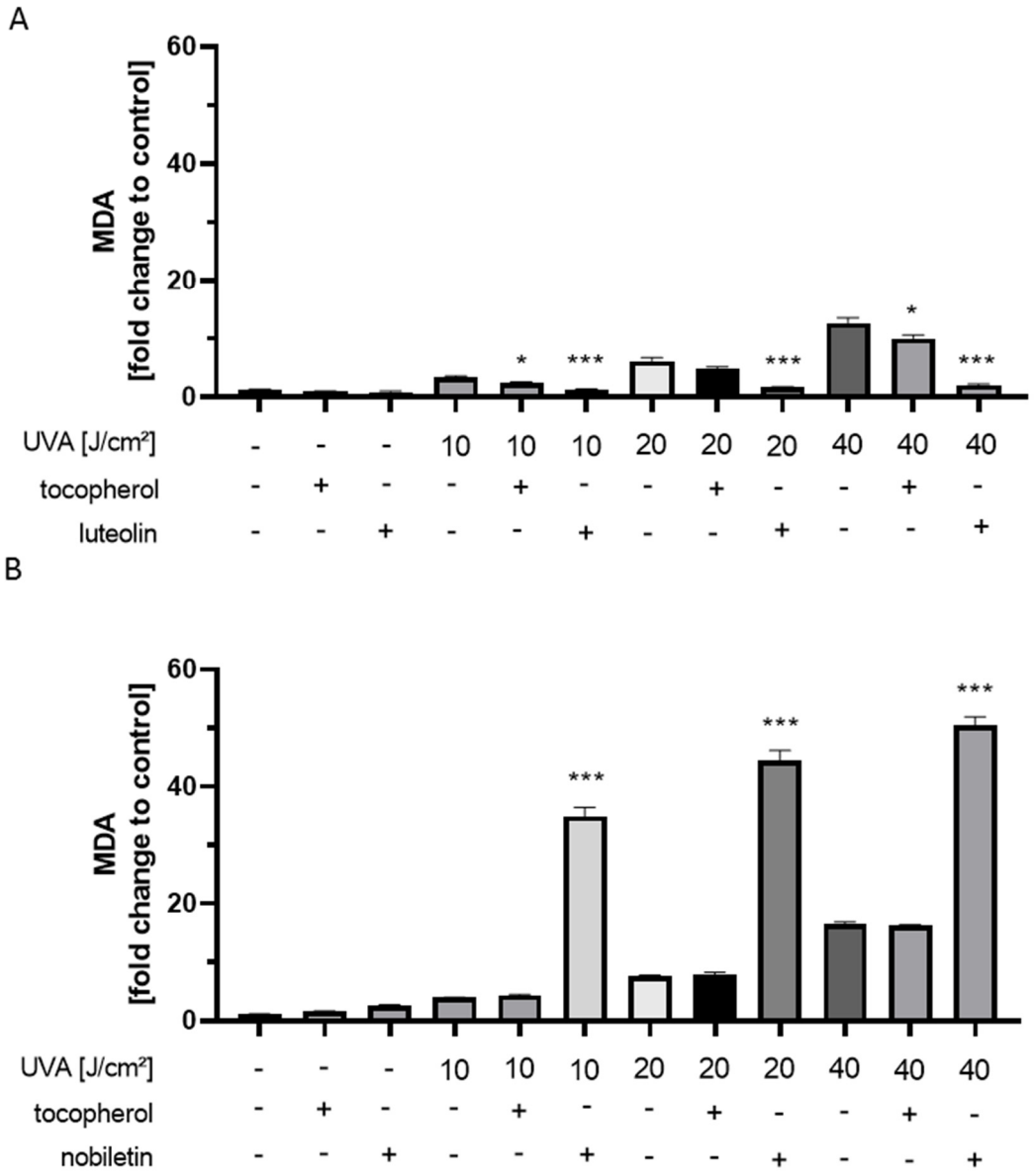

*Figure 3.12 Irradiation of PC liposomes containing nobiletin or luteolin. Liposomes containing DMSO as a solvent control, α-tocopherol (100 µM) as a positive control, luteolin (100 µM) (A) or nobiletin (100 µM) (B) were irradiated with UVA doses from 10 to 40 J/cm² or left unirradiated. MDA peak area was measured by HPLC and is given as fold change to the unirradiated DMSO control. Data represent means ± SEM. One-way Anova with Dunnett's multiple comparison test was used to determine statistical difference to the respective control. *p < 0.05, **p < 0.01, ***p < 0.001.*

Figure 3.12 shows a dose-dependent increase of relative MDA levels in control liposomes after irradiation with increasing doses of UVA (A and B). The antioxidant α-tocopherol, when added

to liposomes, partly prevents MDA formation. It might therefore be addressed as a weak antioxidant in the present settings. Luteolin decreases MDA levels statistically significant during irradiation of liposomes with all applied UVA doses (B). There is no effect of luteolin on MDA levels in the absence of UVA. Addition of nobiletin to liposomes without radiation slightly increases the amount of MDA in the sample compared to the control (A). After irradiation of nobiletin containing liposomes with UVA, MDA levels dose-dependently increase up to 50-fold. Luteolin therefore acts as an inhibitor of lipid peroxidation in liposomes, while nobiletin acts as an enhancer of lipid peroxidation. Prooxidant properties of nobiletin are strongly increased upon irradiation.

In order to expand these studies in the model system to a setting with NHDF, the irradiation doses for MDA formation in cells measured by HPLC were established. For this, NHDF were irradiated with 10 to 40 J/cm² UVA or left unirradiated and MDA in the medium was determined by HPLC according to the method (see 2.13). Results are shown in Figure 3.13.

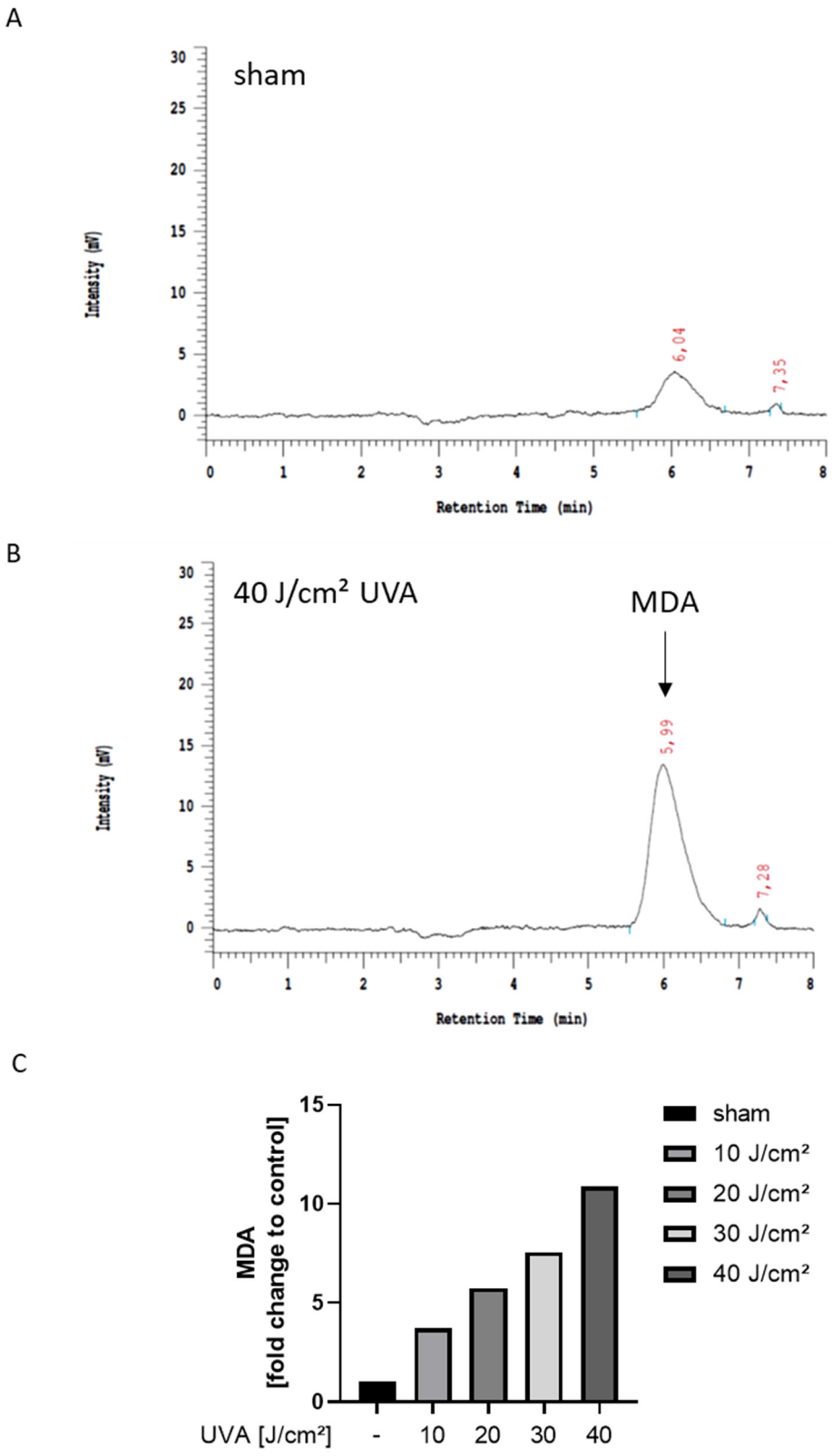

Figure 3.13 MDA formation in NHDF upon irradiation with UVA. Exemplary HPLC chromatograms show MDA peaks in medium of unirradiated (sham, A) or irradiated (40 J/cm² UVA, B) NHDF. H_2O was used as a blank. The MDA peak area is shown in C as fold-change to the unirradiated control.

According to Figure 3.13, the MDA signal can be detected at a retention time of approximately 6 minutes in the given settings. There is a dose-dependent increase in MDA formation in NHDF following irradiation with increasing doses of UVA. Although the unirradiated control (sham) shows a small peak at the retention time of interest (A), there is an increase from 10 to 40 J/cm² UVA that exceeds the levels of the control (C). There is a measurable dose-dependent increase in MDA levels compared to the unirradiated control beginning with 10 J/cm² UVA, rendering this low dose suitable for further experiments.

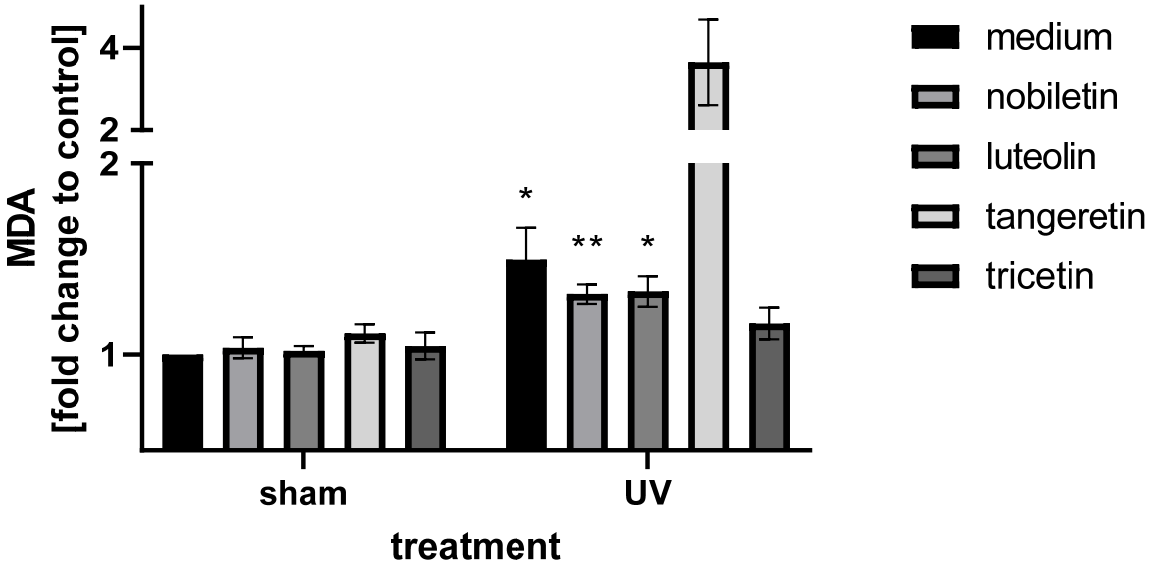

*Figure 3.14 UVA-dependent MDA formation in NHDF preincubated with luteolin, tricetin, nobiletin or tangeretin. MDA levels, measured by HPLC, are given in comparison to the unirradiated medium control (set as 1). Cells were preincubated (2h) with 50 µM flavone followed by irradiation (10 J/cm² UVA) or sham treatment. Data represent means ± SEM. Unpaired student's t-test was used for the determination of statistical significance to the medium sham control. *p < 0.05, **p < 0.01, ***p < 0.001.*

Figure 3.14 shows, that relative MDA levels in unirradiated (sham) NHDF were unchanged after preincubation with luteolin, tricetin, nobiletin or tangeretin. Applying a low dose of UVA increases MDA levels statistically significant in control cells (medium). Preincubation with nobiletin or luteolin did not prevent an increase in MDA levels. Tangeretin strongly increased MDA levels around 4-fold upon irradiation with 10 J/cm² UVA. Only preincubation with tricetin decreased MDA levels after irradiation to a level comparable with the unirradiated control.

3.7 Measurement of reactive oxygen species (ROS)

Lipid peroxidation results from the interaction of ROS with unsaturated fatty acids in lipophilic compartments of cells. ROS levels in fibroblasts were investigated by means of the H_2DCF-DA assay. Cells were incubated with flavones and the formation of ROS was followed with (Figure 3.17, Figure 3.18) and without UV irradiation (Figure 3.15, Figure 3.16).

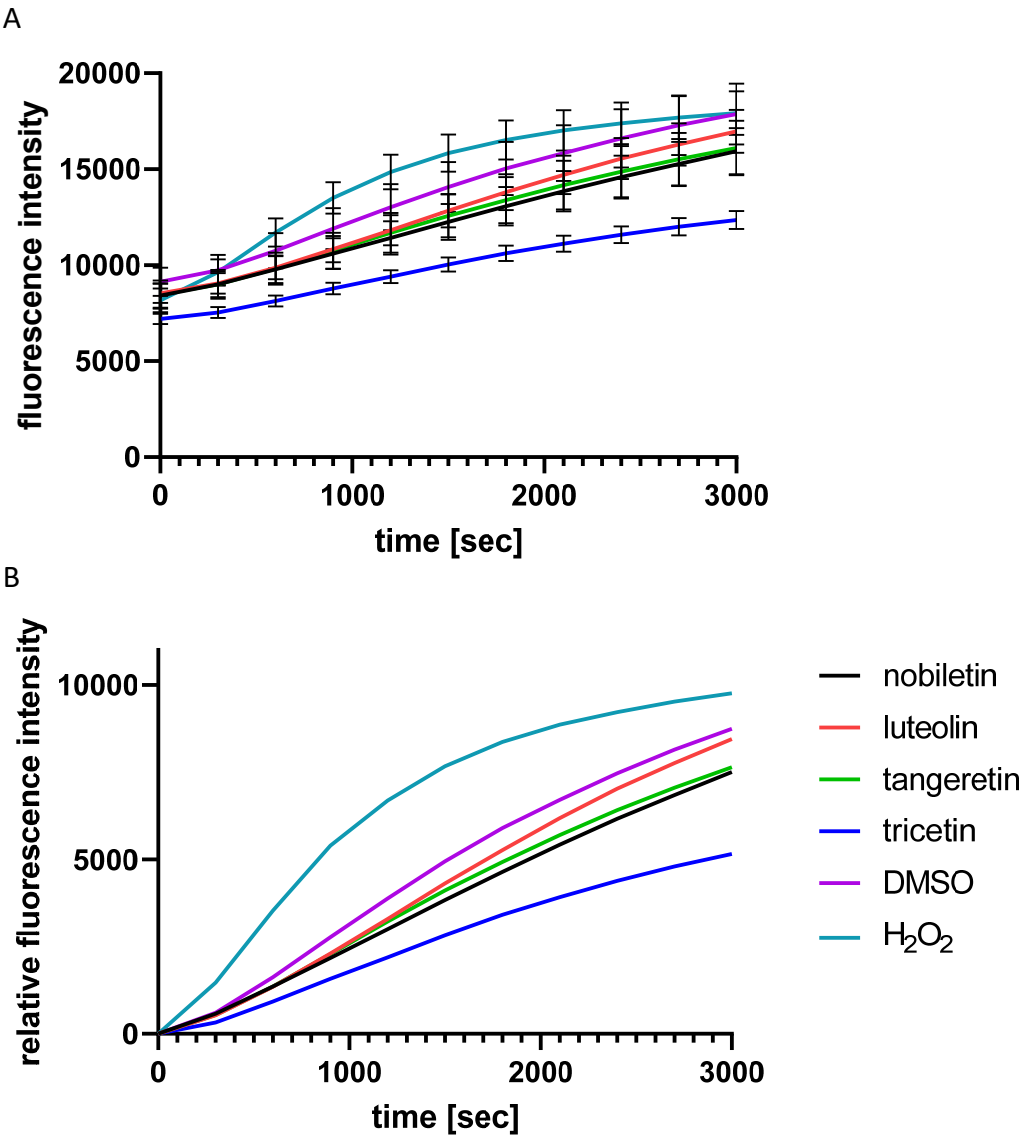

Figure 3.15 Flavone-induced changes in ROS levels of fibroblasts over time without UV exposure. Absolute (A) and relative (B) fluorescence intensity was measured over the course of 50 minutes (3000 sec) using the H_2DCF-DA assay. Flavones (50 µM) were added directly before start of the measurement. H_2O_2 (2 mM) and DMSO were used as a positive and negative control, respectively. For relative values, all absolute values at timepoint 0 were set as 0. Data represent means ± SEM.

Figure 3.15 shows that there is an increase of ROS levels in fibroblasts over time. This increase is the most pronounced in the positive control (B). Compared to this control, all other treatments show lower levels and a slower increase in ROS. Compared to the solvent control (DMSO), addition of luteolin, tangeretin and nobiletin to NHDF does not or only moderately alter ROS levels. A slower increase in ROS and decreased ROS levels at later timepoints are evident after addition of tricetin to NHDF.

In the following experiments, the influence of a two-hour preincubation with the respective flavone was tested.

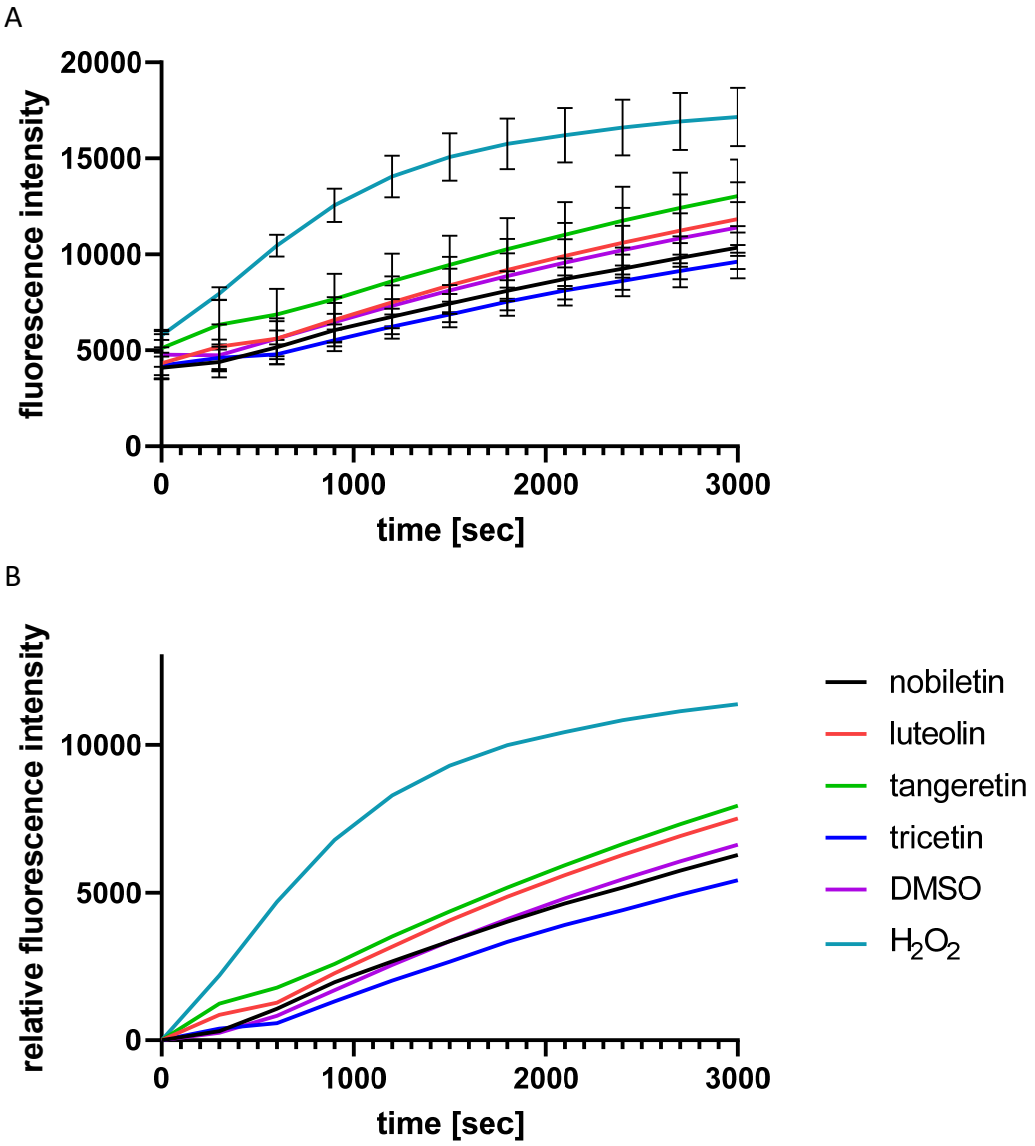

Figure 3.16 Changes in ROS levels of fibroblasts over time after preincubation with flavones without UV exposure. Absolute (A) and relative (B) fluorescence intensity was measured over the course of 50 minutes (3000 sec) using the H_2DCF-DA assay. Fibroblasts were preincubated for two hours with flavones (50 µM) as indicated. H_2O_2 (2 mM) and DMSO were used as a positive and negative control, respectively. For relative values, all absolute values at timepoint 0 were set as 0. Data represent means ± SEM.

After preincubation of fibroblasts with the flavones, time-dependent ROS formation was statistically not different to a solvent control (Figure 3.16). Again, only treatment with tricetin shows a minor decreasing effect.

In addition to the previous experiments, the effect of the flavones on intracellular ROS formation was investigated in combination with UV radiation.

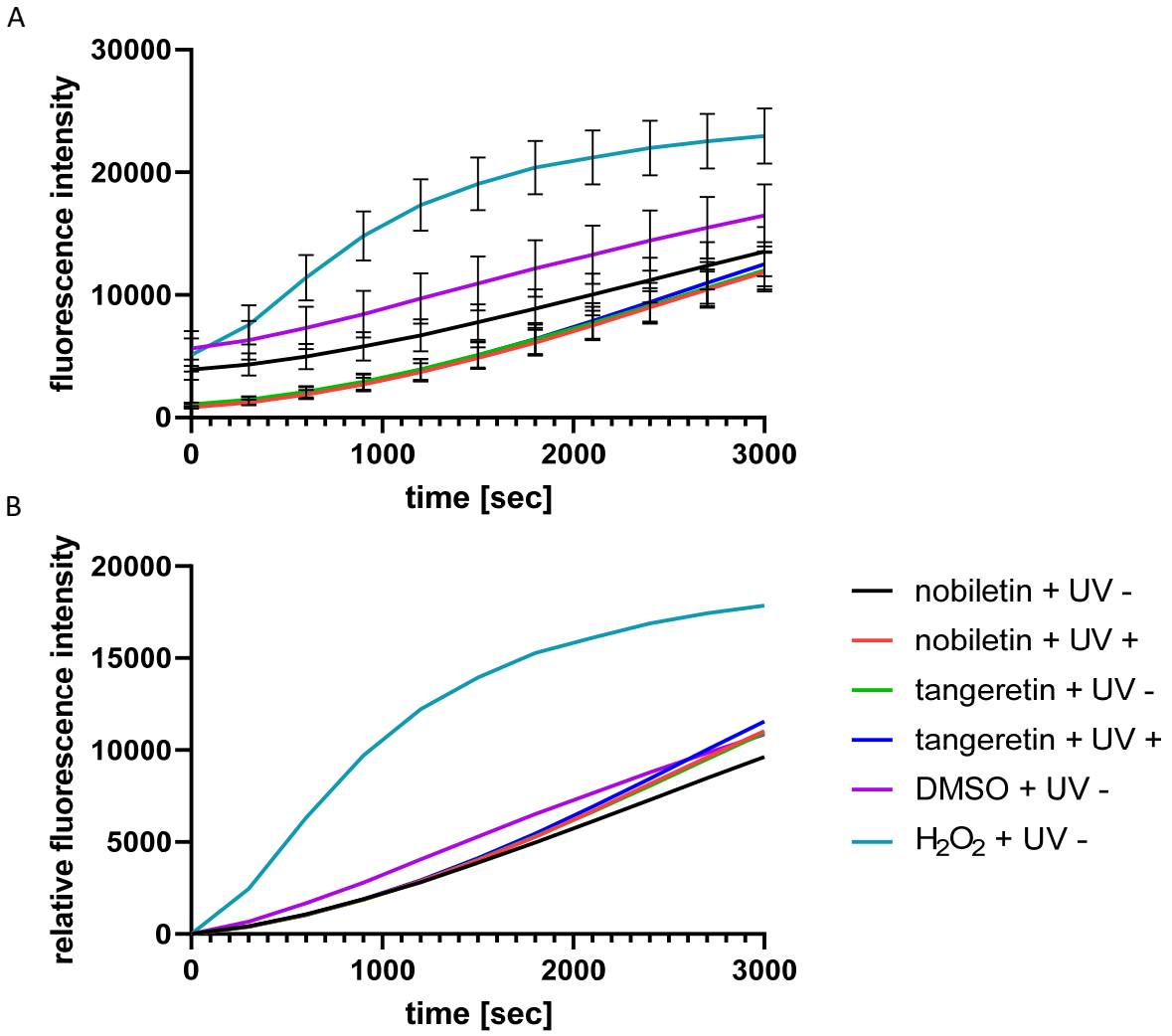

Figure 3.17 Changes in ROS levels in fibroblasts after irradiation in the presence and absence of nobiletin and tangeretin. Absolute (A) and relative (B) fluorescence intensity was determined over the course of 50 minutes (3000 sec) using the H_2DCF-DA assay. Cells were preincubated for two hours with the depicted flavonoids and then irradiated with 10 J/cm² UVA in HBSS medium (+ UV -) or cells were preincubated and then irradiated in HBSS supplemented with the respective flavonoid (+ UV +). DMSO and H_2O_2 (2 mM) were used as a negative and positive control, respectively. Data represent means ± SEM.

Figure 3.17 shows the measurement of intracellular ROS after treatment with nobiletin and tangeretin in combination with low-dose UVA. The positive control shows an increase of ROS levels that is faster than any other treatment and that results in the highest levels of ROS. Compared to the solvent control, nobiletin and tangeretin did not alter the formation of ROS, either with or without exposure to low dose UVA radiation (B). Interestingly, there is a difference in absolute levels from both tangeretin and nobiletin + UV + treatments to the DMSO control at the start of the measurement (A). This effect is abrogated towards the end of the measurement.

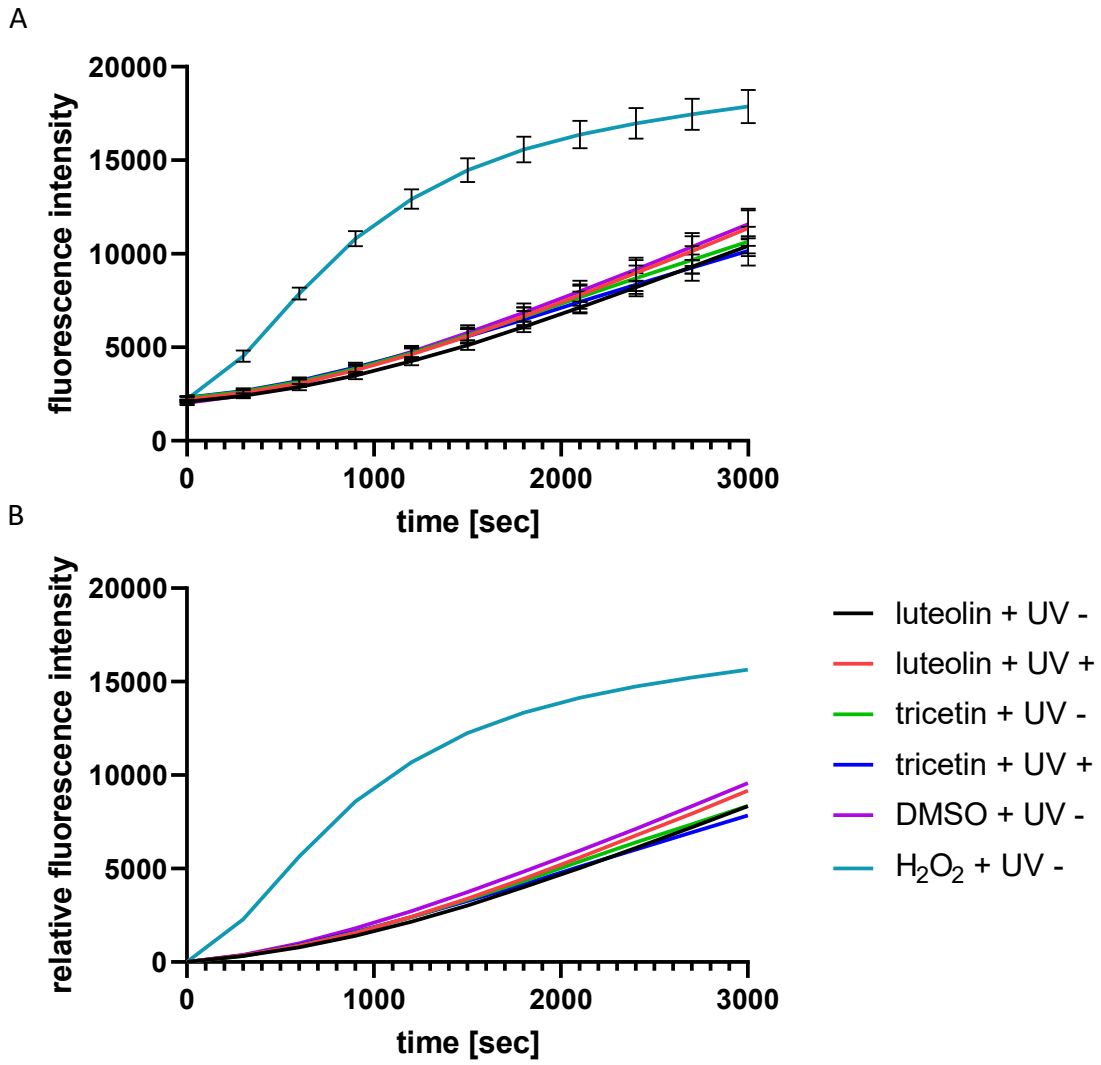

Figure 3.18 Changes in ROS levels in fibroblasts after irradiation in the presence and absence of luteolin and tricetin. Absolute (A) and relative (B) fluorescence intensity was measured over the course of 50 minutes using the H_2DCF-DA assay. Cells were preincubated for two hours with the depicted flavonoids and then irradiated with 10 J/cm² UVA in HBSS medium (+ UV -) or cells were preincubated and then irradiated in HBSS supplemented with the respective flavonoid (+ UV +). DMSO and H_2O_2 (2 mM) were used as a negative and positive control, respectively. Data represent means ± SEM.

Luteolin and tricetin were tested in the same setting (Figure 3.18). Fluorescence in the positive control (H_2O_2) shows a fast increase in the beginning of the measurement and the highest values compared to all other treatments at the end of the measurement. ROS levels after treatment with luteolin or tricetin show no difference compared to the solvent control,

independent of absence (+ UV -) or presence (+ UV +) of the flavones during irradiation with low-dose UVA (Figure 3.18 A and B).

The data indicate that the flavones investigated in this thesis do not affect the generation of ROS in NHDF exposed to low doses of UVA light. However, they might still initiate a response from cellular antioxidant defense pathways, e.g. through Nrf2, via other mechanisms.

3.8 Thiol reactivity

Studies on putative photoprotective compounds are not limited to their UV absorbing properties or antioxidant effects. Interactions with biologically relevant signalling systems are of interest, as well. In this context, chemical reactions of flavones or their decomposition products with functional groups were investigated. Thiol groups on proteins are especially prone to alterations as they can react with electrophiles. One example are α-β-unsaturated carbonyl compounds which react in a Michael-type reaction[173]. One example for a biologically relevant reaction of such type is the interaction of flavonoids with Keap1, as already known for cardamonin. The selected flavones bear an α-β-unsaturated carbonyl structure, therefore the reactivity of the flavones towards 2-mercaptoethanol (2-ME) was investigated.

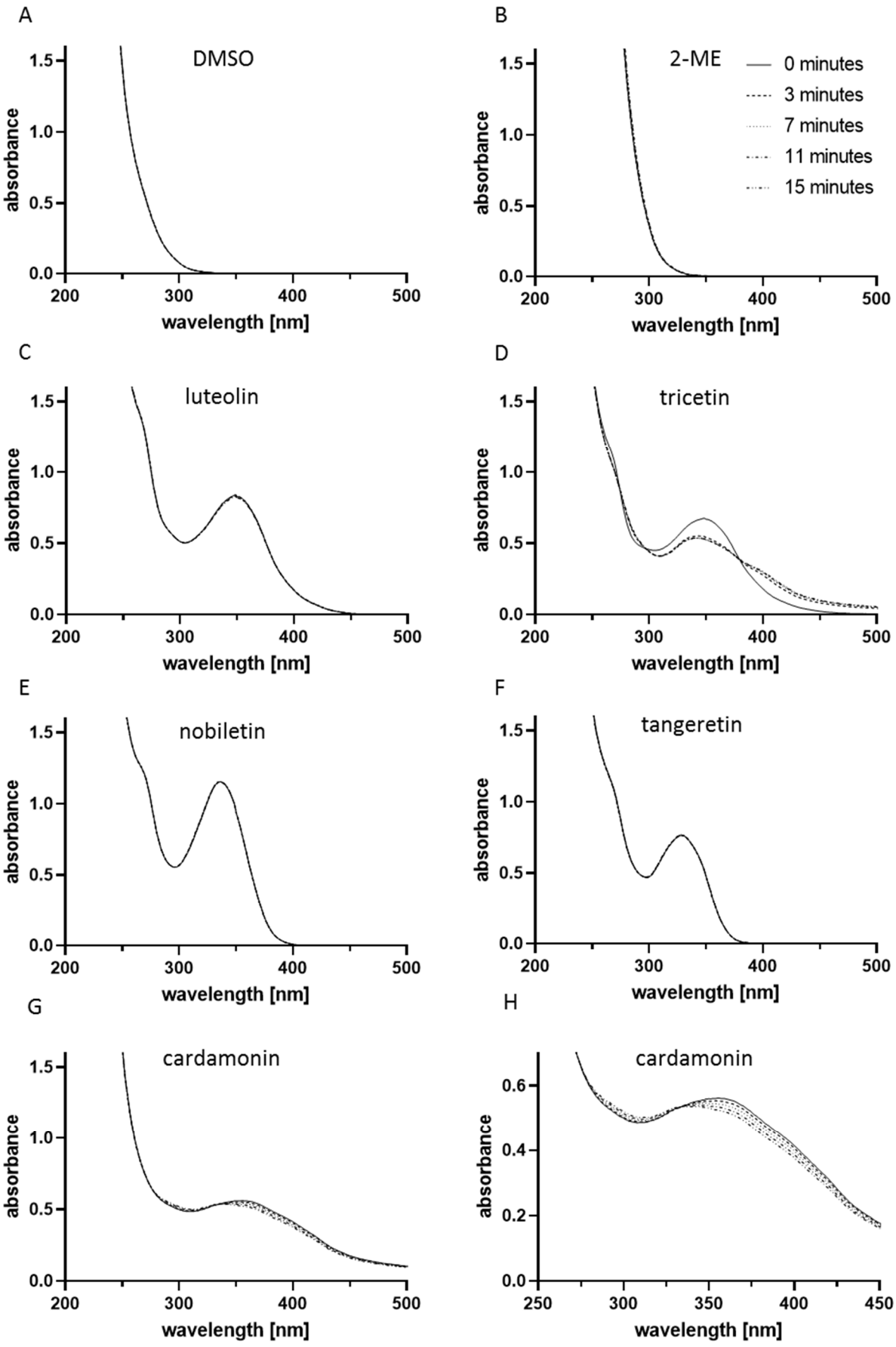
A
DMSO
absorbance
wavelength [nm]
B
2-ME
0 minutes
3 minutes
7 minutes
11 minutes
15 minutes
absorbance
wavelength [nm]
C
luteolin
absorbance
wavelength [nm]
D
tricetin
absorbance
wavelength [nm]
E
nobiletin
absorbance
wavelength [nm]
F
tangeretin
absorbance
wavelength [nm]
G
cardamonin
absorbance
wavelength [nm]
H
cardamonin
absorbance
wavelength [nm]

Figure 3.19 Thiol reactivity of luteolin, tricetin, nobiletin and tangeretin in a cell-free test-system. The absorbance of the flavones dissolved in 0.1 mM phosphate buffer was followed over time (0 - 15 minutes) in a wavelength range of 200 - 500 nm in the presence of 25 mM 2-mercaptoethanol. A = DMSO, B = 2-mercaptoethanol, C = luteolin, D = tricetin, E = nobiletin, F = tangeretin, G = cardamonin, H = cardamonin, altered scale.

Figure 3.19 shows absorbance spectra of the flavones after addition of 2-ME. In none of the spectra, except that from cardamonin, a shift in absorbance maxima was observed. Cardamonin, chosen as a positive control, shows a clear time-dependent spectral change where the maximum at 360 nm decreases and to the same extent absorbance at 300 nm increases. As a negative control, spectra from DMSO and 2-ME alone were measured, as well (A and B).

It is known that phytochemicals with suitable structure can interact with thiol groups of Keap1 and therefore lead to translocation of Nrf2 into the nucleus, where target genes are activated and antioxidant protein expression induced, e.g. expression of HO-1[174]. Due to the lack in thiol reactivity, the chosen flavones should not induce HO-1 expression *per se*. Nevertheless, UVA radiation is known to upregulate HO-1, raising the question whether the flavones have an effect on UVA-induced expression of HO-1.

3.9 Effect of the flavones on expression of hemeoxygenase-1

Stress-inducible hemeoxygenase-1 (HO-1) is known to be upregulated by UVA and several flavonoids as a response to oxidative stress[175,176]. Therefore, the effect of the selected flavones in combination with low-dose UVA radiation on HO-1 expression was investigated.

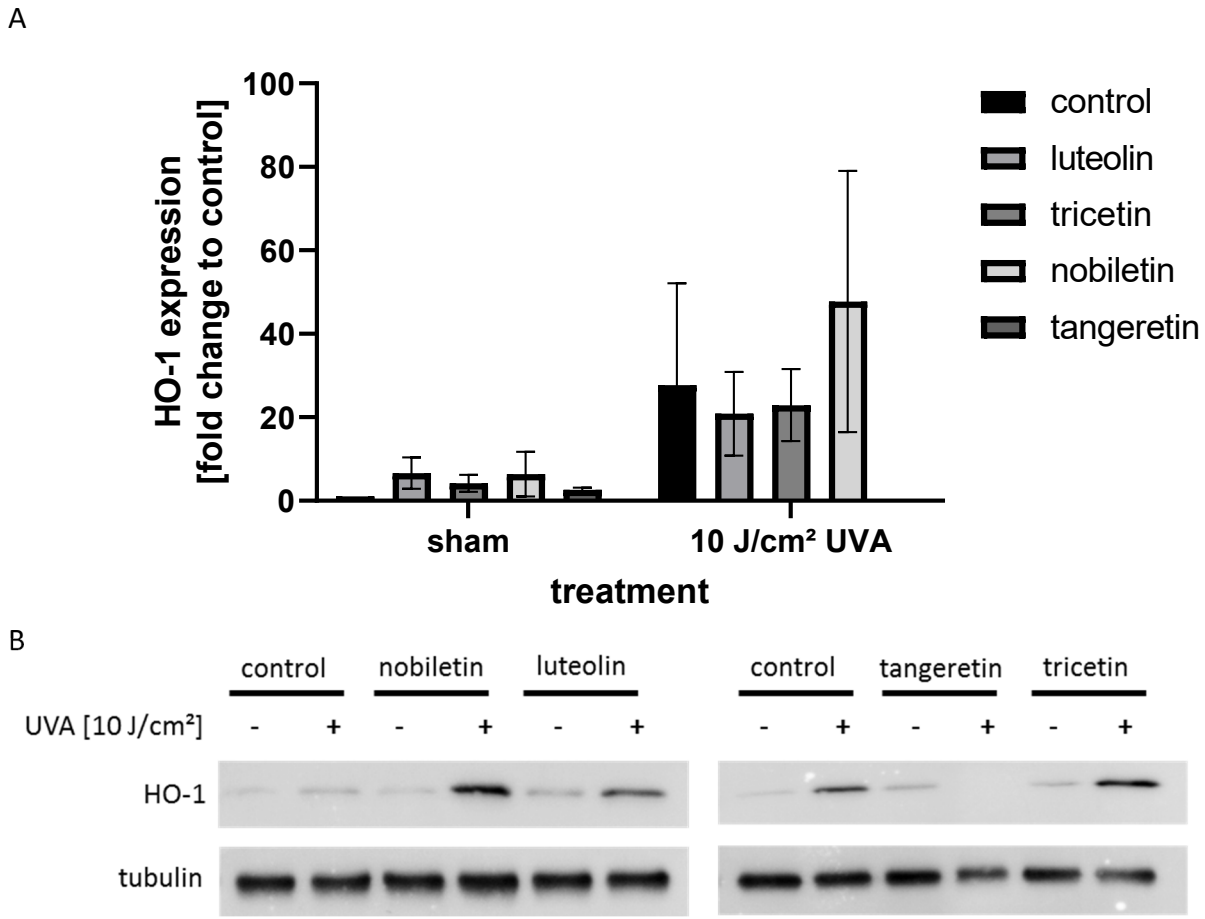

Figure 3.20 Expression of HO-1 in NHDF preincubated with flavones with or without UVA irradiation. Cells were preincubated with 50 µM of the respective flavone for two hours and exposed to 10 J/cm² UVA or sham treatment. The quantification of Western Blots shows the relative change in expression of HO-1 after varying treatments (A). Representative Western Blot membranes show protein bands for HO-1 and for tubulin as a control (B). Data represent means ± SEM.

Figure 3.20 shows the influence of the four flavones on HO-1 expression. Irradiation of NHDF with low-dose UVA induced HO-1 expression as compared to the unirradiated control (A). Although preincubation with any of the substances yields no effect with statistical significance, preincubation with nobiletin shows a tendency to increase HO-1 levels after irradiation with 10 J/cm² UVA. Surprisingly, tangeretin preincubation diminished all detectable protein levels of HO-1 after irradiation, while HO-1 levels were similar to the control when no UV was applied. Luteolin and tricetin show a decrease of HO-1 expression compared to the irradiated control only by trend.

Although endogenous photoprotective effects of the flavones on cell culture are minimal and the polymethoxylated flavones nobiletin and tangeretin present even negative effects, e.g. on MDA formation and in regard to their photostability, luteolin and tricetin show promising effects, e.g. a decrease of MDA formation in liposomes by luteolin and in cell culture by tricetin, accompanied by superior photostability and optimal absorbance. Therefore, the polyhydroxylated compounds might be suitable for topical photoprotection.

3.10 Photoprotective effects of the flavones

Based on the previous results, the photoprotective properties of the selected flavones were now examined in a cell viability assay using a UVA dose level of 45 J/cm². To distinguish between endogenous and exogenous effects of the flavones on NHDF, cells were irradiated with or without presence of the flavone in the medium.

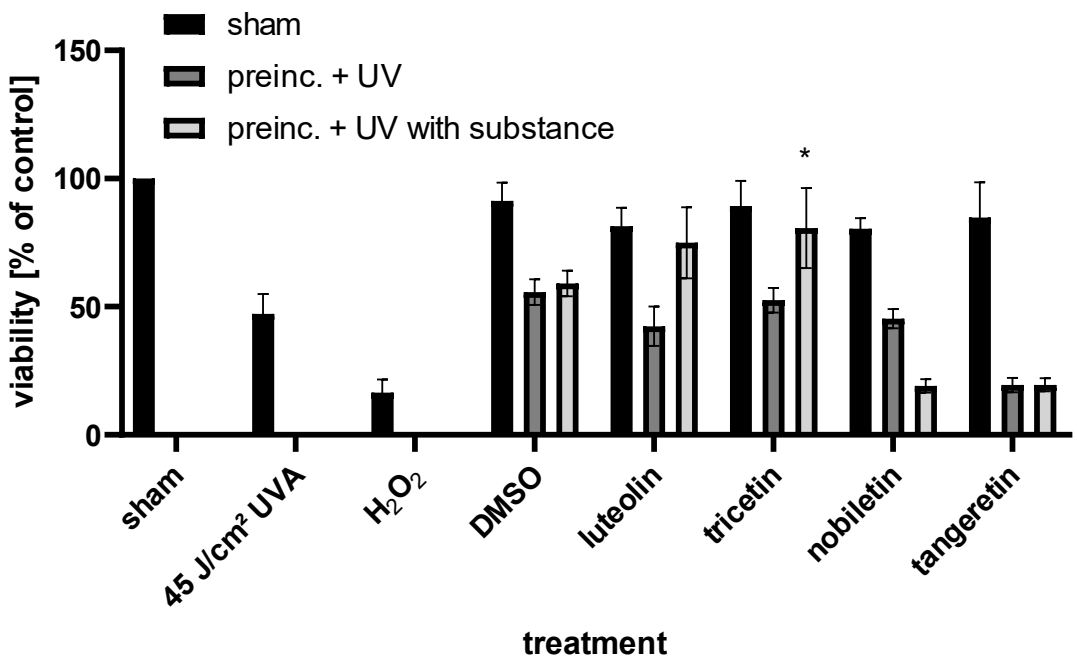

*Figure 3.21 Viability of NHDF after preincubation with flavones and irradiation with 45 J/cm² UVA. Cells were preincubated with 50 µM of each flavone and irradiated with 45 J/cm² UVA in the absence (preinc. + UV) or presence of flavones in the medium (preinc. + UV with substance). Viability of unirradiated fibroblasts was set as 100 %. 2 mM H_2O_2 and DMSO were used as positive and negative controls, respectively. Data represent means ± SEM. One-way Anova with Dunnett's multiple comparison test to the 45 J/cm² UVA control without including sham was performed. *p < 0.05, **p < 0.01, ***p < 0.001.*

Using the MTT assay, changes in the viability of fibroblasts after different treatments were observed (Figure 3.21). Three types of treatment were employed. First, the effect of preincubation with the substances on unirradiated (sham) cells was investigated. Second, cells were preincubated with the flavones and after removal of the flavones, cells were irradiated with 45 J/cm² UVA in HBSS (preinc. + UV). Third, cells were preincubated with flavones and then irradiated in HBSS supplemented with the same concentration of flavones as in the preincubation (preinc. + UV with substance). Upon treatment with H_2O_2 (positive control) and irradiation with 45 J/cm² UVA, cell viability was decreased. Treatment with luteolin and tricetin increased viability when the compounds were present in the irradiation medium. Therefore, luteolin and tricetin rescue the decrease in viability after irradiation with a toxic dose of UVA, although only the effect of tricetin is statistically significant. Nobiletin, when present in the medium during irradiation, further decreases viability, rendering it unsuitable for topical photoprotection, while it has no effect on viability when located intracellularly. Tangeretin decreases viability irrespective of its intra- or extracellular application and therefore is an unsuitable photoprotectant for topical and endogenous use. On the contrary, it shows phototoxic effects.

In order to evaluate the effects of luteolin and tricetin as possible topical photoprotectants, they were incorporated into a cream and tested for their efficacy in a cell viability assay, measured by protection from a toxic UVA dose. For that, the cream was evenly distributed onto a cover glass covering cell culture dishes with NHDF in HBSS during irradiation with 45 J/cm² UVA.

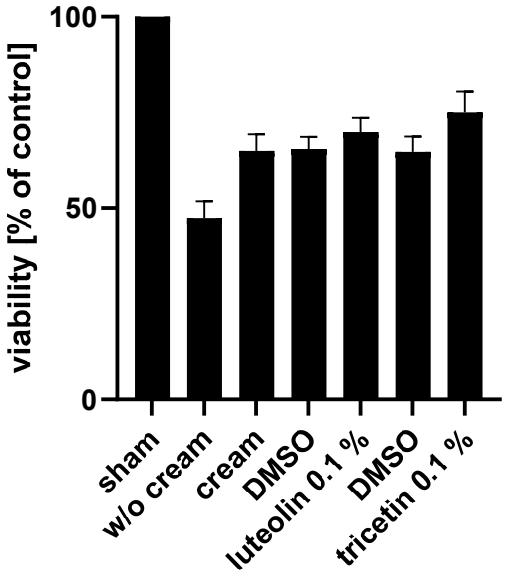

Figure 3.22 Viability of NHDF after irradiation (45 J/cm² UVA) under a cover glass with a cream containing luteolin or tricetin. A cream (see 2.15.4) was supplemented with 0.1 % (w/w) flavone or the corresponding volume of DMSO (control for each flavone) and spread over a cover glass, in compliance with the standard sunscreen testing surface density of 2 mg/cm². The unirradiated control (sham) was set as 100 %. A control without cream was used as a negative control (w/o cream). Data represent means ± SEM.

Figure 3.22 shows the effect of a cream supplemented with luteolin or tricetin on viability in NHDF after irradiation with high-dose UVA. When the cells were irradiated with UVA through a bare cover glass (without any cream - w/o cream) the viability was decreased to about 50 %. Application of the cream to the cover glass provided some protection and the viability was less decreased with about 60 % remaining. Addition of DMSO to the cream provided no further photoprotection. However, upon addition of luteolin and tricetin to the cream base, further protective effects were observed and viability after UVA exposure was higher, although not statistically significant. In principle, luteolin and tricetin display their photoprotective effects via absorbance of UVA photons in a cream formulation.

3.11 Establishment of an artificial aging model

In sunscreen development one important aspect is hardly addressed: the increasing human life expectancy and with it the increase in the population with old age. Hence, sunscreens are likely to be used exceedingly by the older generations. In most studies, this aspect is insufficiently recognized so far. Complications that might arise from this lack of information might be due to the alterations of young and aged skin, which are well known, but little studied with regard to UV radiation, especially in the UVA range. Here, differences between artificially aged and normal fibroblasts were studied in combination with exposure to UVA radiation and possible photoprotection by flavones.

By now, several methods of artificial aging in cell culture have been established, many of which provide only a transient senescence with respect to loss of aging markers over cell passages. Here, a drug-induced accelerated aging (DIAS) model was adopted that induces a more stable, persistent senescence by use of the alkylating and ROS-producing agent mitomycin c (MMC). Artificially aged cells derived from said treatment are named MMC cells in this study. As shown below, several markers for cellular aging were used to evaluate and validate the drug-induced artificial aging model with mitomycin c in NHDF. One of these markers in fibroblasts is an increase in cell size[177].

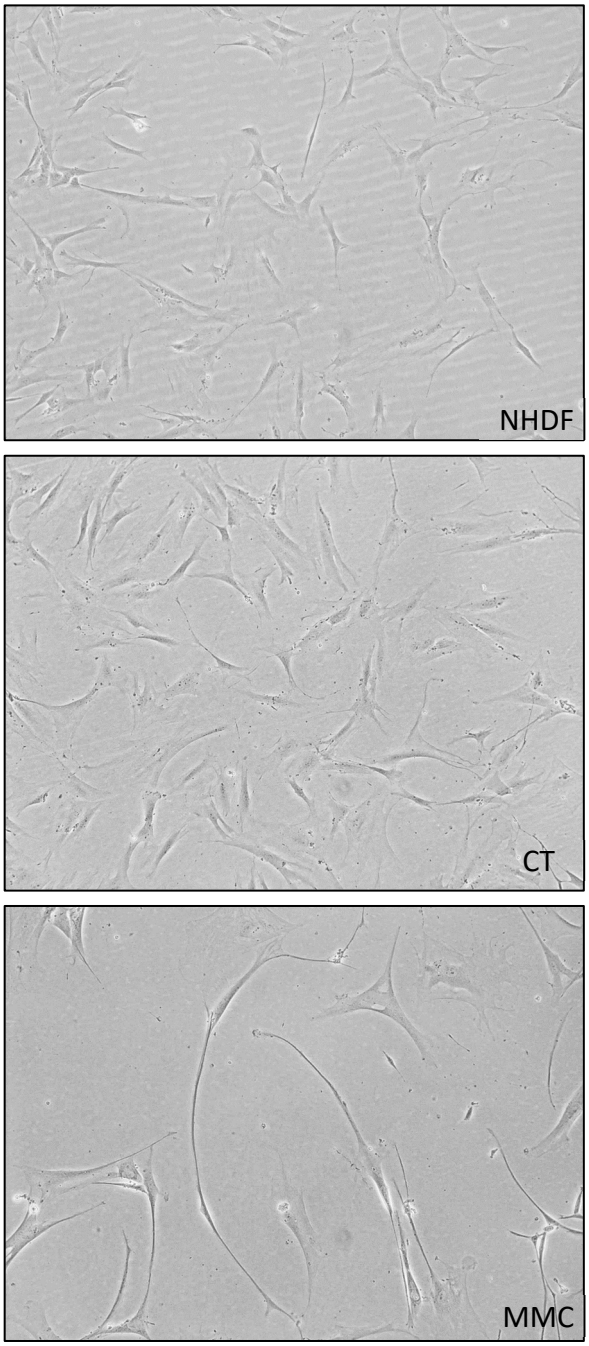

Figure 3.23 Morphology of normal human dermal fibroblasts (NHDF), DMSO-treated fibroblasts (CT) and artificially aged fibroblasts (MMC). Pictures were taken with 10 x magnification with an inverted microscope.

Figure 3.23 shows the morphology of the three differently treated fibroblasts. Treatment with MMC did not alter typical fibroblast morphology (elongated, spindle-like), but induced a considerable increase in size. Control cells treated with DMSO (CT) and NHDF are very similar in size and shape. In conclusion, MMC cells show fibroblast-associated morphological characteristics but an increase in cell size.

To characterize the cells obtained with the established artificial aging model, cell proliferation and cell size were determined by means of the BrdU incorporation assay and by flow cytometry, respectively. An increase in size and the inability to proliferate upon stimulation, e.g. with FCS supplementation in the medium, are common markers for aging in cells[178].

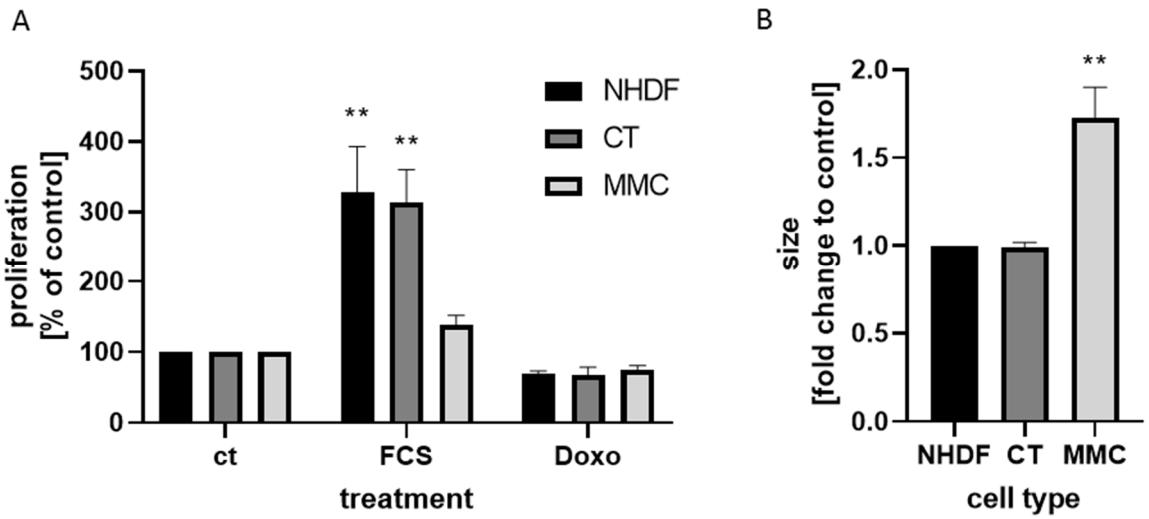

*Figure 3.24 Differences in proliferation and size between NHDF, CT and MMC cells. BrdU incorporation is given in % to the control (ct) of the respective cell type (set as 100 %) (A). Cells were incubated with starvation medium, 10 % FCS supplemented medium (positive control) or with 10 µM doxorubicin (negative control). Relative size of the three cell types was measured using flow cytometry (B). Size of NHDF was set as 1. Data represent means ± SEM. One-way Anova with Dunnett's multiple comparison to the NHDF ct was performed. *p < 0.05, **p < 0.01, ***p < 0.001.*

According to Figure 3.24, cell proliferation was increased by supplementing medium with 10 % FCS in NHDF and CT cells, while no statistically significant increase in proliferation was seen in MMC cells (A). The increase in size of MMC cells compared to CT cells and NHDF, as already shown by microscopy (Figure 3.23), was further verified by means of flow cytometry (B). In relation to the size of NHDF, CT cell size was similar while MMC cell size was increased 1.8-fold with statistical significance.

Additionally, to the observed signs of cellular aging, the expression of a senescence-associated ß-galactosidase was used as further proof of the model system.

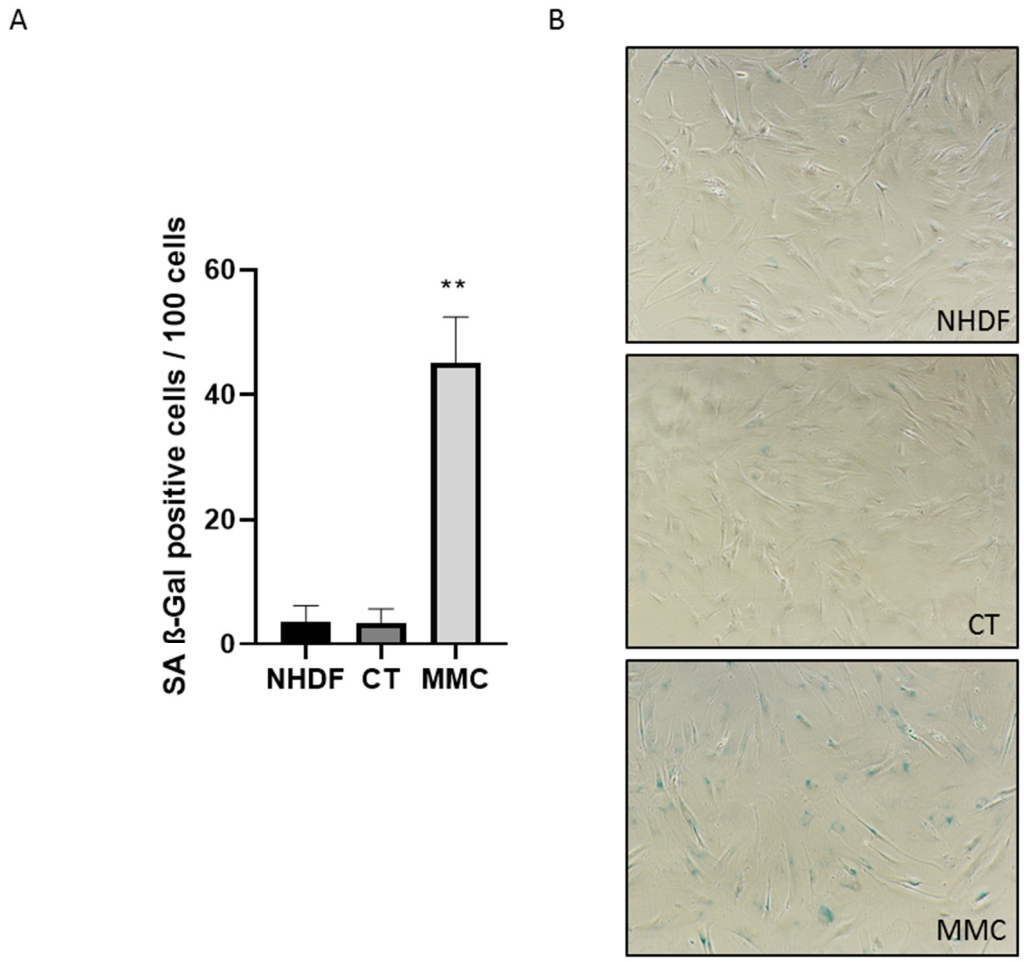

*Figure 3.25 Senescence-associated ß-galactosidase staining in NHDF, CT and MMC cells. Quantification of positively stained cells for SA-ß-Gal (A). Examples of microscopic images taken to evaluate SA-ß-Gal are presented in B. Pictures of the cells after staining were taken under an inverted microscope with 10 x magnification. Data represent means ± SEM. One-way Anova with Dunnett's multiple comparison to NHDF was performed. *p < 0.05, **p < 0.01, ***p < 0.001.*

In Figure 3.25, the number of cells stained positive for the presence of a senescence-associated ß-galactosidase is given. On average, in 100 counted cells from NHDF and CT cell cultures, less than 5 were positive for SA-ß-Gal compared to around 40 in MMC cells (A). Examples of microscope images of the respective cell cultures are shown in B. Blue staining indicates the presence of SA-ß-Gal. Therefore, the senescence-associated protein is mainly present in MMC and not in CT and NHDF, providing another positive marker for aging present in the model system. In all of the tested parameters above, CT cells show high similarity to NHDF. Thus, they were used as the proper control for the following experiments.

3.12 UV sensitivity of aged and control cells

In order to achieve an overview of the general response of artificially aged cells compared to control cells in regard to UV sensitivity, a cell viability assay was performed.

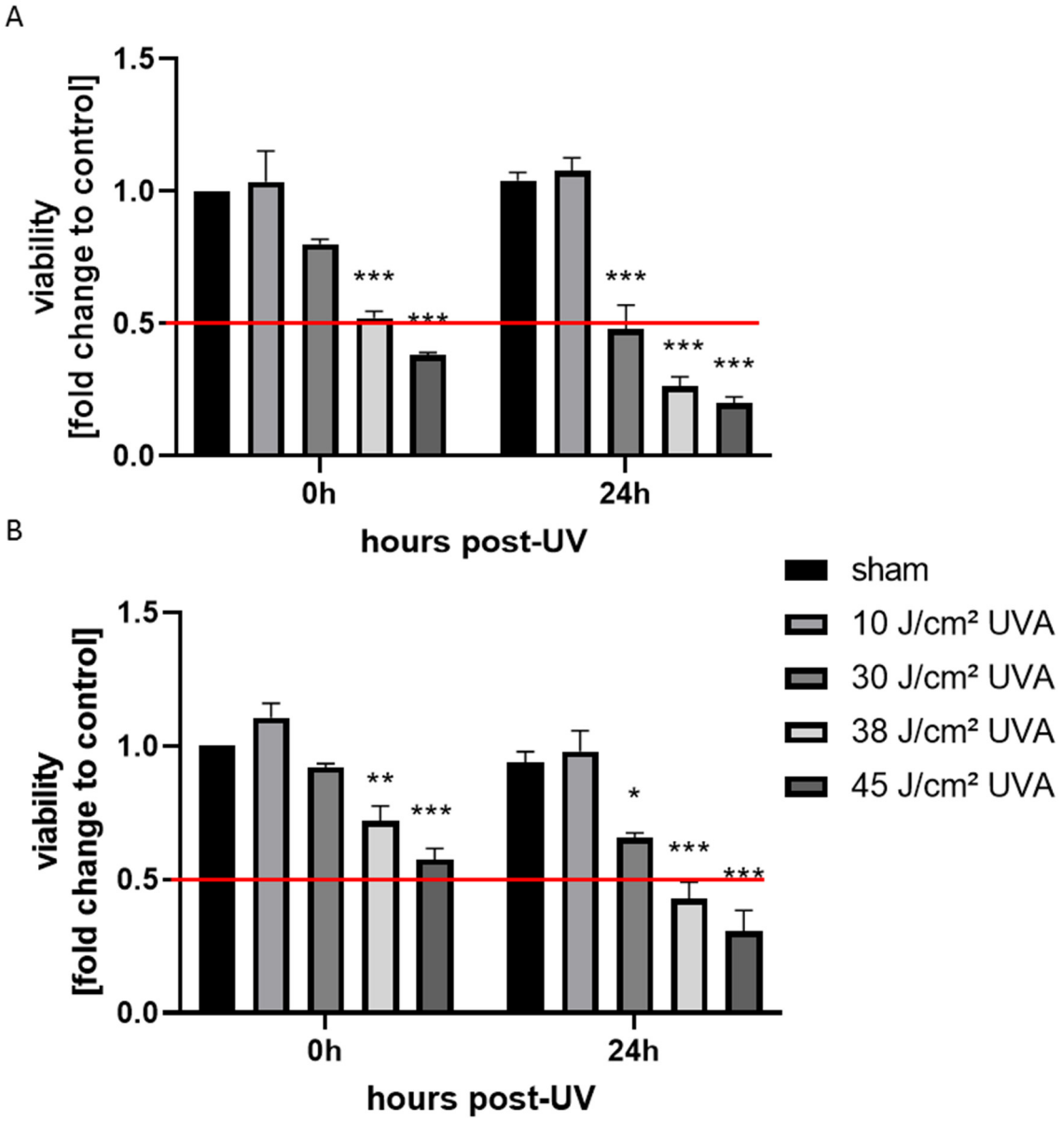

*Figure 3.26 UV sensitivity of CT and MMC cells. The MTT assay was used to determine changes in viability 0 and 24 hours after irradiation with different doses of UVA in control (A) and artificially aged fibroblasts (B). The red bar indicates the threshold of 50 % viability. Unirradiated controls at timepoint 0 were set to 1. Data represent means ± SEM. One-way Anova with Dunnett's multiple comparison test to the respective NHDF timepoint control was performed. *p < 0.05, **p < 0.01, ***p < 0.001.*

In Figure 3.26, the viability of CT (A) and MMC (B) cells is shown after irradiation with low and increasingly high doses of UVA. As shown before, irradiation with 10 J/cm² UVA did not alter viability significantly in both cell types, whereas higher doses negatively affected viability. Interestingly, the threshold of 50 % viability compared to the control was reached at later timepoints and only after higher doses in MMC cells (compare e.g. 38 J/cm² UVA at 0 h post-UV in CT and MMC cells).

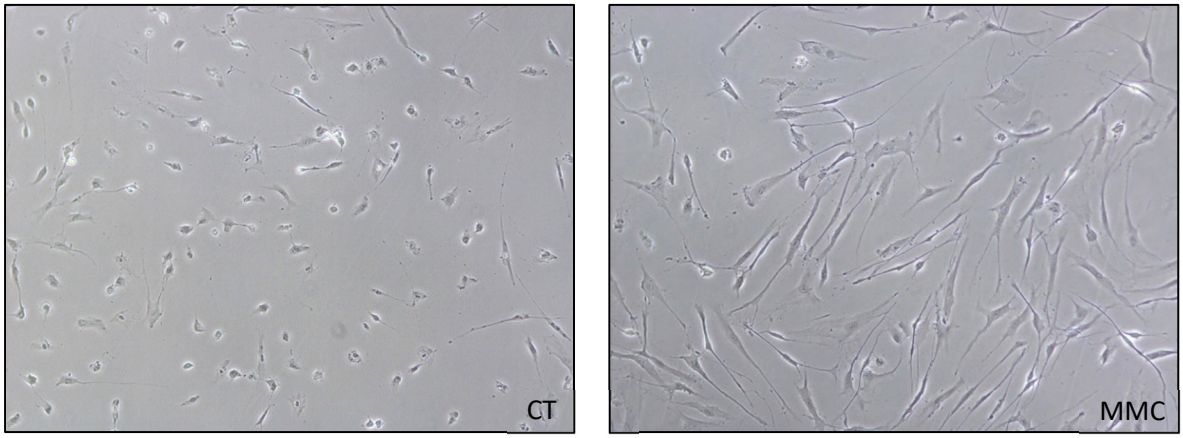

Figure 3.27 Microscope images of CT and MMC cells 24 hours after irradiation with 38 J/cm² UVA.

Figure 3.27 shows the morphology of CT and MMC cells 24 hours after irradiation with 38 J/cm² UVA before determination of viability using the MTT assay (Figure 3.26). The majority of CT cells exhibits a rounded shape, indicative of high stress. MMC cells show slight stress-induced alterations in shape, but present an overall healthier morphology than CT cells (almost no rounded cells, elongated shape). The microscope images suggest a higher sensitivity towards irradiation of CT cells compared to MMC cells and confirm the data from viability assays after irradiation.

According to Figure 3.26, cell death is evident directly after irradiation at doses from 38 J/cm² UVA upwards. Thus, earlier pathways may be activated before cell death induction, which might be observable in cells irradiated with lower UVA doses, e.g. initiation of DNA damage repair. Therefore, the time course of the DNA damage recognition and response after low dose UVA treatment was investigated.

3.13 Low-dose UVA-induced DNA damage

Upon DNA damage, histone protein H2AX is one of the first proteins to be phosphorylated. Therefore, it's phosphorylated form (γ-H2AX) is a suitable and frequently determined marker for early DNA damage. For that reason, immunostaining for γ-H2AX was performed in cultured cells.

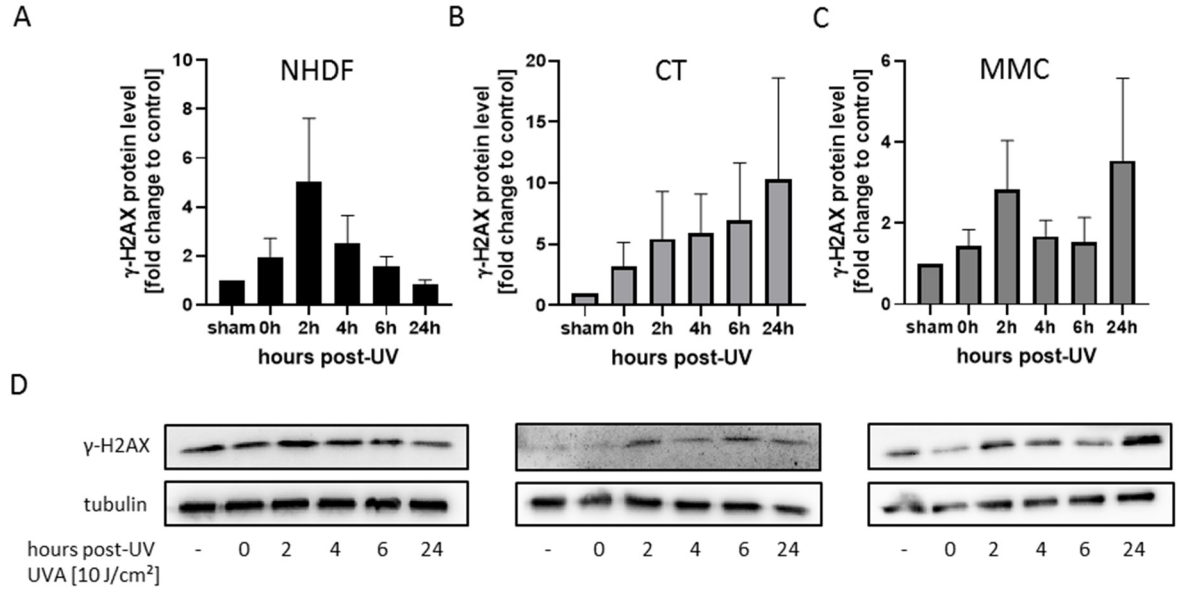

Figure 3.28 Protein levels of γ-H2AX in NHDF, CT and MMC cells after irradiation with UVA. Cells were irradiated with 10 J/cm² UVA or left unirradiated (sham) and samples were taken 0 to 24 hours after treatment. Protein levels in NHDF (A), CT (B) and MMC (C) were determined by Western Blot and are given as fold change to the unirradiated control (sham, set as 1). Bar graphs show quantification of the protein bands in relation to ß-tubulin levels on PVDF membrane below (D). Data represent means ± SEM.

The γ-H2AX protein level in NHDF, CT and MMC cells was investigated in response to irradiation with 10 J/cm² UVA over a time course up to 24 hours. Figure 3.28 shows that all cell types encounter DNA damage after exposure to low-dose UVA radiation, since formation of γ-H2AX is an indicator of DNA damage. In NHDF, protein levels of γ-H2AX are the highest two hours after UVA exposure with subsequent decrease of protein levels until the control level is reached 24 hours after exposure (A). For CT cells, the protein pattern is difficult to interpret due to high standard errors (B). Nevertheless, there is a similar increase of γ-H2AX until two hours post UV, followed by a tendency for further increase up to 24 hours later. Up to 6 hours after irradiation, NHDF and MMC cells show a similar pattern of γ-H2AX levels, but

a second increase of γ-H2AX levels at 24 hours was observed in MMC (C). In conclusion, there might be differences in terms of low-dose UVA-induced DNA damage response between NHDF and MMC that need to be further elucidated.

In order to further investigate possible differences between NHDF and MMC cells, the formation of a well-known UV-induced DNA lesion was measured. Cyclobutane pyrimidine dimers (CPD) are the major type of UV-induced DNA photolesions responsible for its mutagenicity. Here, the Comet assay as a tool to observe CPD formation and repair was employed. This single cell electrophoresis-based analysis combines alkaline treatment of DNA and application of lesion-specific repair enzymes to determine CPD-dependent lesions (for details see 2.17). By use of a CPD repair enzyme, T4 endo V, dimers are transformed into DNA breaks, that can be detected as an increased percentage of DNA in the tail of the comet. The amount of DNA in the tail is a direct measure of DNA damage[179].

A

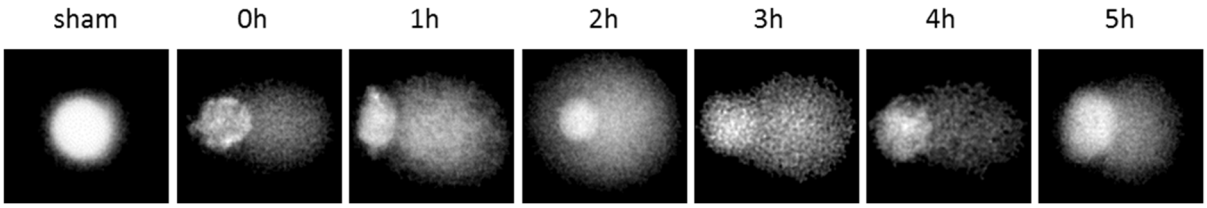

B

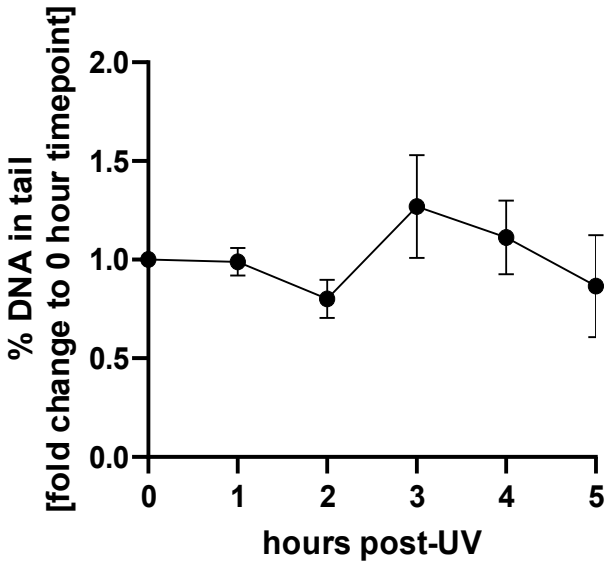

Figure 3.29 CPD-dependent % of DNA in the tail in NHDF after irradiation with 10 J/cm² UVA. Cells were irradiated and the percentage (%) of DNA in the comet tail was measured 0 to 5 hours post-UV by the Comet assay. Unirradiated cells were used as a control (sham). Representative images are shown in (A). Quantification by CometScore software is shown in (B). Data represent means ± SEM.

Figure 3.29 shows the CPD-dependent % of DNA in the tail as determined by the Comet assay using the lesion specific repair enzyme T4 endonuclease. CPD-induced DNA damage is measured as the percentage of DNA that resides in the tail region of the comet (see 2.17). As depicted in (A), low-dose UVA irradiation increases the formation of CPD-dependent lesions in NHDF. The quantification (B) was performed in relation to the initial CPD-dependent damage at timepoint 0 after irradiation. A decrease in CPDs was measured from one to two hours after UV exposure, followed by an increase three hours after irradiation and subsequent

decrease until the initial level of damage is approximately reached after 5 hours. CPD-dependent DNA lesions unexpectedly increase at later post-irradiation timepoints.

An unexpected, delayed increase in CPD-induced lesions after UVA-irradiation was seen in the Comet assay. Therefore, a second method for direct detection of CPDs was used to confirm this result. Additionally, measurements of CPDs in MMC cells were included. The second method for CPD measurement detects CPDs by a CPD-specific antibody via ELISA (see 2.18).

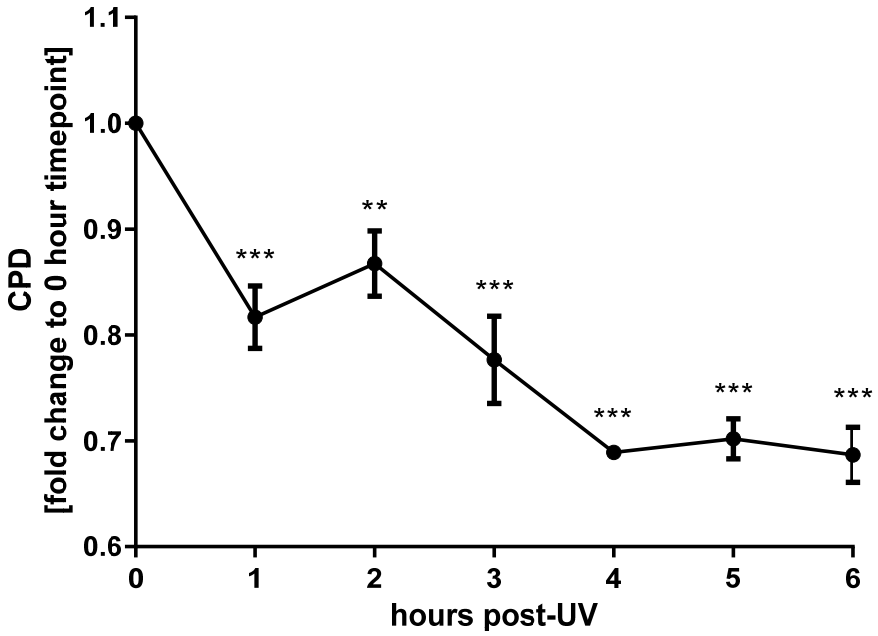

*Figure 3.30 CPD formation in NHDF after irradiation with 10 J/cm² UVA. CPD lesions were measured by ELISA 0 to 6 hours post-UV and are given in fold change to the irradiated control at 0 hours post-UV. Data represent means ± SEM. One-way Anova with Dunnett's multiple comparison test to the 0-hour timepoint was performed. *p < 0.05, **p < 0.01, ***p < 0.001.*

In Figure 3.30, the formation of CPDs is followed by a change in absorbance after low-dose UVA irradiation of NHDF. The initial amount of CPDs at the 0-hour timepoint after irradiation decreases in the first hour post-UV. From one to two hours, an increase in CPDs is seen. From two to 6 hours post-UV, lesions decrease until basal CPD levels are almost achieved (unirradiated control, data not shown). Consistent with the data obtained in the Comet assay, a second, smaller increase in CPDs is shown two hours post-UV. In contrast to the initial CPD damage, this increase is independent of direct UV radiation, since the exposure to UVA has already stopped.

Here again, the formation of deleterious DNA lesions was shown after low-dose UVA irradiation in NHDF. A delayed increase of CPDs was shown for the second time. In order to further verify and emphasize the delayed formation of CPDs, repair inhibitors were used. The use of repair inhibitors aims at preventing the rate of repair to interfere with the rate of formation of CPDs. Aphidicolin is an inhibitor of DNA polymerase α, δ and ε[180], which are required for DNA synthesis and of which the latter are involved in late steps of nucleotide excision repair (NER). X80 is an inhibitor of xeroderma pigmentosum group A protein (XPA) interaction with DNA, which is required for early steps of NER[181].

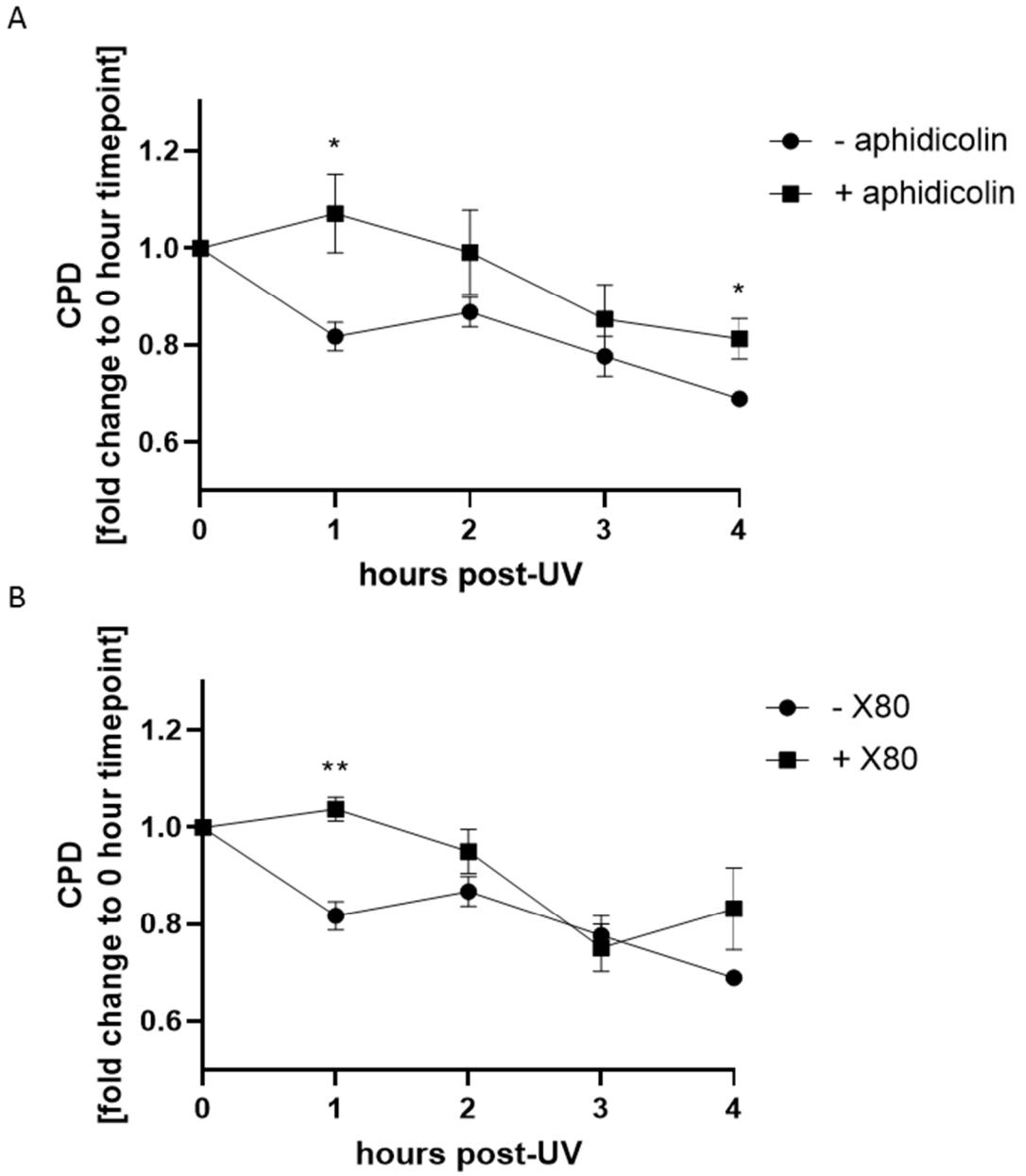

*Figure 3.31 CPD formation in NHDF after irradiation with 10 J/cm² UVA in the presence and absence of DNA repair inhibitors. CPD levels were measured by ELISA (0 - 4h) and are given in fold change to the irradiated control at 0 hours post-UV. A control time course without inhibitor is given. Aphidicolin (2.9 µM) was added 24h pre-UV (A). X80 (100 µM) was added directly and was resupplied hourly after irradiation (B). Data represent means ± SEM. The unpaired t-test to the respective timepoint control was performed. *p < 0.05, **p < 0.01, ***p < 0.001.*

In Figure 3.31, addition of repair inhibitors to NHDF before or after irradiation with low doses of UVA leads to prevention of initial repair as seen in comparison to control samples (-inhibitor). The effect is statistically significant. An increase of CPDs is shown in both time

courses with addition of repair inhibitors aphidicolin (A) and X80 (B) after irradiation has ended, implying the existence of delayed CPD. Repair proceeds after one-hour post-UV.

With the use of two differently targeted DNA repair inhibitors and varying incubation patterns, the finding of delayed formation of CPD post-irradiation was confirmed.

Finally, CPD formation was investigated in the established aging model.

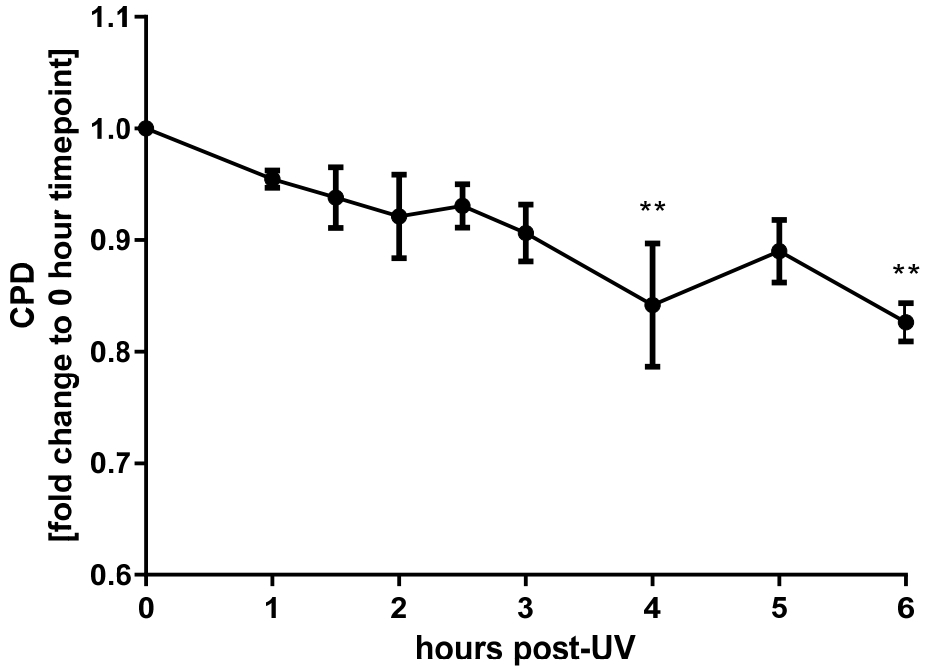

*Figure 3.32 CPD formation in MMC cells after irradiation with 10 J/cm² UVA. CPD levels were measured by ELISA (0 - 6h) and are given in fold change to the irradiated control at 0 hours post-UV. Data represent means ± SEM. One-way Anova with Dunnett's multiple comparison test to the 0-hour timepoint was performed. *p < 0.05, **p < 0.01, ***p < 0.001.*

Figure 3.32 shows the formation of CPDs in MMC cells 0 to 6 hours after irradiation with low-dose UVA. In comparison to NHDF, there is no increase in CPD one to three hours post-UV. Although there is a subsequent decrease in CPD lesions after irradiation, the decrease is only statistically significant to the 0-hour control at later timepoints.

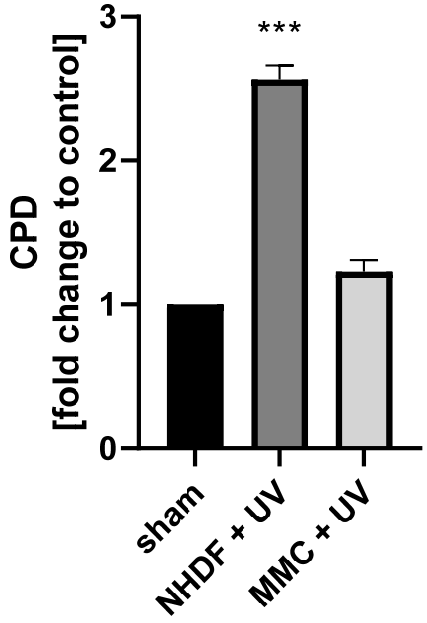

*Figure 3.33 CPD formation directly after irradiation with 10 J/cm² UVA in NHDF and MMC cells. CPD lesions at timepoint 0 after irradiation were measured by ELISA and are given in relation to the respective unirradiated control (sham, set as 1). Data represent means ± SEM. One-way Anova with Dunnett's multiple comparison test to the sham control was performed. *p < 0.05, **p < 0.01, ***p < 0.001.*

The initial level of CPD photolesions was then compared between NHDF and MMC cells. Figure 3.33 shows a statistically significant increase of CPDs in NHDF after irradiation with low-dose UVA compared to an unirradiated control. Interestingly, CPD levels in MMC cells were not statistically different to the unirradiated control, implying low levels of CPD formation in these cells.

Using different approaches, the formation of low-dose UVA induced CPDs was shown in NHDF and the delayed formation of CPD has been repeatedly observed. MMC cells do not show "dark" dimer formation and exhibit lower initial CPD levels compared to NHDF.

3.14 Photoprotection from low-dose UVA-induced CPD

To investigate whether luteolin and tricetin might be effective in the prevention of direct or delayed CPDs, NHDF were preincubated with the selected flavones and irradiated with a low dose of UVA, followed by measurement of CPD levels via ELISA.

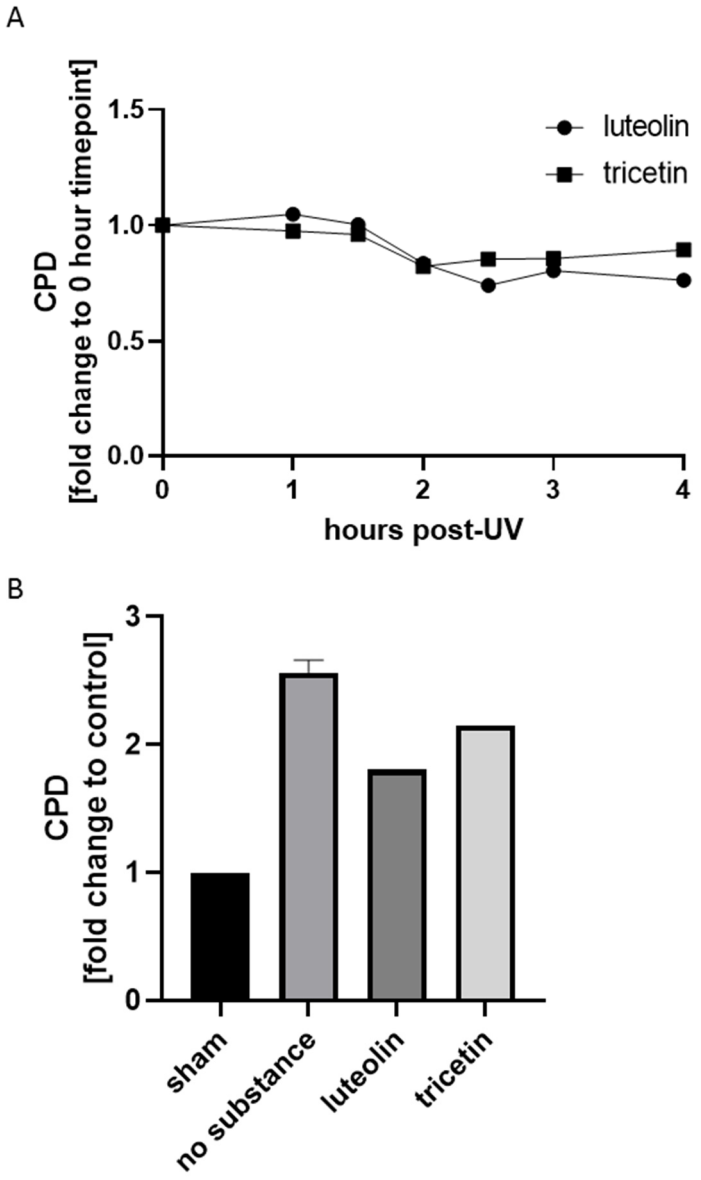

Figure 3.34 CPD formation in irradiated NHDF preincubated with luteolin or tricetin. Cells were preincubated (2h, 50 µM) with luteolin or tricetin and CPDs were measured by ELISA (0 - 4 h post-UV) (A). CPD formation at 0 h post-UV is shown in fold change compared to the untreated sham control (B). N = 1 for luteolin and tricetin time courses. Error bars in NHDF (no substance) represent means ± SEM.

The repair of CPDs after irradiation with 10 J/cm² UVA in luteolin and tricetin preincubated NHDF shows little to no progression in the first four hours after irradiation (Figure 3.34 A). Comparing the amount of CPDs (given in relation to the sham control) formed directly after irradiation with 10 J/cm² UVA from preincubated NHDFs to the irradiated control with no substance (from previous experiments) shows a decrease in CPD lesions (Figure 3.34 B). Irradiation increases CPDs around 2.5-fold in untreated NHDF compared to the sham control. Although the time courses with luteolin and tricetin were only performed once, results show a trend towards a lower initial level of CPD lesions in both cases.

3.15 Low-dose UVA-induced effects on HO-1 expression

Besides DNA damage, UVA radiation is known to increase the formation of ROS and therefore promotes oxidative stress[25]. Cells respond to an increased oxidative load with several defense mechanisms. One response is an elevated expression of the enzyme HO-1. Thus, a time course of HO-1 upregulation was investigated.

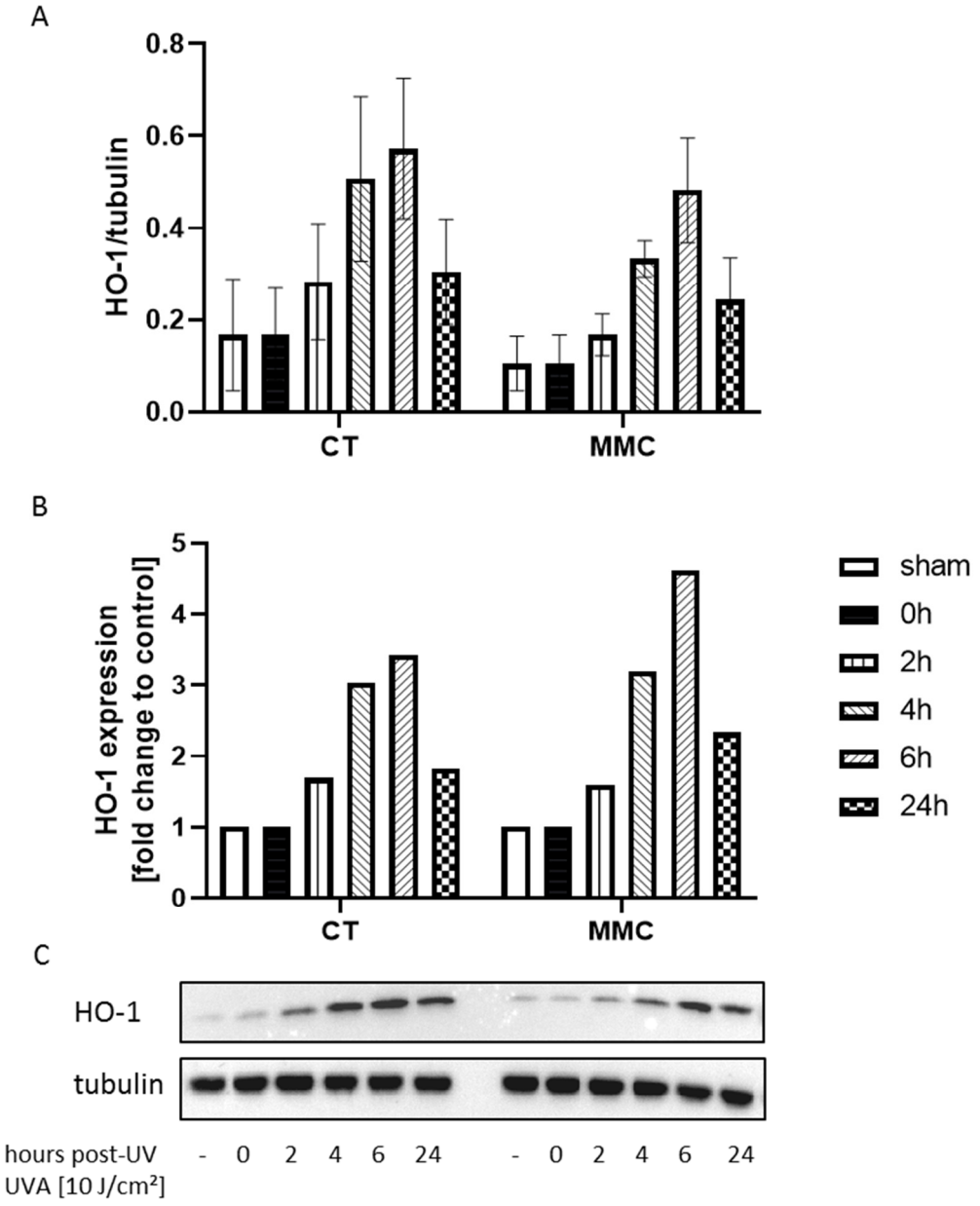

Figure 3.35 Expression of HO-1 in CT and MMC cells after irradiation with 10 J/cm² UVA. Protein levels of HO-1 and ß-tubulin were followed by Western Blot from 0 to 24h after irradiation (C) and quantification is given as ratio (A) and fold change to the unirradiated control (B, sham set as 1). Data represent means ± SEM.

Figure 3.35 shows the expression of HO-1 as a response to low-dose UVA irradiation in CT and MMC cells. As can be seen from the ratio of HO-1 to tubulin expression, levels of HO-1 do not differ between cell types (A). The change of expression from unirradiated controls (sham) to irradiated cells shows a similar expression pattern in both CT and MMC cells (B). HO-1 levels begin rising two hours post-UV with a maximal increase after 6 hours, followed by a decrease at 24 hours after irradiation. HO-1 is upregulated by low-dose UVA in control and artificially aged fibroblasts.

As HO-1 is a protein known to respond to oxidative stress, the general load of oxidants in a basal (untreated) state of all three cell types was investigated.

3.16 Comparison of basal ROS levels in NHDF, CT and MMC

A DCF assay was employed to investigate possible differences in intracellular ROS levels between NHDF, CT and MMC cells.

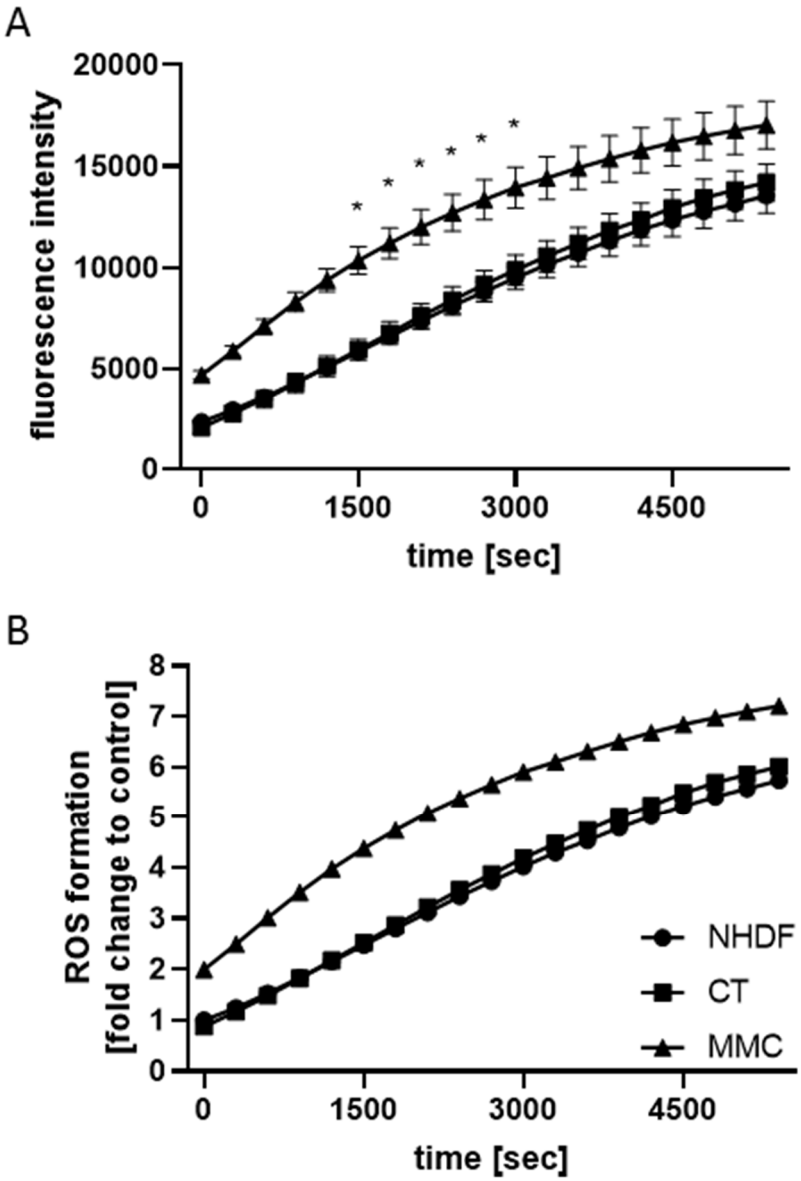

*Figure 3.36 ROS production in NHDF, CT and MMC cells. ROS formation was measured over time via fluorescence intensity of DCF (A). Fluorescence of NHDF at timepoint 0 was set as 1, further data points were shown as fold change to the control (B). Error bars depict SEM. One-way Anova with Tukey's multiple comparison test was performed. *p < 0.05, **p < 0.01, ***p < 0.001.*

Figure 3.36 shows differences in ROS production over time in NHDF, CT and MMC cells. In MMC cells, the level of ROS at the start of the measurement is approximately 2-fold higher than in NHDF and CT cells. Over time, the difference in ROS production between MMC and both CT and NHDF cells becomes statistically significant. Towards the end of the measurement, ROS levels converge, but stay higher in MMC than both controls (NHDF and CT). In general, between start and end of the experiment, ROS levels have increased by approximately 6-fold.

As leakage of the respiration of mitochondria is the major source of ROS production in the cell, mitochondrial respiration was investigated using a Seahorse metabolic flux analyser.

3.17 Low-dose UVA-induced effects on mitochondrial function

Mitochondria are the organelles which host oxidative phosphorylation and contribute a great proportion of physiological ROS production via electron leakage of the respiratory chain. The Mito stress test bioenergetics assay of the Seahorse flux analyzer can be used to assess mitochondrial function. Parameters of the oxygen consumption rate (OCR), that can be investigated by sequential addition of mitochondrial inhibitors, are the basal respiration, maximal respiration, ATP production, spare respiratory capacity, proton leak and non-mitochondrial respiration. Furthermore, the level of extracellular acidification (ECAR) as a measure of proton excretion by glycolysis can be determined. After injection of the inhibitors into the test chamber, changes in proton and oxygen levels are measured by sensors. Oligomycin is an ATP synthase inhibitor, revealing the proportion of basal respiration that is used for ATP production. FCCP is an uncoupling agent and reveals the maximal capacity of the ETC. Rotenone is an inhibitor of the respiratory complex I and antimycin a is an inhibitor of complex III, revealing oxygen consumption from other processes despite mitochondrial respiration, e.g. from cytosolic oxidases.

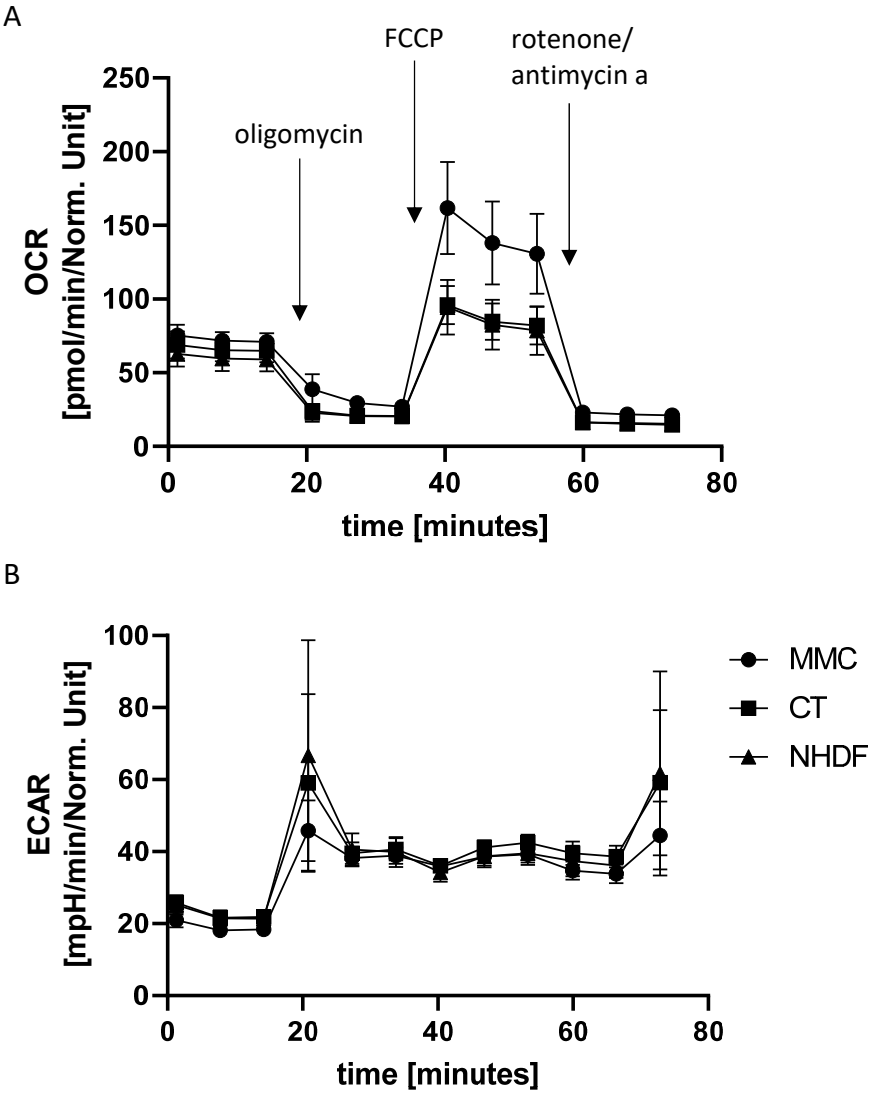

Figure 3.37 Mito stress test in NHDF, CT and MMC cells. Oxygen consumption rate (OCR, pmol/min) and extracellular acidification rate (ECAR, mpH/min), normalized to DNA content, was measured using a Seahorse flux analyzer. Oxygen consumption (A) and extracellular acidification rate (B) was measured over 80 minutes with sequential addition of mitochondrial toxins (see 2.19.2). Data represent means ± SEM.

Figure 3.37 shows differences in mitochondrial functionality between NHDF, CT and MMC as determined with the Mito stress test. The oxygen consumption rate is measured and evaluated as stated in the material and methods section (see 2.19). Basal respiration of all three cell types is similar with 60 to 70 pmol/min (A). Significant differences between the cells are only detectable after injection of the uncoupler FCCP. Uncoupling of the ETC leads to an increase of oxygen consumption in MMC cells to around 150 pmol/min, while the maximal

respiration of CT cells and NHDF is lower with around 100 pmol/min. Extracellular acidification, which is indicative for glycolytic activity, shows no differences between cell types (B).

After the basal conditions of cellular respiration determined with the Mito stress test have been established in all three cell types, the cellular response of respiration to irradiation with low-dose UVA was investigated.

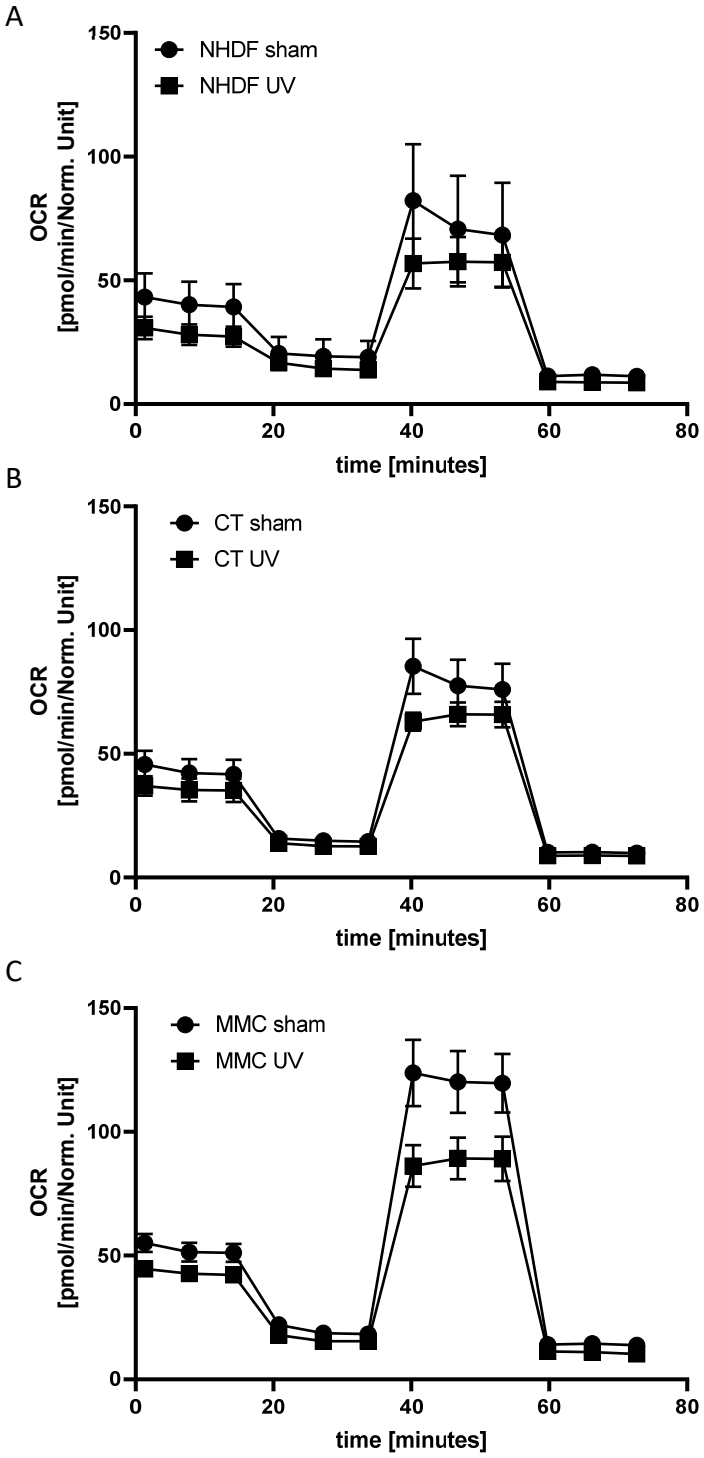

Figure 3.38 Mitochondrial response to low-dose UVA radiation in NHDF, CT and MMC cells determined with the Mito stress test. Oxygen consumption rate (OCR, pmol/min), normalized to DNA content, was measured in cells 24 hours after irradiation (10 J/cm² UVA) or sham treatment using a Seahorse flux analyzer for NHDF (A), CT (B) and MMC (C). Data represent means ± SEM.

Oxygen consumption in response to low-dose UVA radiation was measured in NHDF, CT and MMC cells (Figure 3.38). Generally, irradiation with 10 J/cm² UVA decreases basal and maximal respiration in all three cell types. The effect is less pronounced in NHDF (A) and CT cells (B), where the maximal respiration decreases from around 80 to 60 pmol/min/norm. unit, compared to a decrease from 130 to 80 pmol/min/norm. unit in MMC (C). In MMC cells, maximal respiration is higher than in both control cell types but most severely decreased after exposure to UVA. This experiment demonstrated that 24 hours after irradiation with low doses of UVA light, basal and maximal respiration in control and aged cells were decreased.

In order to gain detailed insight on the responses between cell types and treatments regarding mitochondrial respiration, parameters further derived from the experiments obtained with the Seahorse flux analyzer were evaluated. This includes ATP production, maximal and basal respiration, proton leak, spare respiratory capacity and non-mitochondrial respiration.

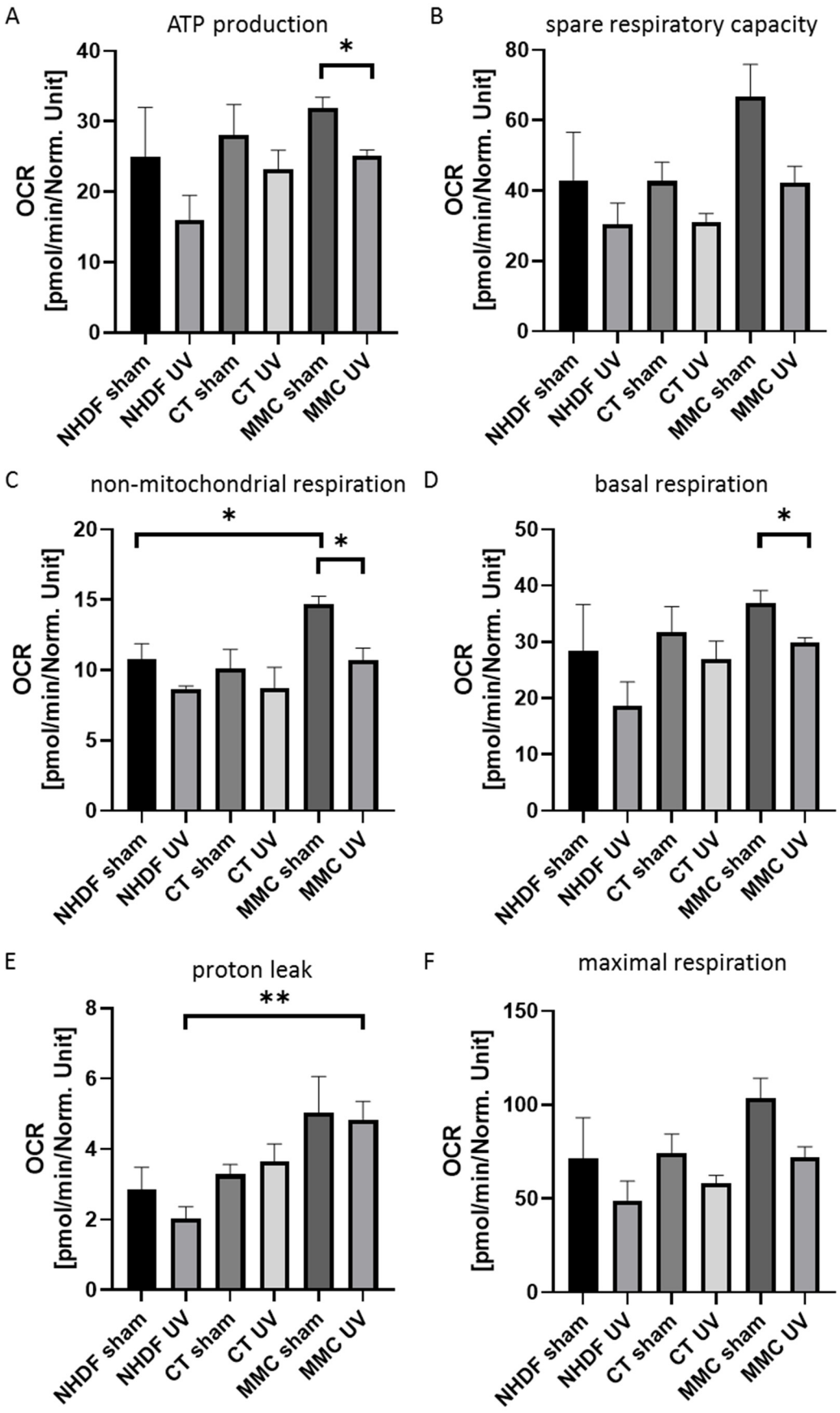
A
ATP production
OCR [pmol/min/Norm. Unit]
*
B
spare respiratory capacity
C
non-mitochondrial respiration
*
*
D
basal respiration
*
E
proton leak
**
F
maximal respiration
NHDF sham
NHDF UV
CT sham
CT UV
MMC sham
MMC UV

*Figure 3.39 Oxygen consumption rate in response to mitochondrial toxins in NHDF, CT and MMC cells as determined with the Mito stress test. Additional Seahorse parameters were obtained from data shown in Figure 3.38, where OCR was measured 24 hours after sham treatment or irradiation with 10 J/cm² UVA. Parameters indicate ATP production (A), spare respiratory capacity (B), non-mitochondrial respiration (C), basal respiration (D), proton leak (E), maximal respiration (F). Data represent means ± SEM. Unpaired t-test was performed. *p < 0.05, **p < 0.01, ***p < 0.001.*

Figure 3.39 shows that low-dose UVA radiation has manifold and long-lasting (24 hours post-UV) effects on mitochondrial respiration in NHDF, CT and MMC cells, although only in MMC cells with statistical significance to the unirradiated control.

ATP production after sham treatment is similar in all three cell types (A). ATP production is decreased upon irradiation. The UV-induced decrease is only statistically significant in MMC cells. However, ATP production is the lowest in irradiated NHDF.

The spare respiratory capacity, which results from subtraction of the basal from the maximal respiration, is around 20 pmol/min higher in MMC cells compared to NHDF and CT cells (B). Upon irradiation, the spare respiratory capacity in all cells decreases. The spare capacity in irradiated MMC is approximately as high as in unirradiated NHDF and CT cells.

Non-mitochondrial respiration in unirradiated cells is higher in MMC cells compared to control cells with statistical significance (C). Irradiation decreases non-mitochondrial respiration in all cell types, although the decrease is only statistically significant in MMC cells.

The basal respiration between cell types is unaltered (D). Low doses of UVA light decrease the basal respiration in all cell types. Due to higher standard errors in replicates of control cells, the decrease is only statistically significant in MMC cells.

A higher basal proton leak is shown for MMC cells compared to control cells (E). Upon irradiation, the proton leak decreases in NHDF, but not in CT and MMC cells. The proton leak in MMC cells after irradiation is significantly higher than in NHDF.

The maximal respiration in MMC cells is higher than in control cells (F). Irradiation decreases the maximal respiration in all cell types. The maximal respiration after irradiation in MMC cells is slightly higher than in control cells.

In summary, MMC cells display a significantly decreased ATP production (A), non-mitochondrial respiration (C) and basal respiration (D) upon irradiation, with similar tendencies in spare respiratory capacity (B) and maximal respiration (F). Furthermore, there are differences independent of UVA irradiation between cell types. Non-mitochondrial respiration in MMC cells is significantly higher than in NHDF (C). Due to the increased maximal respiration in MMC cells compared to NHDF, the spare capacity is increased, as well, although these levels are drastically reduced in MMC after irradiation (B). Additionally, there is a significant difference in the proton leak between MMC cells and NHDF after irradiation (E). The proton leak in MMC cells compared to control cells is higher even in basal state without irradiation.

In most of the parameters, CT cells act identical to NHDF cells. Only in some parameters, e.g. basal respiration or ATP production, CT cells show an intermediate state between NHDF and MMC.

A previously identified cytotoxic dose of UVA was investigated, as well. The effect of higher doses of UVA on mitochondria was studied by exposing cells to 45 J/cm² UVA.

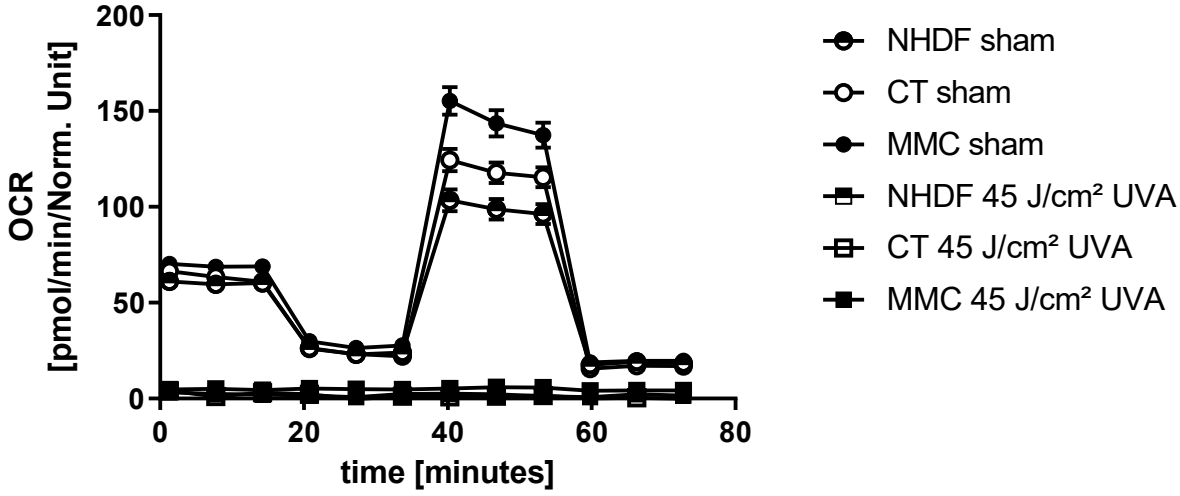

Figure 3.40 Mitochondrial response to high-dose UVA radiation in NHDF, CT and MMC cells as determined with the mito stress test. Oxygen consumption rate (OCR, pmol/min), normalized to DNA content, was measured with and without exposure to radiation (45 J/cm² UVA) using a Seahorse flux analyzer. Data represent means ± SEM.

Irradiation with high doses of UVA (Figure 3.40) reveals a total loss of mitochondrial function in NHDF, CT and MMC cells, while unirradiated controls (sham) show similar oxygen consumption rates as measured in previous experiments.

3.18 Effects of low-dose UVA on the ATP/NAD^+/Ado axis in control and aged fibroblasts

Thus far, intracellular processes have been investigated differentiating between normal and artificially aged fibroblasts, and between irradiated and non-irradiated fibroblasts. Here, the influence on irradiation and cell "age" on purinergic extracellular signalling was investigated.

The ATP/NAD^+/Ado axis comprises two pathways that ultimately converge to form adenosine, a key extracellular signalling molecule in inflammation. Mainly three cell surface proteins, the ectoenzymes CD38, CD39 and CD73, anchored in the cell membrane, are involved in cleaving extracellular purinergic substrates. Here, their expression on the cell surface of sham treated and irradiated NHDF, CT and MMC cells was investigated.

A

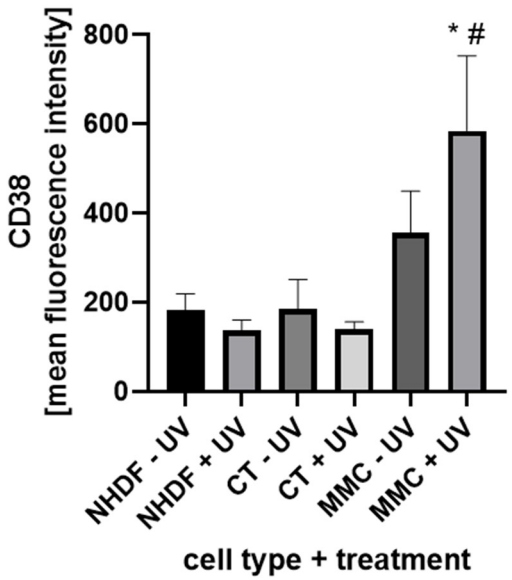
CD38
[mean fluorescence intensity]
800
600
400
200
0
* #
NHDF - UV
NHDF + UV
CT - UV
CT + UV
MMC - UV
MMC + UV
cell type + treatment

B

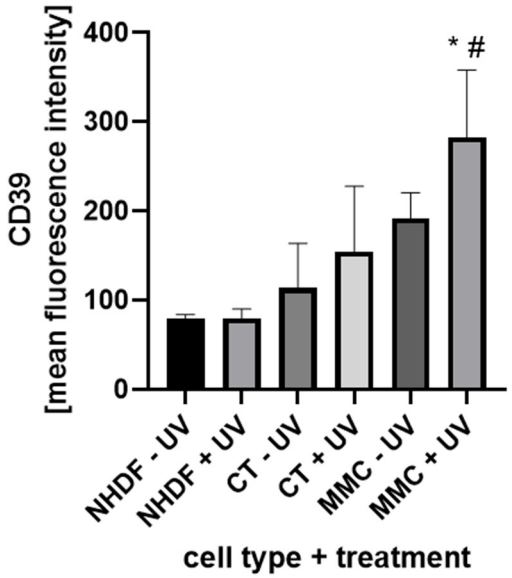
CD39
[mean fluorescence intensity]
400
300
200
100
0
* #
NHDF - UV
NHDF + UV
CT - UV
CT + UV
MMC - UV
MMC + UV
cell type + treatment

C

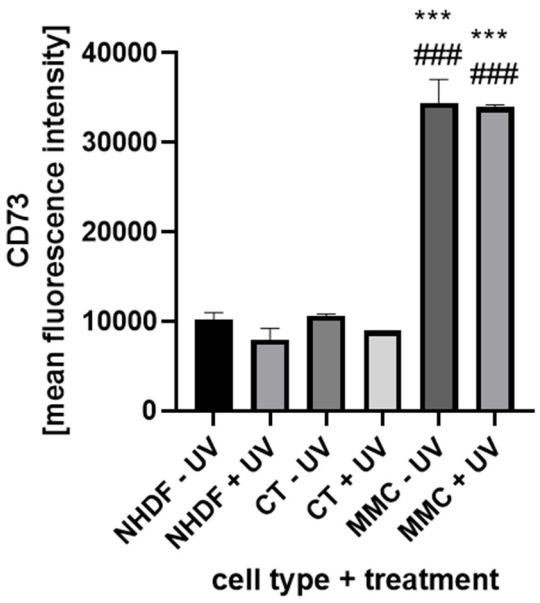
CD73
[mean fluorescence intensity]
40000
30000
20000
10000
0
*** ###
*** ###
NHDF - UV
NHDF + UV
CT - UV
CT + UV
MMC - UV
MMC + UV
cell type + treatment

*Figure 3.41 Expression of CD38 (A), CD39 (B) and CD73 (C) in NHDF, CT and MMC cells. Expression after sham or low-dose UVA treatment was measured by flow cytometry and is given as the mean fluorescence intensity. Data represent means ± SEM. One-way Anova with Dunnett's multiple comparison test was performed, * to NHDF - UV, # to NHDF + UV. *p < 0.05, **p < 0.01, ***p < 0.001; #p < 0.05, ##p < 0.01, ###p < 0.001.*

The expression of cell surface proteins involved in the ATP/NAD^+/Ado axis is shown in Figure 3.41. Expression of CD38 (A), CD39 (B) and CD73 (C) in NHDF, CT and MMC cells was measured by flow cytometry detection.

Basal CD38 levels are higher in MMC cells than in control cells (A). Upon irradiation, the level decreases in NHDF and CT cells, but increases in MMC cells. CD38 is approximately 4-fold increased in irradiated MMC cells compared to NHDF.

CD39 expression without irradiation is higher in MMC cells compared to NHDF and CT cells (B). Irradiation increases expression levels only in MMC cells, where the increase is significantly altered compared to the NHDF control.

The expression of CD73 in sham treated cells is significantly higher in MMC cells compared to both control cell types (C). Upon irradiation, the level of expression slightly decreases in NHDF and CT cells, but is unaltered in MMC cells. The CD73 levels are significantly increased around 3.5-fold in MMC cells compared to NHDF and CT cells with and without irradiation.

There are general differences in expression levels between the three proteins. In all three cell types, CD39 is the least abundantly expressed ectoenzyme, followed by CD38. CD73 shows the highest expression levels between the ectoenzymes in all cell types. CD38, CD39 and CD73 levels are increased in MMC cells compared to NHDF and CT.

Here again, CT cells show similar expression of proteins to NHDF and are therefore suitable control cells.

To investigate whether the altered expression levels reflect changes in enzyme activity, the conversion of the substrates NAD^+, ATP, AMP by CD38, CD39 and CD73 was measured by means of UPLC.

3.19 Effects of low-dose UVA on purinergic signalling in control and aged fibroblasts

Substrates for enzymes of the ATP/NAD^+/Ado axis (see Figure 1.2) were added to cell cultures and levels of products along this axis were measured by means of UPLC analysis, thereby revealing the conversion of substrate to product by the ectoenzymes CD38, CD39 and CD73. With the conversion of the substrate NAD^+ to ADPR, AMP and adenosine the pathway led by CD38 activity can be followed. With addition of the substrate ATP, the conversion to ADP, AMP and adenosine via the CD39 pathway can be followed. Addition of the CD73 substrate AMP reveals direct conversion to adenosine. As the substrate contains traces of all involved metabolites, the trace amount found in the substrate sample was set as 100 % and changes over time were given in relation to the initial substrate. The trace amounts found by UPLC are given in Table 3.1.

Table 3.1 Absolute values of the metabolites in the added substrate, measured by UPLC. Values represent 100 % of substrate in Figures 3.42 - 3.45.

addition of…	**metabolite**	**molarity found by UPLC [M]**	**[µM]**
2 µM ATP	ATP	1,87E-06	1,87
	ADP	3,07E-07	0,31
	AMP	5,66E-08	0,06
	Ado	2,29E-08	0,02
20 µM AMP	AMP	2,57E-05	25,73
	Ado	2,44E-07	0,24
2 µM Ado	Ado	1,62E-06	1,62
2 µM NAD^+	NAD^+	2,01E-06	2,01
	ADPR	1,92E-07	0,19
	AMP	2,14E-08	0,02
	Ado	7,05E-08	0,07

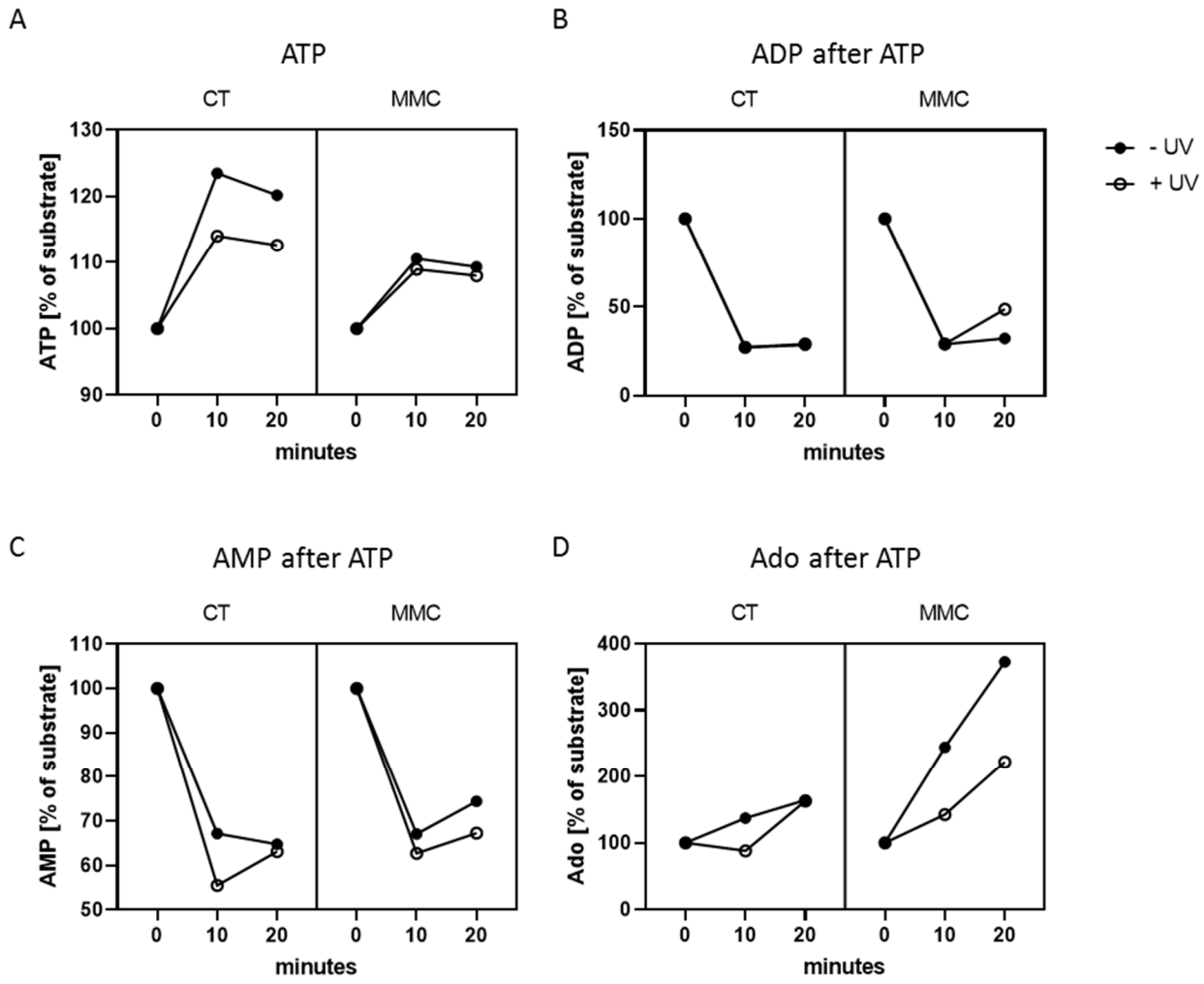

Figure 3.42 Change in extracellular levels of ATP (A), ADP (B), AMP (C) and adenosine (D) in CT and MMC cells upon incubation with 2 µM ATP. Analyte levels in the medium were measured by UPLC after irradiation with 10 J/cm² UVA or sham treatment and subsequent incubation with ATP as substrate for 0, 10 or 20 minutes. Levels are given in % of the initial substrate. N = 1.

Figure 3.42 shows extracellular levels of analytes along the ATP/AMP/Ado axis after addition of 2 µM ATP in irradiated and sham treated CT and MMC cells over time. ATP levels increase in both cell types in the first 10 minutes of incubation after irradiation with low doses of UVA. There is no further increase in ATP levels from 10 to 20 minutes. In CT cells, ATP levels rise higher above the initial substrate level than in MMC cells, especially without irradiation (A). ADP and AMP levels are decreasing in the first 10 minutes in both cell types with little effect of irradiation (B and C). A remarkable increase in adenosine levels can be seen in MMC cells compared to CT cells, especially without irradiation (D). The increase in adenosine is nearly 4-

fold to the basal level at timepoint 0 in MMC cells, while the increase in CT cells is only approximately 0.5-fold. Low-dose UVA irradiation slows the increase in adenosine in MMC cells, while there is no impact on CT cells. Analysis of ATP and its metabolites indicates a higher turnover from ATP to Ado in the ATP/AMP/Ado axis of MMC cells compared to CT cells.

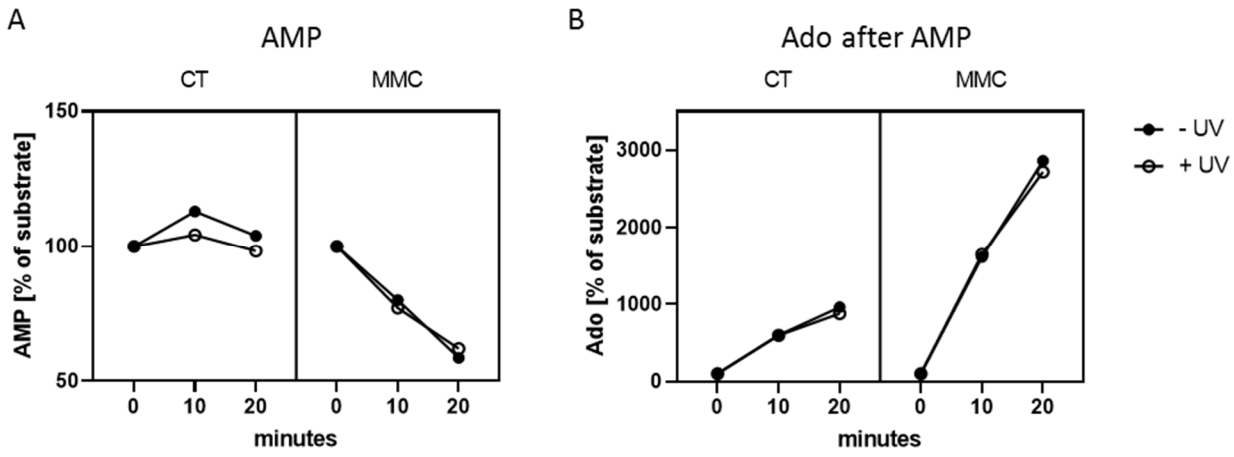

Figure 3.43 Change in the extracellular level of AMP (A) and adenosine (B) in CT and MMC cells upon incubation with 20 µM AMP. Analyte levels in the medium were measured by UPLC after irradiation with 10 J/cm² UVA or sham treatment and subsequent incubation with AMP as substrate for 0, 10 or 20 minutes. Levels are given in % of the initial substrate. N = 1.

Figure 3.43 shows the direct conversion of 20 µM AMP to adenosine in CT and MMC cells with and without irradiation. AMP is quickly degraded by enzymes of MMC cells, while levels remain around the substrate concentration in CT cells, with no further effect of irradiation (A). Accordingly, adenosine levels in medium of MMC cells rise quickly to approximately 30-fold of the basal level (B). The increase in CT cells is 10-fold to the basal substrate concentration. Low-dose UVA radiation has no influence on the extracellular formation of adenosine in this setting.

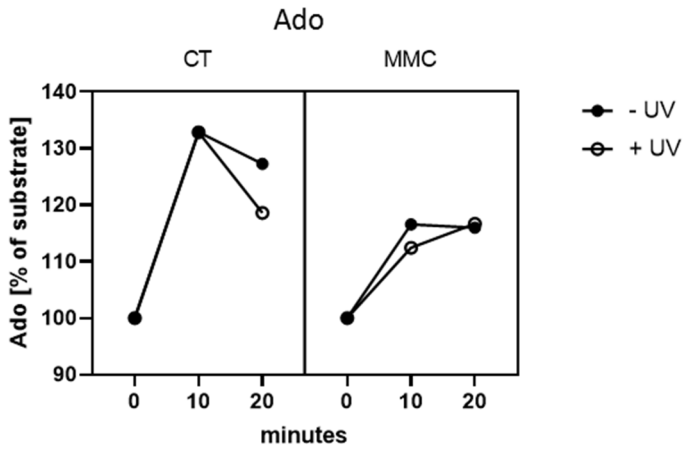

Figure 3.44 Change in the extracellular level of adenosine in CT and MMC cells upon incubation with 2 µM adenosine. Analyte levels in the medium were measured by UPLC after irradiation with 10 J/cm^2 UVA or sham treatment and subsequent incubation with adenosine as substrate for 0, 10 or 20 minutes. Levels are given in % of the initial substrate. N = 1.

The alterations in adenosine levels after addition of 2 µM adenosine to CT and MMC cells are shown in Figure 3.44. In the first 10 minutes after irradiation, adenosine levels are rising in the medium of both cell types. After 20 minutes, the increase in Ado levels has slowed down (MMC), or the levels decreased (CT), but are still higher than the initial substrate concentration, indicating a higher rate of formation of adenosine compared to its degradation. Irradiation with a low dose of UVA has only marginal effects on Ado levels in the first 20 minutes after exposure.

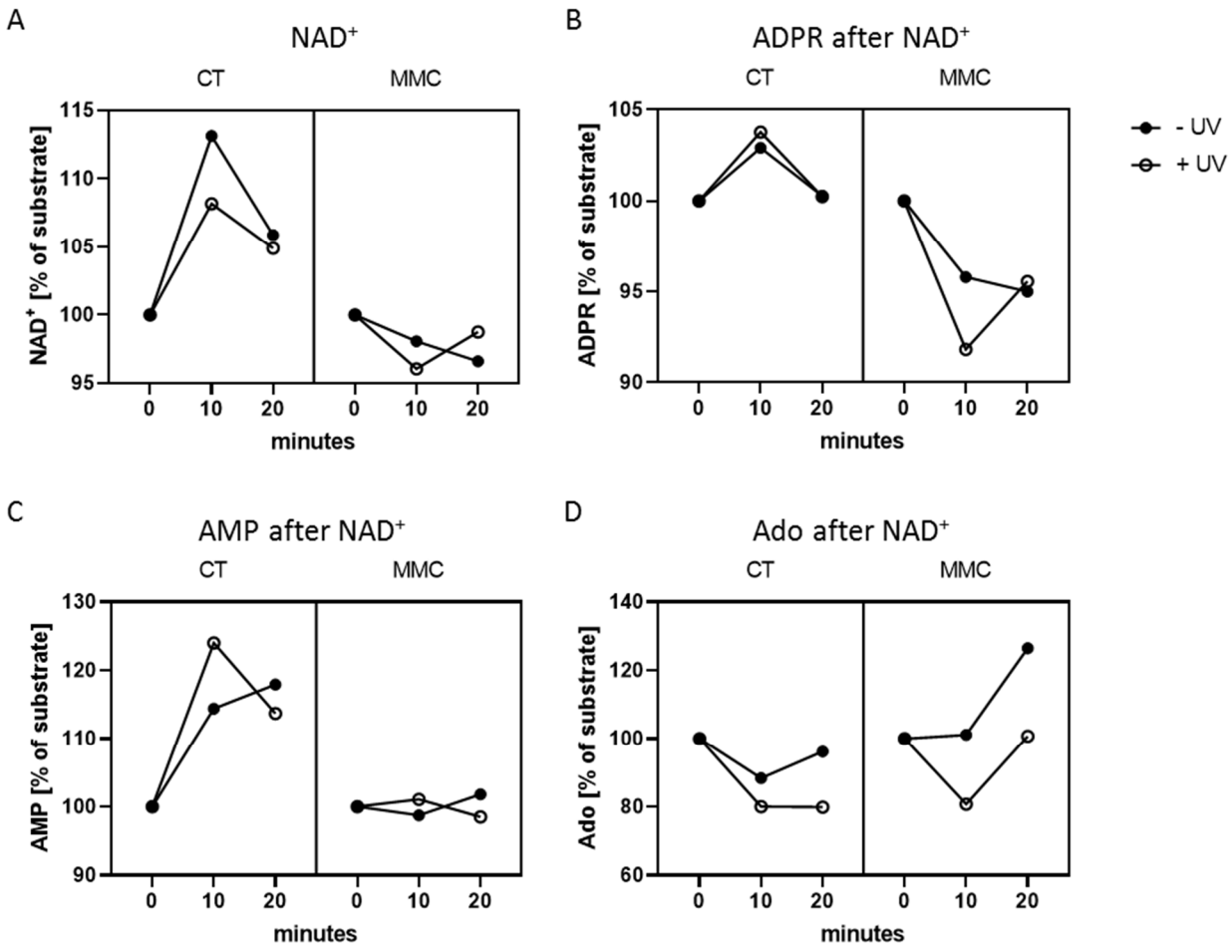

Figure 3.45 Change in extracellular levels of NAD⁺ (A), ADPR (B), AMP (C) and adenosine (D) in CT and MMC cells upon incubation with 2 µM NAD⁺. Analyte levels in the medium of cells were measured by UPLC after irradiation with 10 J/cm² UVA or sham treatment and subsequent incubation with NAD⁺ as substrate for 0, 10 or 20 minutes. Levels are given in % of the initial substrate. N = 1.

Alterations in the levels of extracellular NAD⁺ and metabolites after addition of 2 µM NAD⁺ are shown in Figure 3.45. NAD⁺ levels rise above the initial concentration of the added substrate in CT cells, whereas the levels are slightly below the initial concentration in MMC cells (A). Since ADPR is derived from NAD⁺, ADPR levels show similar behaviour (B). AMP increases in CT cells, while no change appears in MMC cells (C). In comparison to the initial substrate level, the levels of adenosine in CT cells are slightly lower, while the levels in MMC cells are higher after 20 minutes of incubation (D). Collectively, these data indicate a higher engagement of the NAD⁺/AMP/ado axis in MMC cells. Irradiation has a decreasing effect on analyte levels in the medium.

As previously shown (Figure 3.41), the expression of CD73 was dramatically increased in MMC compared to NHDF and CT cells. Elevated protein levels are accompanied by an increased conversion of AMP to adenosine (Figure 3.43) and increased flux along the ATP/AMP/Ado (Figure 3.42) and NAD^+/AMP/Ado axis (Figure 3.45). The data indicates an increased cleavage of AMP to adenosine in MMC cells. Adenosine is an important molecule in purinergic signalling and has been shown to exert pro-tumoral and pro-invasive functions[182]. An indirect assay to determine a possible role for adenosine from MMC cells in cancer cell invasion was performed. To investigate biological effects of the increased level of CD73 and adenosine from MMC cells, an invasion assay with conditioned medium from MMC or CT cells was established.

3.20 Effect of conditioned media from control and aged fibroblasts on tumor cell invasion

The effect of secreted cytokines, chemokines and other substances involved in paracrine signalling can be investigated by use of an invasion assay. Medium containing the secreted substances from CT and MMC cells (conditioned medium) was collected and used as a possible chemoattractant in a semipermeable system. The invasion of cancer cells into the conditioned media can be measured by counting of the number of invading cells through a basement layer-resembling matrix on a membrane. SCL-1 cutaneous squamous cell carcinoma cells were used, as this cancer type is frequently used in studies on UV radiation and cancer and because it is especially prone to UVA-induced mutations[77].

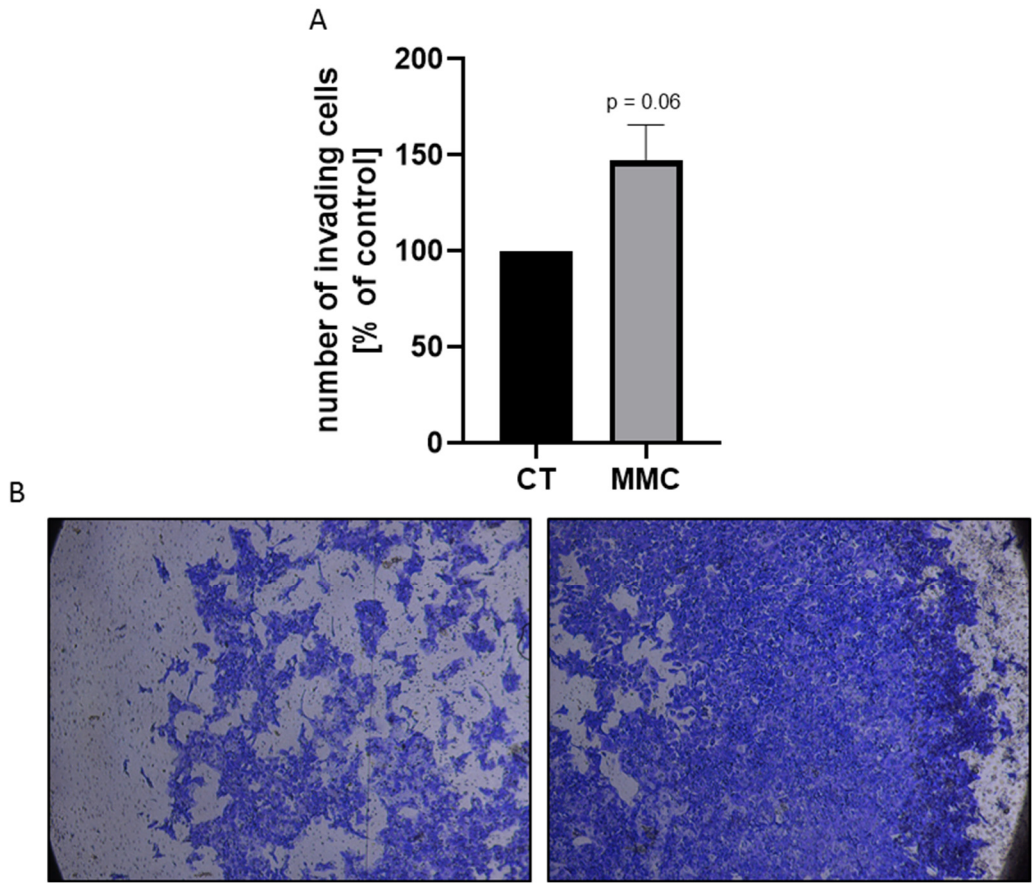

Figure 3.46 Invasion of SCL-1 cancer cells into conditioned medium from CT or MMC cells. Invading cells were counted under an inverted microscope with 10 x magnification (B) and are given as % to the number of invading cells into CT medium (A). Data represent means ± SEM. An unpaired t-test was performed to the control.

Figure 3.46 shows invasion of cutaneous squamous cell carcinoma cells (SCL-1) through a matrix resembling a basal membrane of the skin. As can be seen by microscopy (B), the number of invading cells into the conditioned medium from MMC cells was higher than invading cell numbers in CT conditioned medium (A). Although not statistically significant, the preference of SCL-1 cells to invade into medium derived from MMC cells was evident in all three independent experiments.

3.21 Photoprotective effects of flavones on aged fibroblasts

As a concluding experiment, the photoprotective capacity of the selected flavones luteolin, tricetin, nobiletin and tangeretin was tested in the established aging model. As performed with NHDF (see Figure 3.21), the MTT viability assay was used to determine endogenous or exogenous protective effects of the selected flavones on irradiated MMC cells (see method 2.15.3). Cells were either incubated with the respective flavone to test their effect on cell viability (sham), or cells were incubated with the flavones and then irradiated in flavone-free HBSS to test for endogenous phototoxicity (preinc. + UV). The third treatment included incubation with the flavones and irradiation in flavone containing HBSS (preinc. + UV with substance) to test for possible exogenous photoprotection properties.

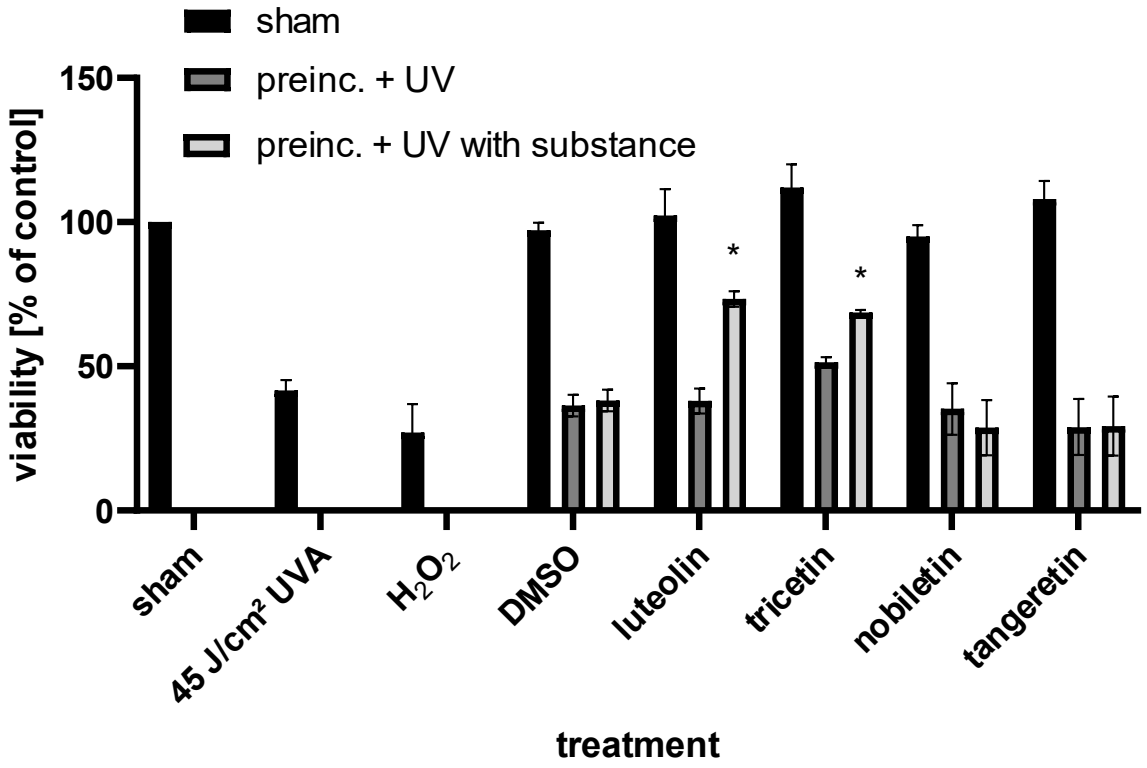

*Figure 3.47 Viability of MMC cells after preincubation with flavones and irradiation with 45 J/cm² UVA. Cells were preincubated with 50 µM of each flavone and irradiated with 45 J/cm² UVA in the absence or presence of flavones in the medium. Viability of unirradiated fibroblasts (sham) was set as 100 %. 2 mM H_2O_2 and DMSO were used as positive and negative controls, respectively. Data represent means ± SEM. One-way Anova with Dunnett's multiple comparison to the 45 J/cm² UVA control was performed without including sham. *p < 0.05, **p < 0.01, ***p < 0.001.*

Figure 3.47 shows effects of the selected flavones on cell viability with or without irradiation with a high dose of UVA. In MMC cells, preincubation with any of the flavones in the absence of UV radiation does not affect viability (sham). Upon irradiation, cell viability decreases to around 50 %, which is not rescued by preincubation of the cells with luteolin, nobiletin or tangeretin (preinc. + UV). Preincubation with tricetin shows a small protective effect. The presence of luteolin and tricetin during irradiation significantly prevents cell death after a toxic dose of UVA (preinc. + UV with substance). Nobiletin and tangeretin further decrease cell viability upon irradiation.

In conclusion, photoprotective effects of luteolin and tricetin are based on their absorbing properties and are therefore independent of the recipient cell. Conditions that influence endogenous sunscreen efficacy, e.g. cell type and age, are irrelevant for topical sunscreen agents. Hence, luteolin and tricetin are effective photoprotective compounds in normal und artificially aged fibroblasts.

4 Discussion

UVA radiation was long proposed to be the minor damaging type of UV radiation and only few studies on its effects on human skin compared to UVB radiation have been performed. Over time, some aspects of damaging UVA radiation were discovered, e.g. its contribution to cytotoxicity in keratinocytes[24]. In this early study, it was found that UVA radiation contributes to cytotoxicity even when the sun is at zenith and the maximal UVB radiation is reached. Additionally, this study predicted that UVA might play the major role in cytotoxicity at earlier and later times of the day. Nowadays, the damage profile of UVA radiation on human skin has been studied to a higher extent, revealing its DNA damaging, lipid oxidating and ROS generating properties. However, damaging effects of realistic doses that can be achieved by everyday life are still only marginally investigated. Furthermore, proper protection from UVA radiation in aged skin is seldomly discussed, consequently leading to a lack of information on photoprotection in the elderly.

A leading cause of death in the elderly is cancer, with skin cancer being among the most common[75,183]. UV radiation is a prime carcinogen and described as the main cause of skin cancers[75]. Since the population with old age is exceeding the younger population, it should be considered, that sunscreens or other prevention strategies need to be developed mainly for aged skin. In most studies, this aspect is scarcely included in the experimental setup. Here, differences between normal and aged fibroblasts in regard to UVA radiation and the use of flavones for photoprotection were studied.

4.1 Luteolin and tricetin show promising features for use in photoprotection

Flavonoids are plant secondary metabolites with a variety of functions. Their biosynthesis in plants is upregulated in response to UV radiation, highlighting their role in photoprotection[104]. Especially those flavonoids with antioxidant properties, e.g. a catechol structure, are then synthesized, together with those flavonoids that absorb in the UV range[33]. Here, flavonoids belonging to the subgroup of flavones were investigated, that display different structural features, e.g. a catechol moiety or methoxylation of the -OH groups.

After the selection of two polyhydroxylated and two polymethoxylated flavones as possible photoprotecting compounds, they were evaluated for their efficacy using different endpoints related to UVA radiation. Luteolin and tricetin were chosen due to their absorbance in the

UVA region and their possible utility as antioxidants. Nobiletin and tangeretin were chosen to evaluate the effect of methoxy groups instead of hydroxy groups on the selected parameters. Luteolin and tricetin showed an absorbance peak at around 350 nm in phosphate buffer (Figure 3.3). The peak of absorbance was at around 330 nm for nobiletin and tangeretin. All compounds except tricetin were stable in phosphate buffer. In methanol, all compounds were stable over 24 hours (Figure 3.4). In starvation medium, which was used for cell studies, the flavones were less stable (Figure 3.5). Only nobiletin was recovered in the concentration prepared for HPLC determination up to 24 hours. Luteolin was stable up to 5 hours. Tangeretin was not recovered since only about 4 µM were detected by HPLC while 10 µM were applied but it was stable for 24 hours. Tricetin was not stably recovered in medium. Initially, only 5 of 10 µM were recovered by HPLC. Tricetin was not detectable after two hours, indicating a rapid degradation of the compound.

Although the uptake into NHDF was considerably different between compounds, all were taken up after a two-hour incubation time (Figure 3.6). Polymethoxylated flavones are anticipated to be taken up by the cell more effectively compared to polyhydroxylated flavones due to their hydrophobic nature. The uptake data does only partly reflect the structure-based predictions. The uptake data showed: tangeretin > tricetin > luteolin > nobiletin.

Effects of the flavones on cell viability were tested via MTT assay (Figure 3.7). None of the compounds affected cell viability after two or 24 hours of incubation at various concentrations. Thus, they are non-toxic in the present settings.

Since the compounds are intended for photoprotective purposes, their photostability upon irradiation with increasing UVA doses was studied. Complete photostability in phosphate buffer was only shown for luteolin and less for the other flavones (Figure 3.8). In liposomes however, luteolin and tricetin were both stable. The main absorbing peak in the UVA area was decreased in nobiletin and tangeretin containing liposomes (Figure 3.9). It can be deduced, that for a formulation resembling a sunscreen, luteolin and tricetin provide good photostability while nobiletin and tangeretin are not suitable. Upon examination of the liposomal supernatant, nobiletin showed an increasing peak in the lower wavelength region of the UV spectrum after irradiation (Figure 3.10). This suggests a UV-dependent decomposition of the parent compound. Several studies have reported that commercially available sunscreens are often photoinstable, especially after UVA exposure[184,185].

Photoinstability decreases the efficacy of the sunscreen and therefore increases the risk for UV-induced deleterious effects on skin cells. Additionally, there might be undesired side effects of decomposition products of the parent compound.

Taking together all obtained data on photostability, toxicity and absorbance, the basic requirements for a photoprotecting compound are best provided by luteolin, but tricetin might also be considered. Nobiletin and tangeretin are less suitable compounds for photoprotection.

Antioxidant properties of the flavones were determined by analysing MDA by means of HPLC in a liposomal suspension prepared from PC (Figure 3.12). The prevention of UVA-induced MDA formation by the compounds was analysed as a parameter for antioxidative activity towards lipid oxidation. Also, egg yolk derived liposomes were tested, but did not yield expected increases in MDA, likely due to their high carotenoid content which interferes with the initiation of oxidation. In the PC model system, luteolin showed higher antioxidative capacity than the positive control α-tocopherol at all doses. On the contrary, nobiletin highly increased MDA formation, although exclusively upon irradiation. Since nobiletin increased lipid oxidation only in combinatorial treatment with UV radiation, the parent compound itself has no effect on MDA formation in the given setting. This suggest a pro-oxidative function of the nobiletin decomposition product, that was already detected in the liposomal supernatants (Figure 3.10).

A low dose of UVA was chosen to evaluate the antioxidant properties of the flavones in a cellular system (Figure 3.14). No compound itself increased MDA levels in NHDF in the given setting. Upon UVA exposure, increased MDA levels were measured. MDA formation in NHDF induced by UVA exposure could only be prevented by preincubation with tricetin. On the contrary, upon incubation with tangeretin, MDA levels in irradiated NHDF increased around 4-fold to the control, suggesting a role of tangeretin in lipid peroxidation. Since there is no effect on lipid oxidation without irradiation, tangeretin is unlikely to show lipid peroxidation initiation function, but a propagating role can be discussed. However, as with nobiletin in the PC model system, a decomposition product after irradiation might also be responsible for the oxidation of lipids. Nobiletin increased MDA levels in liposomes but not in NHDF. Luteolin decreased MDA levels to the basal unirradiated level in liposomes, but not in NHDF. Of note, the concentrations used in the assays differed. In liposomes, 100 µM of the compound were

used, whereas only 50 µM were used in cell culture experiments. The difference in concentration and in the test system could be the reason for inconsistent results.

The polymethoxylated flavones used here increased lipid peroxidation either in the liposomal or the cellular test system. Inconsistency between the systems can be caused by the test systems themselves or by the low-dose irradiation regimen, that might sometimes provide significant results and sometimes does not exceed the threshold for significance. The polyhydroxylated compounds showed antioxidative capacity either in the liposomal or the cellular system, probably caused by the reasons stated above.

To investigate, whether the compounds themselves increased ROS levels in NHDF by acting as prooxidants, a H_2DCF-DA assay was performed. The flavones were either directly added before measurement or the cells were preincubated with the flavones for two hours, followed by subsequent removal of the flavones. Only direct addition of tricetin to the medium prior to the assay provided a minor decrease in ROS generation (Figure 3.16). Since the compounds are to be used in photoprotection, ROS levels in NHDF were measured with and without flavones present in the irradiation medium. Compared to the solvent control, the flavones did not alter ROS levels with or without irradiation (Figure 3.17, Figure 3.18). Since the ROS levels were unaltered after irradiation with either of the flavones, the increased lipid oxidation might depend on ROS that are not detectable in the H_2DCF-DA assay, e.g. superoxide[152].

The flavones were tested for the ability to react with thiols, in order to predict a possible role in antioxidant defence signalling, e.g. with Nrf2. Since flavones are completely unsaturated and exhibit an α, β-unsaturated carbonyl, they might show reactivity towards thiols[33]. However, none of the flavones displayed a change in absorbance spectra upon incubation with 2-ME as observed with the positive control cardamonin (Figure 3.19). The decrease in absorbance seen in tricetin samples is likely to be caused by its instability in phosphate buffer.

To investigate, whether the flavones have a direct effect on expression of the antioxidant protein HO-1, which is under control of the Nrf2-Keap1 signalling pathway, NHDF were preincubated with the compounds before irradiation (Figure 3.20). Incubation with luteolin, tricetin and nobiletin did not alter the HO-1 response to UVA, but tangeretin preincubation completely abrogated the HO-1 signal. To date, no studies on tangeretin and HO-1 in response to UVA radiation are available. Interestingly, the two polymethoxylated flavones reacted quite differently, suggesting that the slight alterations in substitutions would have a role in their

effect on HO-1 expression. Alternatively, they might specifically trigger other signalling pathways that trigger a Nrf2-Keap1 response.

In regard to UV-induced DNA damage, luteolin and tricetin showed protective effects (Figure 3.34). By use of the CPD ELISA, the initial level of damage compared to an irradiated control was decreased in fibroblasts that were incubated with the flavones. It might be caused by the decreased initial CPD damage that there is no direct repair visible in the first 1.5 hours in samples with luteolin and tricetin. The fewer initial damage might be below a threshold for DNA damage repair initiation or might only induce a slower initiation of repair. The two flavones protected the cells from UVA-induced formation of CPDs via an endogenous mechanism, since they were not present in the irradiation medium. The photoprotection might therefore extend from absorption of photons to intracellular mechanisms, which remain elusive in this thesis.

Finally, the flavones were tested for their photoprotective effect by use of an MTT assay (Figure 3.21). A toxic dose was employed to identify possible protective effects of the flavones. Indeed, the presence of luteolin and tricetin in the medium during irradiation provided protection as seen by an increased cell viability. On the contrary, tangeretin and nobiletin exerted phototoxic effects, as seen by an even stronger decrease of viability compared to the irradiation with 45 J/cm² UVA. Preincubation with tangeretin showed phototoxic effects even when the flavone was removed before irradiation, suggesting an endogenous mechanism. Since the compounds did not change the ROS levels in NHDF upon irradiation (Figure 3.17), the phototoxicity has to be mediated ROS-independently, through direct interaction of a possible degradation product of the parent compound with cellular structures, or via ROS that are not detectable via H_2DCF-DA assay. As seen in Figure 3.14, tangeretin induced lipid oxidation upon irradiation but not on itself. It is therefore likely that upon uptake and irradiation, a decomposition product as seen for nobiletin is responsible for endogenous phototoxicity via interaction with intracellular macromolecules, e.g. lipids.

Assuming tangeretin shows a similar absorbance spectrum in liposomal supernatant after irradiation as nobiletin - the only structural difference of the parent compounds is a second methoxy group on the B ring in nobiletin - the decomposition product might show similar alterations (Figure 3.10). Since the decomposition product of nobiletin shows absorbance in

the lower wavelength region compared to the parent compound (340 nm → 260 nm), it might have lost the integrity of the conjugated π electron system.

Luteolin and tricetin are non-toxic, photostable in liposomal suspensions, show no reactivity towards thiols and do not alter ROS levels or HO-1 expression. Additionally, they were able to decrease CPD formation in NHDF. Luteolin and tricetin proved useful in regard to photoprotection, possibly via absorption of photons in the UVA wavelength region, but also via intracellular, yet unknown mechanisms. Hence, they are promising candidates for use in further photoprotection studies.

4.2 The DIAS aging model of cellular senescence

The aging model established here was adapted from the literature and was verified by the use of suitable biomarkers[167]. It provides a drug-induced accelerated senescence (DIAS) model, that allows aging of fibroblasts in a fraction of the time needed for replicative senescence. The treated cells, named MMC cells due to the treatment with mitomycin c, developed an aging-related phenotype 5 days after treatment. Two types of control cells were included in the experiments: control cells (CT) that were simultaneously treated with the solvent DMSO and untreated NHDF. MMC cells increased in size as studied by microscope (Figure 3.23) and flow cytometry (Figure 3.24). These cells also stained positive for the senescence-associated ß-galactosidase (Figure 3.25), unlike CT cells or NHDF. MMC cells proved to be unresponsive to FCS, a proliferative stimulus (Figure 3.24), which was not found for CT cells and NHDF. In contrast, NHDF and CT cells displayed increased proliferation upon FCS stimulation. The artificial aging model was used to determine differences between young and aged fibroblasts and their responses to UVA irradiation.

4.3 Metabolic differences in young and aged fibroblasts

The process of aging imposes profound alterations on cellular morphology and function. As the powerhouse of the cell, mitochondria are essential for cell survival and optimal functionality and are often involved in those alterations[186]. Changes in mitochondrial respiration are often linked to pathologies, such as Alzheimer's disease, which is also correlated to aging[187].

Several studies have investigated the effects of aging on mitochondrial respiration. Depending on the cell type and aging model, results varied. It is commonly believed that mitochondrial

dysfunction is a prerequisite and marker of cellular and organismal aging, leading to an accumulation of damaged macromolecules, mitochondrial DNA (mtDNA) mutations and ROS, all of which further increases mitochondrial dysfunction. However, not all studies confirmed mitochondrial dysfunction with age. Goldstein et al. investigated the energy metabolism in aging fibroblasts and did not observe differences in ATP levels or respiration rates between young and aged cells[188]. They further observed that aged fibroblasts are viable for several month after loss of monolayer formation functionality. The same observation was made during this thesis. MMC cells that were left under normal culture conditions for two months without further medium exchange never reached confluence but were still viable, whereas CT cells reached confluence and died earlier (data not shown).

In depth studies of the mitochondrial respiration made great progress by implementation of semi-automated assays as the Seahorse energetic flux analyzer, which was used in this thesis. Measurement of the real-time flux in oxygen and proton levels in the medium of cells under different stresses allows for the distinction between contributions of the different ETC complexes to the oxygen consumption rate (OCR). According to the data from this thesis, metabolism as determined by the OCR in young and aged fibroblasts differs in response to certain mitochondrial toxins.

The first measurements in the Seahorse flux analyzer are performed in the absence of mitochondrial toxins to determine the basal oxygen consumption. Basal respiration was unaltered in MMC cells compared to control cells, suggesting similar energy demand under unstressed conditions.

Injection of the complex V inhibitor oligomycin decreases the OCR and reveals the amount of respiration for energy maintenance by ATP production. ATP production under basal conditions was not changed in MMC compared to NHDF and CT cells (see Figure 3.39). The remaining oxygen consumption after oligomycin injection subtracted from the non-mitochondrial respiration yields a value for the so-called proton leak. Protons can evade further gradient formation by leaking through the mitochondrial inner membrane or by shuttling through the ATP synthase. A leak independent of ATP synthesis is considered an indication for decreased mitochondrial membrane integrity or an impaired regulation of ATP synthesis. The proton leak in unirradiated MMC cells was significantly increased in comparison to both NHDF and CT cells (see Figure 3.39). The proton leak might therefor be an indicator of decreased membrane

integrity, e.g. through lipid peroxidation, probably induced via increased ROS levels (Figure 3.36). The elevated proton leak in aged fibroblasts as seen here has also been observed in a study on heart mitochondria from aged mice and might therefore be a general marker for aged mitochondria under careful consideration with other parameters[189].

The injection of rotenone and antimycin a blocks the electron transfer of the ETC, as it inhibits complex I and III. The remaining oxygen consumption is driven by extramitochondrial oxidases and assigned as non-mitochondrial respiration[190]. Non-mitochondrial respiration was increased in MMC cells. One example of a non-mitochondrial oxidase is xanthine oxidase, which is involved in the oxidation of the adenosine degradation product hypoxanthine. Other examples are the cytochrome P450 enzymes or NADPH oxidases. The increased non-mitochondrial respiration in artificially aged cells might be caused by increased activity of one or several of those oxidases. In combination with the achieved data on elevated adenosine levels in aged fibroblasts as discussed below (4.5), this might suggest increased activity of the xanthine oxidase due to increased substrate availability. Indeed, xanthine oxidase expression and activity was shown to be increased in aged mice[191].

Glycolysis, as seen by the rate of extracellular acidification (ECAR), increases upon inhibition of the ETC by oligomycin, rotenone and antimycin a, probably as a compensatory mechanism to ensure ATP supply[192]. However, there are no differences between cell types (Figure 3.37).

The major difference between MMC and control cells was observed in the maximal respiration after uncoupling with FCCP (see Figure 3.37) and hence in the spare respiratory capacity (maximal - basal respiration). The capacity of MMC cells to increase mitochondrial respiration during high energy demand is greater than in control cells, indicating a possible increase in the rate of amino acid, lipid or carbohydrate oxidation. Since the basal respiration is unaltered, the cell might have advanced access to other substrates for oxidation in times of high energy demand compared to control cells. This might have implications for the cells response to stresses, since DNA repair and other responses require additional energy in form of ATP. Furthermore, the data indicates, that NHDF respire close to their theoretical maximum, whereas MMC cells still have additional respiratory capacity.

The data obtained in this thesis suggest, that MMC cells might have increased capacity to respond to stresses. Although unexpected, the increased maximal respiration of MMC cells

observed in this thesis has been reported in other studies, together with several studies observing mitochondrial respiration unfit for the mitochondrial dysfunction theory of aging.

The same OCR profile as shown in this thesis has been shown in a study using fibroblast-like cells. Takebayashi et al. have shown an increased maximal respiration in IMR-90 cells that have reached their replicative senescence in comparison to proliferating cells, while all other parameters (ATP production, basal respiration) were sustained[193]. In this study, an oncogene-induced senescence (OIS) model has been used, as well. The OIS model showed an increase in basal and maximal respiration compared to proliferating cells. They postulate, that senescent cells used the increased respiration to induce oxidation of fatty acids in order to sustain the SASP[193]. Another study by Kaplon et al. used OIS fibroblasts to show an increased oxygen consumption rate compared to proliferating fibroblasts[194]. In a model of doxorubicin-induced senescence, OCR was increased, as well as in replicative senescent fibroblasts, both in a study from Wang et al[195]. Lung and cardiac fibroblasts have been described with mitochondrial hyperactivity regarding all parameters of the ETC, e.g. ATP production, basal and maximal respiration[196]. In a study on temozolomide-induced senescent melanoma cells, mitochondrial respiration was increased compared to non-senescent cells[197]. Basal, ATP-dependent and non-mitochondrial respiration were increased, but the most dramatic increase was seen in the maximal respiration. Martinez et al. postulate that, although often described, mitochondrial dysfunction is not a characteristic feature of senescence[197]. Data from this thesis support this finding.

Quijano et al. observed an increase in basal respiration in a model of OIS fibroblasts that shows metabolic and bioenergetic changes different to those in replicative senescent cells, implicating that different aging models might exert differences in certain aspects[198]. Further, there are studies showing no effects of senescence on mitochondrial activity. In a model of senescent primary human mammary epithelial cells, Delfarah et al. did not find alterations in glucose uptake or lactate excretion[199].

The diversity of reported effects of senescence on mitochondrial respiration highlights the need for further investigations with increased depth, e.g. by use of further advantages of metabolic flux analyses studying the involvement of fatty acid metabolism, TCA cycle contribution and other pathways. In conclusion, the anticipated mitochondrial dysfunction is contradicted in many studies covering cellular senescence and metabolism. Studies on

metabolism in aging should be interpreted with caution and cannot be extrapolated from one cell type to another. The DIAS aging model used in this thesis is therefore a suitable but not universally accepted model system.

4.4 Investigation on the effects of low-dose UVA on young and aged fibroblasts

To evaluate the effects of low doses of UVA radiation on NHDF and MMC cells, different doses were tested to obtain a dose non-toxic over the time course of at least 24 hours. Doses from 5 to 20 J/cm² UVA did not alter cell viability directly after irradiation as measured by the MTT assay (Figure 3.1). An increased viability, which might be interpreted as an increased proliferative capacity, was observed 24 hours after irradiation. This proliferative burst has also been shown in studies with mouse skin[200]. The increase in proliferation is part of the skins response to UV radiation and causes hyperplasia of the epidermis as a protective measure and to replace apoptotic keratinocytes[201]. It might be possible that also the dermis reacts with hyperplasia under exposure of low doses of UVA radiation. In the present study, an irradiation dose of 45 J/cm² UVA directly decreased cell viability below 50 % of unirradiated controls. After 24 hours, cell viability was further decreased, indicating non-reversible cell damage. In the experiments on UV sensitivity in CT and MMC cells, similar results were achieved for 10 and 45 J/cm² UVA (Figure 3.26). However, the use of 30 and 38 J/cm² UVA revealed that the approximate threshold for direct UVA-induced cytotoxicity is situated around a dose of 30 J/cm². This dose already reduces cell viability 24 hours after irradiation. Furthermore, these experiments revealed, that MMC cells appear less sensitive to UVA radiation compared to CT cells, as seen by a delayed decrease in viability.

For further studies, 10 J/cm² UVA were chosen as a comparable physiological dose, since this is achievable by daily human life. Wenczl et al. for example estimated a dose of 14 to 18 J/cm² UVA when exposed to summer sun for one hour[202].

Low-dose UVA radiation, although not decreasing viability, has been shown to induce damage to macromolecules as indicated by the experiments conducted during this thesis. Irradiation of NHDF with 10 J/cm² UVA resulted in increased levels of MDA, one of the end products of lipid peroxidation (see Figure 3.14). A similar increase in lipid peroxidation as shown here was shown by Marionnet et al. via another marker, 8-isoprostane[25]. They described the induction of a lipid oxidation chain reaction via UVA-induced ROS in reconstructed skin and in cell

culture[25]. In this thesis, ROS measured via H_2DCF-DA assay were elevated at low doses of UVA radiation showing a dose-dependent increase.

HO-1 is an (oxidative) stress-inducible isoform of the heme oxygenases, which degrade heme. The breakdown products of heme, bilirubin and biliverdin, exert antioxidant functions by a redox cycling process from bilirubin to biliverdin and recycling back via activity of the biliverdin reductase[203]. HO-1 is thus often stated to be cytoprotective[175]. HO-1 upregulation and subsequent heme release is described to act anti-inflammatory[83]. In this thesis, increased HO-1 expression upon low-dose UVA irradiation has been observed in NHDF (Figure 3.20). The expression pattern is similar for CT and MMC cells and displays a peak at 6 hours post-UV (Figure 3.35). This is in accordance with studies on HMOX1 gene upregulation in fibroblasts of reconstructed skin in response to irradiation with slightly higher doses of UVA[25].

As the time course for the HO-1 expression has been shown to be unaltered between cell types in response to UVA radiation, a time course for DNA damage was investigated. Upon DNA damaging insults of various sources, the histone H2AX is phosphorylated at serine 139 (γ-H2AX). It is dephosphorylated quickly afterwards, which signals DNA repair complex assembly[204]. γ-H2AX measurement is often used as a marker for double strand breaks, although it has been found in UVA-irradiated mice to be a marker for oxidative damage and ss breaks[205]. Additionally, a role of H2AX phosphorylation in NER is discussed[206]. Literature on UVA-induced γ-H2AX is scarce. Single UVA treatment and subsequent measurement of H2AX phosphorylation has been conducted with doses too low (< 3 J/cm²) to obtain signals[207]. Wischermann et al. showed that γ-H2AX foci in keratinocytes after irradiation with 10 J/cm² UVA are very similar to unirradiated controls[35]. The low-dose regime is expected to only yield marginal damage, which might explain difficulties in interpreting results. Here, γ-H2AX protein levels have been measured by immunoblotting and were found to increase in responses to low-dose UVA radiation in NHDF, CT and MMC cells (Figure 3.28). The time course shows a peak at two hours post-UV in all three cell types, although there was a second peak at 24 hours post-UV in MMC cells. Irrespective of DNA double or single strand break detection or NER activity, there might be a difference in DNA damage resolution in MMC cells compared to control cells. The results should be interpreted with caution due to high standard errors. Since the levels of γ-H2AX in response to UVA have been reported to be critically low in the

literature, as well, another marker for DNA damage or repair should be used to validate the results.

Although direct DNA strand breaks have not been investigated in this thesis due to the low dose regimen, the major UV-induced lesion, the CPD, has been evaluated. Two approaches, namely ELISA and Comet assay, have been used to detect the formation of CPDs. The modified Comet assay coupled with repair enzyme treatment specific for CPDs was performed in this thesis. The modified Comet assay displays CPD formation on a single-cell basis, but the results are accompanied by relatively high standard errors due to the lengthy procedure prone to slight differences in handling. By measuring the levels of CPD from 0 to 5 hours after irradiation with 10 J/cm² UVA, the expected repair after the initial damage formation was followed by a second peak in CPD lesions three hours post-UV (Figure 3.29). Due to the high standard errors, a second approach was performed to confirm the finding. By ELISA with a specific antibody for CPDs, the levels of CPDs were measured over a time course of 6 hours (Figure 3.30). The initial amount of CPDs was decreased in the first hour after irradiation but was followed by a second increase in CPDs two hours post-UV. Both assays showed the formation of delayed CPDs after UV exposure has already ended, indicative of lesion formation in the dark. This phenomenon has just recently been described in melanocytes, leading to the postulation of a chemiexcitation theory. Premi et al. described, that a chemiexcitation process in the dark can generate energy similar to that of a photon and consequently induce CPD lesion without direct exposure of cells to radiation. They postulate, that the formation of “dark” CPD in melanocytes occurs via interaction of ROS with melanin, involving peroxynitrite and fragmentation of melanin. Further, translocation of the melanin fragments into the nucleus and reaction with peroxynitrite leads to the formation of a dioxetane and subsequent triplet energy transfer of excited carbonyls to DNA[208]. However, “dark” CPD have been postulated in keratinocytes two years later, indicating that melanin might not be essential for this process[209]. As a result, the delayed dimers observed in this thesis are the first indication for “dark” CPD formation in fibroblasts. There might be a common, yet unknown sensitizer, that is responsible for the delayed CPD formation in fibroblasts and keratinocytes that is independent of melanin.

In order to enhance the increase of CPDs observed with the CPD ELISA, repair inhibitors were used. Aphidicolin is an inhibitor of DNA polymerases α, δ and ε[180]. X80 inhibits the interaction of XPA with DNA[181]. Treatment of the irradiated cells with the inhibitors led to an increase of

the delayed CPD lesions at one hours post-UV. This treatment revealed that the “dark” CPD are formed to an extent above the initial damage level. This finding suggests that the delayed CPDs found in cells without repair inhibitors are covered by subsequent repair that occurs simultaneously and that actual CPD levels might be underestimated by the lesion-specific Comet assay without repair inhibition.

CPD measurement in MMC cells revealed no delayed peak in CPD formation as seen in NHDF (Figure 3.32). This might correlate with the increased ability of the aged fibroblasts to respond to high energy demand situations with an increase in respiration. The adaption to high ATP demand, for example through ongoing DNA repair, might be faster or more complete in MMC cells compared to NHDF. This might also coincide with the reduced sensitivity of MMC cells to UVA radiation (Figure 3.26). The lack of delayed CPD formation and decreased sensitivity in MMC cells might coincide with a lack in the suggested but yet unknown sensitizer responsible for melanin-independent dark CPD formation.

Summarizing the DNA damage data from this thesis, both assays displayed CPD formation in NHDF caused by low doses of UVA. Additionally, data on the phosphorylation of H2AX showed a peak at two hours post-UV, which is paralleled by the formation of delayed CPDs as measured by ELISA and Comet assay. Since the initial CPDs are not recognized in the γ-H2AX time course, as seen by a γ-H2AX level close to that of unirradiated cells, there might be an exclusive link between delayed CPDs and H2AX phosphorylation. This would suggest that delayed and initial CPDs are repaired differently. However, this theory is highly speculative and further studies have to be conducted. One experimental setup could consist of repair-inhibited NHDF and subsequent irradiation to measure the level of H2AX phosphorylation and hence the contribution of repair incisions to the H2AX phosphorylation.

Apart from DNA damage, UVA radiation has been shown to influence energy metabolism in young and artificially aged fibroblasts in this thesis. Real-time bioenergetic measurements have been conducted using the Seahorse flux analyzer. Independent of the cell type, low-dose UVA radiation decreased the basal and maximal respiration (Figure 3.38). The basal respiration covers all oxygen consuming processes in a cell and a decrease in basal respiration might therefor indicate an adaptive stress response. By injection of specific inhibitors, the cause for a decreased respiration can be elucidated. Here, the basal decrease in respiration is accompanied by a decrease in the maximal respiration. The reason could be a decreased

substrate supply, a decrease in mitochondrial mass or poor ETC integrity[190]. Furthermore, a decreased maximal respiration suggest some kind of mitochondrial dysfunction[210].

Low-dose UVA radiation also decreased ATP production in young and aged fibroblasts (Figure 3.39), which can represent a low ATP demand, poor substrate availability or a damaged ETC[190]. The proton leak was also decreased, giving rise to two theories: proton leak was decreased caused by an adaptive increase in the coupling efficiency to compensate for a possible loss of membrane or ETC integrity, or UVA radiation damaged mitochondria, their membranes and consequently their functionality in metabolism.

Since only a low dose of UVA was applied, only few parameters are significantly changed, while others show a clear tendency, e.g. the decrease in ATP production in NHDF (Figure 3.39).

4.5 Purinergic signalling in young and aged fibroblasts in response to low-dose UVA

Apart from intracellular alterations caused by low-dose UVA radiation, alterations were also observed regarding extracellular proteins and pathways. Fibroblasts play a significant role in intercellular purinergic signalling, especially in cancer progression, as cancer cells depend on the secretion of ECM proteins by fibroblasts for remodelling and vascularization purposes[211]. Additionally, specialized fibroblasts, called cancer-associated fibroblasts (CAFs), are known to provide an immunosuppressive tumor microenvironment[19]. In this thesis, the expression of the key cell surface proteins CD38, CD39 and CD73 involved in purinergic signalling was investigated (Figure 3.41). Upon irradiation with a low dose of UVA, NHDF and CT cells showed decreased expression of CD38 and CD73. Both enzymes are responsible for the degradation of NAD^+ to adenosine. CD39, the enzyme converting ATP to AMP, was not affected. In contrast, the expression of CD38 and CD39 was increased in MMC cells. CD73 levels were unaltered, although they were already profoundly higher in MMC cells compared to NHDF and CT cells. Taken together, young and artificially aged fibroblasts regulate the proteins on their cell surface differently in response to low doses of UVA. Functionally, the altered expression might result in an increased rate of adenosine production in MMC cells via both pathways, NAD^+ and ATP-dependent. For NHDF and CT cells, the altered expression of CD38 could lead to an increased extracellular availability of NAD^+, as it is metabolized to AMP to a lesser extent. NAD^+ is described as a danger signal, similar to ATP, and has pro-inflammatory function[212]. According to this data, NHDF might increase pathways that lead to pro-inflammatory signalling

in response to low-dose UVA radiation, while MMC cells might increase the flux of purinergic signalling metabolites towards an anti-inflammatory, immunosuppressive outcome.

According to the data achieved by FACS analysis, MMC cells might exhibit increased extracellular adenosine formation via an increased CD73 expression. To investigate, if the change in expression is accompanied by a change in substrate conversion, UPLC analyses were performed.

The rate of conversion from AMP to adenosine was directly measured by supplementing fibroblast cell cultures with the substrate AMP and sampling of the medium after 10 and 20 minutes. As suspected from the FACS analysis data, the increased expression of CD73 in MMC cells led to an increased conversion of AMP to adenosine (Figure 3.43). Adenosine levels after 20 minutes were 3-fold increased in MMC cells compared to CT cells. However, since AMP levels were unchanged in CT cells, but adenosine levels were elevated, another source for adenosine formation must be present. There was no effect of low-dose UVA radiation on the direct conversion of AMP to adenosine.

The conversion of ATP to ADP, AMP and adenosine by supplementing cells with ATP displays the same effect (Figure 3.42). Adenosine formation in MMC cells is faster and exceed the levels achieved in CT cells. This is accompanied by an increased ATP generation in CT cells compared to MMC cells, probably due to the higher flux of ATP to Ado in MMC cells.

In agreement with the flow cytometry data, elevated CDx expression levels are linked to an increased conversion of substrates to adenosine in MMC cells (Figure 3.42, Figure 3.43, Figure 3.45). However, the effect of UVA radiation on CDx expression is not mirrored in substrate conversions. It has to be noted, that the time of preparation for the FACS analysis was longer than for the UPLC experiments, possibly causing the effects to be less pronounced.

The final concentration (in % of the substrate) of adenosine formation between experiments cannot be compared, as the AMP substrate concentration was 10-fold higher than ATP concentration, which explains the factor of 10 between adenosine levels after AMP and ATP supplementation.

An increase in CD38 levels as found by FACS analysis (Figure 3.41) has been described in aging tissue, along with a decline in NAD^+ [213]. The NAD^+ decline has not been directly measured here, but a decreased NAD^+ level after supplementation has been observed (Figure 3.45).

In summary, the profound increase in CD73 expression in MMC cells compared to NHDF and CT cells was accompanied by an increased rate of adenosine formation. Here, it is shown for the first time that MMC cells express CD73 to such high extent. It should be investigated, if replicative senescent cells display the same CDx expression pattern. In a study on age-related changes in CDx mRNA levels, CD39 and CD73 mRNA levels were increased in aged subjects compared to young ones[214].

As adenosine is a known anti-inflammatory, immunosuppressive and pro-tumoral signalling agent, this would indicate that in aged tissues, CD73 might promote immunosuppression and therefore simplify cancer cell development[215]. To investigate this hypothesis, an assay to measure cancer cell invasion into conditioned media was performed.

The invasion assay allows the study of invasion of cancer cells, here SCL-1, into a medium conditioned by CT or MMC cells through an artificial matrix. It is usually designed to test chemoattractants, which are located in the lower of the two compartments, for their ability to promote cancer cell invasion. The preference of SCL-1 cells to invade into conditioned medium from MMC cells, measured by an increased number of cancer cells in the compartment harboring the medium of MMC cells, can be interpreted as an indirect evidence for the pro-invasive effect of adenosine (Figure 3.46). The result indicates a possible pro-tumoral effect of artificially aged fibroblasts mediated by elevated extracellular adenosine levels. Transferred into the aging context, purinergic signalling of aged fibroblasts might promote cancer development via establishment of a pro-tumoral environment. This effect is already known for cancer-associated fibroblasts[16]. Furthermore, a specific secretome called the senescence-associated secretory phenotype (SASP) is also known for cancer promotion in senescent cells[139]. These concepts are based on a modification of the tumor microenvironment, which shows some correlation to the data presented in this thesis. It is not known, if adenosine is the cancer promoting molecule in aged cells. It would be interesting to study whether adenosinergic signalling plays a role in the increased cancer incidence in the elderly.

To promote this hypothesis, further studies to establish a direct correlation between tumor promotion and adenosine in aged cells are recommended. The invasion assay can be used to directly measure the effect of pure adenosine supplementation in the lower compartment for its effect on invasion of cancer cells. In order to test the immunosuppressive and anti-

inflammatory effects of adenosine, the experimental design would have to include immune cells and would probably best be performed in a 3D skin model.

If and where the adenosinergic signalling acts is also a matter of suitable receptors. Adenosine receptors A1, A2A, A2B and A3 are responsible for signal transduction and are present on various cell types[11]. The A2A and A2B receptors are known to be involved in the immunosuppressive signalling of adenosine[215,216]. However, especially as A2B and A3 are low-affinity receptors, they might be involved in the high adenosine environment of MMC cells[11]. High concentrations of adenosine are also found in the tumor microenvironment, where adenosine receptors are expressed on tumor cells as well as on immune cells[215]. A contributing role for aged cells in the setup of tumor microenvironment might be possible.

As a hypothesis, aged fibroblasts in a surrounding with non-senescent fibroblasts and tumor, as well as immune cells, might convert ATP as danger signals from young fibroblasts into adenosine. Adenosine might act via paracrine signalling on adenosine receptors on immune cells and suppress the production of inflammatory cytokines. Furthermore, adenosine might activate A2A and A2B receptors present on cancer cells[215].

Adenosine is believed to mainly exerts its immunosuppressive function via inhibition of cytokine signalling and immune cell infiltration[216]. However, some of the substances from conditioned media of MMC cells, one of which is adenosine as seen by UPLC, have shown to increase cancer cell invasion independent of immune cell presence. Further experiments might enable to distinguish between direct effects on cancer cells and those on immune cells.

Inhibition of CD73 or A2A signalling has been shown to reduce tumor growth[216]. Therapy with an anti-CD73 antibody has shown efficacy against breast cancer cell growth and metastasis, while knockdown of CD73 promoted tumor growth and metastases in mice[217]. Furthermore, activation of A2B signalling increased cancer cell chemotaxis in vitro and metastasis in vivo[217]. Currently, several clinical trials investigate compounds that interfere with the adenosine pathway in cancer cells in concert with other cancer therapeutics or alone, highlighting its outstanding role in the cancerous environment[218].

Continuative experiments might also include pharmacological inhibitors of enzymes involved in purinergic signalling to elucidate the roles of single components. Additionally, the adenosine receptor expression can be studied by flow cytometry to determine cell types that

might respond to increased adenosine levels. By that measure, it can be determined if fibroblasts exert autocrine, paracrine or both signalling pathways.

4.6 Luteolin and tricetin provide topical photoprotection in young and aged fibroblasts

The selection and testing of the four flavones culminated in a viability assay that determines if the compounds are able to reverse the toxic effect of a high dose UVA irradiation. NHDF (Figure 3.21) or MMC cells (Figure 3.47) were preincubated with the flavones, and either irradiated in HBSS or in HBSS plus flavones. The preincubated cells were unable to revert the toxic effect of 45 J/cm² UVA, while the presence of luteolin and tricetin in the irradiation medium partly rescued the viability. These results indicate a topical photoprotection effect of luteolin and tricetin, which is likely caused by their absorbance in the UVA region. Luteolin and tricetin might therefore be beneficial ingredients in sunscreen regardless of recipient age, since the absorbing effect is mostly unaffected by the skin's physiology. The rescuing effect was not seen with nobiletin or tangeretin. Tangeretin even exerted phototoxicity, as the presence of the compound in the cells or in the medium decreased viability further. Tangeretin has shown some protective effects on UVB irradiated epidermal cells from mice in a study from Yoon et al.[128]. However, they did not test phototoxicity of tangeretin in this study, which is representative of several studies investigating protective substances without directly showing the effect of the compound on cell viability upon irradiation.

To test the flavones for their efficacy in photoprotection in a sunscreen like cream, a method from Brugé et al., in accordance with the COLIPA guidelines, was adopted[154]. Luteolin and tricetin were incorporated into a commercially available cream base to mimic their potential use in a sunscreen (Figure 3.22). The cream itself exerted some photoprotection because of its opaque nature, mainly due to the ingredient shea butter. Low concentrations (0.1 %) of luteolin and tricetin further increased the protective effect, although not significantly. However, there is still capacity for improvement of the assay, as sunscreen agents are commonly incorporated into a formulation up to 5 or even 10 %. Further experiments should investigate the effects of higher concentrations of luteolin and tricetin and of other cream bases with less absorbing carrier ingredients. In the current setting and with the cream base chosen, luteolin and tricetin might be promising as photoprotecting compounds in a cosmetic formulation like a day cream, which only requires a low sun protection factor. For use in a

sunscreen, other cream bases should be tested as well as the combination of luteolin and tricetin with other sunscreen agents to provide a high sun protection factor.

It has been published, that the addition of non-sunscreen antioxidants into sunscreens can increase protection[91]. The incorporation of luteolin or tricetin into sunscreen formulations might therefore provide additional benefits besides photoprotection, as they have shown to reduce lipid oxidation in liposomes.

5 Summary

The effects of UVA radiation on human health have long been anticipated to only induce photoaging and oxidative damage. Recently, studies have revealed more serious deleterious effects of UVA and established a link to cancer formation. However, most studies investigated effects of high doses of UVA exposure, which are unlikely to receive in everyday life. Here, low doses of UVA radiation were administered to skin fibroblasts to investigate the damaging effects on macromolecules and cellular signalling. Results indicate an UVA-dependent induction of oxidative stress as determined by lipid peroxidation and upregulation of hemeoxygenase-1, together with an impaired cellular respiration according to a decrease in basal and maximal respiration. Analysis of biomarkers for DNA damage show an UVA-dependent induction of H2AX phosphorylation and formation of direct and delayed cyclobutane pyrimidine dimers (CPDs). Furthermore, the expression of ectoenzymes essential in immune-relevant purinergic signalling was altered after irradiation. These data provide evidence for deleterious effects of low-dose UVA radiation on human skin fibroblasts.

Thus, photoprotection from such low-dose UVA-dependent insults is demanded in light of the evolving role of UVA in skin damage and cancer formation. Hence, plant secondary metabolites from the group of flavones were investigated for their efficacy to alleviate low-dose UVA-induced damage. Luteolin and tricetin were selected due to promising features regarding stability, toxicity, phototoxicity and thiol reactivity. The two flavones were further investigated for their photoprotective effects in different cellular and cell-free model systems, where they displayed antioxidant function via inhibition of lipid peroxidation and DNA damage prevention as seen by a decreased CPD formation. Additionally, the presence of luteolin and tricetin in the irradiation medium of fibroblasts rescued cell viability after irradiation with lethal UVA doses. Luteolin and tricetin, incorporated into a sunscreen-like formulation, showed protective effects in a cell culture model for topical application, which is assigned to their absorption in the UVA region.

An aging model was established to investigate differences in low-dose UVA-induced damage responses in young and aged skin cells and the efficacy of the flavones in photoprotection of aged skin. Aged skin fibroblasts displayed pronounced differences in regard to cellular respiration with an increased capacity to maximize respiration in response to stresses. Furthermore, aged fibroblasts showed decreased sensitivity towards UVA radiation as

measured by MTT assay. Basal ROS levels in aged cells were increased and the time courses of H2AX phosphorylation and CPD lesion formation differed from that of young fibroblasts. Interestingly, purinergic signalling was affected, as seen by altered expression of ectonucleotidases and substrate conversion measured by flow cytometry and UPLC analysis. These data indicate an increased extracellular formation of adenosine by aged fibroblasts, which is known to exert immunosuppressive and pro-tumoral effects and which was indirectly correlated to an increased invasive capacity of skin cancer cells.

Finally, the photoprotective capacity of the selected flavones on young and aged fibroblasts was evaluated. Supplementation of the irradiation medium of aged cells with luteolin or tricetin rescued the toxic effect of high UVA doses similar to the effect seen in young fibroblasts. Conclusively, luteolin and tricetin exert photoprotection in young and aged skin fibroblasts and provide additional antioxidative properties for a possible future use in sunscreen products.

6 Zusammenfassung

UV-Strahlung verursacht molekulare Schäden in der menschlichen Haut, die mit der Initiation und Progression verschiedener Krankheiten assoziiert sind. Im Kontext mit Hautkrebs standen bisher Effekte von UVB-Strahlung im Vordergrund. Die Wirkung von UVA-Exposition auf zellulär relevante Makromoleküle und Signalketten ist dagegen insbesondere im Niedrigdosisbereich nur wenig untersucht. Im Rahmen dieser Arbeit wurden Hautfibroblasten mit geringen, nicht letal-toxischen UVA-Dosen bestrahlt, um die Effekte auf Makromoleküle und Signalwege zu untersuchen. Die Ergebnisse zeigen eine UVA-abhängige Steigerung des oxidativen Stresses, gemessen an einem Anstieg der Lipidperoxidation und eine Induktion der Hämoxigenase-1 Expression. Bestrahlung mit niedrigen UVA-Dosen verringerte die basale und maximale Zellatmung, gemessen als verringerter Verbrauch von Sauerstoff mit Hilfe der bioenergetischen Flux Analyse. Die Untersuchung von Biomarkern für DNA-Schäden zeigte einen Anstieg der Phosphorylierung von Histon H2AX, sowie die Bildung direkt generierter und zeitlich verzögert gebildeter (indirekter) Cyclobutan Pyrimidin Dimere (CPD). Es konnte außerdem gezeigt werden, dass die Expression von Immunantwort-regulierenden Ektoenzymen nach Bestrahlung mit niedrigen Dosen UVA verändert war. Diese Daten zeigen, dass niedrig dosierte UVA-Strahlung Schäden in Hautfibroblasten verursacht und zusätzliche Photoprotektion im UVA-Bereich wünschenswert ist. In dieser Arbeit wurden daher pflanzliche Sekundärmetabolite aus der Gruppe der Flavone auf ihre Effektivität in der Photoprotektion untersucht. Luteolin und Tricetin wurden aufgrund ihrer Eigenschaften in Bezug auf Absorption, Stabilität, Toxizität, Phototoxizität und Thiolreaktivität ausgewählt. In Untersuchungen mit zellfreien und zellulären Testsystemen zeigten Luteolin und Tricetin antioxidative Wirkung auf UVA-induzierte Lipidperoxidation und die Prävention von DNA-Schäden nach Bestrahlung, gemessen an der Menge der gebildeten CPD. In einem Viabilitätsassay mit toxischen UVA-Dosen wurde ein schützender Effekt von exogen appliziertem Luteolin und Tricetin auf Hautfibroblasten gezeigt. Als photoprotektive Komponente einer Sonnenschutzcreme-adaptierten Formulierung zeigten Luteolin und Tricetin Photoprotektion aufgrund ihrer Absorption im UVA-Bereich.

Es wurde in dieser Arbeit außerdem ein Alterungs-Modell etabliert, um die Unterschiede in der niedrig dosierten UVA-Antwort zwischen jungen und alten Hautfibroblasten untersuchen zu können und um die Effektivität der ausgewählten Flavone speziell in gealterten Hautzellen

zu testen. Die gealterten Fibroblasten zeigten eine Stress-abhängig gesteigerte maximale Zellatmung im Vergleich zu normalen Fibroblasten. In Viabilitätsassays zeigten sie außerdem eine geringere Sensitivität gegenüber UVA-Strahlung und eine gesteigerte basale Bildung von reaktiven Sauerstoffspezies. In Zeitverläufen konnte gezeigt werden, dass sich die UVA-induzierte Phosphorylierung von H2AX und die Bildung von CPDs zwischen jungen und alten Zellen deutlich unterscheidet. Zudem war auch die Expression von Ektoenzymen des extrazellulären Purin Signalweges und die entsprechende Substratkonversion verändert, was mittels Durchflusszytometrie und Chromatographie gezeigt werden konnte. Aus den Daten ergibt sich eine gesteigerte extrazelluläre Verfügbarkeit von immun-suppressivem und pro-tumoral wirkendem Adenosin in gealterten Fibroblasten. Es konnte entsprechend in einem Invasions-Experiment gezeigt werden, dass Hautkrebszellen vermehrt in das Medium von gealterten Zellen einwandern.

Abschließend wurde die photoprotektive Wirkung der Flavone auf junge und alte Fibroblasten untersucht. Die Abnahme der Zellviabilität nach Bestrahlung mit hohen UVA Dosen konnte durch Zugabe von Luteolin und Tricetin in das Bestrahlungsmedium von jungen und alten Fibroblasten verhindert werden.

7 Danksagung

Ich möchte zuallererst meinem Doktorvater Prof. Wilhelm Stahl danken, der es mir ermöglichte, an einem für mich sehr interessanten Thema zu arbeiten. Es gab in meiner Zeit als Doktorandin viel von ihm zu lernen, besonders in den Bereichen Lehre und Storytelling. Danke Willi, für deine Geduld und die Freiheiten, die du mir während dieser Zeit gegeben hast.

Ich danke weiterhin Frau Prof. Vlada Urlacher für die Betreuung und Begutachtung meiner Arbeit und für ihre Zeit und Beiträge in zusätzlichen Meetings.

Dank geht außerdem an Prof. Peter Brenneisen für hilfreiche Ratschläge während der letzten drei Jahre, die Bekanntmachung mit seinem Hautalterungs-Modell und die Akzeptanz als außerordentliches Mitglied in der Brenneisen Gruppe.

Danke an David Stucki für die erste Einarbeitung und für die rege Diskussion und hilfreiche Ideen. In gleichem Atemzug danke ich Peter Graf, denn er hat außerordentlich zu meiner Arbeit beigetragen und zusammen mit David für eine eher umstrittene Art der Büro-Verschönerung gesorgt. Auch Heide Krahl möchte ich nennen und danken, da Sie mir bei der Durchführung wichtiger Experimente dieser Arbeit geholfen hat.

Herzlichster Dank gilt meinen Mädels Lara Ebbert, Lisa Haasler und Julia Steinhausen, die immer für mich da waren. Ihr werdet mir auch nach der Zeit am Institut als Freunde erhalten bleiben und das ist ein ganz besonderes Achievement. Ohne euch wäre die Zeit viel koffeinloser, ungesüßter und ungesprächiger gewesen.

Dr. Claudia von Montfort bin ich sehr dankbar für Ihre Offenheit in Gesprächen über berufliche, sowie private Themen und für die ständige Versorgung mit Süßigkeiten.

Ich danke Bodo Steckel für tatkräftige Unterstützung bei verschiedenen Methoden und für sein Interesse an meiner Forschung, sowie die vielen Diskussionen zum Thema.

Auch möchte ich Claudia Wyrich für die Unterstützung und nette Atmosphäre danken. Oft war Sie die erste und wichtigste Anlaufstelle bei Fragen rund um’s Labor.

Laura Bierwald war immer für ein nettes Gespräch zu haben und hat sich hervorragend um die nicht zu knapp vorhandenen bürokratischen Fragen und Belange gekümmert – danke dafür!

Dr. Nahal Brocke-Ahmadinejad hat uns Soft- und Hardware-technisch bestens ausgestattet und war ebenfalls eine sehr nette Kollegin.

Mit Alexandra Zepina konnte ich erste Erfahrung in der Konzeption und Betreuung einer Bachelorarbeit sammeln, auch dafür bin ich dankbar. Außerdem trugen ihre Experimente zu dieser Arbeit bei.

Prof. Klaus-Dietrich Kröncke danke ich für seine Offenheit in Seminaren und für seine Hilfsbereitschaft.

Weiterer Dank geht an den Institutsdirektor Prof. Andreas Reichert und seine Arbeitsgruppe, die in zahlreichen Seminaren und Meetings mit Fragen und Ideen die Diskussion zu meinem Thema angeregt hat. Hiermit danke ich auch allen ehemaligen und aktuellen Mitgliedern der AGs, die zu einer angenehmen Arbeitsatmosphäre beigetragen haben.

Letztendlich ist die Familie das Wichtigste, daher möchte ich meiner Familie den größten Dank aussprechen! Allen meinen Lieben und Nahestehenden danke ich für ihre Geduld und für den Zuspruch während der gesamten drei Jahre. Ihr habt immer an mich geglaubt und das ist ungemein motivierend.

8 List of References

1. Arda, O., Göksügür, N. & Tüzün, Y. Basic histological structure and functions of facial skin. *Clin. Dermatol.* **32**, 3–13 (2014).

2. Halprin, K. M. Epidermal 'turnover time' - a re-examination. *Br. J. Dermatol.* **86**, 14–19 (1972).

3. Elias, P. M. The skin barrier as an innate immune element. *Semin. Immunopathol.* **29**, 3–14 (2007).

4. Wang, J. X., Fukunaga-Kalabis, M. & Herlyn, M. Crosstalk in skin: melanocytes, keratinocytes, stem cells, and melanoma. *J. Cell Commun. Signal.* **10**, 191–196 (2016).

5. Bliss, D. Skin Anatomy: Image Details - NCI Visuals Online. *National Cancer Institute* https://visualsonline.cancer.gov/details.cfm?imageid=4604 accessed on 05/01/2021 (2010).

6. Eble, J. A. & De Rezende, F. F. Redox-relevant aspects of the extracellular matrix and its cellular contacts via integrins. *Antioxidants Redox Signal.* **20**, 1977–1993 (2014).

7. Theocharis, A. D., Manou, D. & Karamanos, N. K. The extracellular matrix as a multitasking player in disease. *FEBS Journal* vol. 286 2830–2869 (2019).

8. Gilchrest, B. A., Karassik, R. L., Wilkins, L. M., Vrabel, M. A. & Maciag, T. Autocrine and paracrine growth stimulation of cells derived from human skin. *J. Cell. Physiol.* **117**, 235–240 (1983).

9. Burnstock, G. & Boeynaems, J. M. Purinergic signalling and immune cells. *Purinergic Signal.* **10**, 529–564 (2014).

10. Lu, D. & Insel, P. A. Cellular Mechanisms of Tissue Fibrosis. 6. Purinergic signaling and response in fibroblasts and tissue fibrosis. *Am. J. Physiol. - Cell Physiol.* **306**, (2014).

11. Ferretti, E., Horenstein, A. L., Canzonetta, C., Costa, F. & Morandi, F. Canonical and non-canonical adenosinergic pathways. *Immunol. Lett.* **205**, 25–30 (2019).

12. Allard, B., Longhi, M. S., Robson, S. C. & Stagg, J. The ectonucleotidases CD39 and CD73: Novel checkpoint inhibitor targets. *Immunol. Rev.* **276**, 121–144 (2017).

13. Hesse, J. *et al.* CD73-derived adenosine and tenascin-C control cytokine production by epicardium-derived cells formed after myocardial infarction. *FASEB J.* **31**, 3040–3053 (2017).

14. Gao, Z. W., Dong, K. & Zhang, H. Z. The roles of CD73 in cancer. *BioMed Research International* vol. 2014 (2014).

15. Antonioli, L., Blandizzi, C., Pacher, P. & Haskó, G. Immunity, inflammation and cancer: A leading role for adenosine. *Nat. Rev. Cancer* **13**, 842–857 (2013).

16. Yu, M. *et al.* CD73 on cancer-associated fibroblasts enhanced by the A2B-mediated feedforward circuit enforces an immune checkpoint. *Nat. Commun.* **11**, (2020).

17. Riches, D. W. H., Watkins, J. L., Hensen, P. M. & Stanworth, D. R. Regulation of macrophage lysosomal secretion by adenosine, adenosine phosphate esters, and

related structural analogues of adenosine. *J. Leukoc. Biol.* **37**, 545–557 (1985).

18. Priebe, T., Nelson, J. A. & Platsoucas, C. D. Adenosine Receptors and Modulation of Natural Killer Cell Activity by Purine Nucleosides. *Cancer Res.* **50**, 4328–4331 (1990).

19. Monteran, L. & Erez, N. The dark side of fibroblasts: Cancer-associated fibroblasts as mediators of immunosuppression in the tumor microenvironment. *Front. Immunol.* **10**, 1–15 (2019).

20. Mouret, S. *et al.* Cyclobutane pyrimidine dimers are predominant DNA lesions in whole human skin exposed to UVA radiation. *Proc. Natl. Acad. Sci. U. S. A.* **103**, 13765–70 (2006).

21. Courdavault, S. *et al.* Larger yield of cyclobutane dimers than 8-oxo-7,8-dihydroguanine in the DNA of UVA-irradiated human skin cells. *Mutat. Res. - Fundam. Mol. Mech. Mutagen.* **556**, 135–142 (2004).

22. Douki, T., Reynaud-Angelin, A., Cadet, J. & Sage, E. Bipyrimidine photoproducts rather than oxidative lesions are the main type of DNA damage involved in the genotoxic effect of solar UVA radiation. *Biochemistry* **42**, 9221–9226 (2003).

23. Godar, D. UV Doses Worldwide. *Photochem. Photobiol.* **81**, 736–749 (2005).

24. Tyrrell, R. M. & Pidoux, M. Action Spectra for Human Skin Cells: Estimates of the Relative Cytotoxicity of the Middle Ultraviolet, Near Ultraviolet, and Violet Regions of Sunlight on Epidermal Keratinocytes. *Cancer Res.* **47**, 1825–1829 (1987).

25. Marionnet, C., Pierrard, C., Golebiewski, C. & Bernerd, F. Diversity of biological effects induced by longwave UVA rays (UVA1) in reconstructed skin. *PLoS One* **9**, (2014).

26. Rünger, T. M. & Kappes, U. P. Mechanisms of mutation formation with long-wave ultraviolet light (UVA). *Photodermatol. Photoimmunol. Photomed.* **24**, 2–10 (2008).

27. Seebode, C., Lehmann, J. & Emmert, S. Photocarcinogenesis and Skin Cancer Prevention Strategies. *Anticancer Res.* **36**, 1371–8 (2016).

28. Nilsen, L. T. N., Aalerud, T. N., Hannevik, M. & Veierød, M. B. UVB and UVA irradiances from indoor tanning devices. *Photochem. Photobiol. Sci.* **10**, 1129–1136 (2011).

29. Veierod, M. B. *et al.* A Prospective Study of Pigmentation, Sun Exposure, and Risk of Cutaneous Malignant Melanoma in Women. *JNCI J. Natl. Cancer Inst.* **95**, 1530–1538 (2003).

30. Piotrowska, A., Wierzbicka, J. & Zmijewski, M. A. Vitamin D in the skin physiology and pathology. *Acta Biochim. Pol.* **63**, 17–29 (2016).

31. Schuch, A. P., Moreno, N. C., Schuch, N. J., Menck, C. F. M. & Garcia, C. C. M. Sunlight damage to cellular DNA: Focus on oxidatively generated lesions. *Free Radic. Biol. Med.* **107**, 110–124 (2017).

32. Kimbrough, D. R. The Photochemistry of Sunscreens. *J. Chem. Educ.* **74**, 51–53 (1997).

33. Sisa, M., Bonnet, S. L., Ferreira, D. & Van Der Westhuizen, J. H. Photochemistry of flavonoids. *Molecules* **15**, 5196–5245 (2010).

34. Wicks, N. L., Chan, J. W., Najera, J. A., Ciriello, J. M. & Oancea, E. UVA

phototransduction drives early melanin synthesis in human melanocytes. *Curr. Biol.* **21**, 1906–1911 (2011).

35. Wischermann, K. *et al.* UVA radiation causes DNA strand breaks, chromosomal aberrations and tumorigenic transformation in HaCaT skin keratinocytes. *Oncogene* **27**, 4269–4280 (2008).

36. Cadet, J., Douki, T. & Ravanat, J. L. Oxidatively generated damage to cellular DNA by UVB and UVA radiation. *Photochem. Photobiol.* **91**, 140–155 (2015).

37. Young, A. R. *et al. Human Melanocytes and Keratinocytes Exposed to UVB or UVA In Vivo Show Comparable Levels of Thymine Dimers*. *Journal of Investigative Dermatology* vol. 111 (1998).

38. Ikehata, H. *et al.* UVA1 genotoxicity is mediated not by oxidative damage but by cyclobutane pyrimidine dimers in normal mouse skin. *J. Invest. Dermatol.* **128**, 2289–2296 (2008).

39. Bosca, F., Lhiaubet-Vallet, V., Cuquerella, M. C., Castell, J. V. & Miranda, M. A. The triplet energy of thymine in DNA. *J. Am. Chem. Soc.* **128**, 6318–6319 (2006).

40. Rochette, P. J. *et al.* UVA-induced cyclobutane pyrimidine dimers form predominantly at thymine-thymine dipyrimidines and correlate with the mutation spectrum in rodent cells. *Nucleic Acids Res.* **31**, 2786–2794 (2003).

41. Cadet, J., Mouret, S., Ravanat, J. L. & Douki, T. Photoinduced damage to cellular DNA: Direct and photosensitized reactions. *Photochem. Photobiol.* **88**, 1048–1065 (2012).

42. Ito, K., Inoue, S., Yamamoto, K. & Kawanishis, S. 8-Hydroxydeoxyguanosine formation at the 5’ site of 5’-GG-3’ sequences in double-stranded DNA by UV radiation with riboflavin. *J. Biol. Chem.* **268**, 13221–13227 (1993).

43. Yoshimoto, S., Kohara, N., Sato, N., Ando, H. & Ichihashi, M. Riboflavin plays a pivotal role in the UVA-induced cytotoxicity of fibroblasts as a key molecule in the production of H2O2 by UVA radiation in collaboration with amino acids and vitamins. *Int. J. Mol. Sci.* **21**, 1–20 (2020).

44. Baptista, M. S. *et al.* Type I and Type II Photosensitized Oxidation Reactions: Guidelines and Mechanistic Pathways. *Photochem. Photobiol.* **93**, 912–919 (2017).

45. Hiraku, Y., Ito, K., Hirakawa, K. & Kawanishi, S. Photosensitized DNA Damage and its Protection via a Novel Mechanism. *Photochem. Photobiol.* **83**, 205–212 (2007).

46. Perrett, C. M. *et al.* Azathioprine treatment photosensitizes human skin to ultraviolet A radiation. *Br. J. Dermatol.* **159**, 198–204 (2008).

47. Dissemond, J. *et al.* Protective and determining factors for the overall lipid peroxidation in ultraviolet A1-irradiated fibroblasts: In vitro and in vivo investigations. *Br. J. Dermatol.* **149**, 341–349 (2003).

48. Ayala, A., Muñoz, M. F. & Argüelles, S. Lipid peroxidation: Production, metabolism, and signaling mechanisms of malondialdehyde and 4-hydroxy-2-nonenal. *Oxid. Med. Cell. Longev.* **2014**, (2014).

49. Karran, P. & Brem, R. Protein oxidation, UVA and human DNA repair. *DNA Repair*

(Amst). **44**, 178–185 (2016).

50. Moreno, N. C. *et al.* The key role of UVA-light induced oxidative stress in human Xeroderma Pigmentosum Variant cells. *Free Radic. Biol. Med.* **131**, 432–442 (2019).

51. Clydesdale, G. J., Dandie, G. W. & Muller, H. K. Ultraviolet light induced injury: Immunological and inflammatory effects. *Immunol. Cell Biol.* **79**, 547–568 (2001).

52. Farr, P. M. & Diffey, B. L. Quantitative studies on cutaneous erythema induced by ultraviolet radiation. *Br. J. Dermatol.* **111**, 673–682 (1984).

53. Paunel, A. N. *et al.* Enzyme-independent nitric oxide formation during UVA challenge of human skin: Characterization, molecular sources, and mechanisms. *Free Radic. Biol. Med.* **38**, 606–615 (2005).

54. Warin, A. P. The ultraviolet erythemas in men. *Br. J. Dermatol.* **98**, 473–477 (1978).

55. Ziegler, A. *et al.* Sunburn and p53 in the onset of skin cancer. *Nature* vol. 372 773–776 (1994).

56. Hruza, L. L. & Pentland, A. P. Mechanisms of UV-Induced Inflammation. *J. Invest. Dermatol.* **100**, 35S-41S (1993).

57. Halliday, G. M., Bestak, R., Yuen, K. S., Cavanagh, L. L. & Barnetson, R. S. C. UVA-induced immunosuppression. *Mutat. Res. - Fundam. Mol. Mech. Mutagen.* **422**, 139–145 (1998).

58. Halliday, G. M. & Rana, S. Waveband and dose dependency of sunlight-induced immunomodulation and cellular changes. *Photochem. Photobiol.* **84**, 35–46 (2008).

59. Nguyen, P., Vin-Christian, K., Ming, M. E. & Berger, T. Aggressive squamous cell carcinomas in persons infected with the human immunodeficiency virus. *Arch. Dermatol.* **138**, 758–763 (2002).

60. Poon, T. S. C., Barnetson, R. S. C. & Halliday, G. M. Prevention of immunosuppression by sunscreens in humans is unrelated to protection from erythema and dependent on protection from ultraviolet A in the face of constant ultraviolet B protection. *J. Invest. Dermatol.* **121**, 184–190 (2003).

61. Krutmann, J., Hönigsmann, H. & Elmets, C. A. Dermatological phototherapy and photodiagnostic methods. in *Dermatological Phototherapy and Photodiagnostic Methods* 1–447 (2009).

62. Battie, C. *et al.* New insights in photoaging, UVA induced damage and skin types. *Exp. Dermatol.* **23**, 7–12 (2014).

63. Kammeyer, A. & Luiten, R. M. Oxidation events and skin aging. *Ageing Res. Rev.* **21**, 16–29 (2015).

64. Farage, M. A., Miller, K. W., Elsner, P. & Maibach, H. I. Intrinsic and extrinsic factors in skin ageing: A review. *Int. J. Cosmet. Sci.* **30**, 87–95 (2008).

65. Herrmann, G. *et al.* UVA irradiation stimulates the synthesis of various matrix-metalloproteinases (MMPs) in cultured human fibroblasts. *Exp. Dermatol.* **2**, 92–97 (1993).

66. Wlaschek, M., Briviba, K., Stricklin, G. P., Sies, H. & Scharffetter-Kochanek, K. Singlet oxygen may mediate the ultraviolet A-induced synthesis of interstitial collagenase. *J. Invest. Dermatol.* **104**, 194–198 (1995).

67. Sinha, R. P. & Häder, D.-P. UV-induced DNA damage and repair: a review. *Photochem. Photobiol. Sci.* **1**, 225–236 (2002).

68. Fousteri, M. & Mullenders, L. H. F. Transcription-coupled nucleotide excision repair in mammalian cells: Molecular mechanisms and biological effects. *Cell Research* vol. 18 73–84 (2008).

69. Lans, H., Hoeijmakers, J. H. J., Vermeulen, W. & Marteijn, J. A. The DNA damage response to transcription stress. *Nat. Rev. Mol. Cell Biol.* **20**, 766–784 (2019).

70. Chatterjee, N., Walker, G. C. Mechanisms of DNA damage, repair, and mutagenesis. Environmental and molecular mutagenesis. *Physiol. Behav.* **58**, 235–263 (2017).

71. Mazouzi, A. *et al.* Repair of UV-Induced DNA Damage Independent of Nucleotide Excision Repair Is Masked by MUTYH. *Mol. Cell* **68**, 797-807.e7 (2017).

72. Juzeniene, A., Grigalavicius, M., Baturaite, Z. & Moan, J. Minimal and maximal incidence rates of skin cancer in Caucasians estimated by use of sigmoidal UV dose-incidence curves. *Int. J. Hyg. Environ. Health* **217**, 839–844 (2014).

73. Cancer burden statistics and trends across Europe. *ECIS- European Cancer Information System* https://ecis.jrc.ec.europa.eu/ accessed on 03/02/2021.

74. Didona, D., Paolino, G., Bottoni, U. & Cantisani, C. Non melanoma skin cancer pathogenesis overview. *Biomedicines* **6**, 1–15 (2018).

75. D'Orazio, J., Jarrett, S., Amaro-Ortiz, A. & Scott, T. UV radiation and the skin. *Int. J. Mol. Sci.* **14**, 12222–12248 (2013).

76. Brash, D. E. Sunlight and the onset of skin cancer. *Trends in Genetics* vol. 13 410–414 (1997).

77. Agar, N. S. *et al.* The basal layer in human squamous tumors harbors more UVA than UVB fingerprint mutations: A role for UVA in human skin carcinogenesis. *Proc. Natl. Acad. Sci. U. S. A.* **101**, 4954–4959 (2004).

78. Sies, H. Hydrogen peroxide as a central redox signaling molecule in physiological oxidative stress: Oxidative eustress. *Redox Biol.* **11**, 613–619 (2017).

79. Thiele, J. J., Dreher, F. & Packer, L. Antioxidant defense systems in skin. *J. Toxicol. - Cutan. Ocul. Toxicol.* **21**, 119–160 (2002).

80. Stahl, W. & Sies, H. Antioxidant activity of carotenoids. *Molecular Aspects of Medicine* vol. 24 345–351 (2003).

81. Lewis, K. N., Mele, J., Hayes, J. D. & Buffenstein, R. Nrf2, a guardian of healthspan and gatekeeper of species longevity. in *Integrative and Comparative Biology* vol. 50 829–843 (2010).

82. Lee, J. M., Calkins, M. J., Chan, K., Kan, Y. W. & Johnson, J. A. Identification of the NF-E2-related factor-2-dependent genes conferring protection against oxidative stress in

primary cortical astrocytes using oligonucleotide microarray analysis. *J. Biol. Chem.* **278**, 12029–12038 (2003).

83. Tyrrell, R. M. Solar ultraviolet A radiation: An oxidizing skin carcinogen that activates heme oxygenase-1. *Antioxidants and Redox Signaling* vol. 6 835–840 (2004).

84. Kubben, N. *et al.* Repression of the antioxidant NRF2 pathway in premature aging. *Cell* **165**, 1361–1374 (2016).

85. Hirota, A. *et al.* Ultraviolet A irradiation induces NF-E2-related factor 2 activation in dermal fibroblasts: Protective role in UVA-induced apoptosis. *J. Invest. Dermatol.* **124**, 825–832 (2005).

86. d'Ischia, M. *et al.* Melanins and melanogenesis: From pigment cells to human health and technological applications. *Pigment Cell Melanoma Res.* **28**, 520–544 (2015).

87. Nasti, T. H. & Timares, L. MC1R, eumelanin and pheomelanin: Their role in determining the susceptibility to skin cancer. *Photochem. Photobiol.* **91**, 188–200 (2015).

88. Noonan, F. P. *et al.* Melanoma induction by ultraviolet A but not ultraviolet B radiation requires melanin pigment. *Nat. Commun.* **3**, 810–884 (2012).

89. Ben-Dor, A. *et al.* Carotenoids activate the antioxidant response element transcription system. *Mol. Cancer Ther.* **4**, 177–186 (2005).

90. Stahl, W. & Sies, H. β-Carotene and other carotenoids in protection from sunlight. *Am. J. Clin. Nutr.* **96**, 1179–1184 (2012).

91. Matsui, M. S. *et al.* Non-sunscreen photoprotection: Antioxidants add value to a sunscreen. *J. Investig. Dermatology Symp. Proc.* **14**, 56–59 (2009).

92. Tampucci, S., Burgalassi, S., Chetoni, P. & Monti, D. Cutaneous permeation and penetration of sunscreens: Formulation strategies and in vitro methods. *Cosmetics* **5**, (2018).

93. Wang, J. *et al.* Recent advances on endocrine disrupting effects of UV filters. *Int. J. Environ. Res. Public Health* **13**, 1–11 (2016).

94. Saewan, N. & Jimtaisong, A. Natural products as photoprotection. *J. Cosmet. Dermatol.* **14**, 47–63 (2015).

95. Fuehring, S. Standardisation mandate assigned to cen concerning methods for testing efficacy of sunscreen products. *Eur. Comm.* 1–78 (2006).

96. Thilakarathna, S. H. & Vasantha Rupasinghe, H. P. Flavonoid bioavailability and attempts for bioavailability enhancement. *Nutrients* **5**, 3367–3387 (2013).

97. Camera, E. *et al.* Astaxanthin, canthaxanthin and β-carotene differently affect UVA-induced oxidative damage and expression of oxidative stress-responsive enzymes. *Exp. Dermatol.* **18**, 222–231 (2009).

98. Zerres, S. & Stahl, W. Carotenoids in human skin. *Biochimica et Biophysica Acta - Molecular and Cell Biology of Lipids* vol. 1865 (2020).

99. Kaulmann, A. & Bohn, T. Carotenoids, inflammation, and oxidative stress-implications

of cellular signaling pathways and relation to chronic disease prevention. *Nutr. Res.* **34**, 907–929 (2014).

100. Eichler, O., Sies, H. & Stahl, W. Divergent optimum levels of lycopene, beta-carotene and lutein protecting against UVB irradiation in human fibroblaststst. *Photochem. Photobiol.* **75**, 503–6 (2002).

101. Lawrence, K. P., Long, P. F. & Young, A. R. Mycosporine-Like Amino Acids for Skin Photoprotection. *Curr. Med. Chem.* **25**, 5512–5527 (2017).

102. Stahl, W. & Sies, H. Photoprotection by dietary carotenoids: Concept, mechanisms, evidence and future development. *Mol. Nutr. Food Res.* **56**, 287–295 (2012).

103. Hostetler, G. L., Ralston, R. A. & Schwartz, S. J. Flavones: Food sources, bioavailability, metabolism, and bioactivity. *Advances in Nutrition* vol. 8 423–435 (2017).

104. Sisa, M., Bonnet, S. L., Ferreira, D. & Van Der Westhuizen, J. H. Photochemistry of flavonoids. *Molecules* vol. 15 5196–5245 (2010).

105. Harborne, J. B. & Williams, C. A. Advances in flavonoid research since 1992. *Phytochemistry* **55**, (2000).

106. Catarino, M., Alves-Silva, J., Pereira, O. & Cardoso, S. Antioxidant Capacities of Flavones and Benefits in Oxidative-Stress Related Diseases. *Curr. Top. Med. Chem.* **15**, 105–119 (2015).

107. Tsimogiannis, D., Samiotaki, M., Panayotou, G. & Oreopoulou, V. Characterization of Flavonoid Subgroups and Hydroxy Substitution by HPLC-MS/MS. *Molecules* **12**, 593–606 (2007).

108. Lopez-Lazaro, M. Distribution and Biological Activities of the Flavonoid Luteolin. *Mini-Reviews Med. Chem.* **9**, 31–59 (2008).

109. Wölfle, U. *et al.* UVB-induced DNA damage, generation of reactive oxygen species, and inflammation are effectively attenuated by the flavonoid luteolin in vitro and in vivo. *Free Radic. Biol. Med.* **50**, 1081–1093 (2011).

110. Verschooten, L. *et al.* The flavonoid luteolin increases the resistance of normal, but not malignant keratinocytes, against UVB-induced apoptosis. *J. Invest. Dermatol.* **130**, 2277–2285 (2010).

111. Wölfle, U. *et al.* Luteolin prevents solar radiation-induced matrix metalloproteinase-1 activation in human fibroblasts: A role for p38 mitogen-activated protein kinase and interleukin-20 released from keratinocytes. *Rejuvenation Res.* **15**, 466–475 (2012).

112. Martos, I., Ferreres, F. & Tomás-Barberán, F. A. Identification of flavonoid markers for the botanical origin of Eucalyptus honey. *J. Agric. Food Chem.* **48**, 1498–1502 (2000).

113. Campos, M. G., Webby, R. F. & Markham, K. R. The unique occurrence of the flavone aglycone tricetin in Myrtaceae pollen. *Zeitschrift fur Naturforsch. - Sect. C J. Biosci.* **57**, 944–946 (2002).

114. Yao, L. *et al.* Quantitative High-Performance Liquid Chromatography Analyses of Flavonoids in Australian Eucalyptus Honeys. *J. Agric. Food Chem.* **52**, 210–214 (2004).

115. Singh, B., Sahu, P. M. & Sharma, R. A. Flavonoids from Heliotropium subulatum exudate and their evaluation for antioxidant, antineoplastic and cytotoxic activities II. *Cytotechnology* **69**, 103–115 (2017).

116. Geraets, L. *et al.* Inhibition of LPS-induced pulmonary inflammation by specific flavonoids. *Biochem. Biophys. Res. Commun.* **382**, 598–603 (2009).

117. Chung, T. Te *et al.* Tricetin suppresses human oral cancer cell migration by reducing matrix metalloproteinase-9 expression through the mitogen-activated protein kinase signaling pathway. *Environ. Toxicol.* **32**, 2392–2399 (2017).

118. Chang, P. Y. *et al.* Tricetin inhibits human osteosarcoma cells metastasis by transcriptionally repressing MMP-9 via p38 and Akt pathways. *Environ. Toxicol.* **32**, 2032–2040 (2017).

119. Yang, X. *et al.* Nobiletin delays aging and enhances stress resistance of Caenorhabditis elegans. *Int. J. Mol. Sci.* **21**, (2020).

120. Walle, T. Methoxylated flavones, a superior cancer chemopreventive flavonoid subclass? *Semin. Cancer Biol.* **17**, 354–362 (2007).

121. Hollman, P. C. H. Absorption, bioavailability, and metabolism of flavonoids. *Pharm. Biol.* **42**, 74–83 (2004).

122. Murakami, A. *et al.* Characteristic rat tissue accumulation of nobiletin, a chemopreventive polymethoxyflavonoid, in comparison with luteolin. *BioFactors* **16**, 73–82 (2002).

123. Kandaswami, C., Perkins, E., Drzewiecki, G., Soloniuk, D. S. & Middleton, E. J. Differential inhibition of proliferation of human squamous cell carcinoma, gliosarcoma and embryonic fibroblast-like lung cells in culture by plant flavonoids. *Anticancer. Drugs* 525–530 (1992).

124. Murakami, A. *et al.* Inhibitory effect of citrus nobiletin on phorbol ester-induced skin inflammation, oxidative stress, and tumor promotion mice. *Cancer Res.* **60**, 5059–5066 (2000).

125. Ozaki, K. *et al.* Quantification of nobiletin and tangeretin in citrus by micellar electrokinetic capillary chromatography. *Food Sci. Technol. Res.* **12**, 284–289 (2006).

126. Li, X. *et al.* Tangeretin inhibits oxidative stress and inflammation via upregulating nrf-2 signaling pathway in collagen-induced arthritic rats. *Pharmacology* **104**, 187–195 (2019).

127. Liang, F. *et al.* Attenuation of tert-Butyl Hydroperoxide (t-BHP)-Induced Oxidative Damage in HepG2 Cells by Tangeretin: Relevance of the Nrf2-ARE and MAPK Signaling Pathways. *J. Agric. Food Chem.* **66**, 6317–6325 (2018).

128. Yoon, J. H. *et al.* Tangeretin reduces ultraviolet B (UVB)-induced cyclooxygenase-2 expression in mouse epidermal cells by blocking mitogen-activated protein kinase (MAPK) activation and reactive oxygen species (ROS) generation. *J. Agric. Food Chem.* **59**, 222–228 (2011).

129. Yancik, R. & Ries, L. A. G. Cancer in Older Persons: An International Issue in an Aging

World. *Semin. Oncol.* **31**, 128–136 (2004).

130. Campisi, J. Aging, cellular senescence, and cancer. *Annu. Rev. Physiol.* **75**, 685–705 (2013).

131. Collado, M., Blasco, M. A. & Serrano, M. Cellular Senescence in Cancer and Aging. *Cell* vol. 130 223–233 (2007).

132. Dimri, G. P. *et al.* A biomarker that identifies senescent human cells in culture and in aging skin in vivo. *Proc. Natl. Acad. Sci. U. S. A.* **92**, 9363–9367 (1995).

133. Hayflick, L. & Moorhead, P. S. The serial cultivation of human diploid cell strains. *Exp. Cell Res.* **25**, 585–621 (1961).

134. Harley, C. B., Futcher, A. B. & Greider, C. W. Telomeres shorten during ageing of human fibroblasts. *Nature* **345**, 458–460 (1990).

135. Harman, D. Aging: a theory based on free radical and radiation chemistry. *J. Gerontol.* **11**, 298–300 (1956).

136. Harman, D. The Biologic Clock: The Mitochondria? *J. Am. Geriatr. Soc.* **20**, 145–147 (1972).

137. Campisi, J. Senescent cells, tumor suppression, and organismal aging: Good citizens, bad neighbors. *Cell* **120**, 513–522 (2005).

138. Williams, G. C. Pleiotropy, natural selection and the evolution of senescence. *Evolution (N. Y).* **11**, 398–411 (1957).

139. Coppé, J. P. *et al.* Senescence-associated secretory phenotypes reveal cell-nonautonomous functions of oncogenic RAS and the p53 tumor suppressor. *PLoS Biol.* **6**, (2008).

140. Chung, H. Y., Sung, B., Jung, K. J., Zou, Y. & Yu, B. P. The molecular inflammatory process in aging. *Antioxidants and Redox Signaling* vol. 8 572–581 (2006).

141. Chung, H. Y. *et al.* Redefining chronic inflammation in aging and age-related diseases: Proposal of the senoinflammation concept. *Aging Dis.* **10**, 367–382 (2019).

142. Blagosklonny, M. V. Aging and immortality: Quasi-programmed senescence and its pharmacologic inhibition. *Cell Cycle* **5**, 2087–2102 (2006).

143. Fenske, N. A. & Lober, C. W. Structural and functional changes of normal aging skin. *J. Am. Acad. Dermatol.* **15**, 571–585 (1986).

144. Cole, M. A., Quan, T., Voorhees, J. J. & Fisher, G. J. Extracellular matrix regulation of fibroblast function: redefining our perspective on skin aging. *J. Cell Commun. Signal.* **12**, 35–43 (2018).

145. Gilchrest, B. A., Stoff, J. S. & Soter, N. A. Chronologic aging alters the response to ultraviolet-induced inflammation in human skin. *J. Invest. Dermatol.* **79**, 11–15 (1982).

146. Hazane-Puch, F. *et al.* Study of fibroblast gene expression in response to oxidative stress induced by hydrogen peroxide or UVA with skin aging. *Eur. J. Dermatology* **20**, 308–320 (2010).

147. Hung, C. F., Chen, W. Y., Aljuffali, I. A., Shih, H. C. & Fang, J. Y. The risk of hydroquinone and sunscreen over-absorption via photodamaged skin is not greater in senescent skin as compared to young skin: Nude mouse as an animal model. *Int. J. Pharm.* **471**, 135–145 (2014).

148. Hung, C. F., Fang, C. L., Al-Suwayeh, S. A., Yang, S. Y. & Fang, J. Y. Evaluation of drug and sunscreen permeation via skin irradiated with UVA and UVB: Comparisons of normal skin and chronologically aged skin. *J. Dermatol. Sci.* **68**, 135–148 (2012).

149. Boukamp, P. *et al.* Phenotypic and genotypic characteristics of a cell line from a squamous cell carcinoma of human skin. *J. Natl. Cancer Inst.* **68**, 415–427 (1982).

150. Esterbauer, H., Schaur, R. J. & Zollner, H. Chemistry and biochemistry of 4-hydroxynonenal, malonaldehyde and related aldehydes. *Free Radical Biology and Medicine* vol. 11 81–128 (1991).

151. Hempel, S. L., Buettner, G. R., O'Malley, Y. Q., Wessels, D. A. & Flaherty, D. M. Dihydrofluorescein diacetate is superior for detecting intracellular oxidants: Comparison with 2',7'-dichlorodihydrofluorescein diacetate, 5(and 6)-carboxy-2',7'-dichlorodihydrofluorescein diacetate, and dihydrorhodamine 123. *Free Radic. Biol. Med.* **27**, 146–159 (1999).

152. Halliwell, B. & Whiteman, M. Measuring reactive species and oxidative damage in vivo and in cell culture: How should you do it and what do the results mean? *Br. J. Pharmacol.* **142**, 231–255 (2004).

153. Mosmann, T. Rapid colorimetric assay for cellular growth and survival: Application to proliferation and cytotoxicity assays. *J. Immunol. Methods* **65**, 55–63 (1983).

154. Brugè, F., Tiano, L., Astolfi, P., Emanuelli, M. & Damiani, E. Prevention of UVA-induced oxidative damage in human dermal fibroblasts by new UV filters, assessed using a novel In Vitro experimental system. *PLoS One* **9**, (2014).

155. Matts, P. J. *et al.* The COLIPA *in vitro* UVA method: a standard and reproducible measure of sunscreen UVA protection. *Int. J. Cosmet. Sci.* **32**, 35–46 (2010).

156. Food and Drug Administration Department of Health and Human Services. *Sunscreen Drug Products for Over-the-Counter Human Use; Final Rules and Proposed Rules*. (2011).

157. Lowry, O. H., Rosebrough, N. J., Farr, A. L. & Randall, R. J. Protein measurement with the Folin phenol reagent. *J. Biol. Chem.* **193**, 265–275 (1951).

158. Laemmli, U. K. Cleavage of Structural Proteins during the Assembly of the Head of Bacteriophage T4. *Nature* **227**, 680–685 (1970).

159. Ostling, O. & Johanson, K. J. Microelectrophoretic study of radiation-induced DNA damages in individual mammalian cells. *Biochem. Biophys. Res. Commun.* **123**, 291–298 (1984).

160. Singh, N. P., McCoy, M. T., Tice, R. R. & Schneider, E. L. A simple technique for quantitation of low levels of DNA damage in individual cells. *Exp. Cell Res.* **175**, 184–191 (1988).

161. Gedik, C. M., Ewen, S. W. B. & Collins, A. R. Single-cell Gel Electrophoresis Applied to the Analysis of UV-C Damage and Its Repair in Human Cells. *Int. J. Radiat. Biol.* **62**, 313–320 (1992).

162. Collins, A. R., Dobson, V. L., Dušinská, M., Kennedy, G. & Štětina, R. The comet assay: What can it really tell us? *Mutat. Res. - Fundam. Mol. Mech. Mutagen.* **375**, 183–193 (1997).

163. Seawell, P. C., Smith, C. A. & Ganesan, A. K. den V gene of bacteriophage T4 determines a DNA glycosylase specific for pyrimidine dimers in DNA. *J. Virol.* **35**, 790–796 (1980).

164. Azqueta, A., Shaposhnikov, S. & R., A. DNA Repair Measured by the Comet Assay. *DNA Repair (Amst).* 615–636 (2011).

165. Chen, Q. M. *et al.* Molecular analysis of H2O2-induced senescent-like growth arrest in normal human fibroblasts: p53 and Rb control G1 arrest but not cell replication. *Biochem. J.* **332**, 43–50 (1998).

166. Maejima, Y., Adachi, S., Ito, H., Hirao, K. & Isobe, M. Induction of premature senescence in cardiomyocytes by doxorubicin as a novel mechanism of myocardial damage. *Aging Cell* **7**, 125–136 (2008).

167. Alili, L., Diekmann, J., Giesen, M., Holtkötter, O. & Brenneisen, P. A drug-induced accelerated senescence (DIAS) is a possibility to study aging in time lapse. *Age (Omaha).* **36**, 1329–1343 (2014).

168. Hanahan, D. & Weinberg, R. A. The Hallmarks of Cancer. *Cell* **100**, 57–70 (2000).

169. Boyden, S. The chemotactic effect of mixtures of antibody and antigen on polymorphonuclear leucocytes. *J. Exp. Med.* **115**, 453–466 (1962).

170. Tarras-Wahlberg, N. *et al.* Changes in ultraviolet absorption of sunscreens after ultraviolet irradiation. *J. Invest. Dermatol.* **113**, 547–553 (1999).

171. Karlsson, I., Hillerström, L., Stenfeldt, A. L., Mårtensson, J. & Börje, A. Photodegradation of dibenzoylmethanes: Potential cause of photocontact allergy to sunscreens. *Chem. Res. Toxicol.* **22**, 1881–1892 (2009).

172. Wagener, T. Untersuchungen zur photoprotektiven Wirkung von Carotinoiden in Modellsystemen und dermalen Fibroblasten. (Heinrich-Heine University, 2009).

173. Surh, Y. J., Kundu, J. K., Na, H. K. & Lee, J. S. Redox-sensitive transcription factors as prime targets for chemoprevention with anti-inflammatory and antioxidative phytochemicals. *J. Nutr.* **135**, (2005).

174. Pae, H. O. *et al.* Roles of heme oxygenase-1 in curcumin-induced growth inhibition in rat smooth muscle cells. *Exp. Mol. Med.* **39**, 267–277 (2007).

175. Xiang, Y., Liu, G., Yang, L. & Zhong, J. L. UVA-induced protection of skin through the induction of heme oxygenase-1. *Biosci. Trends* **5**, 239–244 (2011).

176. Croft, K. D. *et al.* Structural requirements of flavonoids to induce heme oxygenase-1 expression. *Free Radic. Biol. Med.* **113**, 165–175 (2017).

177. Mitsui, Y. & Schneider, E. L. Relationship Between Cell Replication and Volume in Senescent Human Diploid Fibroblasts. *Mech. Ageing Dev.* **I**, 45–56 (1976).

178. Greenberg, S. B., Grove, G. L. & Cristofalo, V. J. Cell size in aging monolayer cultures. *In Vitro* **13**, 297–300 (1977).

179. Fairbairn, D. W., Olive, P. L. & O'Neill, K. L. The comet assay: a comprehensive review. *Mutat. Res. Genet. Toxicol.* **339**, 37–59 (1995).

180. Wright, G. E., Hübscher, U., Khan, N. N., Focher, F. & Verri, A. Inhibitor analysis of calf thymus DNA polymerases α, δ and ϵ. *FEBS Lett.* **341**, 128–130 (1994).

181. Gavande, N. S. *et al.* Design and Structure-Guided Development of Novel Inhibitors of the Xeroderma Pigmentosum Group A (XPA) Protein-DNA Interaction. *J. Med. Chem.* **60**, 8055–8070 (2017).

182. Torres, Á. *et al.* Extracellular adenosine promotes cell migration/invasion of Glioblastoma Stem-like Cells through A3 Adenosine Receptor activation under hypoxia. *Cancer Lett.* **446**, 112–122 (2019).

183. Sample, A. & He, Y. Y. Mechanisms and prevention of UV-induced melanoma. *Photodermatol. Photoimmunol. Photomed.* **34**, 13–24 (2018).

184. Marrot, L. *et al.* Photostability of sunscreen products influences the efficiency of protection with regard to UV-induced genotoxic or photoageing-related endpoints. *Br. J. Dermatol.* **151**, 1234–1244 (2004).

185. Gonzalez, H. *et al.* Photostability of commercial sunscreens upon sun exposure and irradiation by ultraviolet lamps. *BMC Dermatol.* **7**, 1–9 (2007).

186. Birch-Machin, M. A., Russell, E. V. & Latimer, J. A. Mitochondrial DNA damage as a biomarker for ultraviolet radiation exposure and oxidative stress. *Br. J. Dermatol.* **169**, 9–14 (2013).

187. Ferreira, I. L., Resende, R., Ferreiro, E., C.Rego, A. & F.Pereira, C. Multiple Defects in Energy Metabolism in Alzheimers Disease. *Curr. Drug Targets* **999**, 1–11 (2010).

188. Goldstein, S., Ballantyne, S. R., Robson, A. L. & Moerman, E. J. Energy metabolism in cultured human fibroblasts during aging in vitro. *J. Cell. Physiol.* **112**, 419–424 (1982).

189. Zhang, H. *et al.* Reduction of elevated proton leak rejuvenates mitochondria in the aged cardiomyocyte. *Elife* **9**, 1–18 (2020).

190. Hill, B. G. *et al.* Integration of cellular bioenergetics with mitochondrial quality control and autophagy. in *Biological Chemistry* vol. 393 1485–1512 (2012).

191. Vida, C. *et al.* The aged-related increase in xanthine oxidase expression and activity in several tissues from mice is not shown in long-lived animals. *Biogerontology* **12**, 551–564 (2011).

192. Liemburg-Apers, D. C., Schirris, T. J. J., Russel, F. G. M., Willems, P. H. G. M. & Koopman, W. J. H. Mitoenergetic Dysfunction Triggers a Rapid Compensatory Increase in Steady-State Glucose Flux. *Biophys. J.* **109**, 1372–1386 (2015).

193. Takebayashi, S. *et al.* Retinoblastoma protein promotes oxidative phosphorylation

through upregulation of glycolytic genes in oncogene-induced senescent cells. *Aging Cell* **14**, 689–697 (2015).

194. Kaplon, J. *et al.* A key role for mitochondrial gatekeeper pyruvate dehydrogenase in oncogene-induced senescence. *Nature* **498**, 109–112 (2013).

195. Wang, D. *et al.* Apoptotic transition of senescent cells accompanied with mitochondrial hyper-function. *Oncotarget* **7**, 28286–28300 (2016).

196. Nacarelli, T., Azar, A. & Sell, C. Mitochondrial stress induces cellular senescence in an mTORC1-dependent manner. *Free Radic. Biol. Med.* **95**, 133–154 (2016).

197. Martínez, J. *et al.* Mitofusins modulate the increase in mitochondrial length, bioenergetics and secretory phenotype in therapy-induced senescent melanoma cells. *Biochem. J.* **476**, 2463–2486 (2019).

198. Quijano, C. *et al.* Oncogene-induced senescence results in marked metabolic and bioenergetic alterations. *Cell Cycle* **11**, 1383–1392 (2012).

199. Delfarah, A. *et al.* Inhibition of nucleotide synthesis promotes replicative senescence of human mammary epithelial cells. *J. Biol. Chem.* **294**, 10564–10578 (2019).

200. El-Abaseri, T. B., Putta, S. & Hansen, L. A. Ultraviolet irradiation induces keratinocyte proliferation and epidermal hyperplasia through the activation of the epidermal growth factor receptor. *Carcinogenesis* **27**, 225–231 (2006).

201. Ouhtit, A. *et al.* Temporal events in skin injury and the early adaptive responses in ultraviolet-irradiated mouse skin. *Am. J. Pathol.* **156**, 201–207 (2000).

202. Wenczl, E. *et al.* Physiological Doses of Ultraviolet Irradiation Induce DNA Strand Breaks in Cultured Human Melanocytes, as Detected by Means of an Immunochemical Assay. *Photochem. Photobiol.* **66**, 826–830 (1997).

203. Barañano, D. E., Rao, M., Ferris, C. D. & Snyder, S. H. Biliverdin reductase: A major physiologic cytoprotectant. *Proc. Natl. Acad. Sci. U. S. A.* **99**, 16093–16098 (2002).

204. Scarpato, R. *et al.* Kinetics of nuclear phosphorylation (γ-H2AX) in human lymphocytes treated in vitro with UVB, bleomycin and mitomycin C. *Mutagenesis* **28**, 465–473 (2013).

205. Svobodová, A. R. *et al.* DNA damage after acute exposure of mice skin to physiological doses of UVB and UVA light. *Arch. Dermatol. Res.* **304**, 407–412 (2012).

206. Marti, T. M., Hefner, E., Feeney, L., Natale, V. & Cleaver, J. E. H2AX phosphorylation within the G1 phase after UV irradiation depends on nucleotide excision repair and not DNA double-strand breaks. *Proc. Natl. Acad. Sci.* **103**, 9891–9896 (2006).

207. Toyooka, T. & Ibuki, Y. Coexposure to benzo[*a*]pyrene and UVA induces phosphorylation of histone H2AX. *FEBS Lett.* **579**, 6338–6342 (2005).

208. Premi, S. *et al.* Chemiexcitation of melanin derivatives induces DNA photoproducts long after UV exposure. *Science (80-.).* **347**, 842–847 (2015).

209. Delinasios, G. J., Karbaschi, M., Cooke, M. S. & Young, A. R. Vitamin E inhibits the UVAI induction of ‘light’ and ‘dark’ cyclobutane pyrimidine dimers, and oxidatively

generated DNA damage, in keratinocytes. *Sci. Rep.* **8**, 1–12 (2018).

210. Brand, M. D. & Nicholls, D. G. Assessing mitochondrial dysfunction in cells. *Biochemical Journal* vol. 435 297–312 (2011).

211. Liu, T., Zhou, L., Li, D., Andl, T. & Zhang, Y. Cancer-associated fibroblasts build and secure the tumor microenvironment. *Front. Cell Dev. Biol.* **7**, 1–14 (2019).

212. Navas, L. E. & Carnero, A. NAD+ metabolism, stemness, the immune response, and cancer. *Signal Transduction and Targeted Therapy* vol. 6 1–20 (2021).

213. Camacho-Pereira, J. *et al.* CD38 Dictates Age-Related NAD Decline and Mitochondrial Dysfunction through an SIRT3-Dependent Mechanism. *Cell Metab.* **23**, 1127–1139 (2016).

214. Crooke, A. *et al.* Low expression of CD39 and CD73 genes in centenarians compared with octogenarians. *Immun. Ageing* **14**, 11 (2017).

215. Sek, K. *et al.* Targeting adenosine receptor signaling in cancer immunotherapy. *Int. J. Mol. Sci.* **19**, (2018).

216. Vijayan, D., Young, A., Teng, M. W. L. & Smyth, M. J. Targeting immunosuppressive adenosine in cancer. *Nat. Rev. Cancer* **17**, 709–724 (2017).

217. Stagg, J. *et al.* Anti-CD73 antibody therapy inhibits breast tumor growth and metastasis. *Proc. Natl. Acad. Sci. U. S. A.* **107**, 1547–1552 (2010).

218. Roh, M., Wainwright, D. A., Wu, J. D., Wan, Y. & Zhang, B. Targeting CD73 to augment cancer immunotherapy. *Curr. Opin. Pharmacol.* **53**, 66–76 (2020).